Optimisation of Ring-laser Gyroscopes.

A thesis
submitted in partial fulfillment
of the requirements for the Degree
of
Doctor of Philosophy in Physics
in the
University of Canterbury

by

Doug Wright

University of Canterbury
2001

Abstract

Stochastic drift noise sources that usually arise from coupling with the external environment limit the resolution of the Canterbury He:Ne ring-laser gyroscopes as rotation sensors. The characterisation of such stochastic drifts is discussed along with effects that bring about the coupling between the environment and the gyroscope output. Techniques which may be employed to minimise the coupling are also investigated.

The optimal He:Ne gas pressure with respect to the requirement that output power be maximised while retaining single longitudinal mode operation is investigated. In addition to the empirical optimisation of gas pressure the mechanisms that lead to the reported observations are discussed. In particular it is proposed that radiation trapping plays an important role in determining the optimum fill pressure.

The effects of the gain medium when the optical powers of the counter-propagating beams are unequal is analysed in the context of the third-order theory of the laser. With appropriate approximations a dominant term is found that heavily influences frequency pushing and pulling in the 4 m perimeter high-Q gyroscope C-II. Experimental results are in good agreement with the theoretical predictions in the cases where the assumptions of the theory are valid.

Long-term drift sources are analysed and described by the fractional Brownian motion (fBm) model. The impact of this drift process on the resolution of the gyroscope is investigated. The relationship between the quantum limited white frequency noise due to spontaneous emission and the fBm drift noise is of particular interest since it defines the averaging time that produces the best resolution of the rotation rate measured in terms of the beat frequency between the counter-propagating beams of the gyroscope.

The optical frequency stabilisation of C-II is described and analysed. The method employed is somewhat different from traditional stabilisation schemes because the laser possesses very low output powers due to extremely high reflection mirrors. The applicability of traditional stabilisation schemes to a low power ($\sim$ 10 pW) laser, such as C-II, is discussed.

An experimental investigation of injected coloured noise in the ring-laser gyroscope is reported. In particular the probability distribution of the steady-state phase difference between the counter-propagating waves of a locked ring-laser gyroscope is measured for various noise inputs. The results are found to be in good agreement with previous theoretical predictions.

Acknowledgements

First of all I would like to thank my supervisor Geoff Stedman for his guidance throughout my time as a graduate student. I would also like to thank Steven Cooper and Tom King for providing invaluable advice regarding the various aspects of experimental physics relevant to the project.

There are many other people within the Department of Physics and Astronomy at Canterbury who have helped me. In particular I would like to thank Duncan McLeod, Ulli Schreiber, Clive Rowe, Christian Wyss, Bryn Currie,and Josh Wood.

Very little of the work presented in this thesis would have been possible without the substantial contribution of the technical workshops. In particular I would like to thank Graeme MacDonald and Rob Thirkettle.

On a personal note I would like to thank those who have supported me, entertained me, and (sensibly) prevented me from spending too much time underground: Daniel Booth, James Murray, Dale Ellerm, Sarah Beston, Nic Sullivan, Mel Orchard, Cameron Hart, Luke Wagoner, and all of the *good* boys. In particular I would like to thank my mother, Jean Wright, for giving much encouragement.

Finally I would like to acknowledge the assistance of the University of Canterbury Doctoral Scholarship and Edward and Isobel Kidson Scholarship.

Contents

List of Figures

List of Tables

Chapter 1

Introduction

The ring-laser gyroscope was first demonstrated by Macek and Davis soon after the invention of the laser [11]. In the case of a linear laser, the cavity eigenmodes consist of two oppositely directed travelling waves of approximately equal amplitude and frequency which jointly form a standing wave [12]. On the other hand, the oppositely directed waves are independent in a ring-laser, inasmuch as they may oscillate with different frequencies and amplitudes. The expected frequency difference between the counter-propagating travelling waves in the ring-laser gyroscope is given by [13, 14]

$$\delta f = \frac{4\boldsymbol{\Omega} \cdot \mathbf{A}}{\lambda L}, \tag{1.1}$$

where $\boldsymbol{\Omega}$ is the rotation rate, $\mathbf{A}$ and L are the area and the perimeter of the ring-laser, and λ the wavelength at which the laser operates in the absence of rotation. There are many effects observed in ring-laser gyroscopes that cause the observed beat frequency between the oppositely directed travelling waves to differ from the value predicted by Equation (1.1). More complicated descriptions are required in order to understand these effects. The focus of this work is to discuss several examples of these effects that are significant in the Canterbury ring-lasers, investigate methods of characterisation, and attempt to identify and implement experimental approaches that seek to reduce the significance of such effects. This investigation of optimisation of ring-laser gyroscope performance is pursued with the aim of improving the stability and resolution of the gyroscope beat frequency, and consequently the precision with which Earth rotation, in terms of Equation (1.1), may be measured.

At the time of writing the Canterbury ring-laser group has three ring-laser gyroscopes, referred to as C-I, C-II, and G0.[1] A beat signal between the counter-propagating waves that is due to Earth rotation is observed in all three gyroscopes. In addition there is a 1.6 m high-Q linear laser called LI. C-I and C-II are similar instruments in terms of dimension. However the construction of the two instruments is radically different. C-I was the first laser constructed at Canterbury.

[1] A fourth gyroscope, UG, was commissioned in late 2000.

It was moved to a disused military command bunker since the technical noise due to the building in which it was housed proved to be a limiting factor in its performance. All gyros constructed since have been housed in this bunker called the *Cashmere cavern*. The second laser, C-II, is of a much higher technical specification than C-I and has therefore proved to be much more stable than C-I. The laser C-II is the result of a collaboration between the University of Canterbury, Technischen Universität München and Bundesamt für Angewandte Geodäsie. Both C-I and C-II have an area of approximately 1 m^2 and have similar mirror and excitation configurations. The third ring-laser, GO, was commissioned in January 1998. It is much larger, with a perimeter of 14 m. It was designed as a proof-of-principle prototype for a 16 m perimeter gyroscope *Grossring*, currently under construction. *Grossring*, or G for short, is a high-stability instrument, utilising the construction techniques employed on C-II, to be housed in Wettzell, Bavaria.

1.1 Thesis Layout

The content of each of Chapters 3, 5, and 6 is, in the main, independent of the content of the other Chapters. Consequently they may be read in any order without any significant loss of coherence. For the reader who is unfamiliar with the Canterbury ring-laser gyroscopes the first part of Chapter 2 provides a brief overview of the design and operation of the lasers.

The first part of Chapter 2 is devoted to material that is of an introductory nature. The general principles of operation, along with a brief history, of Sagnac interferometers are described. The major reasons why the output of a ring-laser gyroscope deviate from the ideal value described by Equation (1.1) are then introduced to give a background for the discussion presented in subsequent Chapters. This is followed by a brief description of the relevant technical aspects, augmented with a more specific discussion of C-I and C-II. It is the latter part of Chapter 2 that begins the exposition of material that provides some extension of phenomena that have previously been investigated. In Section 2.5 the optimum gas fill pressure is investigated. In this instance, optimum is defined as the pressure that supports the highest lasing power while single longitudinal mode operation is maintained. This work extends previous empirical studies by the Canterbury ring-laser group. The publication that led to the work presented in Section 2.5 is reproduced in Appendix C.2. The insights gained are used to form recommendations on the further work that is required in order to determine the optimum fill pressure and He:Ne ratio based on the laser specification. The ability to do this should prove valuable. Extreme cleanliness of the laser mirrors and cavity is required to achieve the ultimate resolution of rotation. This means that empirical studies are undesirable—it is a distinct advantage to be able to select a gas fill pressure and He:Ne ratio and commission the laser in the knowledge that

this aspect of operation is close to optimum.

For some time now the Canterbury ring-laser group has grappled with the problem of *frequency pushing*. This is the deviation of the gyroscope beat frequency above the nominal value defined by Equation (1.1). Models that only include the effects of scattering of the light from one wave into the counter-propagating wave all predict that only *frequency pulling*, or deviation below the ideal value, may occur. More comprehensive models that include the effects of the gain medium and, in particular, any coupling between the counter-propagating beams predict frequency pushing. However, since these effects were thought to be insignificant in the operation of the Canterbury gyroscopes, a conundrum resulted. Furthermore it has been observed that the phase difference between modulation on the counter-propagating waves that is due to backscatter exhibits much less variation than is expected for the changing backscatter configuration to significantly alter the gyroscope beat frequency [14–16]. In the first half of Chapter 3 it is shown that it is possible to obtain the cross-coupling necessary to predict frequency pushing of the observed magnitude using the third-order theory of the ring-laser developed by Aronowitz [17,18] that is analogous to Lamb's third order theory for the linear laser [12, 19]. In particular it is found that this effect is most pronounced when the ratio of powers of the counter-propagating beams is not close to unity. No pushing is predicted when the powers are equal. To my knowledge, this effect has not previously been explicitly identified by experiment although the effect may be predicted by the standard third-order theory of the ring-laser gyroscope. The reason for this is that in other, less stable, lasers the effect is masked by other phenomena that cause the gyroscope beat frequency to deviate from the ideal. Examples include the axial flow of ions or electrons in the gain medium due to a DC excitation and significant scattering from the mirrors. The strong assumption that scattering is unimportant, in the case of C-II at least, in determining the amount of frequency pushing is used to obtain simple predictions of the amount of frequency pushing that is to be expected for a given set of laser parameters. Although this assumption is not unequivocally justified the predictions made using this assumption agree well with the magnitude of the observed frequency deviations from the nominal value. Consequently these results should provide a useful first estimation of parameters relating to the gain medium in a (necessarily) numerical solution of the equations of motion when backscattering is included.

Chapter 4 contains some results, relevant to drift processes in gyroscopes, that are not reported at all in the core gyro literature. Since the optimum resolution for a given gyroscope is at shorter timescales, where white noise frequency fluctuations dominate drift noise, it was not considered of interest to study this regime. This was because it did not appear to contribute to the goal of improving resolution of the rotation rate. It is shown that understanding of these processes will lead to the ability to optimise any stabilisation of the gyroscope constraining the drift processes. A novel approach to stabilisation is proposed whereby the drift process is used as feedback where it is constrained according to the statistics of the drift

process. This is to be contrasted with any deterministic feedback which may in fact work against the stochastic drift process and degrade performance.

The account of the optical frequency stabilisation of C-II presented in Chapter 5 is my own slant on work that involved a number of people. The published account of this work is reproduced in Appendix C.1. An extended overview of laser stabilisation methods that are commonly used is intended as reference for any future upgraded optical frequency stabilisation schemes that may be implemented. The implementation of the LABVIEW™ stabilisation control software was primarily the work of Professor Ulli Schreiber. A number of data sets are analysed in order to determine the characteristics of the stabilisation scheme. Limits on the noise that may be introduced by a stabilisation scheme on any timescale have been deduced. This leads to a set of design specification criteria to be determined for any future stabilisation schemes. It is worth noting that as the resolution and stability of the laser are improved these limits become tighter and therefore the required performance of any stabilisation scheme becomes an issue that should increasingly be taken into consideration in the design of the stabilisation scheme. Chapter 5 is concluded with a discussion of alternative methods that may result in improved performance of the stabilisation loop. This draws on the discussion of the various approaches to laser frequency stabilisation discussed in the early part of the Chapter.

Chapter 6 presents the first experimental verification of the theory of injected coloured noise in ring-laser gyroscopes. The first half of the Chapter is devoted to a summary of the previously published theory. In order to provide some background to the Fokker-Planck approach that is applied in the theoretical analysis of injected coloured noise the simpler theory of injected white noise is presented first. The white noise theory makes predictions that have been observed many times by the gyroscope community. When viewed in tandem both theories give an important insight into ring-laser gyroscope dynamics that may not be obtained from deterministic models. The connection between the white noise theory and the coloured noise theory is intimate—the white noise model is the zero noise correlation time limit of the coloured noise model. The latter part of Chapter 6 documents the experimental work performed on C-I to test the coloured noise theory. It is found that the statistics describing the distribution of phase differences between the counter-propagating beams behave in a manner that is in agreement with the theoretical predictions.

Finally, I would like to draw attention to Appendix D. It contains material that, despite being outside of the main focus of this thesis, is relevant to automation of data acquisition. All automated experimental control described in this thesis was performed using LABVIEW™ which is the tool of choice for many in this field. Appendix D describes some techniques for LABVIEW™ design and programming that are not documented in the reference material with the distribution. These techniques, which were developed from synthesizing material from personal

experience and various LABVIEW™ resources, allow a more organised approach to program design, resulting in easier and more transparent debugging.

Chapter 2

Ring-laser Gyroscope Fundamentals

2.1 The Sagnac Interferometer

A Sagnac interferometer may be loosely defined as an optical instrument, possessing two light beams, which measures the rate at which it is rotated. The rotation may arise from the instrument being operated on a laboratory turntable, the motion of the an aeroplane or missile in the case of a guidance gyroscope, or, as is the case with the Canterbury gyroscopes, the rotation of the Earth. The rotation rate of the interferometer is measured by means of a non-reciprocal effect, caused by the rotation, between the two counter-propagating beams in a polygonal cavity. Traditionally the counter-propagating beams have been light-waves. The first demonstration of the ring-laser gyroscope was made by Macek and Davis in 1963 [11]. Subsequent experiments have demonstrated that matter-wave Sagnac interferometers may also be used as effective rotation sensors [20,21]. The original explanation is due to Sagnac [22]. The round-trip time difference δt between the two beams for an interferometer of area A rotating at an angular frequency Ω is

$$\delta t = \frac{4\Omega \cdot \mathrm{A}}{v^2}, \tag{2.1}$$

where v is the undragged velocity[1] the round-trip phase difference is

$$\delta\phi = \frac{8\pi\Omega \cdot \mathrm{A}}{\lambda v}, \tag{2.2}$$

where λ is the wavelength of the light. For information the regarding the derivation of these formulae the reader is referred to Refs. [14] and [13]. In 1913 Sagnac reported a fringe shift of the expected size for rotation on a turntable using an interferometer in the passive configuration [22][2]. In 1925 Michelson was the first to observe the Earth rotation rate using a $0.21\,\mathrm{km}^2$ interferometer [23].

[1] That is, the velocity of the beam is unaffected any medium within which it may be propagating.

[2] A *passive* interferometer is defined as an interferometer in which the beams are injected into the cavity. Conversely an *active* interferometer contains a source that generates each of the counter-propagating beams within the cavity. The ring-laser gyroscope is the obvious example.

The corresponding result for the round-trip phase difference observed with matter waves is obtained by substituting the de Broglie relation in Equation (2.2),

$$\delta\phi = \frac{8\pi m\Omega \cdot \mathrm{A}}{h}, \tag{2.3}$$

where m is the mass of the mass of the particles forming the matter wave and h is Planck's constant. Gyroscopes using electrons [24], neutrons [21], and coherent beams of atoms [20, 25] have been demonstrated.

The ring-laser gyroscope and the fibre-optic gyro have proved to be the most fruitful implementations of the concept of the Sagnac interferometer. The rotation rate is measured as a frequency splitting between the counter-propagating waves according to Equation (1.1). These gyroscopes are used in guidance systems on aircraft, ships, missiles, and automobiles [14]. Consequently there has been considerable commercial and military development of these devices based on goals such as making them compact, reliable, and affordable. On the other hand, there has relatively little research investigating how maximal sensitivity of ring-laser gyroscopes may be obtained. One of the major motivations of the Canterbury group for pursuing such research is to develop a local sensor of Earth rotation which has the sensitivity necessary to usefully observe the variations in the Earth's rate of rotation that are due to tidal and seismic effects [4, 14, 26, 27]. Other effects that may, at some stage, be experimentally investigated using ring-laser gyroscopes have been comprehensively reviewed in Ref. [14].

2.2 Complications Introduced by Real Ring-laser Gyroscopes

The two main sources of perturbation that cause the observed gyroscope beat frequency to differ from the nominal value for the Sagnac splitting given by Equation (1.1) are introduced in this Section.

2.2.1 Backscatter and Beat Frequency Pulling

In the first demonstration of the ring-laser gyroscope [11] it was found that when the rotation rate was reduced below some critical value the frequency difference between the oppositely directed travelling waves disappeared and the gyroscope did not respond to changes in the rotation rate that kept the rotation rate below the critical value. On the other hand, if the rotation rate was increased above the critical value a gyroscope beat frequency proportional to the rotation rate reappeared. This effect, subsequently called lock-in, is due to the mutual coupling between the counter-propagating waves [28]. Backscattering of the light from one beam into the other due to mirror imperfections and contamination is

the predominant source of this coupling. The gyroscope beat frequency at which lock-in occurs is referred to the *lock-in threshold.*

As well as the disappearance of the beat frequency below the lock-in threshold it is found that, for rotations only slightly greater than the lock-in threshold, the average gyroscope beat frequency is reduced or *pulled* below the value indicated by Equation (1.1). Furthermore the beat frequency waveform is found to be distorted. More frequency pulling and waveform distortion is observed when the rotation rate is close to the value specified by the lock-in threshold [18, 29]. Figure 2.2.1 demonstrates the pulling characteristics of a ring-laser gyroscope. A more detailed discussion of this phenomenon is presented in Section 3.4.

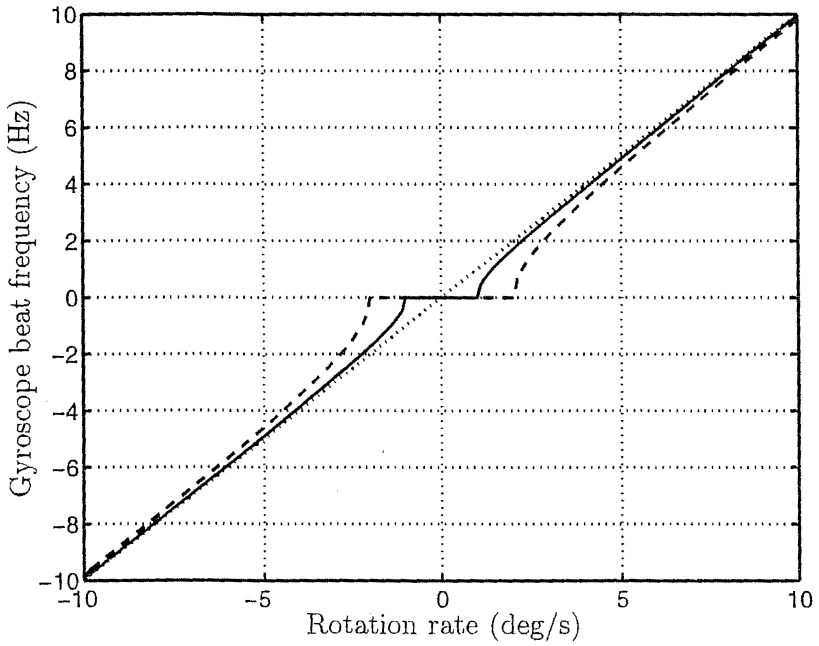

Figure 2.1: Variation of the average gyroscope beat frequency with rotation rate Ω for a lock-in threshold of 1 Hz (solid line) and 2 Hz (dashed line). The dotted line is the nominal beat frequency defined by Equation (1.1), where the constants in Equation (1.1) have been chosen such that $\delta f = \Omega$.

2.2.2 The Gain Medium

The laser requires a gain medium in order to provide light amplification. A number of properties of the laser are dependent on the nature of the gain medium. In the case of a gas laser the motion and density of the atoms is important. Various processes within the gain medium lead to a pulling of the optical frequency toward gain centre or pushing away from gain centre. Generally the differential

effect on the counter-propagating waves is negligible for small rotation rates[3]. This is not always the case however. Further discussion of the effects which arise from the gain medium is presented in Sections 3.4 and 3.5. In particular the effects of mode pushing on the gyroscope beat frequency when the powers of the counter-propagating beams are unequal is investigated. It is found that this mechanism can give rise to substantial *pushing* and *pulling* of the Sagnac beat frequency.

2.3 Resolution and Performance Limits

There are two types of limit in the resolution of Earth rotation that are observed in the Canterbury ring-laser gyroscopes. The first is a "fundamental" limit due to the quantum mechanical nature of laser operation. The second type may be broadly classified as noise sources possessing a $1/f^{\alpha}$ type power spectrum where α is positive but need not be an integer. This type of noise is sometimes referred to as *technical noise.*

2.3.1 Quantum Noise

The random walk in phase, caused by spontaneous emission [30], provides the fundamental limit of resolution of the rotation rate in ring-laser gyroscopes. It may be shown that the random walk in phase is equivalent to white frequency noise [4]. For a square ring-laser gyroscope, possessing an angular optical frequency ω_0 and operating in single longitudinal mode[4], the theoretical prediction for the quantum noise contribution to the RMS fluctuations in the gyroscope beat frequency for a measurement time T is given by [3, 4],

$$\begin{aligned}\Delta f_{\text{RMS}} &= \frac{1}{2\pi}\sqrt{\frac{\hbar\omega_0^3 t}{4Q^2P_0 l}}\frac{1}{\sqrt{T}}, \\ &= \frac{1}{2\pi}\sqrt{\frac{\hbar\omega_0^2 t\Delta\nu_{\text{FSR}}}{QP_0}}\frac{1}{\sqrt{T}}, \\ &= \frac{1}{2\pi}\sqrt{\frac{\hbar\omega_0^3}{2Q^2P}}\frac{1}{\sqrt{T}},\end{aligned} \tag{2.4}$$

where P_0 is the *combined beam* radiant power observed at each mirror port. The total losses and mirror transmission are denoted by l and t respectively. Q is the cavity quality factor. The power injected per mode[5], P, is related to the combined

[3]Small rotation rates may be defined as rates which induce a frequency splitting given by Equation (1.1) that is small in comparison to the scale of the gain-frequency curve.

[4]Please refer to Section 2.4.1 for an explanation of single longitudinal mode operation.

[5]Single longitudinal mode operation is assumed in the derivation of Equation (2.4). Therefore the power injected per mode is equal to the power injected in each direction.

beam output power at each port according to $P = 2P_0 l/t$. The relationship $\omega_0 = 4lQ\Delta\nu_{\text{FSR}}$, where $\Delta\nu_{\text{FSR}} = c/L$ is the frequency separation between adjacent longitudinal cavity modes is used to obtain the second equation. As one would expect for a white noise process the RMS frequency fluctuations obey a $1/\sqrt{T}$ temporal scaling law.

Equations (2.4) may be deduced using a number of methods including the minimum uncertainty relations for coherent states [31]. This approach was employed by Dorschner *et al.* [32] as well as Statz *et al.* [3]. An alternative derivation utilises the tools of stochastic differential equations [33]. The Langevin equation of motion for the phase difference between the counter-propagating waves is solved yielding the Lorentzian spectrum and associated linewidth [34–37][6].

The first demonstration of a ring-laser gyroscope operating at the quantum limit was made by Dorschner et al. [32]. Analysis of the relevant scale factors has shown that the Canterbury ring-lasers described in this work also operate at the quantum limit on timescales defined by the mechanical stability of each instrument [2, 4]. To improve resolution of the Earth rotation rate Equation (2.4) makes it clear that the cavity quality factor and radiant power should be maximized. This is the motivation for the work described in Section 2.5.

Various schemes have been proposed to circumvent the limitation imposed by spontaneous emission. One approach involves the injection of squeezed light [31] into the cavity [43–45]. Correlated excitation schemes, using different transitions from a three-level model, provide an alternative method to circumvent the "quantum limit" [46, 47]. The potential application to the ring-laser gyroscope was discussed by Scully [48].

2.3.2 $1/f^{\alpha}$ Noise Sources

The goal of this Section is to demonstrate that technical noise is an important factor in determining the long-term resolution of the gyroscope. An extended discussion on the identification and classification of technical noise sources is given in Section 4. In the case of C-II atmospheric pressure has been a major source of drift.

Figure 2.2 displays an example the dependence of the C-II beat frequency on atmospheric pressure due to compression and expansion of the ZERODUR^{TM} monolith and mirror mounts. Power spectrum analysis (Figure 2.3) of an extended data set

[6]The Langevin equation is simply a deterministic equation of motion for the phase difference between the counter-propagating waves with the addition of a term representing additive white noise. It is solved using standard methods for the analysis of stochastic differential equations [33]. Chapter 6 gives an experimental account and comparison with theory [6, 38–40] when the additive noise is coloured. For a theoretical account of the effects of multiplicative white noise see Refs. [41] and [42].

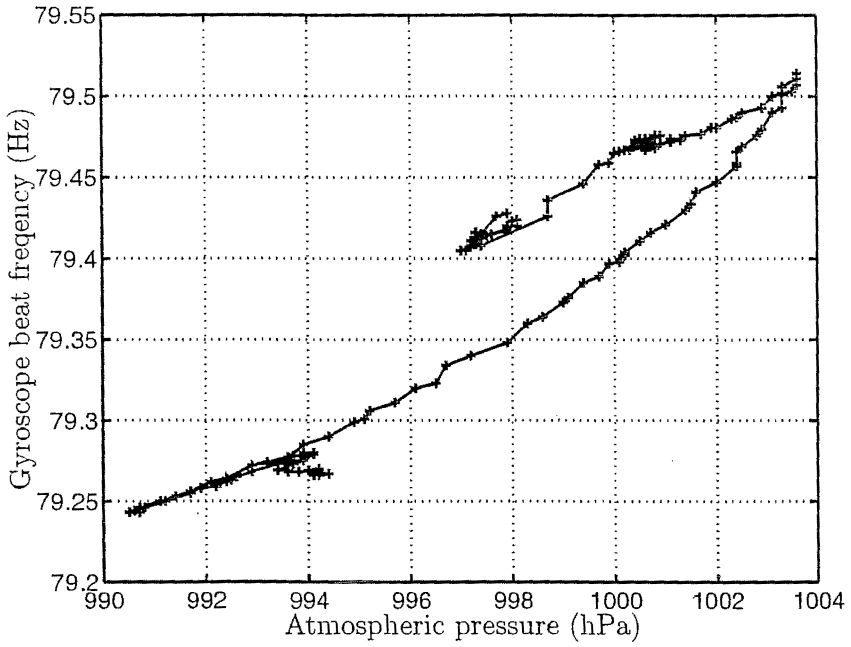

Figure 2.2: Variation of C-II gyroscope beat frequency with atmospheric pressure. The pressure estimates were made... by a sensor attached to the C-II monolith.

of atmospheric pressure measurements shows that the pressure fluctuations may be modelled (at least in part) by a $1/f^{\alpha}$ noise process[7]. Given the correlation between the C-II gyroscope beat frequency and atmospheric pressure exhibited in Figure 2.2 it is expected that the drift in the gyroscope should also exhibit some of the characteristics of a $1/f^{\alpha}$ noise process. In Section 4.2 it is demonstrated using an Allan variance analysis [51] (See Appendix B.2) that white frequency noise due to spontaneous emission dominates on timescales of less than several hundred seconds while the $1/f^{\alpha}$ noise due to atmospheric pressure fluctuations dominates on longer timescales[8]. Furthermore the crossover point between each noise type becoming dominant defines the averaging time that leads to the maximum achievable resolution of Earth rotation that may be obtained with the ring-laser gyroscope. This is because the standard deviation of the quantum noise contribution follows the standard $1/\sqrt{T}$ law for white noise. However this does not apply for the technical noise sources. For noise sources possessing power spectrum of the form $1/f^{\alpha}$ the standard deviation increases with averaging time and may be shown to be mathematically divergent [52]. Further discussion of

[7]It has been shown that the power spectrum is not a particularly reliable method of characterization for $1/f^{\alpha}$-type noise sources [49,50] (See Section 4.1.5). Therefore Figure 2.3 is merely intended to indicate the existence of such a noise process.

[8]Since the data analysed in this work were collected a pressure isolation vessel has been constructed around C-II. This has changed the long-term noise characteristics but as of November 2000 the details of the new operating regime in relation to $1/f^{\alpha}$ noise processes have not been studied.

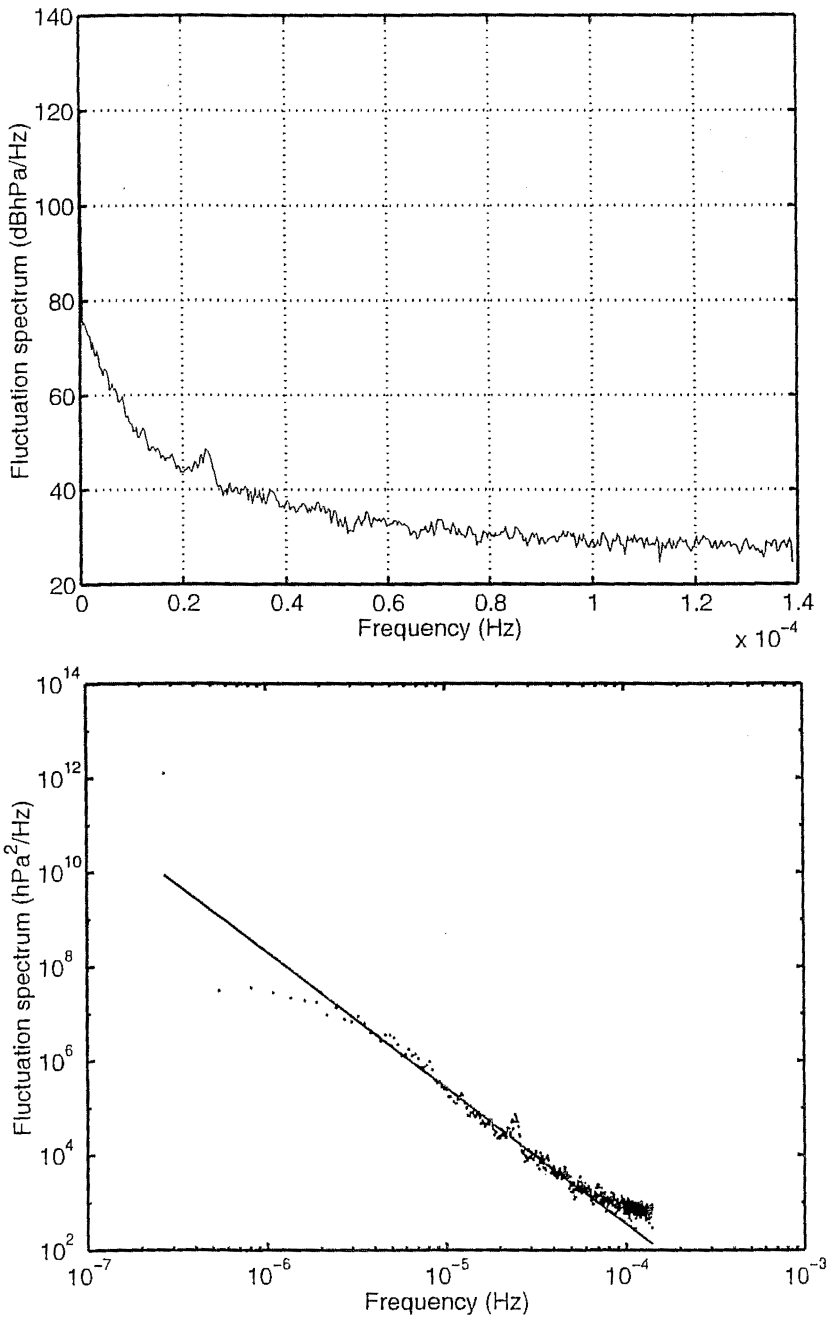

Figure 2.3: Power spectrum of fluctuations (a) in atmospheric pressure at Christchurch airport and (b) a log–log plot of the same data demonstrating the power law dependence for a particular frequency range. The fitted line is $S(f) = (1.10\times^{-9})f^{-2.88}\,\mathrm{hPa}^2/\mathrm{Hz}$. The data set consisted of hourly measurements of the atmospheric pressure taken at Christchurch airport from August 1, 1996–March 30, 1999. The data were supplied by the New Zealand Meteorological Service.

this paradox, sometimes called the *infrared catastrophe*, and its resolution, is presented in Section 4.1.4.

2.4 The Canterbury Ring-lasers

The first part of this Section contains a general introduction to the Canterbury ring-laser gyroscopes. The aim is to present information that pertains to all of the instruments. Following this, relevant details about two of the ring-lasers, known as C-I and C-II, are given.

Vacuum

The laser cavities are pumped to a pressure of $< 10^{-6}$ torr before helium and neon are released into the cavity up to a pressure of a few millibar. The cleanliness of the cavity has a direct bearing on the long-term purity of the laser gas mixture and the length of a run that may be completed before it is necessary to refill the cavity. Pumping is performed using a turbo-molecular pump backed by a rotary-vane pump.

The capacitance manometer gauge (BAROCELL^{TM} from Edwards High Vacuum) may be used to measure pressures that range from atmospheric pressure down to 10^{-6} mbar. It is the primary vacuum gauge type used by the Canterbury ring-laser group. This type of gauge operates by measuring the deflection of a diaphragm using the change in capacitance across the diaphragm as it diaphragm deflects under forces due to the pressure differential across it. Capacitance gauges are one of the most accurate types of pressure gauge and possess a fast response.

The sputter-ion pump (VACION^{TM} from Varian) doubles as a useful low pressure gauge in the range 10^{-3}–10^{-10} mbar. A typical ion pump consists of two flat rectangular cathodes, usually made of titanium, with a stainless steel anode between them made up of a large number of open-ended tubes. The arrangement is surrounded by a permanent magnet. A potential differential of several kV between the anode and cathodes causes electrons and positive gas ions to move toward the anode and cathodes respectively. The titanium is *sputtered*, or knocked off the cathodes. The resultant titanium film readily combines with active gases such as nitrogen, oxygen, hydrogen, carbon dioxide, water vapour, and carbon monoxide. The magnetic field is arranged such that the free electrons within the pump housing travel extended paths in order to increase the probability that ionizing collisions with gas molecules will occur. The ionized gases are attracted to the cathode and buried on the cathode by sputtered titanium. The pumping rates for different gases are therefore dependent on the ease with which the gas is ionized. At higher gas pressures where a lot of ionization occurs more current is

drawn from the high voltage power supply. At low pressures less current is drawn. Therefore the current drawn gives an approximate measure of the pressure.

A mass spectrometer (Dataquad Spectramass) is available to evaluate the cleanliness of the cavity and perform leak tests if it is suspected a seal is faulty.

Plasma Excitation

Radio frequency (RF) excitation of the plasma is used in the Canterbury ring-lasers. Inductive coupling is used to transfer energy to the gain medium. RF excitation is preferred to DC excitation because DC excitation introduces a gyroscope beat frequency null shift due to the flow of electrons, positive ions, or neutral atoms within the gain section [18]. Since this will vary in time due to changes in the power delivered to the gain section DC excitation is likely to introduce drifts that will limit the resolution of Earth rotation.

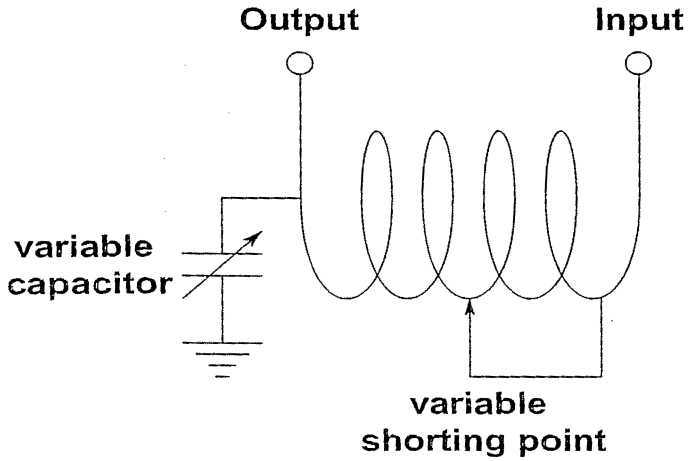

Figure 2.4: A basic inductive RF-matching circuit. The use of two coils to provide an output either side of the ground point on the gain tube is a useful trick that may be used to obtain a longer and more symmetric discharge.

2.4.1 Detection Systems

Photomultiplier Tubes

Photomultiplier tubes (PMTs) are high-speed, high-gain, low-noise light detectors. They can detect single photons over a spectral range of 180 to 900 nm. Therefore PMTs are the ideal detector for lasers such as the Canterbury gyroscopes that possess very low output powers.

Photons which strike the PMT's photo-cathode cause electrons to be ejected by the photo-electric effect. These electrons are accelerated toward the first dynode by a potential difference of 100 to 400 Vdc. Secondary electrons are ejected when the electron strikes the first dynode, and these electrons are accelerated toward the second dynode. The process continues, typically for 8-14 dynodes, each providing an electron gain of about 4-5, to produce 10^6 to 10^7 electrons per photon which are collected by the anode. If these electrons arrive in a 5 ns pulse into a 50 Ω load, they will produce a 1.6 to 16 mV voltage pulse.

There are two basic geometries for photomultiplier tubes: head-on and side-on types. The head-on type has a semi-transparent photo-cathode, and a linear array of dynodes. Side-on types have an opaque photocathode and a circular cage of dynodes that are equi-distant from the vertical axis of the PMT. The Hamamatsu R3896 PMTs used for light detection on the Canterbury lasers are the side-on type.

There are a variety of materials which are used as photocathodes. The work function of the photocathode material will determine the spectral response as well as influence the dark count rate of the PMT. The "quantum efficiency" is an important measure of the PMT performance. A 10% quantum efficiency indicates that 1 in 10 photons which strike the photocathode will produce a photoelectron—the rest of the incident photons will not be detected. The quantum efficiency is a function of wavelength. Therefore the Hamamatsu R3896 PMT which has a peak spectral response at 450 nm and a quantum efficiency of 14% at 633 nm is well suited for use with wavelengths in the visible part of the spectrum.

Spectral Response	Range (nm)	185-900
	Peak Wavelength, λ_p (nm)	450
Cathode Sensitivity	Luminous (μA/lm)	525
	Radiant at λ_p (mA/W)	90
	at 633 nm (mA/W)	73
Anode Sensitivity	Luminous (A/lm)	5000
Anode Dark current (nA)		10
Quantum Efficiency	at 260 nm	30%
	at 633 nm	14%
Time Response	Anode Pulse Rise Time (ns)	2.2
Max rating	Average Anode Current (mA)	0.1
Gain	cathode at 1000 V	9.5×10^6
	cathode at 800 V	1.8×10^6
	cathode at 600 V	2.2×10^5
	cathode at 400 V	2.5×10^4

Table 2.1: Specifications for Hamamatsu R3896 photomultiplier tube [7].

Very often, PMTs will be operated well above the high voltage recommended by

the manufacturer. This results in substantially higher current gains—generally 10× to 100× above specification. There are usually no detrimental effects to the PMT as long as the anode current is kept well below the rated value. However if relatively bright light sources are used it is necessary to reduce the anode-cathode potential differential in order to keep the anode current below the maximum rated value. The maximum recommended incident radiant laser power P_{max} is related to the anode-cathode potential difference via the gain G using the equation,

$$P_{max} = \frac{h\nu i_{max}}{Gq\eta}, \tag{2.5}$$

where i_{max} is the maximum recommended anode current, η is the quantum efficiency, and q the electron charge. Table 2.4.1 gives P_{max} for various anode-cathode potential differences. This is of interest because it indicates the maximum radiant power output that may be observed without causing damage to the PMT.

voltage drop (V)	max power
1000	150 pW
800	800 pW
600	6 nW
400	55 nW

Table 2.2: Estimates of maximum recommended radiant laser power incident on Hamamatsu R3896 PMT for various cathode-anode potential differences. These estimates are based on manufacturers' recommendation for maximum anode current. Note that the gain was measured with equal dynode ratios and will vary if the dynode resistor chain does not conform to this assumption.

In certain applications within the Canterbury ring-laser group it is necessary to detect radiant powers that are very small. An example of this is the stabilisation of the C-II optical frequency described in Chapter 5. Although signals of this level do not fall into the domain of photon counting it is useful to consider the relevant detection limits which limit the signal-to-noise ratio and show at the incident power level at which it will be necessary to replace photo-current measurement with photon counting techniques. It is also important to note that at these signal levels the PMT shot noise contribution has a significant impact on the detection process and that the averaging time required to obtain an adequate signal-to-noise ratio may be an important constraint in the design and implementation of an experiment.

Thermionic emission of electrons from the photo-cathode and from the first few dynodes of the electron multiplier are the source of noise known as dark current. PMT housings which cool the PMT to about $-20°$C can dramatically reduce the dark current. The residual photo-counts arise from radioactive decays of materials inside the PMT and from cosmic rays. The signal-to-noise ratio $(S/N)_d$ due to

the dark current is

$$(S/N)_d = \frac{PG\eta q}{h\nu i_d}, \tag{2.6}$$

where i_d is the anode dark current. Equation (2.6) may be used to give a guide of the limitations of a particular PMT. For example, data from Table 2.1 may be used to show that the Hamamatsu R3896 has a dark current induced detection limit of $P = 0.015(S/N)_d$ pW. This is sufficient to allow for good detection of laser signals of the order of 1 pW.

It is also necessary to account for the quantised nature of light and charge. The *shot noise* contribution to the photo-detection process in a count of N photons is given by $\sqrt{N}$. Some simple manipulation leads to a shot noise signal-to-noise ratio $(S/N)_s$ of

$$(S/N)_s = \sqrt{\frac{Pt\eta}{h\nu}}, \tag{2.7}$$

where t is the measurement time and ν is the optical frequency. For the Hamamatsu R3896 PMT this leads to the requirement $Pt = 2.24 \times 10^{-18}(S/N)_s^2$ J. For an incident power of 1 pW an integration time of $t = 2.2(S/N)_s^2$ μs is required to obtain a given signal-to-noise ratio. A *noise budget* of the detection chain used on C-I has shown that approximately 90% of the observed voltage fluctuation is due to fluctuations in the measured radiant power (laser shot noise), while 10% of the voltage fluctuation was found to derive from thePMT [4]. This estimation was based on measurements taken with C-I operating at a radiant power typical of normal operation (a few tens of nW). The associated electronics were found to make a minimal contribution of about 1%.

The Trans-impedance Amplifier

The PMT is a current source. It is necessary to convert this into a voltage which is a measure of the laser radiant power that may be viewed on an oscilloscope or recorded using a data acquisition PC card. The circuit diagram for the trans-impedance amplifier used to perform this task is shown in Figure 2.5. The transfer function has an RC characteristic[9]. The roll-off frequency is approximately 370 kHz. The variable resistor allows the op-amp offset to be adjusted so that no light input corresponds to zero output volts.

[9]The power transfer function is a one sided Lorentzian [53]:

$$H(\omega) = \frac{G}{1 + \omega^2/\omega_c^2}.$$

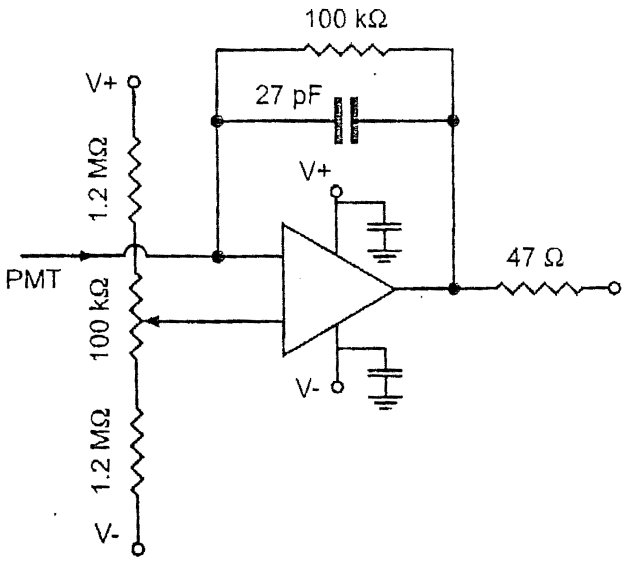

Figure 2.5: Trans-impedance amplifier circuit diagram. Diagram courtesy of Dr. Tom King.

Single Mode Operation

It is generally required that the Canterbury ring-laser gyroscopes are operated with a single longitudinal mode in order to simplify the interpretation of observed phenomena as well as ensuring any complicated mode competition effects are avoided. In the context of ring-laser gyroscopes single mode operation means that there is one longitudinal mode for the clockwise beam and one longitudinal mode for the counterclockwise beam. Single longitudinal mode operation has traditionally been obtained within the Canterbury ring-laser group by employing what has been called the starvation technique [2,14,29]. The laser gain is reduced to a point where only one longitudinal mode is observed to be above threshold. One difficulty with this approach arises as the perimeter is increased to improve the resolution of the gyroscopes. This is because an increase in the perimeter of the laser leads to a reduction in the frequency separation between longitudinal modes. Therefore as the perimeter is increased it becomes increasingly difficult to obtain single longitudinal mode operation using the starvation technique because the gain difference between adjacent longitudinal modes is no longer large enough to select a single longitudinal mode. This is the motivation for the study presented in Section 2.5 of the potential use of increased homogeneous linewidth broadening to suppress unwanted longitudinal modes.

Two approaches to detection of the presence of more than one longitudinal mode are used within the Canterbury ring-laser group. Both rely on observation of the free spectral range (FSR) beat frequency. The first is to directly monitor the beat signal from the photomultiplier tube using a RF spectrum analyser

(Hewlett Packard ESA-L1500A). Data acquisition is automated by controlling the spectrum analyser via the HPIB interface using LABVIEW™[10]. The spectrum analyser is sufficient for use in determining whether or not multiple longitudinal modes are present. However it does not possess the frequency resolution necessary to determine small changes in the FSR beat frequency. If this information is required heterodyne detection [54] is performed using a GPS stabilised RF-signal generator (Hewlett Packard HP8648A) as the local oscillator. The resultant heterodyned signal of a few hundred Hertz may then be analysed with sufficient resolution to observe variation in the carrier signal. For further information regarding this method see Section 3.1.

Data Acquisition

Quantisation noise arises because an analogue signal may only be represented with a finite precision by a digital data acquisition device [55]. There are two critical parameters involved in quantisation, the quantisation step Λ and the number of steps N. A p-bit analogue to digital converter (ADC) has 2^p levels. The Canterbury ring-laser group uses both 12-bit and 16-bit ADCs with 4096 and 65536 quantisation steps respectively.

The maximum quantisation error for any given sample is $\Lambda/2$. If it is (reasonably) assumed that quantisation error is uniformly distributed between $-\Lambda/2$ and $\Lambda/2$ the variance of the error signal is $\langle x^2 \rangle = \Lambda^2/12$. Each extra bit therefore decreases the noise power by a factor of 4 or $\approx 12\,\mathrm{dB}$. The best attainable signal-to-noise ratio SNR_b for the powers may be shown to be [56, p. 89]

$$\mathrm{SNR}_b = 20 \log_{10} \left[(2^p)^2 - 1 \right] \simeq 40p \log_{10}(2)\,(\mathrm{dB}). \tag{2.8}$$

It is assumed that the signal utilises the entire dynamic range of the ADC. A 12-bit and 16-bit ADC will possess a SNR_b of $\approx 145\,\mathrm{dB}$ and $\approx 193\,\mathrm{dB}$ respectively. As expected the 16-bit ADC brings $\approx 48\,\mathrm{dB}$ improvement in SNR_b over the 12-bit ADC. However, as long as the signal is scaled to ensure that it utilises a sizeable fraction of the ADC range, quantisation noise is not a problem with respect to the acquisition of beat-frequency waveforms. However it is not always possible to scale all signals to be acquired to utilise a reasonable portion of the ADC range. This situation would arise when it is necessary to observe signals that are almost constant in time. For example software-based digital control of laser power requires a dynamic range that is large compared to operation once the control loop has settled and the power is almost constant. If the input voltage

[10] LABVIEW™ is a software development environment produced by National Instruments designed to aid the development of effective data acquisition and control procedures. LABVIEW™ uses a graphical programming language, known as G, to implement a dataflow programming paradigm. This is a particularly effective paradigm for use in the applications for which LABVIEW™ is intended.

range is -10 V to +10 V then the voltage stepsize for a 12-bit and 16-bit ADC is $\Lambda = 4.9\,\mathrm{mV}$ and $\Lambda = 0.31\,\mathrm{mV}$ respectively[11].

The (generally high frequency) quantisation noise generated by the ADC is not subject to any anti-alias filtering and is therefore aliased into the same frequency as the signal, degrading the signal-to-noise ratio (SNR). Techniques such as oversampling allow the SNR to be improved by extending the bandwidth into which the quantisation noise is aliased and then digitally filtering out frequencies higher than the signal.

2.4.2 C-I

A comprehensive review of all the equipment, assembly procedures, and operation techniques related to C-I is given in Ref. [4]. Refs. [29] and [14] give a substantial overview of the history and development of C-I. This section therefore only provides a brief summary, highlighting the aspects relevant to the work described in subsequent chapters.

The laser is mounted on $1\,\mathrm{m}^2$ base-plate constructed from ZERODUR™[12]. Each of the four mirror boxes is free-standing on the ZERODUR™ baseplate. A glass plate at the top of each of the mirror boxes allows the scatter from the mirrors to be visually inspected. VITON™ O-rings (made by Du Pont) inserted in grooves in each surface that holds the O-rings are used to seal the interfaces between the mirror box and ZERODUR™ as well as the mirror box and glass lid. As the vacuum in the laser cavity takes hold a tight seal forms. A light coating of SANTOVAC 5™ diffusion pump oil (made by Monsanto) on the O-rings ensures the integrity of the vacuum seal.

Pyrex tubes are used to connect the mirror boxes, thus placing the entire lasing path under vacuum. Once again O-rings coated with diffusion pump oil are used to maintain a vacuum seal at the mirror box-pyrex tube interface.

A schematic of the C-I cavity geometry is shown in Figure 2.6. The mirrors are labelled in a clockwise fashion as M_1, M_2, M_3, and M_4. The curved mirrors M_2 and M_3 both have a radius of curvature of 6 m. The beam sizes defined

[11] In relation to the operation of the Canterbury gyroscopes one situation where this has been observed to be a problem is in the control of the RF amplifier via a digital-to-analogue (DAC) channel of the data acquisition card. This was because, in order to obtain single longitudinal mode operation, it was necessary to operate the laser at the edge of the input RF power:output radiant power curve, near the region of maximum slope. This problem is addressed in Section 2.5 where it is found that overfilling of the laser cavity allows operation of the laser at the peak of the input:output curve. Consequently the variation in RF power for a given DAC output increment is substantially reduced. Therefore the system is much more amenable to software-based digital control and the significant advantages such an approach can yield.

[12] This is low expansion ceramic made by Schott. It has a temperature coefficient of expansion of $0 \pm 5 \times 10^{-8}/^{0}\mathrm{C}$.

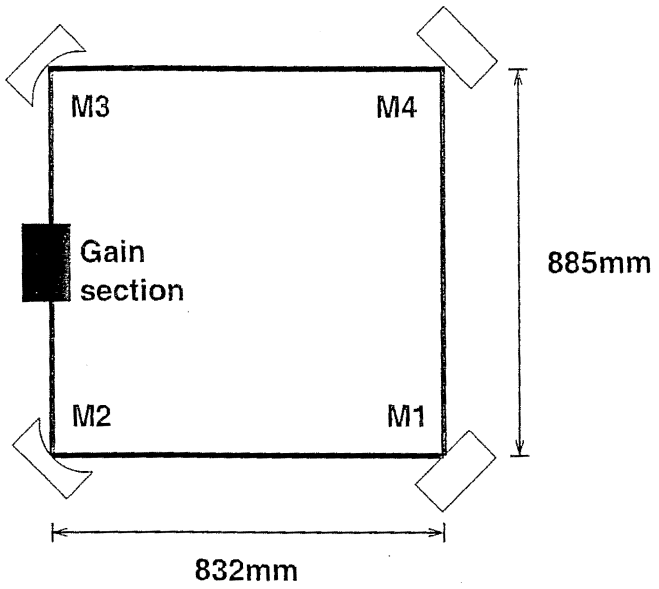

Figure 2.6: Schematic showing C-I dimensions and mirror labelling scheme. The gain section is placed midway between the two curved mirrors M_2 and M_3.

by this mirror configuration are summarised in Table 2.3. The gain section is placed between the two curved mirrors M_2 and M_3. A piezoelectric transducer is attached to M_3. The piezoelectric transducer is controlled using a Thor Labs MDT691-EC piezo controller which generates an output of 0-150 V. This may be adjusted either by the dial on the front of the piezo controller or via a 0-10 V analogue input. The vacuum system is also connected at the M_3 port via stainless steel bellows connected to the mirror box. An isolation valve at the mirror box allows the vacuum system to be disconnected if necessary. The alignment laser is injected at M_1. The combined beam and FSR PMT is located at M_1 and the single beam PMTs for observation of each counter-propagating beam are located at M_4.

Position	r_1 (mm)	r_2 (mm)	$1/e^2$ Area ((mm)^2)
gain tube	0.3843	0.3527	1.7035
M_1	0.3457	0.2653	1.1525
M_2	0.3887	0.3583	1.7501
M_3	0.3887	0.3583	1.7501
M_4	0.3457	0.2653	1.1525

Table 2.3: Beam sizes (accounting for astigmatism) of C-I. The semi-major and semi-minor axes where the power has dropped by the factor $1/e$ from the maximum power are given by r_1 and r_2 respectively. These values were calculated using standard results from the ABCD ray propagation matrices [8, Chapter 2].

Alignment is performed using a Melles Griot GRENE^{TM} laser. This laser emits from the $3s_2 \longrightarrow 2p_{10}$ NE transition at 543.5 nm by use of mirrors with reflectance characteristics that cause this low gain transition to be preferred over the usual red and infra-red neon transitions. Since the dielectric mirrors used in the ring laser are designed for maximum reflectance at 633 nm the green light has a much lower reflectance and consequently higher transmission within the ring-laser cavity. Therefore it is possible to easily observe the re-circulated beam during alignment. On the other hand, it is very difficult to see a re-circulating beam exit the cavity if a red laser is used for alignment purposes. The basic goal of alignment is to ensure the re-circulated beam is coincident with the injected beam. A full description of the alignment procedures for C-I was given by Dr. Tom King [4].

Sufficient vacuum is achieved using a Leybold TMP150 turbomolecular pump, backed by a D16 rotary vane pump from Duniway Stockroom. The turbo pump is connected to a stainless steel manifold. After baking and sufficient pumping a manifold vacuum of 10^{-8} torr is obtained without difficulty. Gas is fed into the manifold via variable leak valves. A stainless steel gas reservoir external to the leak valves is used to supply extra gas to the manifold and laser cavity. In the experiments described later in this Chapter the reservoir was filled with helium. However it is straightforward to use it to store a pre-mix of the desired ratio of helium and neon should the need arise [2, 4]. The materials that provide the most surface area in the laser cavity are the stainless steel mirror boxes and the pyrex tubes joining the mirror boxes. Although the pyrex tubes make the alignment process somewhat easier they are a major source of contamination and outgassing[13]. For this reason it is not possible to achieve a vacuum better than approximately 10^{-3} torr after the cavity has been isolated for one hour, regardless of the quality of the vacuum at the time of isolation. Therefore it is recommended that if long term operation is required the pyrex tubes be replaced with stainless steel tubes.

The RF excitation frequency for the experiments reported in this work is 32 MHz. A frequency and amplitude-stable RF drive signal is provided by a Hewlett-Packard HP8648A RF signal generator. RF amplification is by a SSB RF power amplifier. The forward and reverse RF powers were monitored using a RF power meter, modified to provide an analogue voltage output for each of the forward and reverse RF powers. These voltages were manually calibrated by comparison with the meter gauge.

[13] Although the out-gassing rate per unit area of the VITON^{TM} O-rings is much greater than that of the pyrex a simple estimate of the surface area shows that the contribution from the pyrex tubes dominates the total outgassing rate of the cavity. Note that the outgassing estimates presented in Table 2.4 are for unbaked materials. Since it is possible to submit the stainless steel to much for intensive baking (up to 800 degrees Celsius) the final outgassing rate for stainless steel is much less than that of pyrex.

Material	Outgassing rate (mbar l s^{-1} cm^{-2} $\times$ 10^{-10})	
	1 hour at vacuum	4 hours at vacuum
Pyrex (raw)	99	8
Pyrex (1 mnth. at atm.)	16	3
Stainless Steel (polished)	66	5
Fluoroelastomer (VITON^{TM})	15200	1500

Table 2.4: Some out-gassing rates of materials used under vacuum in the Canterbury ring-lasers [9]. The long-term purity of the gases in the cavity is determined by the initial cleanliness of the cavity and the out-gassing rates of the materials used to construct the cavity.

With a gain tube possessing an inner diameter of 3.8 mm it is possible to obtain two transverse modes ($TEM_{0,0}$ and $TEM_{1,0}$) by adjusting the position of the gain tube with respect to the beam path. The chosen value of the gain tube diameter facilitated straightforward transverse mode selection by adjustment of the position of the gain tube. For larger gain tube diameters it has been found that a variety of transverse modes are observed. Since minor variations in the gain tube position may cause a change of transverse mode it is necessary to monitor the beam with a CCD camera to determine that the laser is operating in the desired transverse mode [4].

2.4.3 C-II

C-II is constructed from a half-tonne solid block of ZERODUR^{TM} in order to maximise the thermal stability of the instrument. The ring-laser cavity is bored out of the ZERODUR^{TM} block. The cavity geometry is summarised in Figure 2.7 and Table 2.5. The curved mirrors both have a radius of curvature of 6 m. The mirror configuration was changed to a symmetrical arrangement with respect to the position of the gain tube in November 1998. In addition, all of the mirrors were mounted on identical blanks in order to retain as much symmetry as possible under expansion and contraction of the monolith. The expansion properties of the C-II monolith listed in Table 2.6 are of interest and relevant to the analysis of the stabilisation of the C-II optical frequency described in Chapter 5. The flexible mirror membrane mount for the piezo-controlled mirror provides the greatest source of frequency shift for a given pressure shift.

Since the data discussed in Chapters 3 and 5 were recorded prior to November 1998 only this configuration is given further attention. Three of the four mirrors (M_2, M_3, and M_4) are mounted on Zerodur^{TM} discs that are 113 mm in diameter and 24 mm thick. The exit hole from the cavity is 60 mm in diameter. The mirror mounts are attached to the monolith by means of optical contact between the two highly polished surfaces. A beam-combiner prism is attached to the mirror M_3

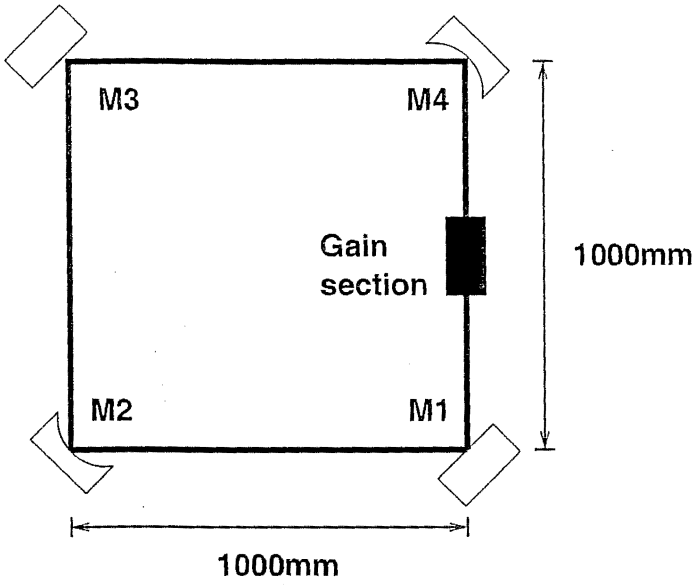

(a)

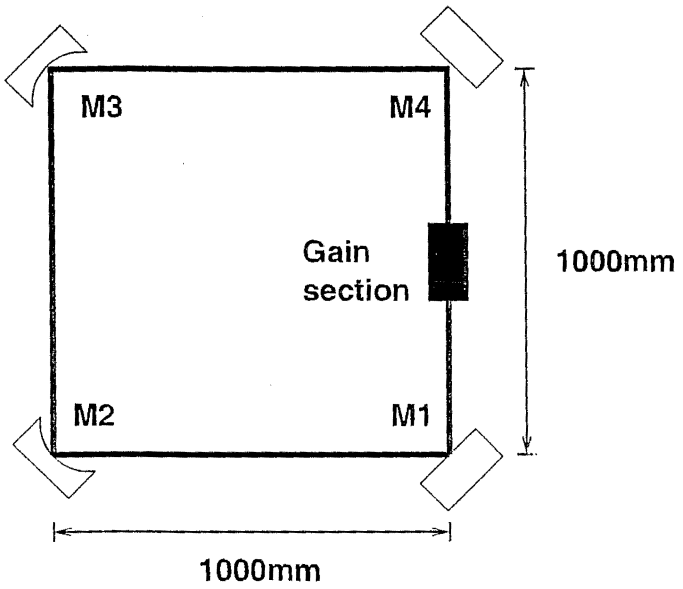

(b)

Figure 2.7: Schematic showing C-II dimensions and mirror labelling scheme (a) prior to November 1998 and (b) since November 1998. The gain section is placed midway between the mirrors M_1 and M_4. Note that in (b) the cavity geometry is symmetric with respect to the position of the gain tube. In the case of the square cavity this means that the gain tube is positioned at one of the beam waists. The aim of this positioning is to minimise any aperture effects that may give rise to unwanted beat frequency drift [3].

Position	r_1 (mm)	r_2 (mm)	$1/e^2$ Area ((mm)^2)
gain tube	0.3771	0.3121	1.4788
M_1	0.3712	0.3011	1.4046
M_2	0.3952	0.3444	1.7106
M_3	0.3712	0.3011	1.7106
M_4	0.3952	0.3444	1.4046

(a)

Position	r_1 (mm)	r_2 (mm)	$1/e^2$ Area ((mm)^2)
gain tube	0.3464	0.2414	1.0503
M_1	0.3541	0.2638	1.4046
M_2	0.4092	0.3952	2.0325
M_3	0.4092	0.3952	2.0325
M_4	0.3541	0.2638	1.1738

(b)

Table 2.5: Beam radii (accounting for astigmatism) of C-II (a) prior to November 1998 and (b) since November 1998. The semi-major and semi-minor axes where the power has dropped by the factor $1/e$ from the maximum power are given by r_1 and r_2 respectively. These values were calculated using standard results from the ABCD ray propagation matrices [8, Chapter 2].

Cause	Magnitude	excursion	ΔP	$\Delta\nu$
T variation	20 nm/K	150 mK	3 nm	0.4 MHz
P-induced block comp.	23 pm/mbar	20 mbar	46 nm	5.5 MHz
Mirror membrane comp.	194 pm/mbar	20 mbar	390 nm	46.3 MHz

Table 2.6: Expansion and compression properties of C-II due to temperature and atmospheric pressure variation [1]. The effects of a pressure change on the bulk Zerodur and on the mirror mount membranes are listed separately. The last two columns give typical values during an experimental run. $\Delta\nu$ is the change in the optical frequency induced by the perimeter variation. It is assumed that the laser does not shift from the longitudinal mode $\mathrm{TEM}_{n,m,q}$ to either of the longitudinal modes $\mathrm{TEM}_{n,m,q+1}$ or $\mathrm{TEM}_{n,m,q-1}$ during the atmospheric pressure excursion.

whereupon the combined beam signal is monitored by a photomultiplier tube. Single beam detection for both directions is performed at M_2 using two photomultiplier tubes. A fourth PMT is installed at M_4 to monitor the clockwise (CW) radiant power. The low frequency component of this signal is used as the process variable in the power control loop. Typically the high frequency component of this signal is used to monitor the FSR beat signal although at times this has been done using the other PMTs, depending on the requirements of the data being collected. A piezoelectric transducer is attached to the mirror M_1[14]. The mount for this mirror has a thickness of 5.5 mm and is much more flexible than the mounting blocks for the other three mirrors and.

Radio frequency excitation is generally performed at approximately 57 MHz using a HP8648A RF signal generator as the source and the RF LABS amplifier to provide the necessary amplification of the RF excitation signal.

Further detail regarding the design and construction of C-II may be found in Refs. [14, 57, 58] and [1].

2.5 Optimisation of Gas Pressure

It has already been noted that the starvation technique which is implemented by reduction of the pump power so that only one mode in each direction oscillates will become inadequate at some sufficiently high perimeter because the free spectral range decreases as the perimeter increases, lowering the gain difference between adjacent modes. One approach that may be employed to circumvent this problem is to increase the He:Ne gas pressure such that the pressure broadened homogeneous linewidth is substantially increased. In a homogeneously broadened medium all atoms behave in the same manner. Consequently any atom that gives up energy in the form of a photon to any field at any frequency can no longer contribute to the gain at another frequency. Therefore the gain is reduced over the entire spectrum while maintaining proportionality with the unsaturated gain profile [8, p. 211]. Therefore, in a homogeneously broadened gain medium, the mode that possesses the most unsaturated gain generally suppresses the other modes within the homogeneously broadened linewidth. This technique has been demonstrated in a very large triangular ring laser 13 m on each side [27]. Further investigation was made by the Canterbury ring-laser group using the 14 m^2 gyroscope G0 [59] but some facets of the interpretation were only partially understood [2]. The aim of this Section is to provide a small advance in the understanding of this mode of operation of the Canterbury ring-lasers as well as to formulate a prescription to allow the optimum gas fill pressure to be determined based on the laser specification. The latter goal is motivated because any re-filling

[14]The piezoelectric transducer was removed in November 1998 in order to reduce the drift in optical frequency associated with the flexible mirror mount.

of the cavity exposes the mirrors to a risk of contamination. Therefore empirical determination of the optimum fill pressure is not possible in instruments such as C-II where the associated risk of contamination is unacceptable.

The choice of gain tube diameter that maximises the output power for a given pump power is of particular interest. A rule-of-thumb for the pressure-diameter product may be found experimentally. The significance of this product comes from the fact that the population inversion is reduced at increased pressure due to excitation of the lower laser level by electrons colliding with atoms in the $1s$ state. The gain tube diameter dependence is due to the fact that atoms decay from the $1s$ state to the ground state by collision with the gain tube walls [60]. For lasers similar to C-I, the best criterion for determining the optimum fill pressure is the pressure-diameter product, and its optimal value has been found to be [2,61]

$$pd = 14.6\,\text{mm torr}. \tag{2.9}$$

The value of 14.6 mm torr for the constant was determined empirically using an RF-excited linear laser [61] and the Canterbury ring-laser G0 which is also RF-excited. The constant is larger than the often quoted value of 6.6 mm torr that was determined by Gordon and White using a DC-discharge linear laser [62]. Equation (2.9) indicates that a gain tube diameter of 3.8 mm implies an optimum fill pressure of ~ 3.8 torr. This result does not, however, provide any information regarding longitudinal mode behaviour. Therefore an investigation of the optimum fill pressure for which single mode operation may be obtained is required. The remainder of this Chapter is devoted to such an investigation.

2.5.1 Experimental Setup and Process

The setup for the experimental investigation of the optimisation of the C-I gas pressure is displayed in Figure 2.8. The LABVIEW^{TM} control program is at the heart of the experiment. It is used to control the DC bias (0-6 V) of the RF power amplifier and hence the input power to the gain section. Data from four sources are collected using the LABVIEW^{TM} control program. The combined beam output power is monitored at the mirror M_1 (See Figure 2.6) using a PMT and associated trans-impedance amplifier connected to a National Instruments PCI-16XE-4 data acquisition card. The output voltage from the PMT and associated electronics was calibrated against radiant power using a Newport 818-SL diode power meter. A second analogue input channel is reserved for the voltage output from the BAROCELL^{TM} pressure gauge. A RF spectrum analyser (HP ESA-L1500A) is used to monitor for the presence of a FSR beat signal. The spectrum analyser is controlled via the GPIB/HPIB bus using a GPIB control card (National Instruments AT-GPIB). Finally the forward and reverse RF powers are monitored by acquisition of the analogue output voltages from the RF power meter using the data acquisition card.

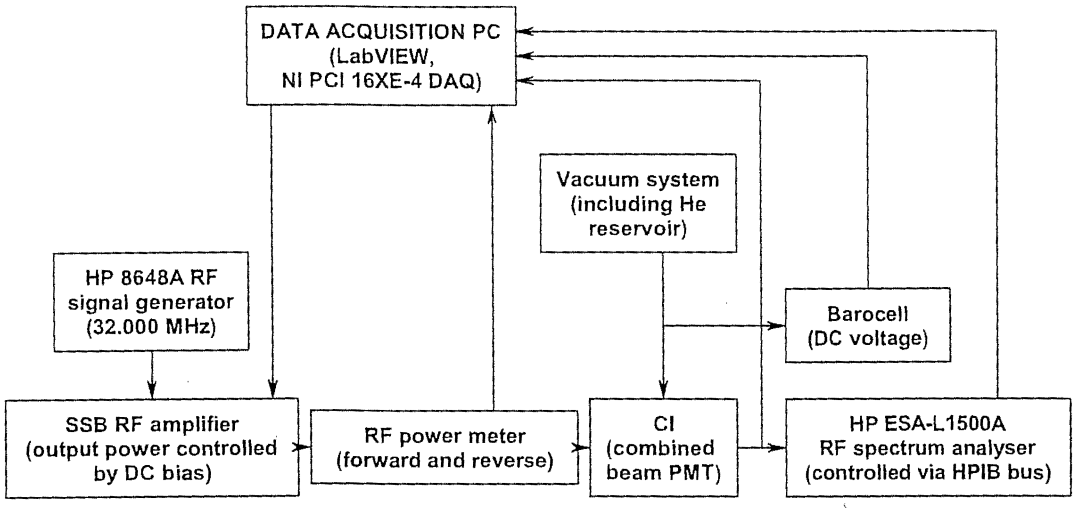

Figure 2.8: Schematic of experimental setup for determining the optimum gas fill pressure.

The process for data acquisition at a single pressure is summarised in Figure 2.9. To begin the data acquisition sequence C-I is filled to the desired neon partial pressure. Helium is added until the desired total pressure is reached. At this point the LABVIEW^{TM} control program is launched. The user is prompted to enter the value of the neon partial pressure chosen. Alteration of the RF amplifier DC bias has the effect of reducing the input RF power. In comparison with the full RF input power operating range afforded by adjustment of the HP8648A RF signal generator, alteration of the SSB RF amplifier DC bias provides a somewhat reduced range of operation. Therefore it is necessary to perform occasional optimisation of the HP8648A output level in order to ensure a suitable range of input RF powers was available. To this end, a pop-up window is launched. This window allows the user to check that the scanning of the RF amplifier DC bias through the range 0-6 V will result in the desired range of RF power being supplied to the gain tube. If the HP8648A amplitude is incorrect the amplitude may be adjusted by hand and the range of bias voltages tested again until satisfactory. The user then selects "OK" and the main data acquisition sequence is launched. The control program scans through the range of DC bias values recording the required data for each power. There is a settling time of 10 seconds after each adjustment of the RF power before data are collected. All data points are an average value based on 3000 samples acquired over 3 seconds. Once the full range of RF input powers has been scanned the user is prompted to increase the pressure by leaking helium into the vacuum manifold and laser cavity from the gas reservoir. Once this is done another data acquisition sequence is begun by ensuring the RF input power scan range is appropriate. This cycle is continued until the pressure is increased to a point where the laser no longer operates. At this point the population inversion no longer exists because of population of the lower laser level from the $1s$ state.

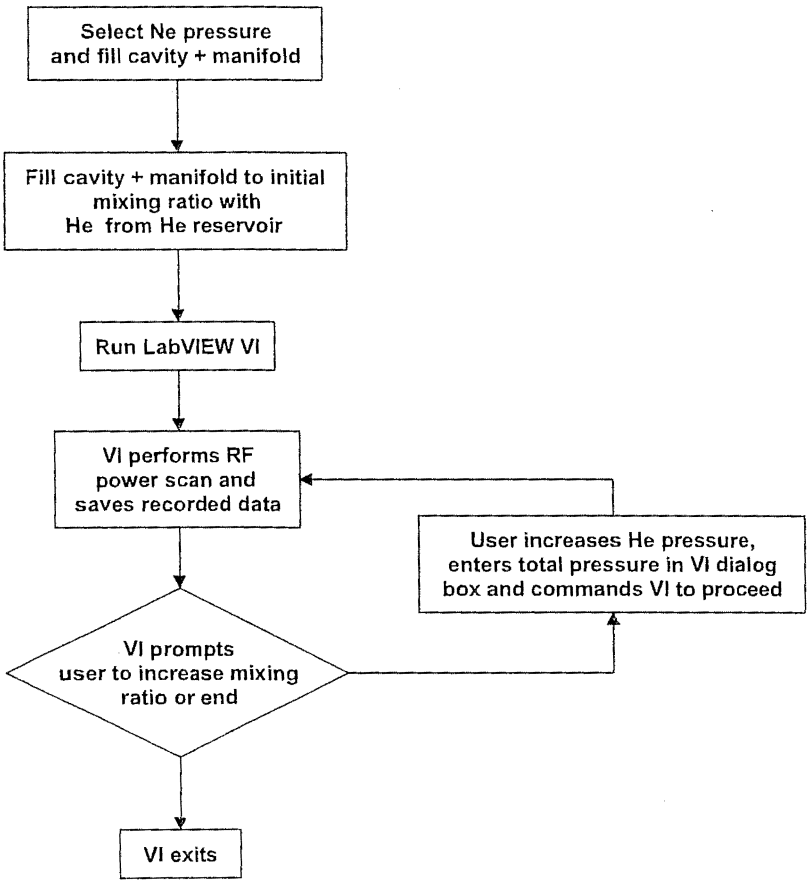

Figure 2.9: Flow diagram describing the operation of the semi-automated procedure for collection of data necessary for determining the optimum gas fill pressure.

2.5.2 Results and Interpretation

Examples of the data collected for two DC bias scans are shown in Figures 2.10 and 2.11. The salient feature is the power in the FSR beat signal. If this is below $\approx$ dBm then there is no mode adjacent to the dominant longitudinal mode (within the detection limits). Figure 2.11 shows an interesting feature. At the DC bias that produces the peak output power no adjacent longitudinal mode is present. However at values of the DC bias that produce lower output powers an adjacent longitudinal mode is observed. Similar behaviour was observed in the previous study of longitudinal mode suppression by the Canterbury ring-laser group [2]. However no explanation for this behaviour was found. Further discussion of this phenomenon may be found later in this Section.

Figures 2.12–2.16 show the complete data set for each neon partial pressure. Figure 2.17 and Table 2.7 summarise the maximum output radiant power for the various values of neon partial pressure.

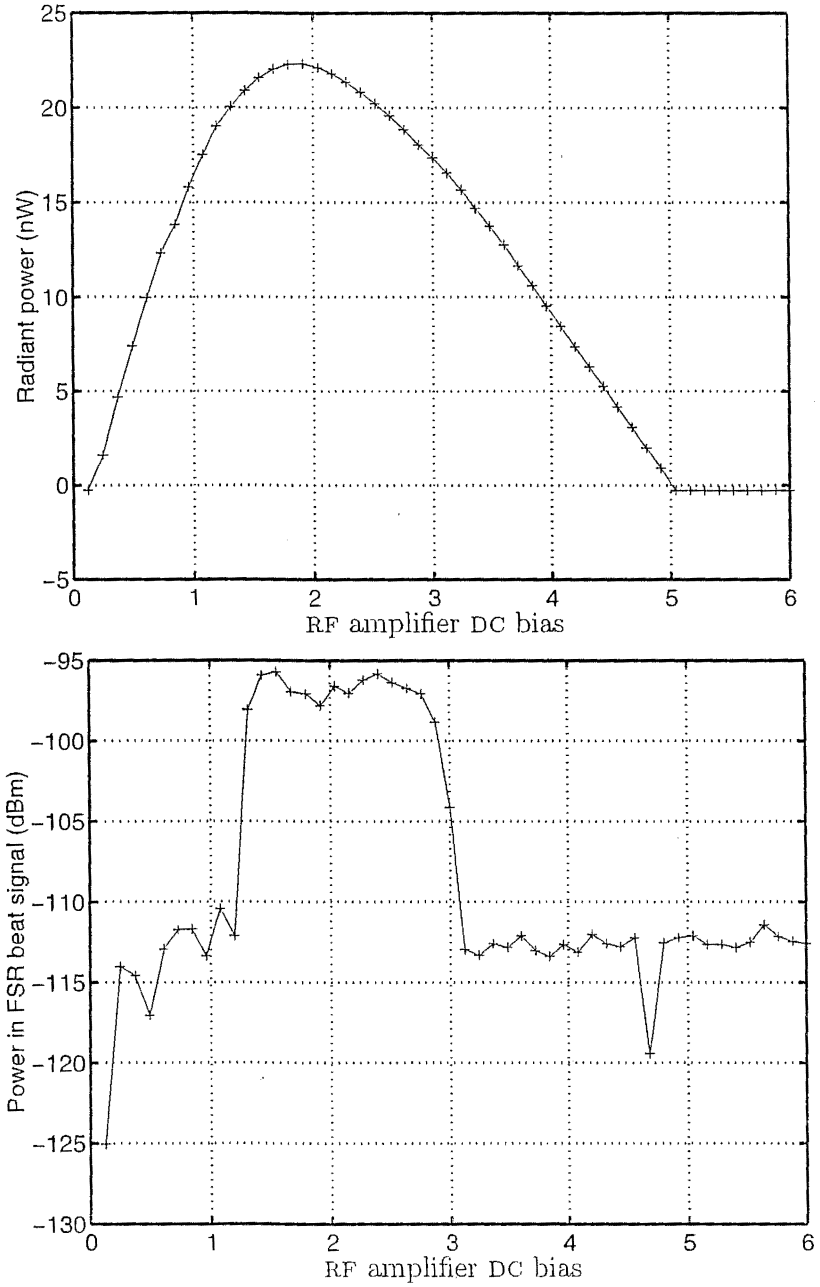

Figure 2.10: Operation in the regime where an adjacent longitudinal mode is observed only for the largest values of the pump power. (a) Output power as a function of the input pump power (in terms of the RF amplifier DC bias); and (b) power level of the FSR beat frequency between adjacent longitudinal modes as a function of the pump power. The absence of the FSR beat signal indicates that the laser is either not working, is operating in a single longitudinal mode, or the adjacent longitudinal modes are suppressed while other longitudinal modes may be above threshold. The absence of a FSR beat signal is implied when the RF power is below $\approx -110\,\mathrm{dBm}$.

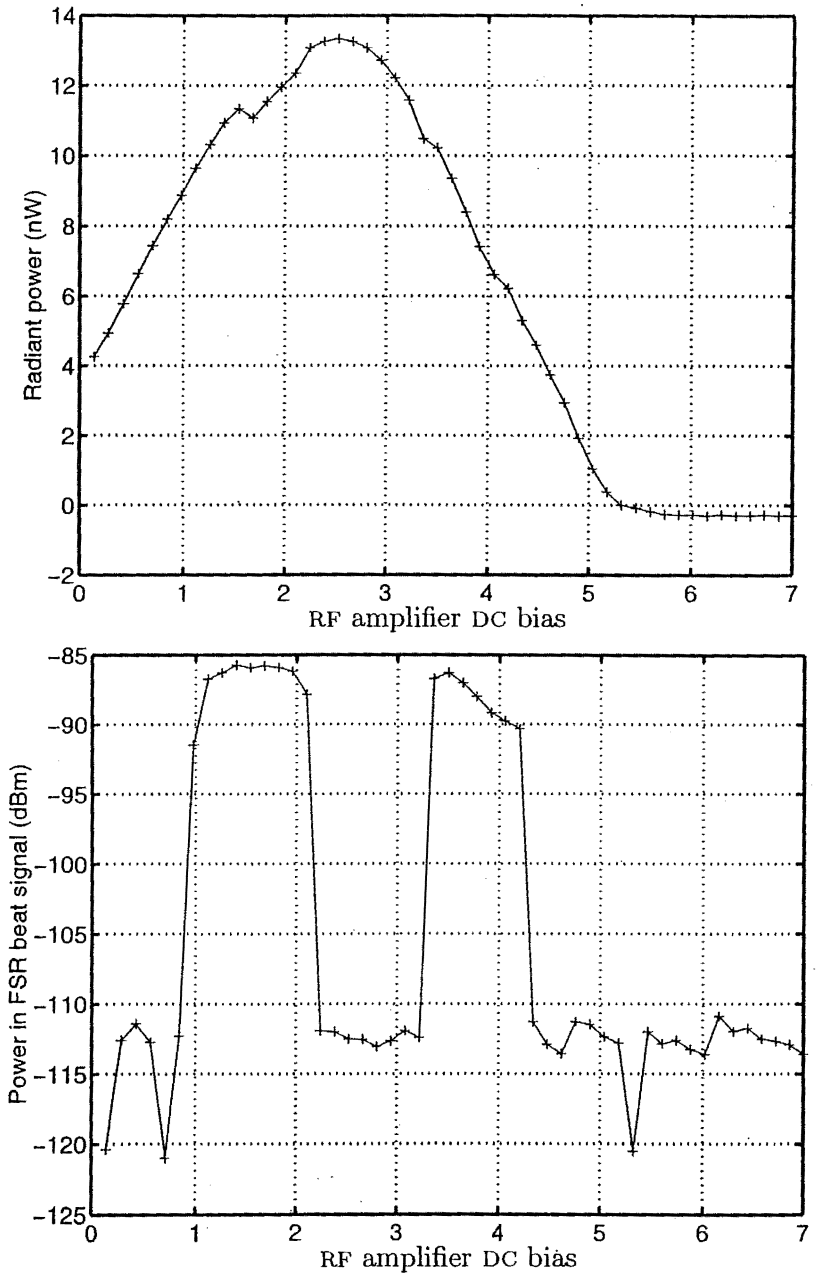

Figure 2.11: Operation in the regime where no adjacent longitudinal mode is present for the largest values of the pump power. (a) Output power as a function of the input pump power (in terms of the RF amplifier DC bias); and (b) power level of the FSR beat frequency between adjacent longitudinal modes as a function of the pump power. The absence of the FSR beat signal indicates that the laser is either not working, is operating in a single longitudinal mode, or the adjacent longitudinal modes are suppressed while other longitudinal modes may be above threshold. The absence of a FSR beat signal is implied when the RF power is below $\approx -110\,\mathrm{dBm}$.

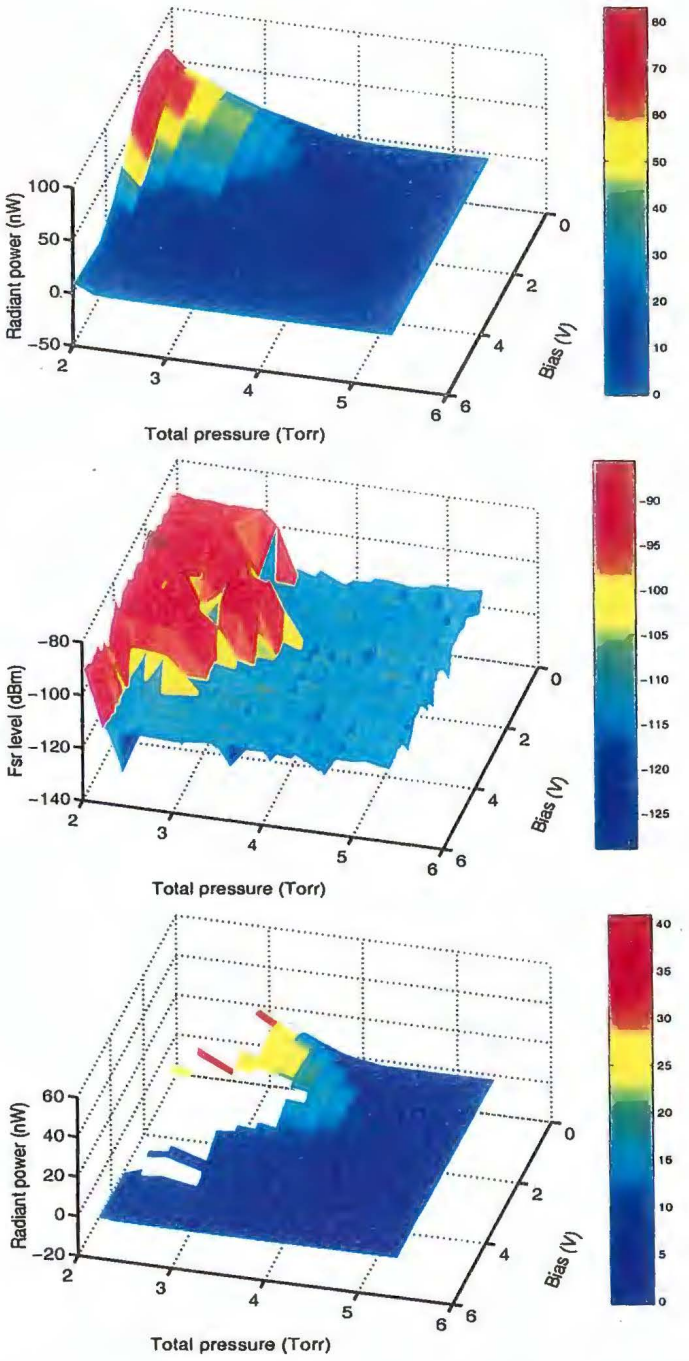

Figure 2.12: C-I output characteristics with variation of input RF power and total gas pressure for a neon partial pressure of 0.08 torr. (a) Output radiant power, (b) power in FSR beat signal, and (c) output power for the regions where no adjacent longitudinal mode is present.

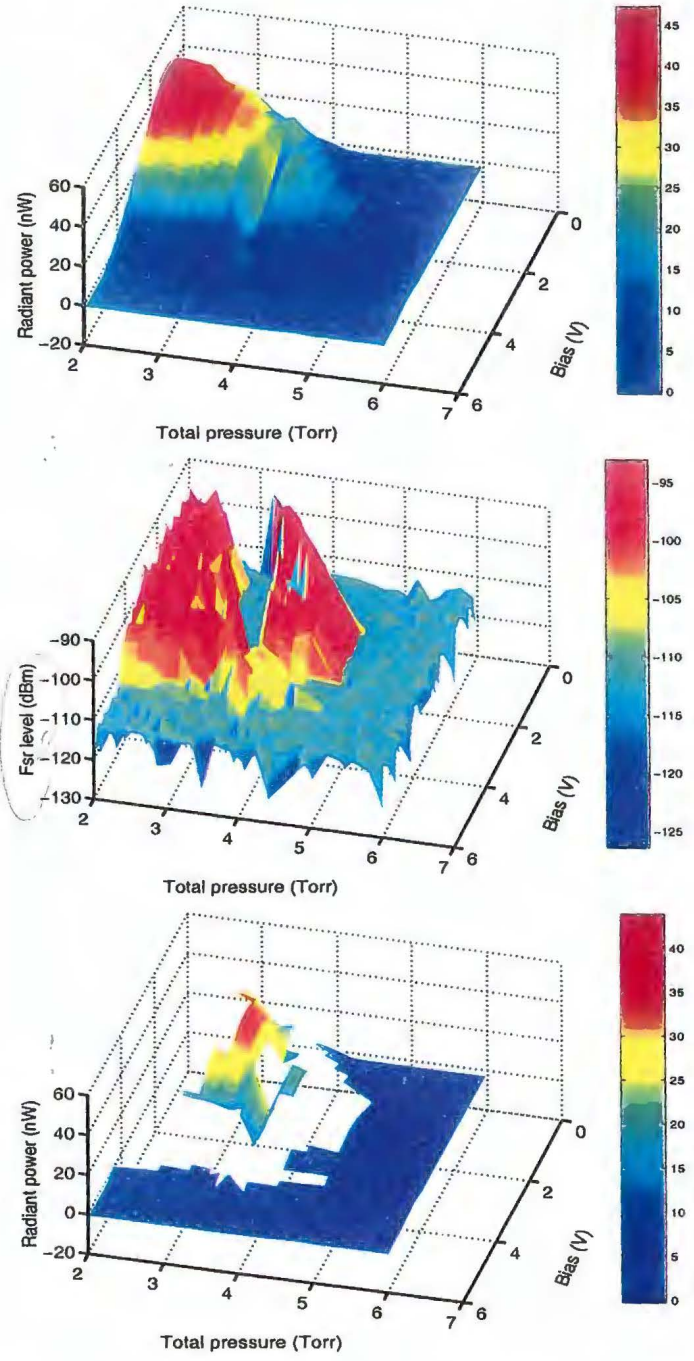

Figure 2.13: C-I output characteristics with variation of input RF power and total gas pressure for a neon partial pressure of 0.10 torr. (a) Output radiant power, (b) power in FSR beat signal, and (c) output radiant power for the regions where no adjacent longitudinal mode is present.

For all gas pressures reported in this experiment, the homogeneous linewidth is much smaller than the inhomogeneous linewidth ($K_u/2\pi \sim 1000\,\mathrm{MHz}$) and spectral hole burning in the Doppler broadened gain curve occurs [8, 63][15]. Also the free spectral range $\Delta\nu_{\mathrm{FSR}} = 86.512\,\mathrm{MHz}$ is much smaller than $K_u/2\pi$. Therefore the laser can, in principle, emit on multiple longitudinal modes. This is clearly seen for the lower gas pressures for all values of neon partial pressure investigated. However as the gas pressure is increased the influence of the increased homogeneous line-width broadening due to the larger collision rate becomes apparent. The homogeneous linewidth increases with increasing pressure [8, 18, 64]. A mode will deplete the gain of adjacent longitudinal modes if the homogeneous linewidth is similar to or larger than the free spectral range. When these operating conditions are present, adjacent modes do not oscillate and the FSR beat signal vanishes.

There are two main points of interest in the series of Figures 2.12–2.16. First of all, there is a critical pressure that defines the point at which for any increase in the total pressure it is guaranteed no adjacent longitudinal mode is observed, regardless of the RF excitation power. The critical pressure falls in the range 3.8-5.0 torr. The other interesting feature is the presence of a range of pressures that are less than the critical pressure where no adjacent longitudinal mode is present for a range of input RF powers that encompass the maximum radiant output power. The precise details of the range and position of this region varied a little for repetitions of the experiment with the same neon partial pressure. However the existence and approximate value of the total pressure required to access this operating regime was easily reproduced. Subsequently this region will be referred to as the region of apparent single mode operation (RASMO). The nomenclature is motivated by the fact that it is not possible to determine if *all* longitudinal modes were suppressed in this region of operation. The minor variation in the position of the RASMO is presumably due to effects such as contamination due to outgassing from the pyrex tubes and the position of the dominant longitudinal mode under the gain frequency curve.

In the case of the $14\,\mathrm{m}^2$ gyroscope G0 no RASMO was found [2]. The fact that the G0 beam ($\mathrm{TEM}_{0,0}$) takes up a much larger fraction of the gain tube may help explain this observation. The G0 cavity geometry defines a $1/e$ beam diameter (not accounting for astigmatism) of 2.2 mm ($15.2\,(\mathrm{mm})^2$ $1/e^2$ area) at the gain tube. The gain tube diameter is 6 mm. Similarly the 1.6 m linear laser LI was observed to possess an unstable RASMO that was of a more limited extent than that observed for C-I [2]. LI has a $1/e$ beam diameter of 1.5 mm ($7.1\,(\mathrm{mm})^2$ $1/e^2$ area), whereas C-I has an average $1/e$ beam diameter of 0.737 mm ($1.7035\,(\mathrm{mm})^2$

[15] K_u is the Doppler broadening constant, determined by the Maxwell-Boltzmann velocity distribution,

$$P(\omega) = \frac{1}{\sqrt{\pi}K_u} \exp\left[\frac{-(\omega-\omega_0)^2}{(K_u)^2}\right],$$

where ω is the oscillation angular frequency and ω_0 is the peak of the gain-frequency curve.

$1/e^2$ area) and a gain tube inner diameter of 3.8 mm. The gain tube diameter is 4 mm. Later in this Section it is proposed that the differences in the observed RASMO between the lasers may be explained in terms of *radiation trapping* [64].

Guaranteed Single Mode Operation

The absence of the FSR beat signal between adjacent longitudinal modes indicates that the laser is either working in single mode or is emitting multiple longitudinal modes with a frequency spacing of at least twice the free spectral range.

A mode separated by two FSR from the dominant lasing mode is necessarily further away from the maximum in the gain curve and requires more than a factor of two larger unsaturated net gain in order to oscillate than a mode adjacent to the lasing mode. It can be seen from Figures 2.12–2.16 that the output power is decreasing with increasing pressure. In the region of decreasing power the gain is also decreasing. The unsaturated gain is about the same or even lower than that required for adjacent modes to lase. Consequently there is insufficient gain to support oscillation of a possible second longitudinal mode in the cavity. The reason for this is that the electron concentration in the plasma rises with increasing pressure. This leads to an increasing excitation of the lower laser level and reduction in the lasing efficiency [8,65]. Although the long-lived $1s$ level does not play a part in He:Ne laser operation it tends to collect atoms reaching it by radiative decay from the lower laser level $2p$. Collisions with discharge electrons cause the atoms to be excited back to the lower laser level. Consequently the population inversion is depleted. The main means for atoms from the $1s$ state to return to the ground state is by collision with the walls of the gain tube. Therefore the gain of the 632.8 nm He:Ne transition is found to increase with decreasing tube diameter [60]. Electron impact from the ground state will also pump the $2p$ level. A reduction in the population inversion due to an effect such as this will cause outlying modes to have negative net gain. Therefore the absence of the FSR beat signal for pressures greater than the critical pressure indicates that single mode operation is guaranteed for the entire range of RF input powers.

It is of interest to compare the critical pressure required to suppress adjacent longitudinal modes with estimates of the homogeneous linewidth $\delta\nu_h$ at the critical pressure. Smith and Hänsch [66] found the homogeneous linewidth for 7:1 mixture of He^3:Ne^{20} to be

$$\Delta\nu_h = 14.9 + 58.5p\,\text{MHz}, \tag{2.10}$$

where p is the total gas pressure in torr. Equation (2.10) predicts a homogeneous linewidth of the order of 200 MHz for pressures of the order of the critical pressure observed in C-I. The estimated homogeneous linewidth is therefore about two–three times as large as the free spectral range.

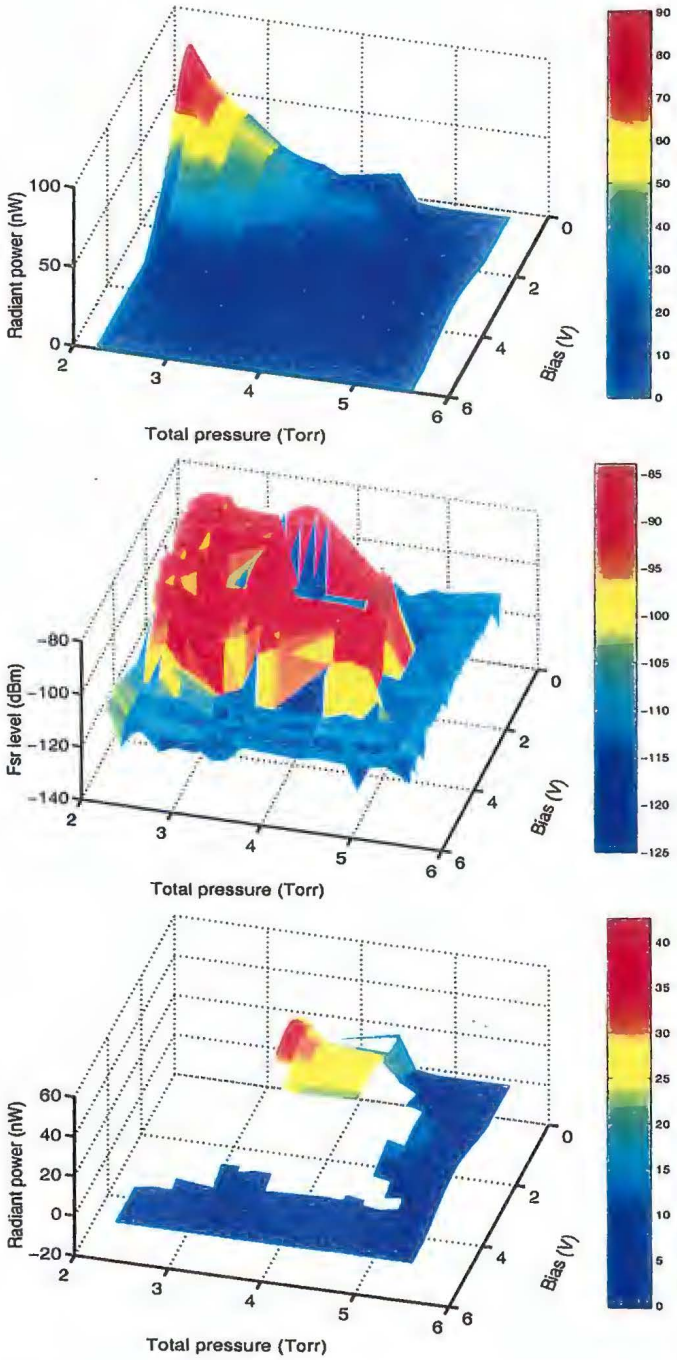

Figure 2.14: C-I output characteristics with variation of input RF power and total gas pressure for a neon partial pressure of 0.12 torr. (a) Output radiant power, (b) power in FSR beat signal, and (c) output radiant power for the regions where no adjacent longitudinal mode is present.

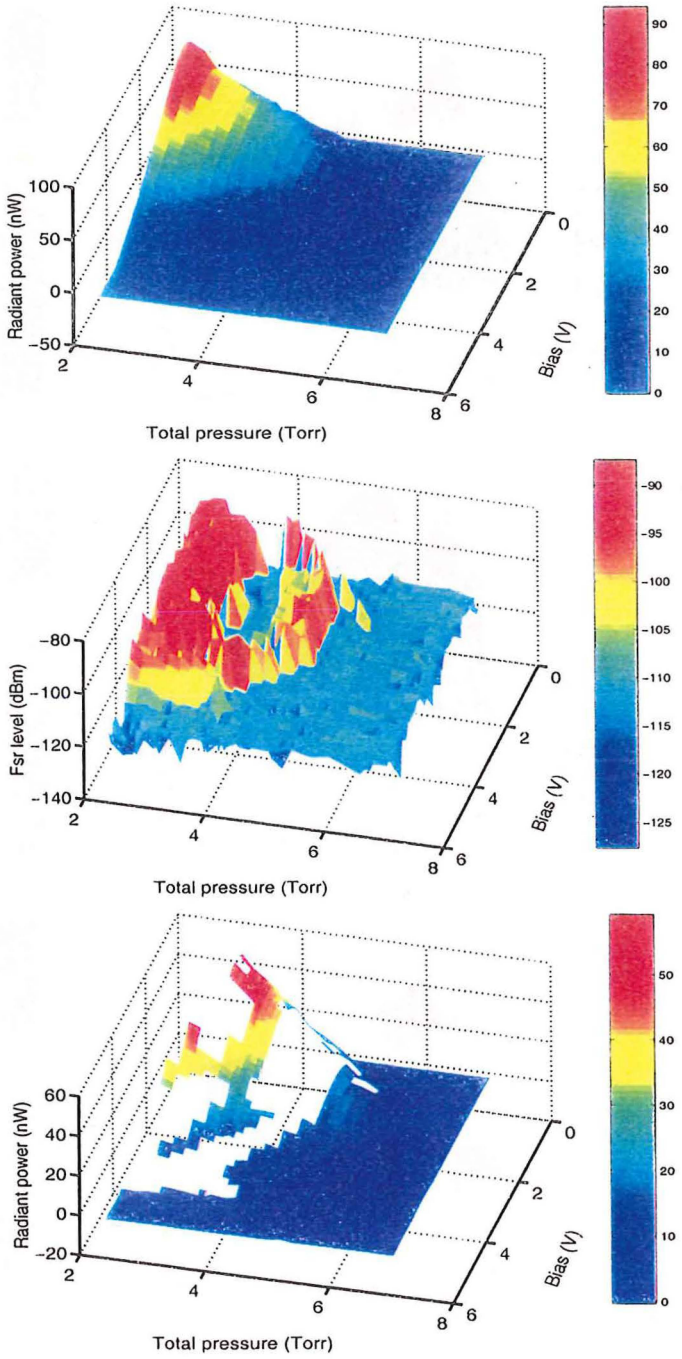

Figure 2.15: C-I output characteristics with variation of input RF power and total gas pressure for a neon partial pressure of 0.14 torr. (a) Output radiant power, (b) power in FSR beat signal, and (c) output radiant power for the regions where no adjacent longitudinal mode is present.

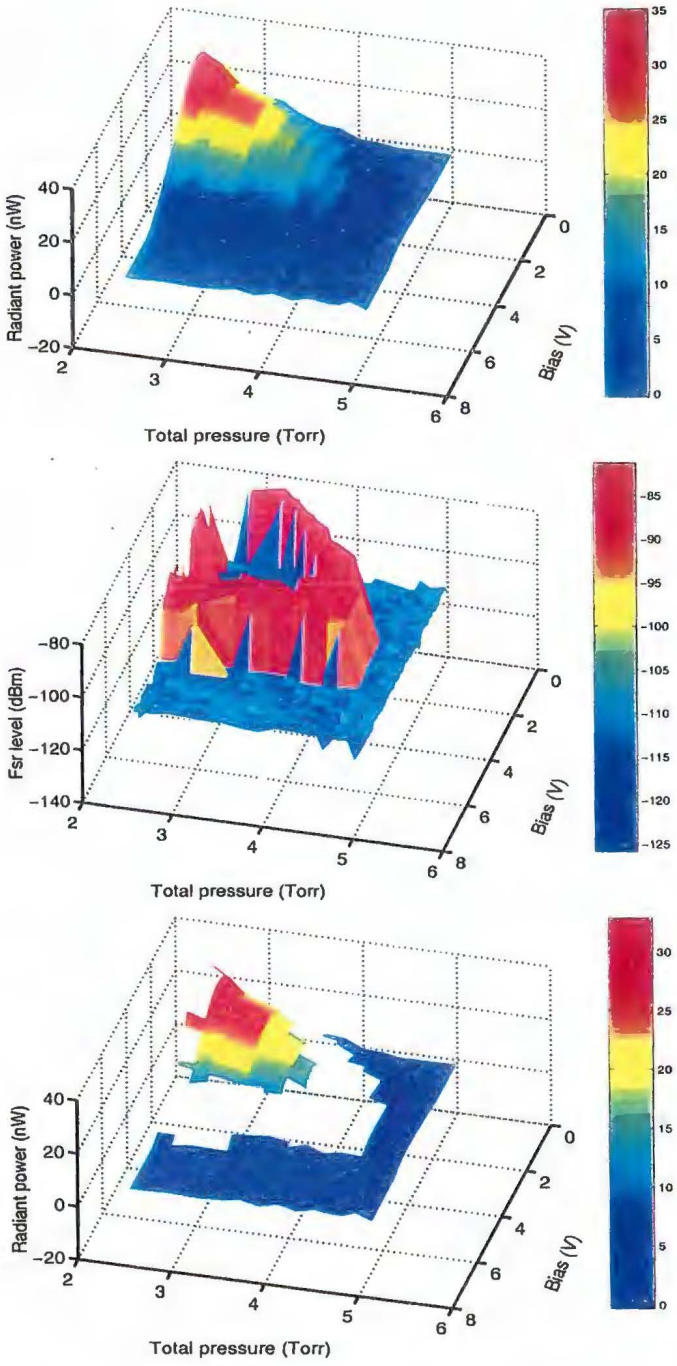

Figure 2.16: C-I output characteristics with variation of input RF power and total gas pressure for a neon partial pressure of 0.16 torr. (a) Output radiant power, (b) power in FSR beat signal, and (c) output radiant power for the regions where no adjacent longitudinal mode is present.

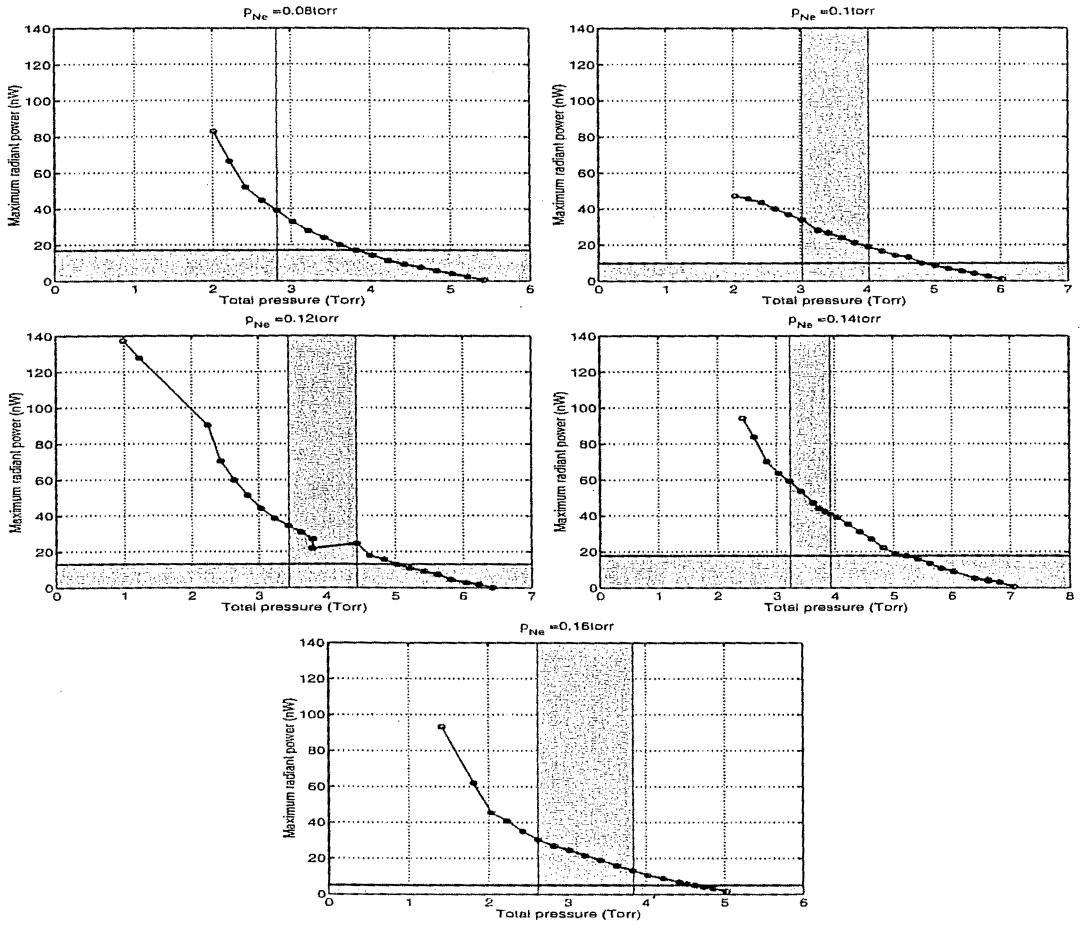

Figure 2.17: Maximum radiant power as a function of total gas pressure for a variety of neon partial pressures. The grey regions indicate the pressures at which no adjacent longitudinal mode was present. In the vertical regions it is only guaranteed that no adjacent longitudinal mode was present for the part of the scan close to peak radiant power. This region is referred to as the region of apparent single mode operation (RASMO). However there may be a longitudinal mode separated by twice the FSR frequency. The horizontal regions are guaranteed single longitudinal mode operation for the entire scan range. For more details see the accompanying text.

Similar data for the RF excited, high-Q 1.6 m linear laser LI installed in the Physics Department at Canterbury [2] indicate that a predicted homogeneous linewidth $\Delta\nu_h \sim 190$ MHz is required to obtain single mode operation over the full range of input powers that sustain laser operation. This value of $\Delta\nu_h$ is about twice the free spectral range. Similarly a predicted homogeneous linewidth of $\Delta\nu_h \sim 145$ MHz is found for the critical pressure for the 14 m^2 ring-laser gyroscope G0 which has a free spectral range of approximately 21 MHz [2]. Therefore the size of the laser does not significantly affect the homogeneous linewidth necessary to obtain single mode operation for the entire range of input RF powers that sustain oscillation.

In a triangular ring laser 13 m on a side it has been observed that pressure broadening may be used to suppress a large number of longitudinal modes with a separation of ~ 7.5 MHz while oscillation is sustained for a mode approximately 200 MHz away from the next mode that is observed to be above threshold [27]. The separation of 200 MHz corresponds with the value of $\Delta\nu_h$ predicted from Equation (2.10). This behaviour is markedly different from that exhibited by the Canterbury lasers and G0 in particular since the dimensions of G0 mean that it is the most likely candidate to furnish such an observation. Unfortunately there are no data regarding the neon partial pressure used so one cannot check the mix ratio and agreement with the data of Smith and Hänsch [66].

There is a significant difference between the device reported by Dunn [27] and the three earliest Canterbury ring-laser lasers. DC excitation is used instead of RF excitation and, more importantly, the plasma tube is 84 cm long. The design of the plasma tube means that it is possible to obtain significantly more gain than is the case with the RF discharge configuration used on the Canterbury gyroscopes. During laser operation this means that there is sufficient gain at higher pressures to sustain modes at frequencies situated 200 MHz and greater from gain centre while modes at lesser frequency shifts from gain centre are suppressed due to spectral hole burning. Given the same homogeneous linewidth a mode ~ 7.5 MHz from the dominant longitudinal mode will experience much more severe gain depletion than a mode, say, 80 MHz from the dominant mode. However two longitudinal modes spaced, for example, ~ 200 MHz apart will cause increased gain depletion, particularly for frequencies midway between the two modes. This net effect will cause these modes with intermediate spacing to be suppressed as well as the modes adjacent to the dominant longitudinal modes.

Although the basic mechanism is the same, the details of suppression of longitudinal modes in the Canterbury lasers is different from that of the laser reported by Dunn [27]. All of the Canterbury lasers require an estimated homogeneous

Pressure (torr)			homogeneous linewidth (MHz)		Max. Radiant power (nW)	
p_{NE}	p_1	p_2	$\Delta\nu_h(p_1)$	$\Delta\nu_h(p_2)$	$P(p_1)$	$P(p_2)$
0.08	3.8	2.8	237	179	18	40
0.10	4.8	3.5	296	220	10	20
0.12	5.0	4.0	307	248	15	30
0.14	5.0	3.6	307	226	19	50
0.16	4.6	3.3	284	208	5	20

Table 2.7: Summary of pressure fill characteristics for various neon partial pressures. p_1 is the critical pressure and p_2 is the pressure at the centre of the region of apparent single mode operation RASMO. $\Delta\nu_h(p_i)$ is the homogeneous linewidth at each of these pressures estimated using Equation (2.10).

linewidth that is a factor 2-7 times the free spectral range[16]. If gain saturation occurs the width $\Delta\nu_H$ of the Lorentzian hole burnt in the Doppler profile is greater than the homogeneous linewidth [8, p. 231];

$$\Delta\nu_H = \Delta\nu_h\sqrt{1+\frac{I_\nu}{I_s}}, \tag{2.11}$$

where I_ν is the irradiance of the oscillation mode and I_s the saturation irradiance.

A qualitative explanation of longitudinal mode suppression in the Canterbury lasers may be formulated from the observations made thus far. It is proposed that in order to suppress adjacent longitudinal modes it is necessary that all modes apart from the dominant mode be suppressed across the entire net positive gain bandwidth by means of spectral hole-burning. This is a direct consequence of the low-gain nature of the lasers and the value of the free spectral range in comparison with the positive net gain bandwidth. Consequently the width of the hole burnt must be significantly greater than, and independent of, the value of the free spectral range. Any gain saturation that occurs will serve to increase the strength of the mode suppression.

The low-gain RF excitation schemes used in the Canterbury lasers mean that a positive net gain bandwidth (ignoring spectral hole-burning) of $\sim 200-300$ MHz

[16]The estimate of the homogeneous linewidth is based on the data of Smith and Hänsch who used a p_{NE} : p_{HE} ratio of 7:1. Consequently this estimate could be called into question for the large mixing ratios used for the data presented here. The critical pressures observed for G0 and C-1 for similar mixing ratios are too close together to produce a difference in linewidth broadening large enough to account for the factor of four difference in the free spectral range. Therefore it is not possible to resolve the apparent contradiction with the results reported for the triangular laser by a naive assumption that the different values of the constants in Equation (2.10) will allow the explanation for the laser reported by Dunn [27] to be applied to the Canterbury lasers.

is plausible for the fill pressures in question[17]. Therefore hole-burning from the dominant mode will suppress all other modes across the entire bandwidth of longitudinal modes that could possibly oscillate. When the hole-burning is of the order of one FSR and the electron concentration is sufficient to cause the population of the lower laser level to rise significantly there is insufficient gain for a mode two FSR from the dominant mode to lase. However the hole burning from the dominant mode is insufficient to completely suppress the mode adjacent to the dominant longitudinal mode. This may be used to explain the observed behaviour for pressures slightly less than the critical pressure. Although this explanation is consistent with observation further work is required in order to quantitatively verify it. This experimentation should include investigation of longitudinal mode behaviour while scanning the pathlength in order to verify the positive net gain bandwidth is of the order of a few hundred MHz. Also it is necessary to determine if the estimates of the homogeneous linewidth (2.10) may be used for the mixing ratios in question.

Region of Apparent Single Mode Operation

Two qualitative explanations of the region of apparent single mode operation or RASMO described in Section 2.5.2 are proposed. One is consistent with a low-gain pumping arrangement that only supports a relatively small positive net gain bandwidth, regardless of gas fill pressure. The other is consistent with the explanation for the operation of a high-gain system operating at fill pressures similar to the critical pressure [27]. It is not possible to differentiate between either explanation using the data presented in the previous Section. Knowledge of the behaviour of longitudinal modes 2 FSR from the dominant longitudinal mode is required to complete the description. Determination of the preferred explanation is of more than academic interest. If the RASMO is indeed a region of true single longitudinal mode operation a useful improvement in the resolution of the Earth rotation will result from operation in this regime. For example, if an increase in the optical power by a factor of two was achieved, the white noise frequency fluctuations in the gyroscope beat frequency will be reduced by a factor of $\sqrt{2}$. Figure 2.17 indicates that an increase by a factor of 2 in the radiant power may be achieved with ease if the RASMO is, in fact, a viable operating regime.

The proposed explanation for the RASMO that is consistent with a high-gain system is as follows. It is necessary that there is sufficient unsaturated gain for

[17]The C-II FSR comb discussed in Section 3.2 shows this in a quantitative manner. Five longitudinal modes, with a spacing of $\approx$ 75 MHz, implies a positive net gain bandwidth of $\approx$ 350 MHz. The fill pressure was small compared to that of the data presented here for C-I. Therefore the population inversion resulting from the conditions leading to this data is not significantly reduced by population of the lower laser state from the $1s$ level. Consequently the net positive gain bandwidth deduced from Figure 3.3 is larger than that of the C-I data presented in this Section.

a second longitudinal mode to have positive net gain at a frequency separation of twice the FSR. At a given pressure within the RASMO the collision broadening from both the longitudinal modes $\text{TEM}_{m,n,q}$ and $\text{TEM}_{m,n,q+2}$ will be sufficient to suppress the longitudinal mode $\text{TEM}_{m,n,q+1}$. If the excitation power is decreased while the pressure is constant the net gain will also be reduced. At some value of the excitation power there will be insufficient gain for the longitudinal mode $\text{TEM}_{m,n,q+2}$ to maintain oscillation. Simultaneously the suppression of the longitudinal mode $\text{TEM}_{m,n,q+1}$ is reduced to that only caused by the longitudinal mode $\text{TEM}_{m,n,q}$ and $\text{TEM}_{m,n,q+1}$ is observed to be above threshold. As the excitation power is further decreased the resultant reduction in gain will cause the longitudinal mode $\text{TEM}_{m,n,q+1}$ to fall below threshold, leaving the laser in single mode. A similar sequence of arguments may be followed to explain the observed behaviour as the helium partial pressure is increased. Once again consider the initial state at a given pressure within the region of apparent single mode operation and assume that the collision broadening from both the longitudinal modes $\text{TEM}_{m,n,q}$ and $\text{TEM}_{m,n,q+2}$ is sufficient to suppress the longitudinal mode $\text{TEM}_{m,n,q+1}$. As the pressure is increased the gain for the mode $\text{TEM}_{m,m,q+2}$ will fall due to the increase in population of the lower laser level. Therefore the mode $\text{TEM}_{m,m,q+1}$ will experience a reduction in mode suppression and an adjacent longitudinal mode will once again be observed for the pump power that produces the maximum output power. Once the pressure is increased to a value greater than the critical pressure $\text{TEM}_{m,m,q+1}$ will no longer possess a population inversion and single mode operation will be observed for all pump powers.

An alternative explanation may be found by consideration of the changes in the saturation iiradiance as the total pressure is varied. Consider the behaviour for a scan of excitation power at a given pressure within the RASMO. The familiar result for the gain $\gamma(\nu, I_\nu)$ in an inhomogeneously broadened medium when the width of the hole is small compared to the inhomogeneous linewidth is [8, p. 232]

$$\gamma(\nu, I_\nu) = \frac{\gamma_0(\nu)}{\sqrt{1 + I_\nu/I_s}}, \tag{2.12}$$

where $\gamma_0(\nu)$ is the small-signal gain coefficient. Conversely if the stimulating field is large enough and the width of the hole is much larger than the inhomogeneous width the gain is [8, p. 234]

$$\gamma(\nu, I_\nu) = \frac{\gamma_0(\nu)}{1 + \bar{g}_h(\nu) I_\nu/I_s}, \tag{2.13}$$

where $\bar{g}_h(\nu)$ is the normalised lineshape function. Note that Equation (2.12) leads to saturation across the entire band while the lineshape function means that, in the approximation of Equation (2.13), there is minimal saturation in the wings of the gain curve. The description of the intermediate case is much more complex and not required for this qualitative analysis.

Consider a pressure that allows access to the RASMO for the input power scan. At low cavity iiradiances ($I_\nu \ll I_s$) there is minimal saturation and adjacent longitudinal modes will not be substantially suppressed. However as the power is increased saturation will suppress the adjacent longitudinal mode. As the pumping is further increased, past the maximum output power, the reduction in irradiance and, in turn, optical power leads to a commensurate reduction in mode suppression. Therefore an adjacent longitudinal mode will once again be observed. This is consistent with the results presented in Figures 2.12–2.16. A small increase in the pressure means the peak output power is reduced. Consequently the gain reduction is not as severe for the adjacent longitudinal mode and it is observed to be above threshold for the peak pumping powers. For pressures greater than the critical pressure single longitudinal mode operation is obtained for the entire range of pump powers that support oscillation. This is because there is never sufficient gain to allow the mode adjacent to the dominant longitudinal mode to rise above threshold.

It is unknown if gain saturation is sufficient for the dominant longitudinal mode to suppress an adjacent longitudinal mode by itself or whether a mode separated by two FSR from the dominant longitudinal mode is required to assist in mode suppression. Note that since any mode two FSR from the dominant mode will have a much lower unsaturated gain the gain saturation will have much less effect than is the case with the dominant longitudinal mode. Furthermore the saturation irradiance is inversely proportional to the lineshape function [8, p. 220] which is reduced for outlying modes. Therefore saturation effects for the outlying modes are further reduced. Consequently it is the dominant longitudinal mode that is the major contributor to this effect. This consideration recognises that a combination of both explanations may describe the observed effects.

In order to obtain a more detailed and quantitative understanding it is necessary to monitor the behaviour of modes two FSR from the dominant mode. Since two adjacent modes either side of the dominant mode will produce a beat frequency at two FSR this is not a trivial task. One approach that may be employed is to utilise the effect of dispersion and look at the small differences in the beat frequencies using heterodyne techniques discussed in Sections 3.1 and 3.2.

Reduction of Mode Suppression by Radiation Trapping

Radiation that is spontaneously emitted to the ground state may be trapped or re-absorbed into the upper laser state. The importance of this effect in the operation of any given He:Ne laser is dependent on the diameter of the beam as well as the diameter of the gain tube and neon partial pressure [64].

When cross-relaxation effects, such as radiation trapping, are taken into account

the saturation irradiance may be rewritten as [64]

$$I'_s = (1 + C)I_s, \tag{2.14}$$

where the cross-relaxation parameter C increases with increasing pressure and is of the order 0.05-2.0 [66]. The saturated gain is given by [64]

$$\gamma(\nu, I_\nu) = \frac{\gamma_0(\nu)}{\sqrt{1 + I_\nu/I'_s} + CI_\nu/I'_s}. \tag{2.15}$$

Therefore the gain saturation behaviour is the same as that of an inhomogeneously broadened medium with the addition of a homogeneous saturation term whose magnitude depends on the cross-relaxation parameter C. Equation (2.15) is obtained by including additional terms to the rate equation describing the population of the upper laser level that are not required for the derivation of Equation (2.11) [8]. To give an example of the magnitude of the parameters involved, it was found that a total pressure of 3.0 torr (7:1 He^3:Ne^{20} mix ratio) results in a value of $C = 0.15$ [66][18]. The saturation irradiance I'_s was found to be $32\,W/cm^2$.

For a He:Ne discharge the trapping length, or distance that a photon (632.8 nm) travels before there remains a probability of $1/e$ that it will not have been absorbed, is given by [64]

$$l_T = \frac{7 \times 10^{-2}}{p_{NE}} \text{mm}, \tag{2.16}$$

where P_{Ne} is the neon partial pressure in torr. Therefore $p_{NE} = 0.08$ torr results in a trapping length of 0.875 mm while for $p_{NE} = 0.16$ torr, $l_T = 0.438$ mm. Therefore for the 3.8 mm inner diameter gain tube used in C-I it may be assumed that for the data presented the majority of spontaneously emitted radiation from the $2p$ state to the $2s$ state is trapped. At lower neon partial pressures, or for smaller gain tubes, the assumption that the majority of radiation is trapped is no longer valid and a dependence in the amount of radiation trapping on the diameter of the gain tube results.

In the case of complete radiation trapping the cross-relaxation decay rate has been found to be dependent on the beam diameter as well as the gas pressure [64]. Therefore this is important in determining the amount of collision-induced broadening. The cross-relaxation decay rate, which defines the width of the broadening and amount of saturation, is dependent on the fraction of atoms which absorb within the laser beam. If the beam area fills a larger fraction of the gain tube cross-sectional area the cross-relaxation parameter decreases leading to a reduction in the saturation. In turn this will reduce the mode suppression due to saturation and create a commensurate reduction in the RASMO when the ratio of spot-size to gain tube diameter is relatively large. This is precisely the behaviour found when comparing C-I, LI and G0.

[18]The laser used to obtain the reported results possessed a gain tube diameter of 3 mm and beam diameter 0.14 mm.

2.5.3 Summary

Several benefits may be enjoyed by operating the laser at a gas pressure that ensures predominantly single mode operation for the entire range of pump powers. The most important is the improvement in resolution of rotation by operating at a higher power while maintaining single mode. Figures 2.12–2.16 show that with an appropriate gas-fill pressure it is possible to increase C-I's radiant output power per port from a few nW (1-5 nW) to approximately 20 nW and maintain single longitudinal mode operation. The reduction in the white frequency noise fluctuations of the gyroscope beat frequency is proportional to the square root of the radiant power increase factor. Secondly, the ability to operate near the region of peak gain means that the variation in gain as the pathlength changes is not as severe as in the wings of the gain curve. This means that the laser is much less sensitive to perturbations in the pathlength which give rise to beat frequency drift via interaction with the gain medium. Further discussion of these effects may be found in Section 3.5.

It should be kept in mind that the explanations for the observed effects are somewhat speculative. The main reason for this is that no data were available for the behaviour of modes 2 FSR from the dominant longitudinal mode. This has a direct bearing on which explanation is to be preferred.

Another point of interest that is unclear is the applicability of the results of Smith and Hänsch for the large mixing ratios used. If a quantitative understanding of the observed phenomena is required, knowledge of the homogeneous linewidth for the larger mixing ratios is required.

A qualitative investigation of radiation trapping indicates that it plays a significant, and hitherto unrecognised, role in the determination of the output characteristics of the Canterbury lasers. As well as affecting the size of the region of apparent single mode operation (RASMO) it will also affect the maximum output power that may be obtained for single mode operation. This will also have an impact on the resolution of the gyroscope due to the relationship (2.4) between the power per mode and the noise contribution due to spontaneous emission. Equation (2.9) gives the preferred gain tube diameter for a given fill pressure. This recommendation is based on consideration of the population of the lower laser level from the $1s$ state, causing a reduction on the population inversion for larger pressures. It is stipulated that the Canterbury gyroscopes are operated in single longitudinal mode. Therefore the pressure implied by (2.9) has to be interpreted in conjunction with the discussion presented in this Chapter. The ultimate goal is to formulate a predictive recipe that finds the maximum output power as a function of gas fill pressure, mirror configuration and gain tube diameter.

Chapter 3

Investigation of Sagnac Frequency Drift Sources in C-II

The aim of this Chapter is to investigate various effects that cause the beat frequency between the oppositely directed travelling waves to be shifted from the nominal value given by the Sagnac formula (1.1). As a result a diverse range of material is presented. Initially, a study is made of the importance of various laser parameters determining the observed Sagnac frequency dependence on the optical pathlength. It is found that dispersion effects due to the gain medium can play a significant role in determining the observed Sagnac beat frequency. In particular, mode pushing when the powers of the counter-propagating beams are unequal, is shown to be a source of beat frequency pushing of the magnitude observed in C-II. This result is contrary to previous understanding within the Canterbury ring-laser group.

3.1 Piezo Calibration

In order to properly analyse the data presented in the following sections a careful calibration of the piezo-electric-transducer used to adjust the laser perimeter is required. In the past the Canterbury ring laser group has used the change in the FSR beat frequency between two longitudinal modes as a function of the piezo driver control voltage to calibrate this voltage against the change in perimeter. However, as discussed later in this Section, it is unreliable due to the effects of mode pushing and pulling due to dispersion in the gain medium [19].

The rationale for calibration using the change in the FSR beat frequency is particularly straightforward. The difference in frequency between two longitudinal modes is given by the free spectral range or FSR beat frequency,

$$\nu_{\mathrm{FSR}} = \frac{c}{L}, \tag{3.1}$$

where L is the optical pathlength for one circuit of the laser. Note that L depends on the index of refraction. For a small variation δL in the perimeter the following

relation holds;

$$\delta L = \frac{-\delta\nu_{\text{FSR}} c}{\nu_{\text{FSR}}^2}, \tag{3.2}$$

where $\delta\nu_{\text{FSR}}$ is the variation in the FSR beat frequency. Therefore an observation of the FSR beat frequency as the pathlength is scanned will allow a calibration of the perimeter change against the piezo driver control voltage. It should be pointed out that this method is most applicable in a passive cavity since, in the presence of an active gain medium, the index of refraction, or more generally the complex polarisation [12, 19], will change depending on the position of the mode along the gain-frequency curve.

Figure 3.1 shows the experimental setup used to implement the calibration. The basic goal is to perform heterodyne detection on the FSR beat waveform using a stable solid-state oscillator as the local oscillator [54]. The carrier signal is amplitude modulated by the local oscillator producing sum and difference frequencies between the two signals. In heterodyne measurements it is advisable to use an *image rejection filter*. This is because a signal symmetrically placed (in frequency space) about the local oscillator will be added to the carrier signal under observation. Since noise constitutes such a signal the absence of an image rejection filter will reduce the signal-to-noise ratio by a factor of two.

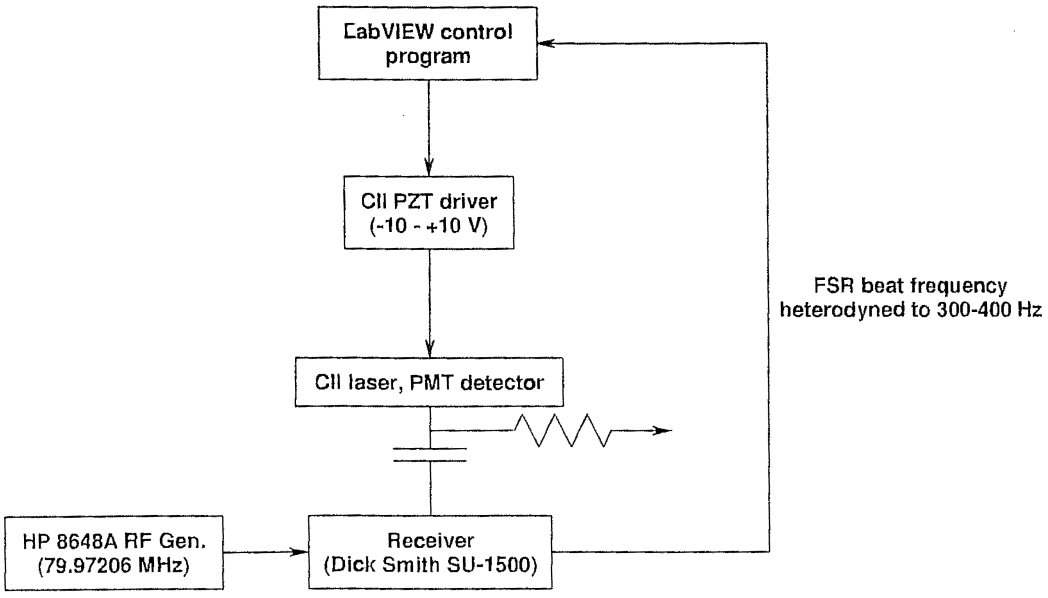

Figure 3.1: Setup for C-II piezo calibration.

Optical detection was performed by a Hamamatsu R3986 PMT described in Section 2.4.1. This was used to observe the beam exiting the combined beam port. A suitable capacitor in series and resistor in parallel with the detection chain allowed the RF beat between the two longitudinal modes to pass down the detection chain,

while simultaneously eliminating low frequency signals. A GPS-stabilised HP8648A RF signal generator provided an accurate frequency reference against which the fsr beat frequency from the ring-laser was compared. The frequency of the HP8648A was set such that it was offset from the FSR beat frequency by 300-400 Hz. This provided a suitable operating region, balancing the demands of maintaining a relatively low beat frequency to minimise the required data acquisition sampling rate while avoiding the attenuation caused by the internal filters in the receiver used to heterodyne the two signals[1]. A radio receiver with its internal oscillator disabled was used to detect the AM modulation of the carrier caused by the local oscillator. The audio tone generated by the heterodyne detection was then recorded using a digital data acquisition card operating at a sampling rate of 1000 Hz with 500 Hz cutoff 5th order Butterworth anti-alias filters inserted in the detection chain prior to the data acquisition card.

Pathlength scanning was performed by a piezo-electric-transducer bonded to one mirror. This was controlled from LABVIEW^{TM} using a digital-to-analogue (d/a) channel of the data acquisition card to provide the -10 to +10 V scan signal required to scan the piezo driver in 0.5 V steps through its entire operating range. A five second segment of data were recorded at each pathlength setting before this was changed. This was followed by a short settling time and another data acquisition.

The RF drive power for the calibration procedure was set such that only two longitudinal modes were present for the majority of the scan interval. Three longitudinal modes were present however at the crossover point denoted as "multimode" in Figure 3.2.

Data processing consisted of making an initial estimate of the beat frequency from the peak of the power spectrum. This estimate was used to define the centre frequency of the bandpass filter for a precise second-order auto-regressive (AR2) estimate of the FSR beat frequency. See Appendix B.3 for a description of this method of frequency estimation which is routinely used by the Canterbury ring-laser group. A filter bandpass of 20 Hz was used to obtain the AR2 estimates. Therefore the uncertainty in each estimate plotted in Figure 3.2 is very small and the departures from nonlinearity may be attributed to effects arising from the properties of the gain medium or nonlinearities in the piezo-electric transducer itself.

There is distinct jump in the FSR beat frequency over the small range of perimeter variation where more than two longitudinal modes were present. Therefore it was necessary to eliminate these regions from the calibration. To do this four line-of-best-fit estimates were made for regions where only two longitudinal modes were present. These estimates were then averaged to obtain a variation in the FSR beat frequency of 4.7 Hz/V. This corresponds to a perimeter variation of

[1]These filters suppressed signals below $\sim$ 250 Hz.

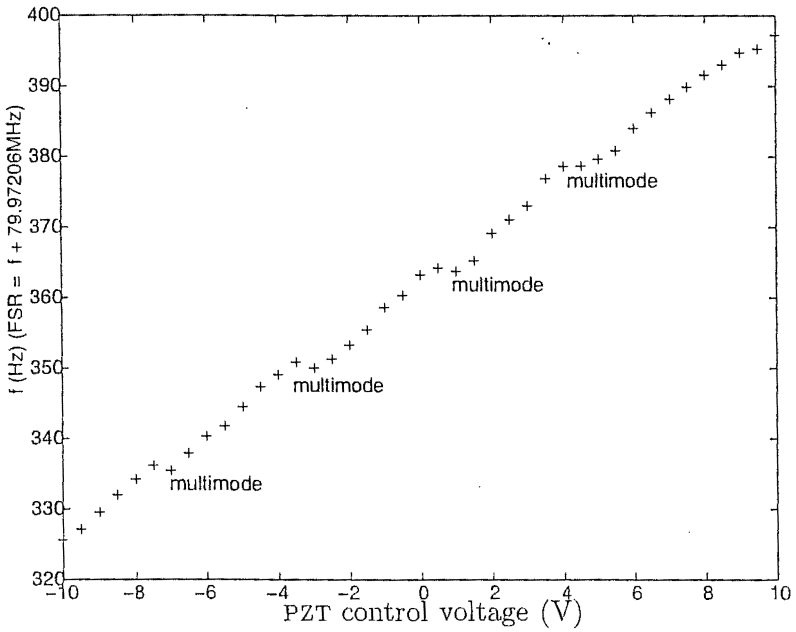

Figure 3.2: Calibration data for C-II piezo. Regions where more than two modes were present are marked as "multimode". The jumps that depart from linearity are due to the transition region where three longitudinal mode are present. Either side of the transition region the calibration data are derived from a different pair of longitudinal modes.

250 nm/V. This result implies a piezo voltage excursion of 2.5 V in order to scan the pathlength through one wavelength. There remains, however, some ambiguity with respect to this calibration. Consider the results presented in Figure 3.7. The spacing between longitudinal mode hops, in terms of the piezo driver input voltage, is of the order of 4 volts implying a calibration of about 160 nm/V. Within the (somewhat limited) accuracy that the position of the mode hop could be observed there was no dependence on the direction in the which the piezo-controlled mirror was scanned. Clearly there is disagreement between the various results. The resolution to this lies in recognition of the fact that there is significant mode frequency pushing and pulling due to the gain medium as the longitudinal mode moves across the gain curve in frequency space. If, instead of treating the data for each longitudinal mode independently and evaluating the line-of-best-fit for each mode pair to obtain a calibration, a linear fit is made using all the data points a calibration of 203 nm/V is obtained. This implies a piezo control voltage excursion of 3.12 V in order to change the pathlength by one wavelength. Once again, this method has obvious deficiencies and can only give an approximate calibration.

In conclusion, it has been found that the effects of mode pushing and pulling are such that it is not possible to produce an accurate calibration of pathlength variation by observation of the FSR beat frequency in the presence of the active gain medium. The lack of a reliable calibration means that observation of the drift of the FSR beat frequency does not furnish well-calibrated information on the pathlength drift of the laser. However if the operating conditions of the gain medium are relatively constant and the powers of the counter-propagating beams do not vary it is possible to relate the drift in the FSR beat frequency to pathlength drift since the mode pushing and pulling effects were seen to be reasonably linear within a given longitudinal mode operating region[2]. To obtain an accurate calibration of the pathlength change with the piezo an alternative method that does not rely on any quantity influenced by the active gain medium is required. In the remainder of this Chapter all pathlength variations are quoted in terms of the piezo driver voltage with the understanding that mode hops with a piezo drive voltage separation of about 4 V imply a pathlength shift of one wavelength. However if, for example, the cavity Q were to change due to the changing of the spot position on the mirrors the exact nature of the cross-over point between longitudinal modes, will not be precisely defined. Therefore, in order to obtain a definitive calibration of the piezo, it is necessary to operate the interferometer in a passive configuration for the purpose of calibration. This approach has its own difficulties however. The low transmission of the C-II mirrors

[2]At the time this investigation was made the gas pressure was such (0.26 mbar ^{20}Ne, 0.14 mbar ^{22}Ne, and 1.60 mbar of He) that the laser operated in the Doppler broadened regime. Subsequently the gas pressure was increased so that the homogeneous pressure broadening dominates. At the time of writing no data were available to assess the impact of dispersion in the pressure broadened regime.

means that very small signals will have to be dealt with.

In this Section it was demonstrated that there is significant differential mode pushing and pulling where the optical frequencies of the adjacent longitudinal mode are separated by one FSR, or approximately 80 MHz. The remainder of this Chapter investigates whether or not there there may be enough differential frequency pushing and pulling to impact on the measurements of Earth rotation in terms of the gyroscope beat frequency.

3.2 Dispersion of the FSR Beat Frequency

If the gain is increased to allow a number of longitudinal modes to rise above threshold a number of FSR beat frequencies with separations of the order of a Hertz are found. The power spectral density of such a signal is displayed in Figure 3.3. This spectral feature is a result of the FSR beats for the beam from

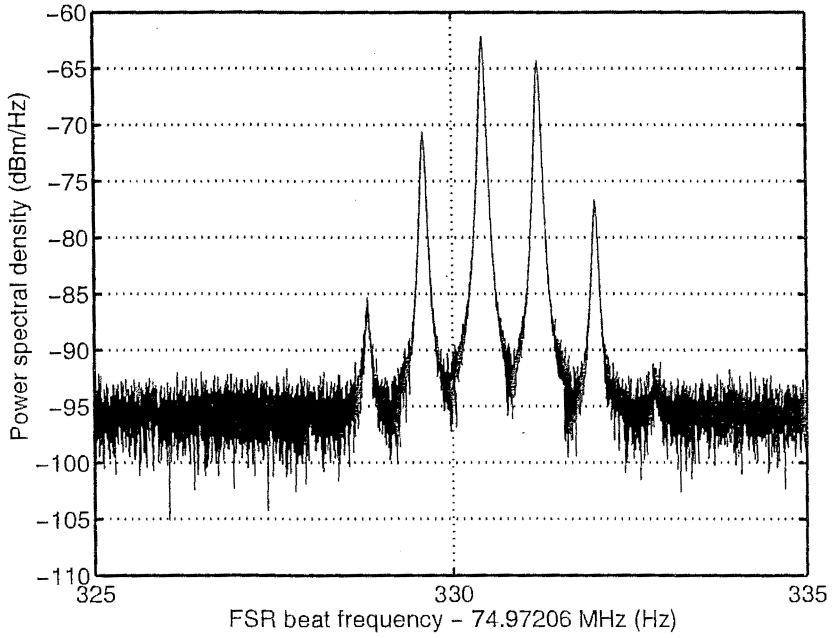

Figure 3.3: Comb of frequencies in the FSR beat spectrum. These are due to a changing intermode separation for a number of longitudinal modes as a function of position under the gain curve. The length of the data set was 100 s.

one direction. A similar feature shifted approximately 80 Hz is observed for the counter-propagating beam. Since the goal of this Chapter is to discuss the effects of dispersion in the single longitudinal mode regime no analysis of this effect will be undertaken. Nevertheless it provides a useful demonstration of the effects of dispersion on the longitudinal modes of the laser.

3.3 Scanning the Cavity Pathlength

This section addresses the effects of scanning of the C-II perimeter on the Sagnac beat frequency. It is found that the beat frequency between the counter-propagating waves is both *pushed* and *pulled* from the nominal Sagnac value. This effect has previously been observed in the normal operation of C-I and C-II [1, 15]. In this Section it is shown that the majority of variation in the C-II Sagnac frequency may be attributed to mode pushing derived from the gain medium rather than coupling due to scattering from the laser mirrors. This leads to the conclusion that the gain medium and, in particular, cross-pushing between the counter-propagating waves cannot be neglected in any model that aims to examine the effects when backscatter is present. At this point it is pertinent to note that backscatter is observed to strongly influence the behaviour of C-I. The best evidence of this is that operation is generally relatively close to the lock-in threshold. For example, it is possible to lock and unlock C-I by moving a small weight about on the Zerodur^{TM} plate. However any model of the gyroscope output frequency still requires the inclusion of some sort of cross-coupling in order to predict frequency pushing. Etrich *et al.* [16] provide some examples of frequency pushing due to cross-coupling. The improved construction and cleanliness of C-II means that scattering is significantly reduced. In order to obtain simple predictions of frequency pushing and pulling the assumption that backscattering may be neglected is made. One argument in favour of this assumption is based on the observation that the phase difference between the frequency modulation at the gyroscope on each beam due to scattering from one beam into the other is relatively constant as long as single longitudinal mode operation is maintained. Theoretical models indicate that this phase difference should change by 90 deg as the gyroscope frequency moves from the operating region where there is maximum frequency pulling to the operating region where there is negligible pulling [14–16]. However it should be noted that a complete description still requires the presence of backscatter. Apart from some special cases [16] it is necessary to solve the equations of motion numerically. Such an approach is avoided in this Chapter in an attempt to gain physical understanding of the behaviour of C-II.

Frequency pushing has also between predicted by King [4]. Data from C-I were found to be well described by numerical solutions of a theory based on the regenerative equation approach used by Siegman in the standard text *Lasers* [4, 67]. The self-consistent model does not explicitly include the cross-coupling used in this Section to explain the observed variation in the C-II gyroscope beat frequency. However it was concluded that a mechanism that affected the size of the scattering amplitudes, that occur as a fitted parameter in the model, with power is required. It was noted that dispersion provides such a mechanism [4]. Furthermore, it should be noted that the data analysed by King [4] were from C-I which has a lock-in threshold frequency that is much larger than C-II because the reflectivity

of the C-I mirrors is much less than the reflectivity of the mirrors installed in C-II. Therefore the dynamics of operation are much more heavily influenced by scattering than is the case with C-II[3]. The approach taken here begins from a somewhat different, but equivalent, starting point to that employed by those who have used the self consistent, or regenerative equations, that satisfy the optical boundary conditions that the fast variables return to the same value after each orbit of the cavity [4,16,67–71]. Instead, the approach of Aronowitz [17,18,72,73], based on the third-order theory of Lamb for the linear laser [12, 19] is followed. This approach begins with Maxwell's equations and has the advantage of leading to a set of self-consistent equations of motion for the electric field with mode pulling and pushing coefficients being expressed in terms of the plasma dispersion function [74] once the appropriate perturbation calculation of the polarisation is made [17, 19, 72]. These equations also satisfy the optical boundary conditions that the fast field variables return to the same values after each cycle around the cavity. This approach allows the fast variables to be eliminated and the evolution of the slowly changing variables to be described. The main advantage of the approach based on Maxwell's equations over the regenerative equation approach is that the former allows the magnitude of the frequency pushing and pulling to be predicted from quantities such the cavity-Q that may be measured independently. On the other hand the regenerative equation approach describes the dynamics of the laser in terms of fluctuation parameters that are fitted to a particular data set and therefore do not provide much predictive power.

Previous investigations within the ring-laser group have addressed the effects of dispersion due to change in the net linear gain [29] which was found to produce a pulling in the optical frequency toward gain centre. This was found to induce changes in the Sagnac beat frequency up to a few tens of milliHertz for realistic values for the gain. In this Section it is found that a mode pushing term in the third-order treatment [17, 19] may induce a much more significant dispersive effect in the Sagnac frequency. This effect is particularly important if the powers of the counter-propagating beams are unequal.

3.3.1 Experimental Setup

The experimental setup was essentially the same as that used in the piezo calibration. However in addition to monitoring the FSR beat on the combined beam PMT two new PMTs to monitor each of the beams independently were installed with the appropriate trans-impedance amplifiers. These amplifiers possessed a low-pass frequency response with a bandwidth of several hundred kiloHertz [4]. In total four data channels were recorded; the clockwise and counterclockwise single beam waveforms, the 50:50 combined beam waveform and the heterodyned FSR beat frequency. Once again a sampling rate of 1000 Hz was chosen with

[3]In practice this means the simplifying assumption made in Equation (3.46) cannot be taken to be valid in the characterisation of C-I.

500 Hz rolloff 5th order Butterworth anti-alias filters in place on all channels. The LABVIEW^{TM} control system scanned the piezo through the required voltage range (-10-+10 V) in steps of 0.2 V. Each voltage was held constant for 5 seconds.

Since an accurate estimate of the internal cavity irradiance is essential in the analysis of dispersion effects a careful calibration of the radiant power striking the PMT was made. The power calibration follows the approach of King which has shown to be a reliable method in the presence of laser power drift [4]. Calibration was performed before and after measurements with the results being averaged. It was found that for the data presented here the CCW detection system had a calibration of 220.5 pW/V and the CW detection system 262.6 pW/V. This was stable to $\sim \pm 20$ pW/V over a month.

The gain tube inner diameter was 4.0 mm. At the time of this work the gas-fill partial pressures were 0.26 mbar ^{20}Ne, 0.14 mbar ^{22}Ne, and 1.60 mbar of He. Therefore the pressure broadened linewidth [64, 75, 76] is much less than the Doppler width and inhomogeneous line broadening dominates.

Mirror transmission was taken as 0.24 ppm in accordance with the manufacturer's specifications [1]. The cavity quality Q is assumed to govern the cavity exponential decay according to $I(t) = I_0 \exp(-\omega_0 t/Q)$ so that $Q = \omega_0 \tau_{1/e}$. The $1/e$ decay time of C-II was measured to be $150 \pm 50\,\mu$s leading to $Q = 4.5 \pm 1.5 \times 10^{11}$ [4]. This implies a total power loss of 22 ± 7 ppm per mirror. The majority of the loss is due to scattering rather than transmission.

The RF excitation frequency was 57.612 MHz for all experiments. This value was chosen because it was found that fine adjustment and optimisation of the RF coupling to the plasma was easiest to achieve by tuning this frequency after an initial adjustment of the impedance matching circuitry.

3.3.2 Scanning the Optical Pathlength: Results

Figures 3.4, 3.5, and 3.6 display the variation in the beat frequency between the oppositely directed travelling waves as the perimeter is scanned for both compression and expansion of the pathlength. Comparison with the nominal Sagnac frequency splitting of 79.43 Hz [1] shows that the majority of the deviation from this value is in fact due to frequency *pushing* rather than frequency *pulling*. Unsurprisingly the results for the CW, CCW, and combined beam channels are virtually identical.

The results for scanning the piezo in each direction are presented. A small difference in the voltage at which each feature occurs is noted. There are two possible explanation for this observation. It is not possible to differentiate between either explanations at this stage. One explanation is that the piezo displays some hysteresis and the other is that there is a scan direction dependence in the laser

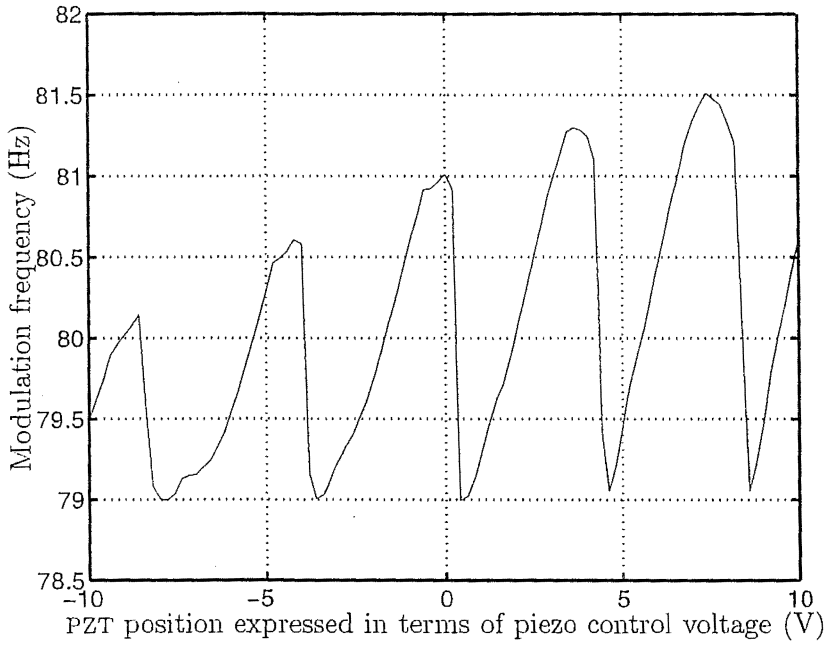

(a)

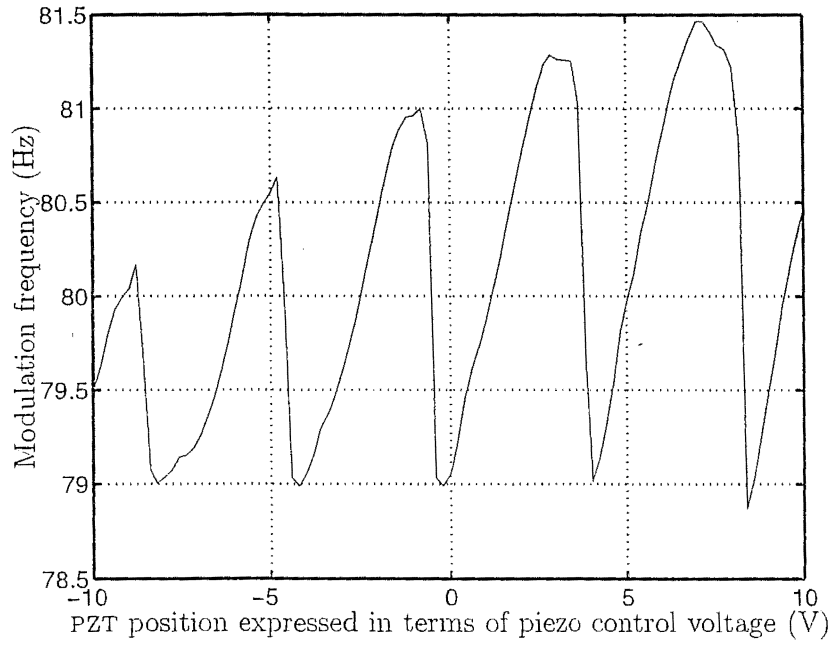

(b)

Figure 3.4: Frequency variation of CCW single beam modulation with pathlength (expressed in terms PZT control voltage) for (a) compression of the monolith and (b) expansion of the monolith.

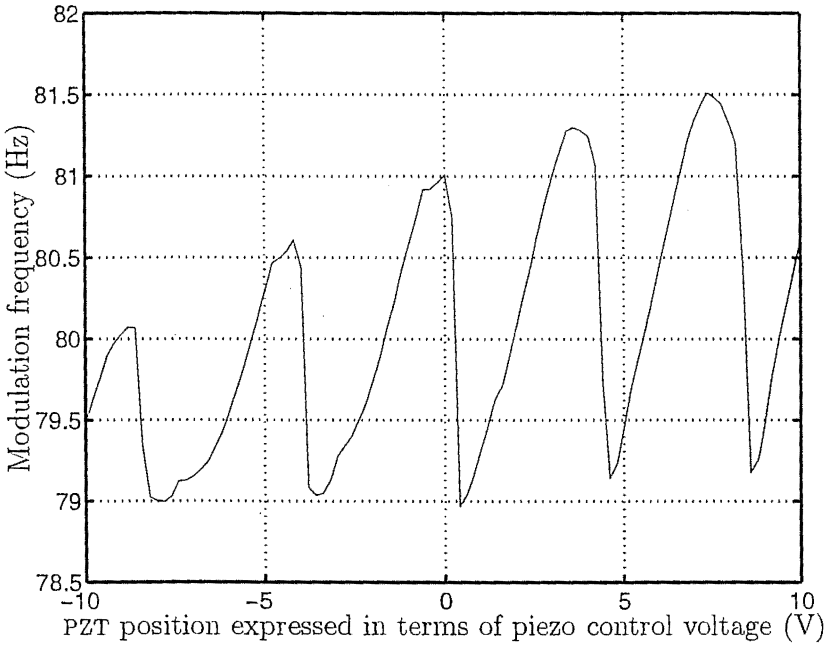

(a)

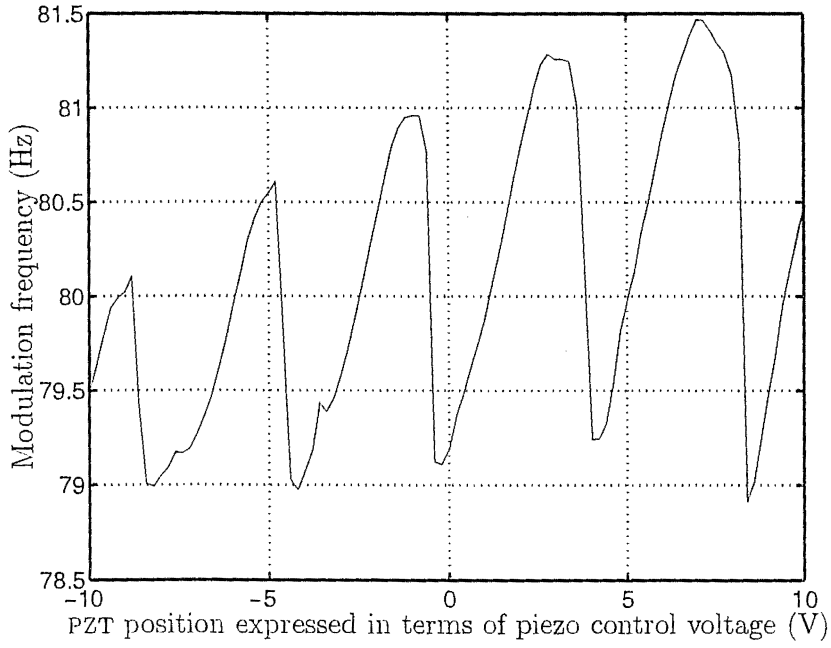

(b)

Figure 3.5: Frequency variation of CW single beam modulation with pathlength (expressed in terms PZT control voltage) for (a) compression of the monolith and (b) expansion of the monolith.

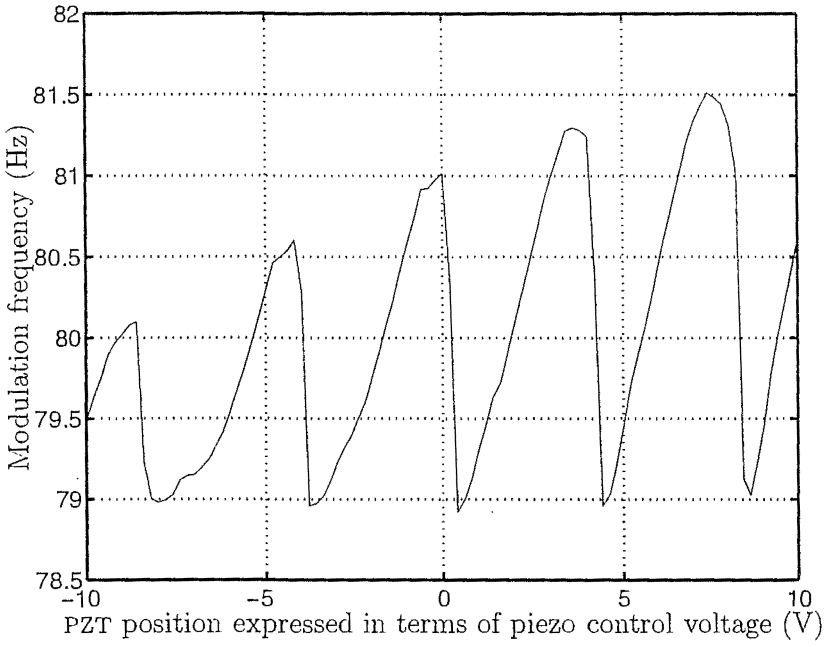

(a)

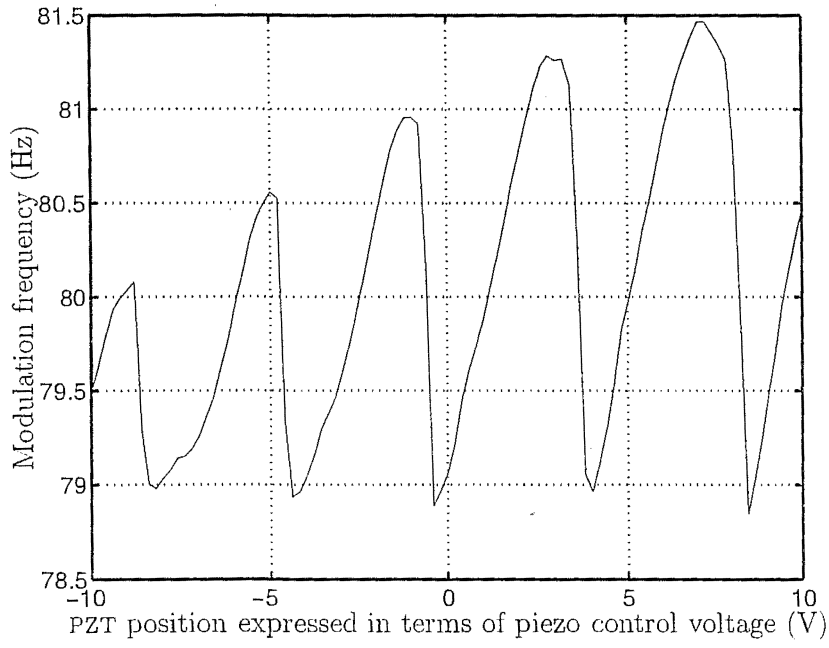

(b)

Figure 3.6: Frequency variation observed on combined beam detector with pathlength (expressed in terms PZT control voltage) for (a) compression of the monolith and (b) expansion of the monolith.

that arises from the behaviour of the longitudinal modes relative to the position of the longitudinal modes under the gain-frequency curve.

The frequency pushing seen here is not predicted by theories concerned with backscatter-induced frequency pulling where the assumption has been made that the effects of the gain medium are unimportant and consequently may be decoupled from backscatter effects in the analysis of the equations of motion for the counter-propagating electric fields [15, 18]. This assumption was thought to be valid for the Canterbury ring lasers [29]. However this type of frequency pushing has been commonly observed in the Canterbury ring lasers [1, 15]. The source of this effect has not previously been clearly identified. One alternative that has been mooted was the effect dispersion may have on the phase parameters of individual scatters, leaving the macroscopic effect of dispersion negligible, while providing the necessary coupling to induce frequency pushing [4]. In subsequent Sections it is shown that it is in fact possible to obtain strong enough dispersion effects from the standard third-order theory of the laser [17, 19, 72] to provide the coupling necessary to induce frequency pushing [12, 18]. This is supported by additional experimental observations.

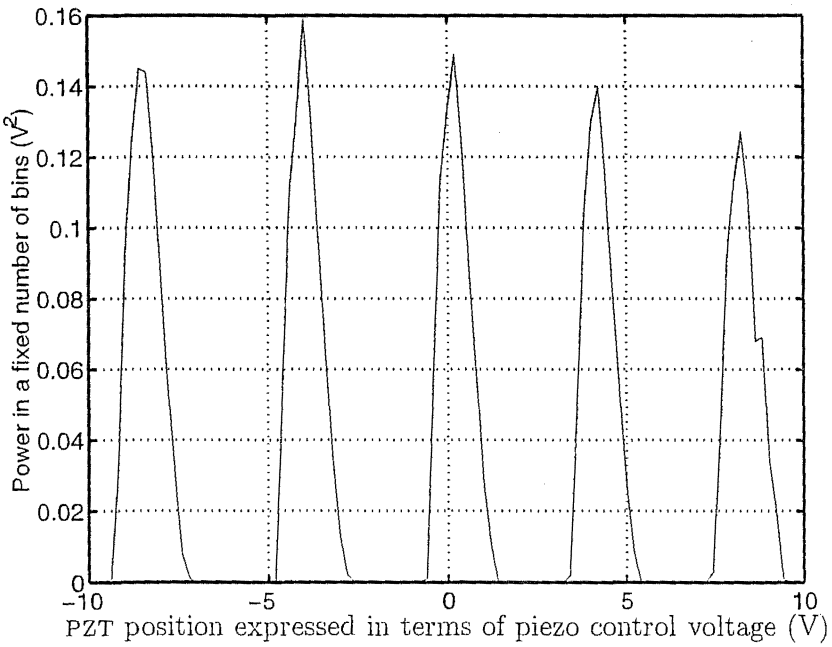

Figure 3.7: Power in fsr beat as a function of pathlength change (expressed in terms PZT control voltage). The gain was adjusted to a level that when the FSR beat was present only two longitudinal modes were above threshold. Note that the units are arbitrary and a result of the local oscillator amplitude setting.

Figure 3.7 shows the power in the FSR beat frequency as a function of the PZT control voltage which is closely related to the variation in the laser pathlength.

The data processing used to obtain the results presented in Figure 3.7 consisted of calculating the power spectrum of the data channel reserved for the FSR beat signal for each data segment. After a check was made to ensure that there was only one FSR beat present the power was calculated by integrating over the Fourier bin of peak power and two bins either side of the peak. There is little to be learnt from the particular value of the power in each peak because this is highly dependent on the amplitudes of the local oscillator and the FSR beat waveform used in the heterodyne detection.

Figure 3.7 provides information critical to the formulation of a successful interpretation. It shows that the sharp jumps from the beat frequency pushing regime to the beat frequency pulling regime coincided with the lasing frequency shifting between adjacent longitudinal modes and hence moving from one side (in frequency terms) of gain maximum to the other. At this point the change in the gyroscope beat frequency must arise from the sudden change that occurs at the mode hop. This could be due to either to the change in dispersion effects when the dominant longitudinal mode changes to a mode on the opposite side of the gain curve or due to the change in the phase of the backscattered light since the new longitudinal mode has a different wavelength from the previous longitudinal mode. The behaviour predicted by the third-order model due to the change in dispersion is investigated here and found to be in agreement with observation. The additional complexity and numerical modelling that is required to include the backscatter effects alongside the dispersion effects is beyond the scope of this investigation.

Since it was required that only two longitudinal modes were present in the longitudinal mode transition region it may be deduced that in this region each mode was placed approximately symmetrically about gain centre. Furthermore each longitudinal mode was toward the edge of the region of the gain-frequency curve possessing positive net gain. Otherwise more than two longitudinal modes would have been observed above threshold. From this knowledge and the fact that the FSR is approximately 80 MHz it is possible to estimate the gain-bandwidth for the region of positive net gain. The pathlength excursion within the transition region is on the order of a half of a wavelength, implying a positive net gain bandwidth (PNGB)[4] of about 120 MHz. This estimate of the PNGB is used in subsequent analysis to infer parameters relating to the population inversion necessary to calculate the mode pushing and pulling predicted by Lamb's third order theory of the laser [12, 18, 19].

The power variation as the pathlength is scanned is also of interest. Figure 3.3.2 shows the mean radiant power of the CCW beam incident on the detector over the scan range. These data introduce an interesting twist. Comparison with Figure 3.7 shows that the minimum radiant power occurs close to the transition between the multiple-mode and single mode regime on the higher frequency (lower

[4]This is defined as the full width between the frequencies possessing zero net gain.

P and higher piezo driver voltage) side of the multiple mode regime. On the other hand the maximum mean radiant power occurs near the lower frequency transition but slightly within the single mode regime. This implies that the simple situation of the internal cavity irradiance being mostly determined by the net gain derived from a symmetric gain curve is not applicable. Otherwise the peak radiant power within the single mode regime would occur approximately midway between two double-mode regions. Clearly an investigation of the electric field dynamics is required to explain this observation. However since the goal of this Chapter is to identify a cause for the observed mode pushing an explanation of this phenomenon may be recommended for further investigations. Figure 3.9 shows

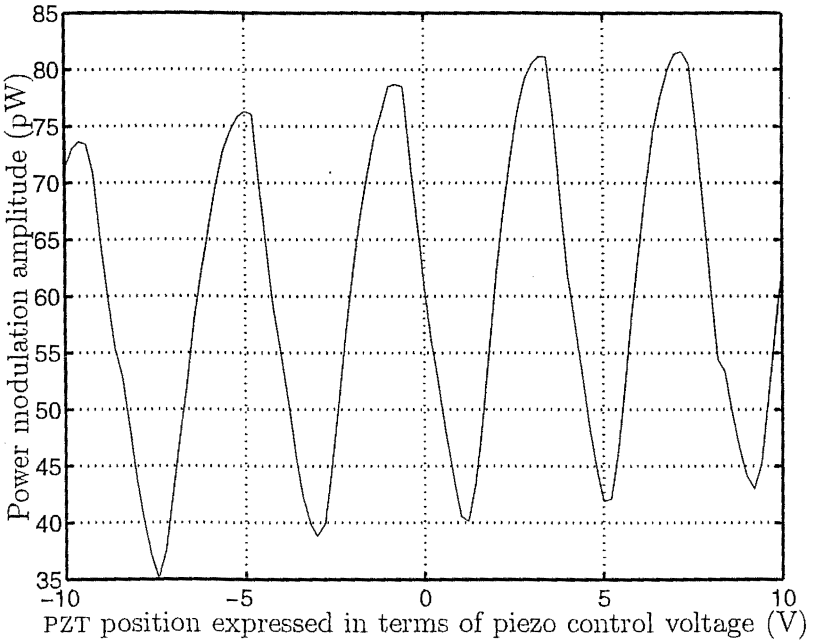

Figure 3.8: Variation of CCW mean radiant power with pathlength (expressed in terms PZT control voltage).

the peak-to-peak value of the radiant power modulation on the CW beam due to backscatter coupling between the counter-propagating waves[5]. This represents the effect of the CCW wave on the CW wave due to coupling. The variation with pathlength is very similar to that of the CCW mean radiant power.

To complete the description of power variation the CW peak-to-peak radiant power to the CCW mean radiant power modulation depth is shown in Figure 3.10.

[5]In Section 3.5 it is shown that the condition that determines the impact of backscatter on frequency pulling and beat frequency waveform distortion is different to the condition governing single beam modulation. Therefore it is possible for there to be significant single beam modulation with minimal backscatter-induced frequency pulling in agreement with the observations presented here.

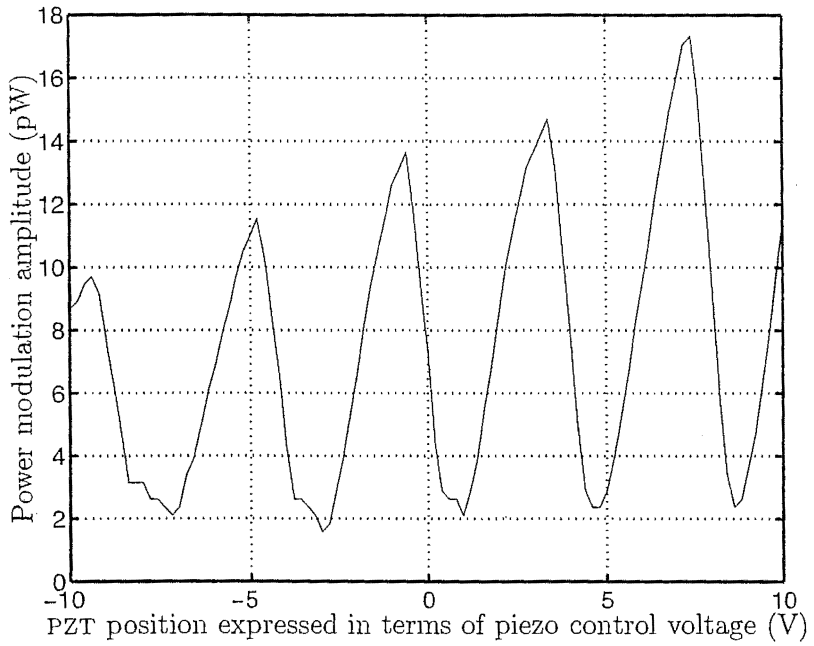

Figure 3.9: Variation of the peak-to-peak amplitude of radiant power modulation of CW beam with pathlength (expressed in terms PZT control voltage).

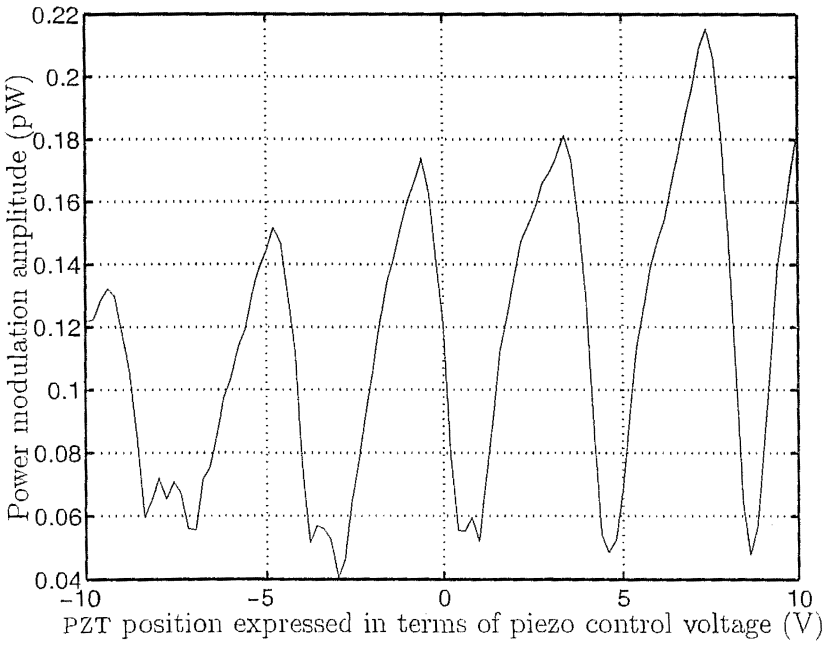

Figure 3.10: CW peak-to-peak radiant power to CCW mean radiant power modulation depth.

Finally, the Fourier analysis of the progression of the frequencies through the region where two longitudinal modes were present is of interest. This is because the AR2 procedure is only valid for a single frequency within the filter passband. If two frequencies are present the AR2 algorithm will produce a frequencies estimate that does not reflect the operating regime described by the measured data. The Fourier analysis shown in Figure 3.11 indicates that two longitudinal modes are present for the piezo scan voltage where the jump in the AR2 estimate of the gyroscope beat frequency was observed. Since there is clearly not a jump in the gyroscope beat frequency of a single longitudinal mode Figure 3.11 gives further evidence that the observed beat frequency is strongly dependent on the gain medium and any other effects which alter the cavity irradiance and, in turn, the optical power.

3.4 Model of the Ring-laser Gyroscope

To begin the formulation of an appropriate model to interpret the results presented in Section 3.3.2 the approach of Aronowitz is followed [17,18,72]. This approach is an adaption with application to the ring-laser gyroscope of Lamb's treatment of the linear laser [19].

In short, the model consists of finding solutions to Maxwell's equations in terms of the macroscopic polarisation which acts as a source term in Maxwell's equations. It is required that the solutions be self-consistent or, in other words, that the fast field variables return to the same values after each cycle around the cavity. A perturbation calculation (to the desired order) is made to obtain the polarisation in terms of the relevant laser parameters, finally arriving at a set of equations describing the evolution of the slowly changing variables of the laser. In the case of the ring-laser gyroscope three equations are found. Two describe the evolution of the cavity electric field in each direction, while the third describes the evolution of the phase difference between the counter-propagating waves.

To begin, Maxwell's equations are expressed in a rotating frame [72]. The wave equation obtained is

$$-\frac{1}{\epsilon_0\mu_0}\frac{\partial^2 E}{\partial z^2}+\frac{\omega}{Q}\frac{\partial E}{\partial t}+\frac{\partial^2 E}{\partial t^2}+\frac{a}{\epsilon_0\mu_0}\frac{\partial^2 E}{\partial z\partial t}=\frac{\omega^2\mathcal{P}}{\epsilon_0}-\frac{\sigma_s}{\epsilon_0}\frac{\partial E_s}{\partial t}. \tag{3.3}$$

It is assumed that the fictional conductivity, averaged over the cavity length, can be expressed in terms of the passive Q of the cavity as

$$\frac{\sigma}{\epsilon_0}=\frac{\omega}{Q}.$$

The coefficient a is proportional to the rotation rate Ω of the laser and is given by

$$a=\frac{4A\Omega}{Lc^2}, \tag{3.4}$$

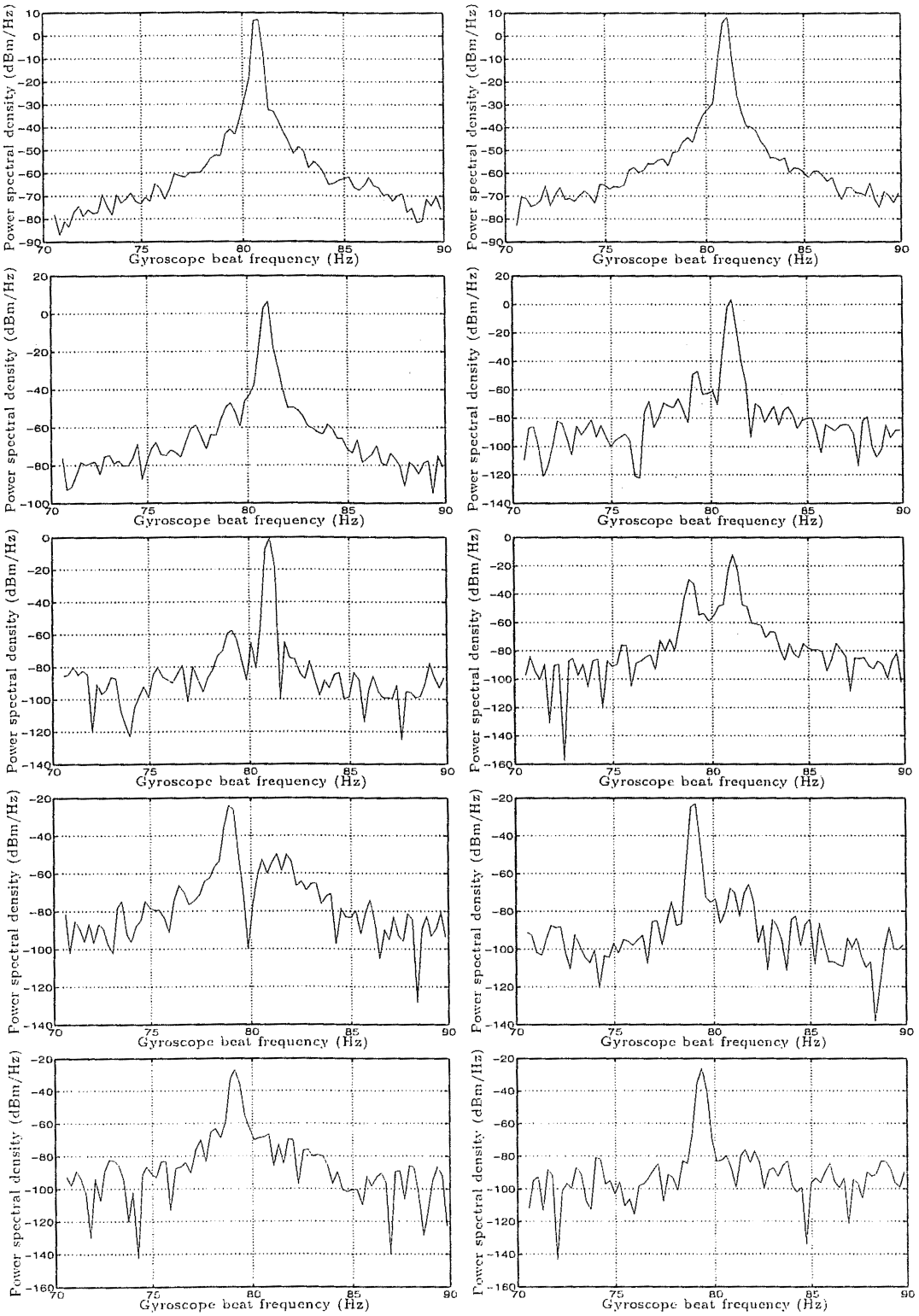

Figure 3.11: Power spectra "animation" showing the presence of two frequencies in some of the combined beam gyroscope beat spectra. The piezo control voltages are (left to right and top to bottom): -0.8 V, -0.6 V, -0.4 V, -0.2 V, 0 V, 0.2 V, 0.4 V 0.6 V, 0.8 V, and 1.0 V. The noise content in the power spectra is due to the short data acquisition time that only allowed a single 4096-point FFT estimation for each piezo driver voltage.

where L is the cavity length and A is the enclosed area. Only terms linear in a are included in Equation (3.3) and since the macroscopic polarisation $\mathcal{P}$ is nearly monochromatic, the second time derivative of $\mathcal{P}$ has been replaced by $-\omega^2\mathcal{P}$. Finally the rightmost term in Equation (3.3) represents the effects of coupling due to scattering. In particular E_s represents the backscattering field.

The electric field may be expanded into the set of empty cavity eigenfunctions given by

$$E(z,t) = \sum_n \left[A_n(t)U_n(z) + \tilde{A}_n(t)V_n(z)\right], \tag{3.5}$$

where

$$\begin{aligned} U_n(z) &= \sin(K_n z), \\ V_n(z) &= \cos(K_n z), \\ K_n &= \frac{2\pi n}{L}. \end{aligned} \tag{3.6}$$

Any time-dependent variation of the amplitude is accounted for by the coefficients $A_n(t)$ and $\tilde{A}_n(t)$. Using the fact that the empty-cavity normal-mode eigenfunctions satisfy the differential equation

$$\left[\frac{\mathrm{d}^2}{\mathrm{d}z^2} + \epsilon_0\mu_0\Omega_n^2\right]\begin{pmatrix} U_n(z) \\ V_n(z)\end{pmatrix} = \begin{pmatrix} U_n(z) \\ V_n(z)\end{pmatrix}. \tag{3.7}$$

Equations (3.3), (3.5), and (3.7) lead to

$$\begin{aligned} \frac{\mathrm{d}^2A_n}{\mathrm{d}t^2} + \frac{\omega}{Q_n}\frac{\mathrm{d}A_n}{\mathrm{d}t} + \Omega_n^2A_n - ac^2K_n\frac{\mathrm{d}\tilde{A}_n}{\mathrm{d}t} &= \frac{\omega^2}{\epsilon_0}\mathcal{P}_n - \frac{\sigma_s}{\epsilon_0}\frac{\mathrm{d}E_{sn}}{\mathrm{d}t}, \\ \frac{\mathrm{d}^2\tilde{A}_n}{\mathrm{d}t^2} + \frac{\omega}{Q_n}\frac{\mathrm{d}\tilde{A}_n}{\mathrm{d}t} + \Omega_n^2\tilde{A}_n - ac^2K_n\frac{\mathrm{d}A_n}{\mathrm{d}t} &= \frac{\omega^2}{\epsilon_0}\tilde{\mathcal{P}}_n - \frac{\sigma_s}{\epsilon_0}\frac{\mathrm{d}\tilde{E}_{sn}}{\mathrm{d}t}, \end{aligned} \tag{3.8}$$

where $\mathcal{P}_n$ and E_{sn} are the respective Fourier components of the empty-cavity normal-mode eigenfunctions.

The ring-laser gyroscope differs from the linear laser since the time-dependent coefficients A_n and $\tilde{A}_n$ represent two oppositely directed travelling waves in an empty cavity [12]. Thus, letting the subscripts 1 and 2 identify the oppositely directed travelling waves,

$$\begin{aligned} A_n(t) &= E_{1n}(t)\cos\theta_{1n} + E_{2n}(t)\cos\theta_{2n}, \\ \tilde{A}_n(t) &= E_{1n}(t)\sin\theta_{1n} - E_{2n}(t)\sin\theta_{2n}, \\ &\text{where} \\ \theta_{in} &= \omega_{in}t + \psi_{in}(t), \quad i = 1, 2. \end{aligned} \tag{3.9}$$

The argument θ_{in} of the trigonometric functions contains a term $\psi_{in}(t)$ that accounts for the non-cyclical changes in phase that are not covered by the cyclical term $\omega_{in}t$.

The Fourier components of the polarisation are then written as an "in phase" and "in quadrature" term with respect to frequency,

$$\begin{aligned} \mathcal{P}_n(t) &= S_{1n}(t)\sin\theta_{1n} + C_{1n}(t)\cos\theta_{1n}, \\ \tilde{\mathcal{P}}_n(t) &= \tilde{S}_{1n}(t)\sin\theta_{1n} + \tilde{C}_{1n}(t)\cos\theta_{1n}. \end{aligned} \tag{3.10}$$

To represent the Fourier components of the scattering field, it is assumed that a fraction r_i of the fields E_i are scattered back into the direction of the other beam with an additional phase angle ϵ_i. Therefore

$$E_{sn} = r_{1n}E_{1n}\cos(\theta_{1n}+\epsilon_{1n}) + r_{2n}E_{2n}\cos(\theta_{2n}+\epsilon_{2n}), \tag{3.11}$$

$$\tilde{E}_{sn} = -r_{1n}E_{1n}\sin(\theta_{1n}+\epsilon_{1n}) + r_{2n}E_{2n}\sin(\theta_{2n}+\epsilon_{2n}). \tag{3.12}$$

Substituting Equations (3.9)–(3.12) into Equation (3.8) and equating coefficients of $\sin\theta_{1n}$ and $\cos\theta_{1n}$ to zero so that Equation (3.8) is satisfied for all values of the arguments of the trigonometric functions, the four equations for the amplitudes and frequencies of the oppositely directed waves of each mode are obtained as

$$\dot{E}_{1n} + \frac{\omega}{2Q_n}E_{1n} = \frac{\omega}{4\epsilon_0}\left(\tilde{C}_{1n} - S_{1n}\right) - \frac{\sigma_s}{2\epsilon_0}r_{2n}E_{2n}\cos(\psi_n+\epsilon_{2n}), \tag{3.13}$$

$$\begin{aligned} \dot{E}_{2n} + \frac{\omega}{2Q_n}E_{2n} &= \frac{\omega}{4\epsilon_0}\left[(\tilde{S}_{1n} - C_{1n})\sin\psi_n - (S_{1n}+\tilde{C}_{1n})\cos\psi_n\right] \\ &\quad -\frac{\sigma_s}{2\epsilon_0}r_{1n}E_{1n}\cos(\psi_n-\epsilon_{1n}), \end{aligned} \tag{3.14}$$

$$\left(\Omega_{1n} - \dot{\theta}_{1n}\right)E_{1n} = \frac{\omega}{4\epsilon_0}\left(C_{1n} + \tilde{S}_{1n}\right) + \frac{\sigma_s}{2\epsilon_0}r_{2n}E_{2n}\cos(\psi_n+\epsilon_{2n}), \tag{3.15}$$

$$\begin{aligned} \left(\Omega_{2n} - \dot{\theta}_{2n}\right)E_{2n} &= \frac{\omega}{4\epsilon_0}\left[(C_{1n} - \tilde{S}_{1n})\cos\psi_n - (S_{1n}+\tilde{C}_{1n})\sin\psi_n\right] \\ &\quad -\frac{\sigma_s}{2\epsilon_0}r_{1n}E_{1n}\cos(\psi_n-\epsilon_{1n}), \end{aligned} \tag{3.16}$$

where Ω_{ij} are the empty cavity frequencies and

$$\psi_n = \theta_{2n} - \theta_{1n} = (\omega_{2n} - \omega_{1n})t + (\psi_{2n} - \psi_{1n}). \tag{3.17}$$

In Equations (3.15) and (3.16) the empty cavity frequencies have been replaced by Ω_{in} where

$$\Omega_{2n} = \Omega_n + \tfrac{1}{2}aK_nc^2, \tag{3.18}$$

$$\Omega_{1n} = \Omega_n - \tfrac{1}{2}aK_nc^2. \tag{3.19}$$

Substitution of K_n shows that the empty cavity mode splitting agrees with standard Sagnac formula 1.1. The dispersive effects due to the active medium and scattering are expressed in the terms containing the polarisation and the backscatter coefficient r_{in} in Equations (3.13)–(3.16) respectively.

From this point we only consider single longitudinal mode operation and therefore drop the subscript "n".

3.4.1 The Passive Cavity Approximation

To gain some understanding of the phenomena described by the Equations presented in the previous section we first consider the effect of neglecting terms dependent on the gain medium. Of course the presence of the gain terms are necessary to describe the action of the laser but for the purpose of discussing the dynamics associated with backscattering it is assumed that they are not significant and simply provide a hidden source term for the electric field.

Substituting Equations (3.15) and (3.16) into the derivative of Equation (3.17), and neglecting the polarisation terms the following equation of motion for the beat frequency is obtained,

$$\frac{\mathrm{d}\psi}{\mathrm{d}t} = \Omega_2 - \Omega_1 + \frac{c}{L}\left[\rho_{21}\sin(\psi + \epsilon_2) + \rho_{12}\sin(\psi - \epsilon_1)\right], \tag{3.20}$$

where $\rho_{ij} \equiv r_{ij}E_i/E_j$. In this instance the backscattering conductivity $\sigma/2\epsilon_0$ is associated with c/L [18]. It is this equation that gives rise to the well-known phenomenon of locking of the counter-propagating waves of a ring-laser gyroscope [18]. Furthermore it leads to a reduction in the beat frequency between the counter-propagating waves but does not lead to the frequency pushing demonstrated in the observations presented in Section 3.3.2. Equation (3.20) has been the starting point for a number of analyses by the Canterbury ring-laser group [1, 14, 15]. In particular the effects of the relative phase between scattered light from the two beams was of interest. It was found [15] that it was possible to account for the Sagnac beat frequency waveform distortion observed in C-I based on such an analysis of backscattering. However it was not possible to account for the observed frequency pushing. It is also important to note that the waveform distortion observed in C-II is negligible compared to that of C-I.

The calculation of the mode pushing and pulling coefficients assumed the presence of a single isotope. In practice dual-isotope neon is used to avoid mode competition due to the coincidence of the holes burnt in the gain medium, between the oppositely directed traveling waves as the laser is tuned over line centre [17, 63]. The generalization to the two-isotope case results in minor changes to the coefficients when expressed in terms of the plasma dispersion function that do not significantly alter the findings presented here. Quantitatively, the two-isotope case is described by the coefficients given above, but with each term replaced by a pair of terms, one with ω replaced by ${}^{20}\omega$ and one with ${}^{22}\omega$, these being weighted according to the quantity of each isotope.

In order to investigate the properties of Equation (3.20) the relative phase difference may be re-defined such that $\bar{\psi} \equiv \psi + (\epsilon_1 - \epsilon_2)/2$ and the net backscatter-phase is defined as $\zeta = (\epsilon_1 + \epsilon_2)/2$. Then, making the simplification $\rho_{12} = \rho_{21} = \rho$, it is easy to show that

$$\frac{1}{2\pi}\frac{d\bar{\psi}}{dt} = f_s - l_\zeta \sin\bar{\psi}, \quad l_\zeta \equiv \frac{c\rho}{P\pi}\cos\zeta. \tag{3.21}$$

where $f_s = (\Omega_2 - \Omega_1)/2\pi$. The consequences of this simplification in relation to the understanding of the backscatter properties of the ring laser gyroscope have been discussed elsewhere [14, 15].

Adler Approximation

If we assume that the laser is sufficiently stable on the timescale of interest that we may take ζ and ρ to be "constant" then Equation (3.21) may be written as

$$\frac{1}{2\pi}\frac{\mathrm{d}\bar{\psi}}{\mathrm{d}t} = f_s - f_l \sin\bar{\psi}, \tag{3.22}$$

where f_s is the Sagnac frequency and f_l is known as the lockin-threshold frequency. This equation appears in a number of contexts in the study of coupled oscillators and is known as the *Adler equation* [14, 15, 18, 77, 78]. The Adler approximation of backscattering effects in a ring-laser gyroscope may also be derived from a straightforward approach considering the effects of backscattering in one direction [18].

The solution of Equation (3.22) yields two important results. If f_l is greater than f_s then there is no frequency splitting between the counter-propagating modes and they are said to be locked together, hence the terminology for f_l. In this case the solution to Equation (3.22) is

$$\bar{\psi} = \sin^{-1}\left(\frac{f_s}{f_l}\right). \tag{3.23}$$

On the other hand if $f_s > f_l$ the solution is [14]

$$\bar{\psi} = \frac{1}{\pi}\tan^{-1}\left(\frac{f_l + f_p\tan(\pi f_p t)}{f_s}\right), \tag{3.24}$$

where $f_p = \sqrt{(f_s^2 - f_l^2)}$. The frequency f_p is known as the *pulled* frequency because it is always less than that of the nominal Sagnac frequency f_s. In the presence of backscatter coupling the beat frequency is not constant. The pulled frequency f_p is therefore defined in terms of the periodicity of the instantaneous phase difference. In the limit $f_s \gg f_l$ a binomial expansion shows that the pulled frequency gives

$$f_p = f_s - \frac{f_l^2}{2f_s}, \tag{3.25}$$

and the gyroscope responds in an approximately linear way. This conclusion remains valid for the solutions of Equation (3.20) [28, 76]. It has been shown that the relation $f_p = \sqrt{(f_s^2 - f_l^2)}$ is still satisfied and that the evolution of the phase difference between the counter-propagating waves are qualitatively similar to the solutions to Equation (3.22) [72, 76]. The effect of frequency pulling does

not however adequately describe the behaviour of the Canterbury ring lasers. This is because it is commonly observed that the beat frequency is *pushed* above the nominal Sagnac value [1, 4, 14]. In the following Section it is shown that by relaxing the assumption that the effects of the gain medium on the Sagnac beat frequency are small compared to those arising from backscattering it is possible to demonstrate frequency pushing of the correct order of magnitude required to explain the results of Section 3.3.2.

3.4.2 Discussion on the Calculation of the Polarisation

This section concentrates on the effects that the gain medium may have on the Sagnac frequency splitting. The number of effects that may be predicted is dependent on the order of the calculation of the Fourier components of the polarisation. A third-order calculation is necessary to describe frequency pushing in a ring laser. First of all the effects described by each order of the perturbation calculation of the polarisation are described. This is followed by a more detailed investigation of the effects that arise from the third order calculation since effects arising from the first and second order calculations are still evident in this calculation.

The Fourier components of the polarisation in a ring laser gyroscope were first calculated using first-order perturbation theory [12, 19] by Aronowitz [17, 72]. Such a calculation relies on the assumption that the gain is low and the active medium is a gas. The transition is broadened due to the Doppler motion of the atoms and the finite lifetime of the states. It is found from substitution of this result for the polarisation in Equations (3.13)–(3.16) that the threshold condition for each beam is independent of the other. It also turns out that the lasing frequency is pulled towards the gain-transition line centre. This pulling is zero at line centre and increases with detuning. Similarly the difference in pulling is such that the Sagnac beat frequency is pulled from its nominal value.

The second-order perturbation calculation [12, 19] gives the population inversion as a function of the velocity distribution of the gas. It can be shown that the velocity distribution is equal to the raw velocity distribution of the gas with two Lorentzian "holes" burnt into the curve [63]. The depth of each hole is determined by the strength of the beam and its width is determined by the width caused by the natural plus collision lifetimes. The position of the hole is determined from the standard Doppler formula for the gas velocity required for the shift in lasing frequency from gain centre. Therefore when the two counter-propagating beams are off gain-centre holes will be burnt on opposite side of the velocity distribution. However when the two counter-propagating beams are close to line centre they will begin to compete for gain from the same atoms. This has been observed to lead to strong asymmetry in the lasing powers of the counter-propagating beams [17, 28, 72, 79]. It is possible to use enriched neon with a

higher proportion of ^{22}Ne than in natural neon to avoid this difficulty [73,79]. In this case the oppositely travelling waves draw gain from different Doppler shifted atomic populations.

The third-order contribution to the polarisation introduces the effects of saturation on the dispersion properties of the active medium. This also describes the mode pushing seen in the results presented in Section 3.3.2.

The contributions to dispersive effects from the various orders of the perturbation calculation of the polarisation may be summarised as:

First order theory $\longrightarrow$ Threshold operation and mode pulling.

Second order theory $\longrightarrow$ Hole burning.

Third order theory $\longrightarrow$ Gain saturation and mode pushing.

3.4.3 The Results of the Third-order Perturbation Calculation

Substitution of the results for the third order polarisation leads to [17,19,72]

$$\frac{2P}{c}\frac{\dot{E}_1}{E_1} = a_1 - \beta_1 I_1 - \theta_{12} I_2 - 2\rho_{21}\cos(\psi + \epsilon_2), \tag{3.26}$$

$$\frac{2P}{c}\frac{\dot{E}_2}{E_2} = a_2 - \beta_2 I_2 - \theta_{21} I_1 - 2\rho_{12}\cos(\psi - \epsilon_1), \tag{3.27}$$

$$\omega_1 + \dot{\phi}_1 = \Omega_1 + \sigma_1 - \tau_{12} I_2 + \frac{c}{P}\rho_{21}\sin(\psi + \epsilon_2), \tag{3.28}$$

$$\omega_2 + \dot{\phi}_2 = \Omega_2 + \sigma_2 - \tau_{21} I_1 - \frac{c}{P}\rho_{12}\sin(\epsilon_1 - \psi). \tag{3.29}$$

The coefficients a_i, β_i, θ_{ij}, and τ_{ij} are all defined in terms of the plasma dispersion function [74]. Following Sargent, Scully and Lamb [12], the dimensionless irradiance I_i is defined as

$$I_i = \frac{\wp^2}{2\hbar^2\gamma_a\gamma_b}E_i^2, \tag{3.30}$$

where $\wp$ is the electric dipole matrix element between the laser energy levels a and b and γ_a and γ_b are the decay rates of the upper and lower laser levels respectively.

In Equations (3.26) and (3.27) describing the evolution of the field amplitude the β_i terms represent gain saturation for each beam on itself due to hole burning, and the θ_{ij} terms show gain saturation for each beam due to hole burning by the other beam. In the frequency equations, the τ_{ij} terms show a mode pushing correction in the dispersion curve. The correction results in a Lorentzian dispersion curve centred at each oscillation frequency with the opposite sign of the Gaussian dispersion curve which is due to the gain curve. Note that the sign of

this correction is dependent on which side of gain centre the longitudinal mode is on.

Taking the Doppler limit $\gamma \ll K_u$ appropriate for the operation of the laser at the time the data were collected leads to the following values for the coefficients [12][6,7]. The corresponding coefficients for the homogeneously broadened laser may be determined without difficulty [80]. Equations (3.31)–(3.38) summarise the coefficients for the inhomogeneously broadened gain medium. All calculations contained in the remainder of this Chapter use the coefficients as they are defined here;

$$a_i = \exp\left[-\frac{(\omega_g - \omega_i)^2}{(K_u)^2}\right] F_1 - \frac{\omega_i}{2Q_i} \quad \text{(Linear net gain)}, \tag{3.31}$$

$$\beta_i = \frac{\gamma_{ab}}{2\gamma} F_1 \exp\left[-\frac{(\omega_g - \omega_i)^2}{(K_u)^2}\right] \quad \text{(Self-saturation)}, \tag{3.32}$$

$$\theta_{ij} = \beta_i \mathcal{L}(\omega_g - \omega_0) \quad \text{(Cross-saturation)}, \tag{3.33}$$

$$\sigma_i = -\frac{2}{\pi} \exp\left(-\xi^2\right) \int_0^{\xi} \exp\left(x^2\right)\, dx, \quad \xi = \frac{\omega_i - \omega_g}{K_u} \quad \text{(Mode pulling)}, \tag{3.34}$$

$$\tau_{ij} = \beta_i \left[\frac{\omega_g - \omega_0}{\gamma}\right] \mathcal{L}(\omega_g - \omega_0) \quad \text{(Cross pushing)}, \tag{3.35}$$

$$\mathcal{L}(\omega_g - \omega_0) = \frac{\gamma^2}{[\gamma^2 + (\omega_g - \omega_0)^2]} \quad \text{(Dimensionless Lorentzian)}, \tag{3.36}$$

$$\omega_0 = \frac{\omega_1 + \omega_2}{2} \quad \text{(Average frequency), and} \tag{3.37}$$

$$F_1 = \frac{\omega\sqrt{\pi}\wp^2 \bar{N}}{2\hbar K u \epsilon_0} \quad \text{(First-order factor)}. \tag{3.38}$$

Note that ω_g refers to the atomic line centre frequency and ω_i the laser oscillation frequency for each of the counter-propagating waves. Both are angular

[6]The atomic dipole decay constant γ is given by the inverse of the of the dephasing time of the atomic dipoles. It is equal to the radiative decay rate plus the collision-induced decay rate.

[7]K_u is the Doppler broadening constant, determined by the Maxwell-Boltzmann velocity distribution,

$$P(\omega) = \frac{1}{\sqrt{\pi} K_u} \exp\left[\frac{-(\omega - \omega_0)^2}{{K_u}^2}\right].$$

frequencies. γ_{ab} is equal to $\frac{1}{2}(\gamma_a + \gamma_b)$ where γ_a and γ_b are the upper and lower level decay constants respectively. γ includes the contribution due to pressure broadening and is given by $\gamma = 10 + 76p\,\mathrm{Mrad/s}$ where p is the gas pressure millibar [75,76]. $\wp$ is the electric-dipole matrix element between the laser states. The case where two isotopes, or more generally, n isotopes, are present is easily addressed by using an appropriate weighting of each isotope in the calculation of the coefficients [76]. Since the spacing of the gain centres of the ^{22}Ne and ^{20}Ne is much greater than the gain bandwidth of operation in the single mode regime it follows that the effect on the mode pushing term τ_{ij} is negligible.

The equation of motion for the phase difference between the counter-propagating waves is found by taking the difference of Equations (3.28) and (3.29),

$$\frac{\mathrm{d}\psi}{\mathrm{d}t} = \Omega_2 - \Omega_1 + \sigma_2 - \sigma_1 + \tau_{12}I_2 - \tau_{21}I_1 + \frac{c}{P}\rho_{21}\sin(\psi + \epsilon_2) + \frac{c}{P}\rho_{12}\sin(\psi - \epsilon_1). \quad (3.39)$$

An important point to note is the $\frac{c}{P}$ dependence in the backscatter terms. On one hand this leads to a reduction in the problems associated with backscatter-induced frequency pulling when the perimeter is increased. On the other hand it should be recognised that the effects due to dispersion from the gain medium will experience a commensurate increase in importance in the determination of the laser dynamics. If the dispersion parameters are bundled in an effective Sagnac beat frequency,

$$\bar{f}_s = \Omega_2 - \Omega_1 + \frac{\sigma_2 - \sigma_1 + \tau_{12}I_2 - \tau_{21}I_1}{2\pi}, \quad (3.40)$$

it is straightforward to deduce the results of Equations (3.20), 3.21, and (3.22) with $\bar{f}_s$ in place of f_s given the appropriate assumptions required to obtain each result. Care should be taken in the interpretation of this Equation however since investigation of Equations (3.26) and (3.27) reveals that the beam irradiances are modulated with the same periodicity as $\psi(t)$. It is a requirement of any theory that this result be predicted since it is clearly evident in all of the Canterbury ring lasers. However this feature also invalidates the assumptions required to cast the equation of motion for $\psi(t)$ in a form resembling the Adler equation. This is because the critical dependence on the backscattering phase parameters ϵ_i will also strongly affect $\psi(t)$ due to the coupling induced by ρ. The important point to note is that, due to the form of Equation (3.39), no matter what the value of ρ is, Equation (3.39) *cannot predict frequency pushing* from the nominal value defined by $\Omega_2 - \Omega_1$ if the dispersion parameters σ_i and τ_{ij} are not considered to be significant in the determination of the dynamics of the laser [28, 72].

In summary the equations that determine Sagnac beat frequency may be ex-

pressed as

$$\frac{2P}{c}\frac{\dot{E}_1}{E_1} = a_1 - \beta_1 I_1 - \theta_{12} I_2 - 2\rho_{21}\cos(\psi + \epsilon_2), \tag{3.41}$$

$$\frac{2P}{c}\frac{\dot{E}_2}{E_2} = a_2 - \beta_2 I_2 - \theta_{21} I_1 - 2\rho_{12}\cos(\psi - \epsilon_1), \tag{3.42}$$

$$\frac{\mathrm{d}\psi}{\mathrm{d}t} = 2\pi\bar{f}_s + \frac{c}{P}\rho_{21}\sin(\psi + \epsilon_2) + \frac{c}{P}\rho_{12}\sin(\psi - \epsilon_1), \tag{3.43}$$

$$\bar{f}_s = \Omega_2 - \Omega_1 + \frac{\sigma_2 - \sigma_1 + \tau_{21} I_2 - \tau_{12} I_1}{2\pi}, \tag{3.44}$$

$$\rho_{ij} = \frac{r_{ij} E_i}{E_j}. \tag{3.45}$$

3.5 Investigation of Magnitude of Mode Pushing Effects in C-II

There are three approaches that may be taken to further describe the properties of the ring laser gyroscope. One is to make the approximation that backscattering is the dominant factor in determining the laser dynamics. This approach has been adopted in a number of previous studies [15, 18] and in light of the results presented in Section 3.3.2 will not be considered here. Alternatively it may be assumed that dispersive effects are the dominant mechanism. This approach is followed in this Section. In many situations, this assumption will also be questionable, and it is necessary to resort to numerical solutions [28]. Further insight may also be obtained from analytic solutions for particular values of the backscattering phase parameters ϵ_i. This has been considered by Stedman *et al.* [15] and Etrich *et al.* [16] among others.

Rather than making the assumption that one or other approximation enjoys significantly more validity than the other the simple assumption that the laser is operating well outside of the locking region is made. This requires

$$\bar{f}_s \gg \frac{c}{P}\rho_{21}\sin(\psi + \epsilon_2) + \frac{c}{P}\rho_{12}\sin(\psi - \epsilon_1). \tag{3.46}$$

In the case of C-II this assumption is justified by the observation that there is minimal distortion of the gyroscope beat waveform. It is well documented that this implies the gyroscope is operating well outside the lock-in threshold regime [29, 76].

This means it is valid to rewrite Equations (3.41)–(3.45) as follows

$$\frac{2P}{c}\frac{\dot{E}_1}{E_1} = a_1 - \beta_1 I_1 - \theta_{12} I_2 - 2\rho_{21}\cos(\psi + \epsilon_2), \tag{3.47}$$

$$\frac{2P}{c}\frac{\dot{E}_2}{E_2} = a_2 - \beta_2 I_2 - \theta_{21} I_1 - 2\rho_{12}\cos(\psi - \epsilon_1), \tag{3.48}$$

$$\frac{\mathrm{d}\psi}{\mathrm{d}t} = 2\pi \bar{f}_s, \tag{3.49}$$

$$\bar{f}_s = \Omega_2 - \Omega_1 + \frac{\sigma_2 - \sigma_1 + \tau_{12} I_2 - \tau_{21} I_1}{2\pi}, \tag{3.50}$$

$$\rho_{ij} = \frac{r_{ij} E_i}{E_j}. \tag{3.51}$$

An important consequence of this approximation is that it does not remove the single beam modulation expressed in Equations (3.47) and (3.48) from the model. It only relies on the reasonable assumption that the rotation rate is large enough with respect to the lock-in threshold. In order for the single beam modulation to be observed it is necessary that $a_i - \beta_i I_i - \theta_{ij} I_i$ is of the same order of magnitude as $2\rho_{ji}$.

From Equation (3.49) the instantaneous beat frequency is simply $\bar{f}_s$. This is the type of result expected in the absence of backscattering and is consistent with the observation that there is no discernible waveform distortion.

Before turning to an evaluation of the dispersion effects a few comments on what may be discerned from a qualitative inspection of the relevant equations is helpful. For example, consider Equation (3.35). It is asymmetric with respect to which side of gain centre the longitudinal mode is on. Since the frequency splitting between the two counter-propagating waves is small $\beta_1 \sim \beta_2$ when operating away from gain centre. Similarly $\tau_{ij} \sim \tau_{ji}$. Hence if the irradiances and, since both beams are the same size, the powers of the counter-propagating beams are the same the mode pushing effects are negligible. However if they are not the same (as is commonly observed) the effects may be much more pronounced. The goal of the next section is to investigate the expected magnitude of the mode pushing when the powers of the counter-propagating beams are unequal. Subsequently these predictions are compared with the amount of mode pushing observed for a given power ratio.

3.5.1 Applying the Third-order Theory to C-II

There are a number of parameters in the equations presented in the previous Section that must be determined in order to estimate the effects on the beat frequency between the counter-propagating waves. Without having the information given by direct measurement of the laser gain it is tempting to make arbitrary

estimates of the gain based on rule of thumb values. This is dangerous, especially considering the unique nature of the Canterbury ring lasers. Therefore a more sophisticated approach is required. The relevant parameters must be inferred from results that are reasonably well specified by the available data. One such method consists of considering the bandwidth of available gain. When a single longitudinal mode is present the positive net gain bandwidth (PNGB) must be such that all other longitudinal modes have negative net gain. However the observation of regions where two longitudinal modes were present, and hence possessed positive net gain, within the pathlength scan indicates that the PNGB must be greater than the FSR beat frequency but less than twice this value. As previously noted the data displayed in Figure (3.7) indicates a PNGB of approximately 120 MHz. This is inferred from the result that two longitudinal modes were present for about half of each pathlength scan cycle.

The other quantity that requires careful estimation is the scale factor between the measured radiant power P_r and the dimensionless irradiance I_i. This is done by multiplying the result of Equation (3.30) relating I_i to the cavity irradiance by $1/tA_b$ where A_b is the beam area and t is the mirror transmission. The electric dipole matrix element may be determined from the Einstein A coefficient [12]. For the $3s_2 \rightarrow 2p_4$ neon transition it is found to 1×10^{-29} Cm [8]. The decay rates of the two states are [75] $\gamma_a = 12 \times 10^6$ rad/s and $\gamma_b = 28 \times 10^6$ rads/s respectively. The manufacturer's specification for mirror transmission of $t = 0.2$ ppm is used. The beam area A_b at the exit port was calculated using the standard methods derived from ABCD ray propagation matrices [8], the results of which for C-II were summarised in Table 2.5. The value $A_b = 1.70\,\mathrm{mm}^2$ was determined from the $1/e^2$ magnitudes of the axes where the elliptical beam profile due to astigmatism was accounted for. Therefore the observed radiant power must be scaled by a factor of

$$\frac{I_i}{tA_b} = \frac{4\wp^2}{\pi^2\hbar^2\gamma_a\gamma_b t A_b} P_r \sim 6.8 \times 10^9\,\mathrm{m}^{-2}$$

to obtain the dimensionless cavity irradiance.

The mode pulling term will not be considered henceforth. This is because it has been considered by previous studies [29] and been found to be insignificant in the determination of the Sagnac beat frequency because it is not possible to produce a large enough differential pulling factor for two counter-propagating beams possessing a relatively small frequency separation. However the irradiance/power dependence of the mode pushing makes it worthy of further investigation in the case where the beam powers are unequal. For cavity quality factors of the order of those relevant to C-II the dependence of τ_{ij} on the estimate of the PNGB is relatively small.

Figure 3.13 shows the amount of frequency pushing expected for one of the travelling waves. If the powers of the counter-propagating beams are equal the amount of pushing experienced by each beam is virtually the same.

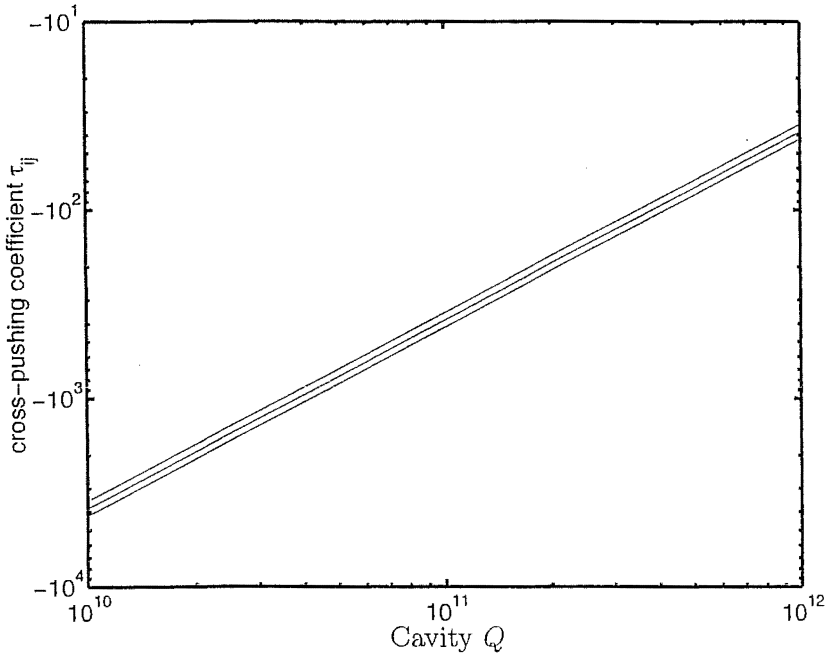

Figure 3.12: Variation of mode pushing coefficient (τ_{ij}) with cavity quality factor for a PNGB of 100, 120, and 140 MHz (top to bottom). Note that the sign of τ_{ij} is determined by what side of gain centre the laser is operating on. It is assumed that the longitudinal mode is 0.8×PNGB/2 to one side of gain centre. This is close to the point of maximal pushing.

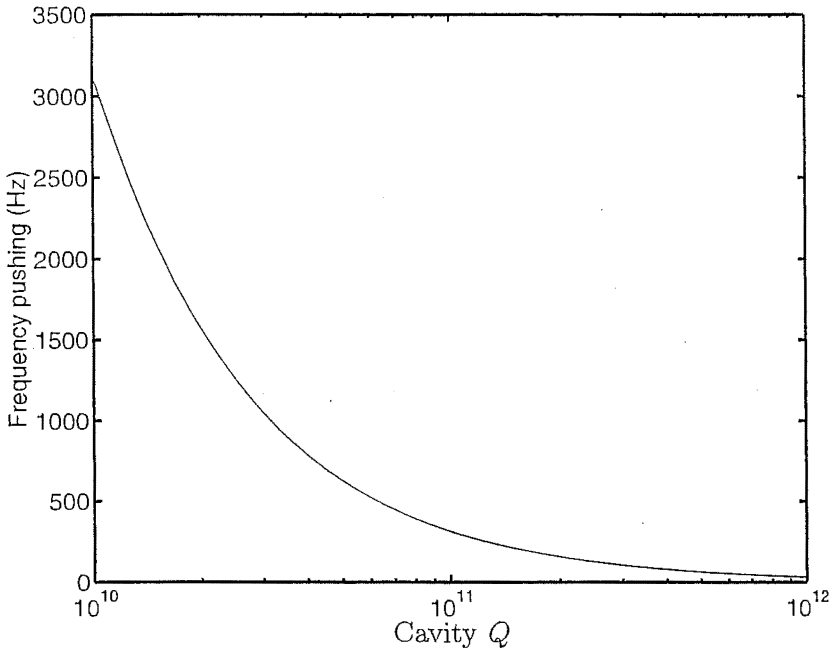

Figure 3.13: Frequency pushing on one travelling wave predicted for a radiant power of 60 pW. It is assumed that the longitudinal mode is 0.8×PNGB/2 one side of gain centre.

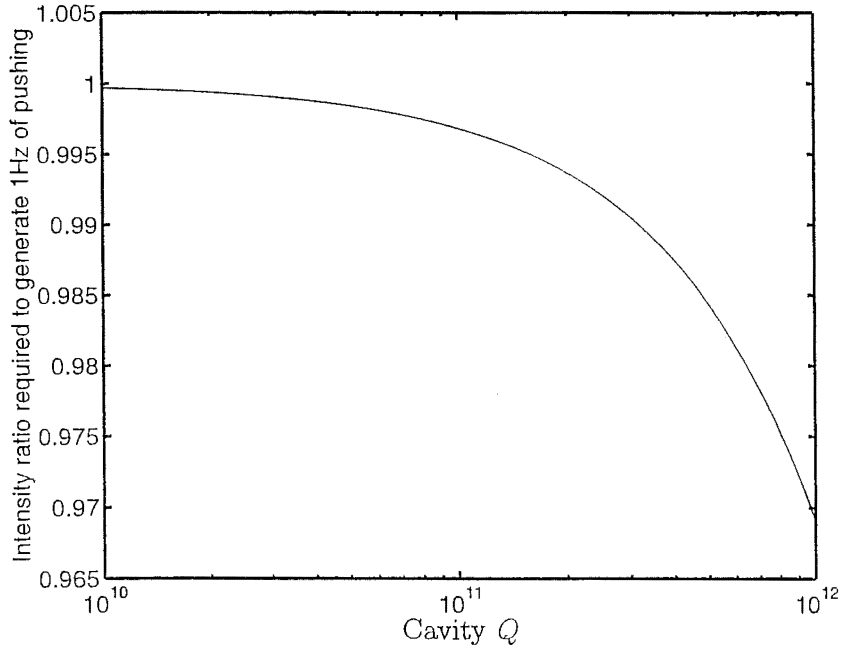

Figure 3.14: Ratio of beam powers required to generate 1 Hz of pushing. A nominal radiant power of 60 pW is assumed for one beam. It is assumed that the longitudinal mode is 0.8×PNGB/2 one side of gain centre.

Figure 3.14 displays the ratio of powers required to generate 1 Hz of pushing in the gyroscope beat frequency. There is clearly a strong incentive to maximise the cavity Q in order to minimise the mode pushing effects.

3.5.2 Supplementary Results

In addition to the results presented in Section 3.3.2 two more plots give the full picture on how mode pushing and pulling due to unequal optical powers can indeed be a significant effect in the operation of C-II. Figure 3.5 shows the variation of the CW mean radiant power with piezo displacement. This is substantially different from the results for the CCW mean radiant power displayed in Figure 3.3.2. First of all the magnitude of the variation is substantially reduced and secondly the progression with changing piezo displacement is much more ragged. This is due to the single beam power servo being present on the CW beam. Since the servo is designed to eliminate low frequency variation in the radiant power and hence has a time constant of the order of a second the CW beam power did not fully settle within the scan interval.

It is important to note that the influence on the CCW radiant power is minimal. Similarly the single beam modulation on either beam was not affected due to the servo because of its limited bandwidth. Therefore the partial control achieved by the single beam radiant power servo was utilised to exaggerate the power difference between the counter-propagating beams and hence exaggerate the effects of the mode pushing and pulling terms in a controllable manner[8]. In order to fully justify the hypothesis that the mode pushing term plays a significant role in C-II Sagnac frequency drift consider Figure 3.16 showing the ratio of the radiant powers between the two counter-propagating beams. Comparison with Figures 3.4 and 3.5 shows that the observed frequency variation is strongly correlated with the variation in the radiant power ratio.

In addition it was observed that when FSR detection was employed on each counter-propagating beam independently there was single longitudinal mode operation on the CW beam but not on the CCW beam[9]. This indication of different gain for each direction is further indication of how the situation leading to mode pushing arises.

[8]Similar drifts in the power ratio between the counter-propagating beams has been observed over long timescales and is consistent with the observed atmospheric pressure dependence of drift in the gyroscope beat frequency. This is because changes in the mirror separation will move the beam spots on the mirror and shift the lasing path thus changing the aperture effects [3] which can give rise to unequal powers between the two counter-propagating beams.

[9]Since only one FSR detection system was available it was not possible to monitor both simultaneously. However the short time (a few seconds) taken to switch between detectors was not long enough to bring the observation into question.

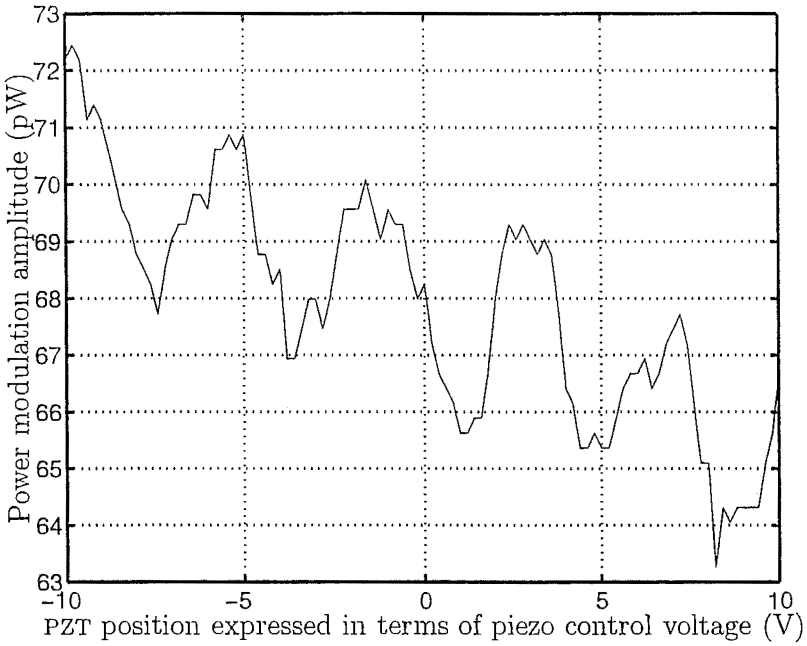

Figure 3.15: Variation of CW mean radiant power with piezo displacement for ring monolith compression.

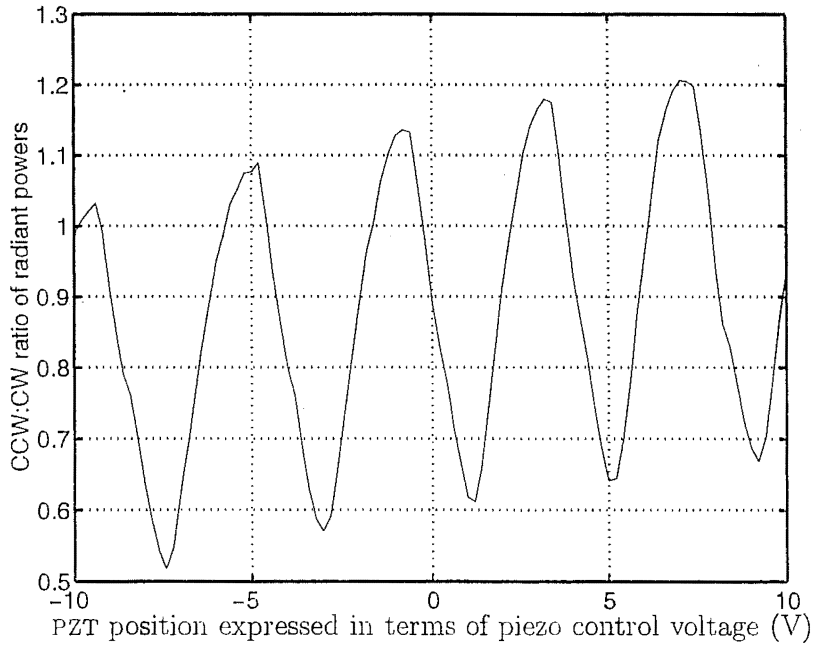

Figure 3.16: The ratio of the radiant powers of the CCW to CW beams shows the variation required to produce the observed mode pushing and pulling (see Figure 3.14).

3.5.3 Further Analysis of Mode Pushing Results

Figures 3.17 and 3.18 show the effects of the mode pushing term in some detail. It should be noted that the amount of pushing is highly dependent on the ratio of the powers of the counter-propagating beams. In particular the change in the pushing contribution as the ratio of CCW to CW beam optical powers changes from 1 to ~ 0.9, for example, is 1-2 Hz. Figure 3.18 shows how the frequency pushing contribution varies with detuning. At gain centre the contribution disappears. As the detuning is increased, more frequency deviation is observed. The gyroscope beat frequency is pushed or pulled depending on which side of gain-centre the longitudinal mode is as well as whether the ratio of powers is greater than or less than one. The variation predicted is similar to that predicted for changes in the single beam optical power ratio.

Taking the observed ratio (CCW/CW) of the radiant powers into account, the value predicted by the frequency variation due to the pushing term is, if anything, somewhat larger than the frequency variation observed. There are two things to note with respect to this observation. First of all, it is likely that some other feature of the ring-laser dynamics is also at work, mitigating the effects of the pushing term. Many of these effects are discussed in the gyro literature. Since the goal of this Chapter is to identify the importance of mode pushing due to unequal powers of the counter-propagating beams no effort is made to synthesize the predictions for each effect to fully account for the observations. This task would represent a considerable amount of work that is beyond the scope of this thesis. Furthermore the numerical model required for such a task would serve to cloud the physical understanding that is desired from this investigation. The second point to note is that the variation in the mean power of the "reference" beam in the ratio should be taken into account. This has a significant impact on the amount of pushing predicted. The variation of the mean power with single beam ratio is shown in Figure 3.19. In general the lower the radiant power of the reference beam the less the contribution from the mode pushing term. Clearly, including the results presented in Figure 3.19 will lead to revision of the predicted pulling. This has been done with some success. The results, discussed later in this Section are presented in Figure 3.21.

Figure 3.20 shows the variation in the gyroscope beat frequency with ratio of mean radiant powers (CCW/CW) for a scan of the full piezo range. The dependence of the beat frequency on the power ratio predicted by the mode pushing term in the third-order theory is clearly observed. The cyclic behaviour occurs as the longitudinal modes move through the gain curve. The region of the scan where mode hops occurred is marked on the Figure. It is interesting that there is some difference in the behaviour between various cycles. The most likely explanation for this is that it is caused by the variation in the CCW radiant power that is not accounted for in this plot. A less likely explanation is that the losses may change enough, as the pathlength is scanned, to alter the magnitude of the frequency

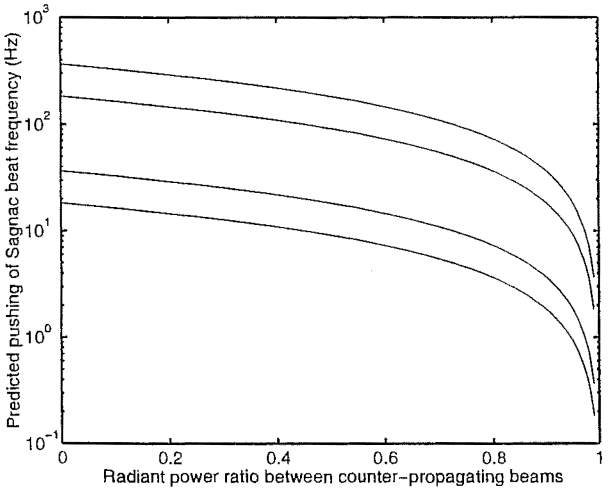

(a)

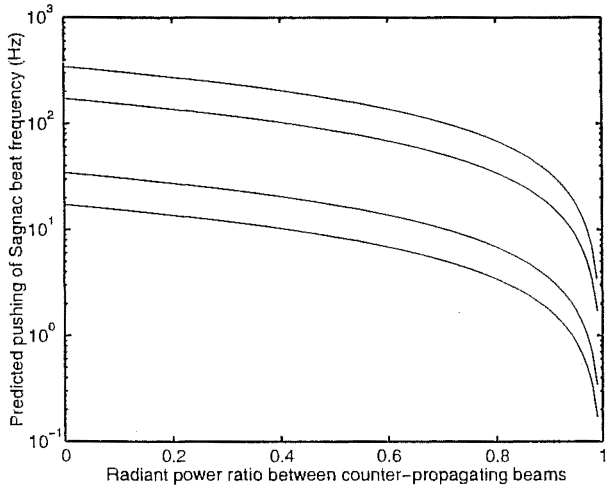

(b)

Figure 3.17: The pushing of the beat frequency between the counter-propagating modes is more pronounced for greater asymmetry in beam powers. In (a) it is assumed the longitudinal mode is 20 MHz from gain centre and in (b) is 40 MHz from gain centre. In both plots the cavity quality factors are (top to bottom) 5×10^{10}, 1×10^{11}, 5×10^{11}, and 1×10^{12}. A fixed radiant power of 60 pW is assumed for one of the beams in both cases.

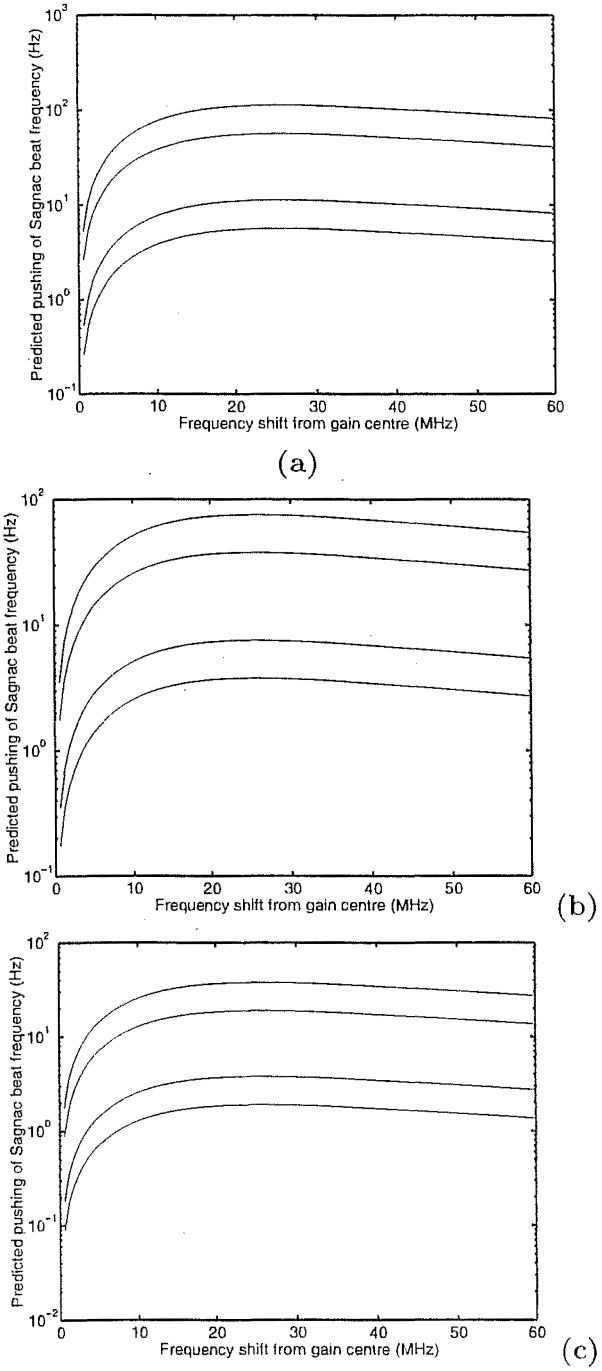

Figure 3.18: Frequency pushing with detuning for (a) radiant power ratio of 0.7, (b) radiant power ratio of 0.8, and (c) a radiant power ratio of 0.9. The cavity quality factors are (top to bottom) 5×10^{10}, 1×10^{11}, 5×10^{11}, and 1×10^{12}. A fixed radiant power of 60 pW is assumed for one of the beams.

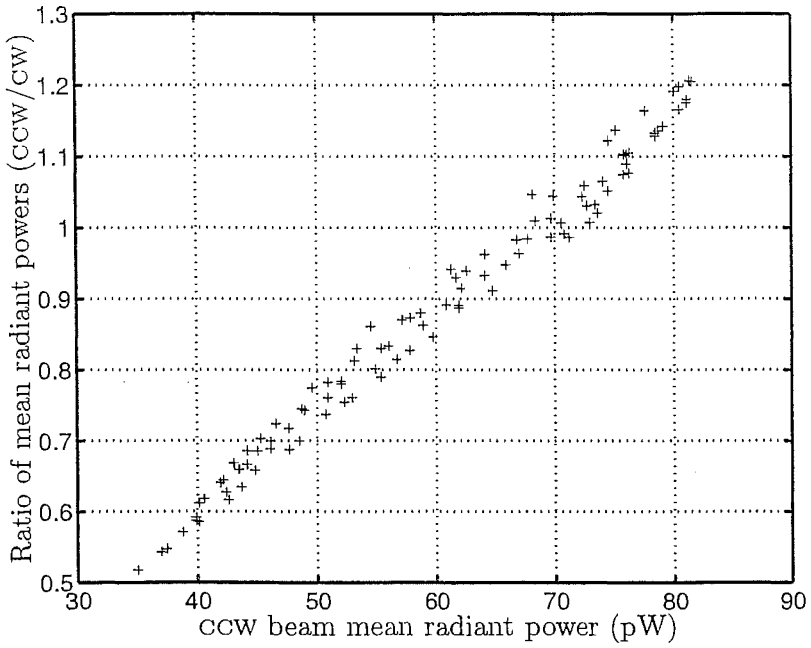

Figure 3.19: Evidence for an intimate connection between the ratio of the single beam powers and the power in the reference (CCW) beam.

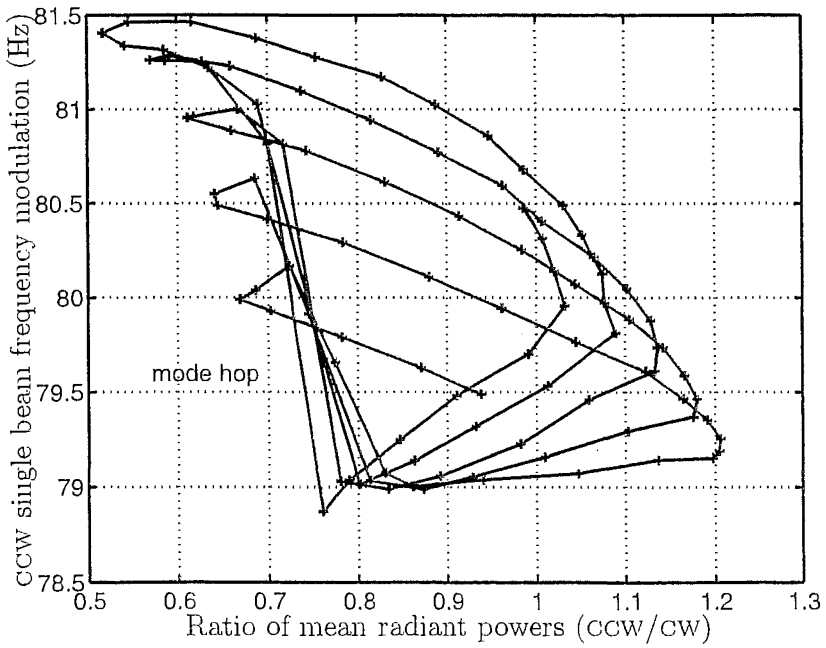

Figure 3.20: The variation of the gyroscope beat frequency with the single beam power ratio. The region where the scan caused a longitudinal mode hop is marked accordingly.

pushing term.

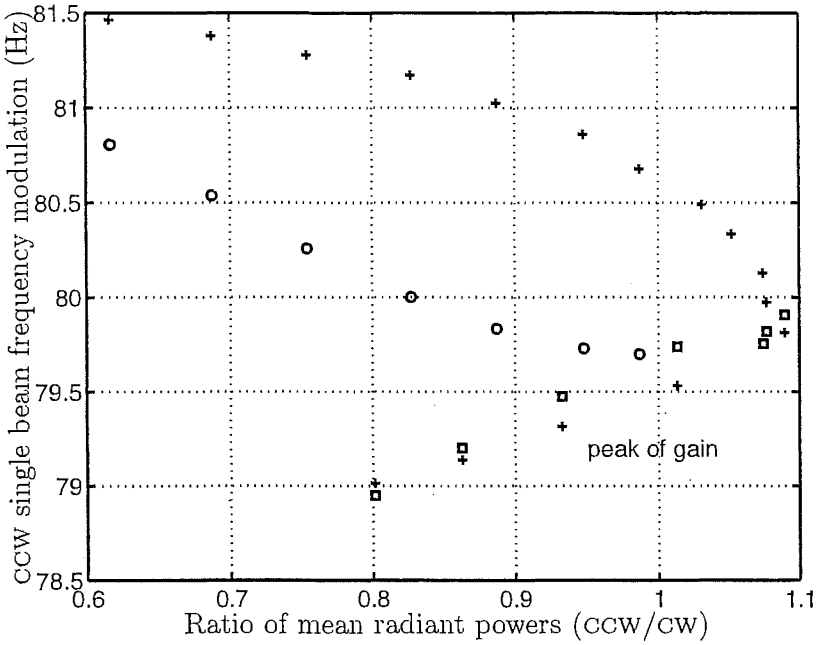

Figure 3.21: The variation of the gyroscope beat frequency with optical power ratio for part of the scan range presented in Figure 3.20. The experimental data are plotted with plus signs and the predictions, based on the third-order theory, are plotted as squares and circles. The distinction between the different predicted values is described in the accompanying text.

Figure 3.21 shows an attempt to fit the pushing term that arises from the third-order theory to the experimental data.

The cavity quality factor was chosen to be 6×10^{11} is accordance with other measurements [1]. It was necessary to estimate the detuning based on the approximate calibration of the piezo (see Section 3.1) and an estimate of when the single longitudinal mode was at gain centre. This was done by finding the point midway between the two points in the scan where a FSR beat signal was detected. Since these estimates are approximate it was necessary to investigate the effects of small shifts in the calibration and position of gain centre. Only relatively minor changes in the resulting fits were found.

The important point to note about the predicted pushing that is plotted is that there is an implicit dependence on the mean power of the "reference" (CCW) beam. This is accounted for by using the measured power for each data point. If this is not done the it is not possible to produce any kind of agreement between the predictions of the model and the observed data for any reasonable choices of parameter.

The fit to the for the lower branch (squares) is in excellent agreement with the

observed data. This part of the data set includes the region near gain centre for a single longitudinal mode. It is pleasing to find that the model predicts the observed dependence on power ratio very well for a highly reasonable set of parameters. The upper branch (circles) follows the slope of the observed data well but with a substantial offset in frequency. An offset of 0.7 Hz allows this part of the data set to furnish predictions in agreement with observation as well. There is no obvious justification for such an offset. However it is possible that this part of the curve may be due to the presence of two longitudinal modes. Further investigation is required to resolve this issue. However there is clearly good agreement in the lower branch and the ability to directly trace frequency pushing to this term in the third-order theory is a useful contribution to the understanding of stable, high-Q, large ring-laser gyroscopes.

3.6 Summary

In this Chapter an experimental investigation of the effects of the mode pushing term in the third-order theory of the ring-laser was performed on the ring-laser gyroscope C-II. The experimental observations were found to be in reasonable aggreement with the pre-existing third-order theory. The mode pushing term, which does not arise in the second-order theory of the ring-laser gyroscope, was found to be of particular importance and it was demonstrated that the mode pushing term does play a significant role in the determination of the C-II gyroscope beat frequency.

For convenience, Table 3.1 summarises the changes in mode pushing caused by changing the relevant parameters. Any increase in the cavity-Q will decrease the

Parameter	Effect
Cavity-Q	Decreases mode pushing term.
Detuning	Mode pushing term increases with detuning.
Irradiance/power ratio	Mode pushing term minimised for $R \approx 1$.
Irradiance/power	Mode pushing increases with cavity irradiance/power.

Table 3.1: Summary of the effects that contribute to mode pushing as described by the third-order theory of the ring-laser gyroscope.

amount of mode pushing. Since the mode pushing increases with detuning there is some motivation to operate close to the centre of the gain curve. However a varying ratio of cavity irradiances between the counter-propagating beams is a much more important contributor to serious differential mode-pushing between the counter-propagating beams. A large detuning from gain centre simply increases the amount of mode pushing. It should be remembered that the term mode pushing is somewhat of a misnomer in context of gyrosvope beat frequency

output since the mode pushing term can give rise to pulling of the gyroscope beat frequency as well as pushing. Both the dependence on the power ratio and the detuning may change the sign of the mode pushing term. In this Chapter it was demonstrated that a substantial fraction of the gyroscope beat frequency pushing and pulling may be attributed this effect. Therefore the mode pushing term should be included in any complete model of a ring-laser gyroscope with a specification that is simailar to C-II. The mode pushing term may not be as important in a different laser. For example, scattering from the mirrors may dominate. In this case, the gyroscope beat frequency will exhibit the characteristics of backscatter-induced pulling or, if the backscatter is very large, frequency locking of the counter-propagating modes.

Chapter 4

Drift Processes with $1/f^{\alpha}$ power spectra

The signatures of the noise sources which contribute to longterm gyroscope beat frequency drift in C-II are identified. In particular, it is found that the significant drift source due to atmospheric pressure variations may be identified as a fractional Brownian motion noise process [81]. To the author's knowledge this result is unique and perhaps of interest within the field of atmospheric physics as well as in the characterization of C-II frequency drift.

4.1 $1/f^{\alpha}$ noise: motivation for study and description

It may be deduced form the integral transform between the power spectrum and the Allan variance (Appendix B.2) that a noise process that exhibits a power spectrum of the form

$$S(f) \sim \frac{C}{f^{\alpha}},$$

where $\alpha \in (1, 3)$, will have an Allan variance that increases with averaging time τ. Figure 4.1 clearly shows this behaviour occurs in the Allan variance for all three lasers studied[1]. There is a characteristic time, τ_0, for each laser where the Allan variance is at a minimum. Since this is the averaging time for which frequency fluctuations are minimised the Allan variance at this point defines the limit of the resolution with which Earth rotation may be measured. For times shorter than τ_0 all lasers exhibit white frequency noise. This is due to the random walk in phase that arises from spontaneous emission. Further information regarding this quantum-limited noise source was presented in Section 2.3.1. For times greater than τ_0 the resolution decreases with averaging time. This is a direct consequence of the stochastic models that produce $1/f^{\alpha}$ power spectra being *non-stationary*. We now turn our attention to the details of models that produce the observed behaviour. This is followed by a careful analysis of the validity of these models in the description of the behaviour of the Canterbury gyroscopes.

[1]Note that Figure 4.1 shows the *relative Allan deviation*. See Appendix B.2 for more information.

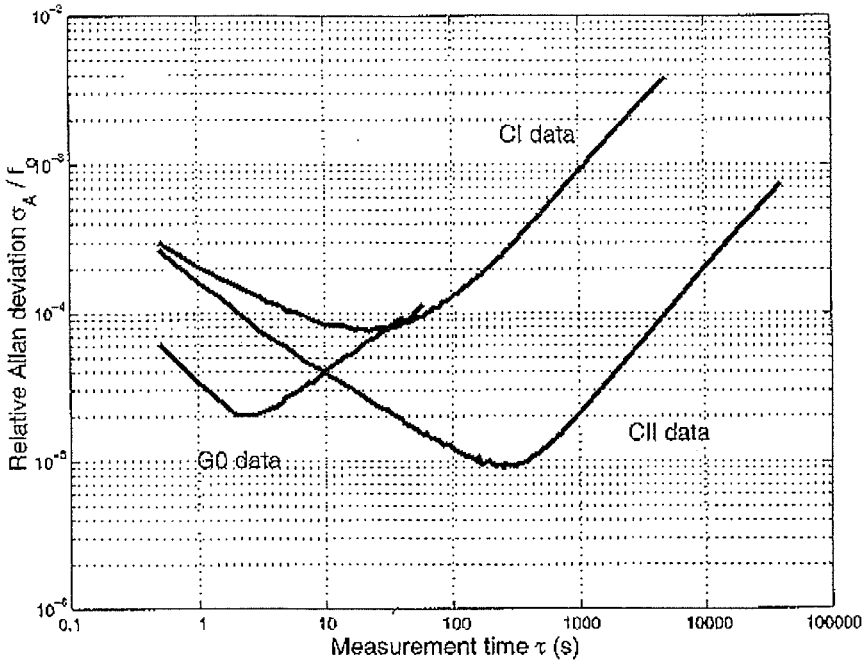

Figure 4.1: A comparison of the performance of the three ring-laser gyroscopes C-I (12 Oct 1998), C-II (26 July 1997), and G0 (29 Jan 1998) has been performed by King [4]. The results are reproduced here for reference.

The presence of $1/f$ noise processes is ubiquitous. It manifests itself in the form of resistance fluctuations in semiconductors, frequency instabilities in atomic clocks [51], traffic flow variations on roads, various economic time-series. A general survey is given by Keshner [82]. Section 4.2 discusses the presence of $1/f^{\alpha}$ noise in the Canterbury ring-laser gyroscope C-II and the timescales on which the $1/f^{\alpha}$ dominates the white frequency noise that results from the random walk in phase that is due spontaneous emission.

4.1.1 Brownian Motion

Brownian motion is a familiar example of the type of stochastic process that is discussed in this Chapter. A microscopic particle in a fluid moves in an erratic fashion due to random collisions with other particles. This phenomenon was first observed by Robert Brown in 1826. Therefore Brownian motion was recognised as a useful model for various physical phenomena long before the general classes of stochastic process discussed in this Chapter were discovered. Brownian motion is in fact a special case of the general model. Brownian motion is often modelled as a one-dimensional random walk. This model is also referred to as the *Wiener process* [83, 84].

The one-dimensional random walk is a discrete time process where the particle,

located initially at the origin, takes a step of magnitude +1 or -1 at each periodic instant. The position , $x(t)$, at the n-th period is

$$x(nT) = x_1 + x_2 + \ldots x_n, \tag{4.1}$$

where x_i is a family of identically distributed random variables assuming the value +1 or -1. The current position of the particle is governed only by the most recent position. Therefore it is a *Markov* process [31, p. 72-73]. It may be shown [31, p. 84-86] that the probability distribution $p(x,t)$ describing the random variable x is

$$p(x,t) = \frac{1}{\sqrt{2\pi t/Ta}} \exp\left(-\frac{x^2 T}{2a^2 t}\right), \tag{4.2}$$

where T is the time interval between successive steps, a is the size of each step. In the limit $a \longrightarrow 0$ and $T \longrightarrow 0$,

$$p(x,t) = \frac{1}{\sqrt{2\pi bt}} \exp\left(-\frac{x^2}{2bt}\right), \tag{4.3}$$

where $b = a^2/T$. Therefore the zero-mean stochastic variable $x(t)$ conforms to a Gaussian probability density. The variance,

$$\langle x^2 \rangle = bt, \tag{4.4}$$

increases with time. On the other hand the variance of a Gaussian white noise stochastic variable decreases with time as $1/T$. The probability distribution of a random walk will be observed to become shorter and wider as the measurement time is increased.

The equation of motion for the stochastic variable x may be determined form the probability distribution $p(x,t)$ [31, p. 87-88],

$$\frac{\partial p(x,t)}{\partial t} = \frac{b}{2} \frac{\partial^2 p(x,t)}{\partial x^2}. \tag{4.5}$$

This is the familiar *diffusion equation*[2].

Since Brownian motion is a non-stationary process it is not possible to directly use the *Wiener-Khintchine* theorem to calculate the spectrum from the autocorrelation function. However if the measurement time is sufficiently long it may be shown that the spectrum for Brownian motion is [52]

$$S(f) = \frac{b}{2\pi^2 f^2}. \tag{4.6}$$

Consequently an Allan variance (Allan deviation) with an averaging time dependence of τ^1 ($\tau^{1/2}$) for a frequency random walk in a ring-laser gyroscope will result.

[2]The diffusion equation is a specific example of the Fokker-Planck equation [33]. Further discussion of the Fokker-Planck equation, with reference to white noise and Lorentzian coloured noise in ring-laser gyroscopes, may be found in Chapter 6.

4.1.2 Fractional Brownian Motion

Brownian motion is an example of a wider class of noise processes that are known as fractional Brownian motion [81, 85].

Fractional Brownian motion has been used to model a diverse range of phenomena. Hazel *et al.* [86] characterised drift noise in a Fourier transform spectrometer using the fBm model in conjunction with Gaussian white noise. It was found that the optimal averaging time τ_0 was dependent on the frequency band of interest. Fractional Brownian motion has also been used in image processing [87], texture classification and image recognition [88], the modelling of polymer molecules [89], ATM networks [90], sand (granular) flow [91], and molecular clouds in astronomy and astrophysics [92]. One of the more amusing applications is a study of the small motions of people when they are standing still [93]. The model was originally developed to describe hydrology data series [81, 94, 95] and has lent itself to the description of geophysical time and spatial series [50, 96, 97].

A paper discussing fBm noise in fibre-optic gyros is of particular interest [98][3]. It was found that the fBm process was the dominant noise source. This is a result of the relative susceptibility to drift exhibited by fibre gyros.

4.1.3 Description of fBm

Fractional Brownian motion (fBm) may be defined as a continuous-path stationary increment Gaussian process. It is important to note that although fBm itself is not a stationary process the stochastic variable defined by the increments between successive measurements of the fBm process is a stationary process. It is required that the increments be zero mean and are described by a Gaussian probability distribution as well as being stationary.

The covariance is divergent,

$$\Gamma_{\text{FBM}}(t_1, t_2) = \frac{c_\gamma}{2}\left[|t_1|^{\alpha-1} + |t_2|^{\alpha-1} + |t_1 - t_2|^{\alpha-1}\right], \tag{4.7}$$

where $c_\gamma = [0, \infty)$. The parameter α is known as the spectral exponent of the fBm process. The reason for this nomenclature will soon become apparent. The definition of the autocorrelation implies that the variance is divergent as the measurement time $t \to \infty$. It follows from Equation (4.7) that the variance when the increment is of length T is $c_\gamma T^{\alpha-1}$. Note that in the case $c_\gamma = 2D$, $\alpha = 1$ we recover the special case known as Brownian motion.

The probability that the process will change by no more than M in a time T is

$$P[x(t+T) - x(t) \leq M] = \frac{1}{\sqrt{2\pi c_\gamma T^{\alpha-1}}} \int_{-\infty}^{M} \exp\left(-\frac{u^2}{2c_\gamma T^{\alpha-1}}\right). \tag{4.8}$$

[3]This paper was discovered after this work was completed.

Therefore the excursions in the stochastic variable $x(t)$ are dependent on the spectral exponent as well as the noise strength.

The power spectral density of a fBm process is [52]

$$S_{\text{FBM}}(f) = \frac{c_s}{4\pi^2 f^{\alpha}}, \tag{4.9}$$

where

$$c_s = 4c_\gamma(\alpha-1)\Gamma(\alpha-1)\sin\left(\frac{\pi}{2(\alpha-1)}\right).$$

It is now clear why α is referred to as the spectral exponent. It is also apparent why the noise process is called fractional Brownian motion. It is the generalisation of Brownian motion where α need not be an integer.

The Allan variance [51], described in Appendix B.2, of a fBm process may be found from the Allan variance–spectral density integral transform, described in Appendix B.2.1, yielding [52, 99]

$$\sigma_{\text{A}}^2(\tau) = c_{\text{A}}\tau^{\alpha-1}, \tag{4.10}$$

where

$$c_{\text{A}} = \frac{4c_\gamma(2^{\alpha-1}-1)}{\alpha(\alpha+1)}.$$

In the study of high precision oscillators, for example, it is customary to describe the behaviour of the oscillators as a sum of stochastic processes [100]. On a particular timescale the dominant process for that timescale will be the most apparent in any analysis of stability. In the case of the Canterbury ring-laser gyroscopes white noise is dominant at "short" timescales while $1/f^{\alpha}$ noise is dominant on "long" timescales. This is deduced directly from Figure 4.1. It should be noted that the definitions of long and short timescales are dependent on the intrinsic stability of the gyroscope. A model that may potentially provide a good description of the noise processes observed in the Canterbury ring-lasers is therefore given by a sum of white noise and fractional Brownian motion. The Allan variance of this model, sometimes called noisy fractional Brownian motion (nfBm) [86, 87], is

$$\sigma_{\text{A}}^2(\tau) = \frac{\sigma_{\text{W}}^2}{\tau} + c_{\text{A}}\tau^{\alpha-1}. \tag{4.11}$$

For $\alpha > 1$ the Allan variance has a minimum at

$$\tau_0 = \left[\frac{\sigma_{\text{W}}^2}{c_{\text{A}}(\alpha-1)}\right]^{1/\alpha}. \tag{4.12}$$

The Allan variance at τ_0 is

$$\begin{aligned}\sigma_{\text{A}}^2(\tau=\tau_0) &= \left[\sigma_{\text{W}}^2\alpha(\alpha-1)\right]^{(\alpha-1)/\alpha} c_{\text{A}}^{1/\alpha} \\ &= \left[\sigma_{\text{W}}\alpha(\alpha-1)\right]^{2(\alpha-1)/\alpha}\left[\frac{4c_\gamma(2^{\alpha-1}-1)}{\alpha(\alpha+1)}\right]^{1/\alpha}.\end{aligned} \tag{4.13}$$

Equation (4.13) lets some important conclusions about what is required of any stabilisation process be drawn. The presence of a drift noise process in a ring-laser gyroscope has some important implications for data processing and the definition for the maximum resolution limit of Earth rotation. Equation (4.11) implies that there is a characteristic time τ_0 for the composite noise process that defines the maximum achievable resolution. This is sometimes referred to as the *knee* of the Allan variance.

If the quantum noise level, represented by σ_w is reduced, the maximum resolution in the Earth rotation is improved as long as there is no change in the drift noise process. Approaches which do this were discussed in Section 2.5.

Similarly, if the drift noise strength c_γ is reduced, the resolution will be improved. It is not clear how stabilisation methods may be implemented that do this in a systematic fashion. It is simply a byproduct of any stabilisation scheme that this will tend to occur.

Figure 4.2 and Equation (4.13) show that the value of the Allan variance at the knee, $\sigma_A^2(\tau = \tau_0)$, is dependent on the spectral exponent as well as the noise strength. With respect to ring-laser gyroscopes this indicates that, as well as the strength of the drift noise, the spectral characteristics of the drift process are important in determining the maximum resolution of Earth rotation. This point has not previously been recognised.

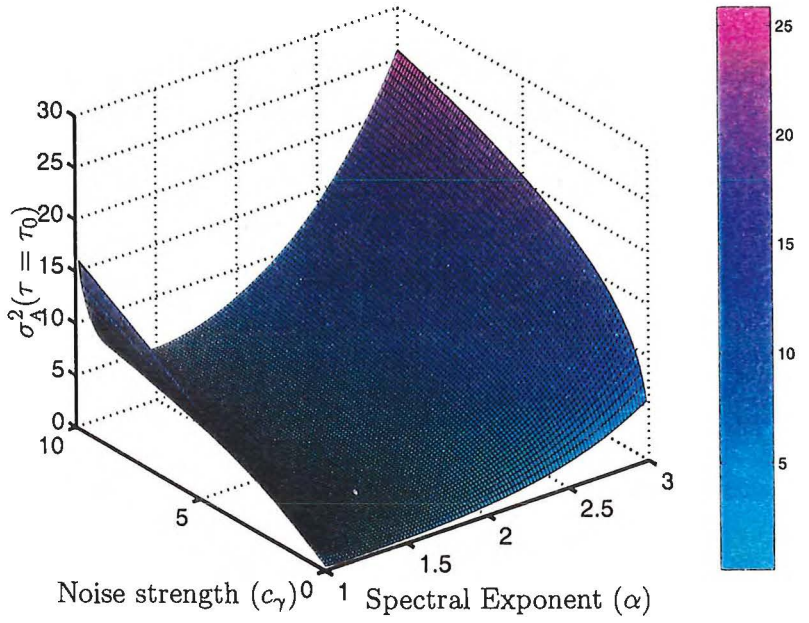

Figure 4.2: The minimum attainable resolution for composite fBm-white noise process has a strong dependency on the spectral exponent of the fBm as well as power of the noise processes. The white noise variance ω_{w^2} was chosen to be unity.

4.1.4 The Problem of Non-stationarity and Divergent Variances

From physical considerations the major objection to the $1/f^{\alpha}$ non-stationary noise model is in the representation of noise generated in stable, time-invariant systems such as high quality quartz crystal oscillators. Furthermore for $\alpha \geq 1$ the variance is divergent. To quote Solo [52]:

> For $\alpha \geq 1$ the spectrum is not integrable, which suggests that the $1/f^{\alpha}$ noise has infinite variance; thus it cannot be second-order stationary and so apparently cannot have a spectrum! Yet $\alpha \geq 1$ has been observed in many studies with evidence of time invariance (e.g., of the spectrum not changing in with time) also being found. All this adds up to a puzzling situation that has been termed the "infrared catastrophe" [85].

A pure $1/f^{\alpha}$ power spectrum is physically impossible because the total power of the process would be infinite [101]. Therefore it is necessary to introduce a low frequency cutoff and a high frequency cutoff in order to describe real signals [102]. Similarly if $\alpha \leq 1$ and there exists no high frequency cutoff an *ultraviolet catastrophe* will result. Even without explicit cutoffs in the model there are implicit cutoffs in the time-series [101]. The low frequency cutoff is determined by the length of the data set and the high frequency cutoff is determined by the sampling rate. The data for the ring-laser C-II that are presented in Figures 4.3–4.7 shows such the necessary low-frequency cutoff occurring at times greater than 10^5 s.

Although processes represented by stationary increment models may be non-stationary the processes exhibit much time invariance. For example the spectrum is time-invariant.

4.1.5 Estimation Methods

Leu and Papamarcou [49] give a careful evaluation of the performance of variance methods of estimation of the spectral exponent for stationary increment processes. Estimation using the periodiogram (empirical spectrum), the maximum-likelihood estimator and the Allan variance estimator are considered. Analysis of the large sample mean square error for each method shows that the periodiogram-based method is inferior to both the Allan variance and maximum-likelihood estimators. The Allan variance estimator is given the strongest recommendation. Wavelet transforms have been shown to provide another reliable method of estimation [50, 103]. Since the Allan variance has been shown to be reliable and is familiar in the context of the analysis of oscillator stability it is used throughout this Chapter.

4.2 Identification of Drift Noise in Ring-laser Gyroscopes

Figures 4.3–4.7 display the Allan variance of the atmospheric pressure and gyroscope beat frequency which, for the data sets analysed, is known to be highly correlated with the atmospheric pressure. The Allan variance for longer timescales is plotted in order to investigate the behaviour of the drift processes. It has been verified that truncation of the data set does not cause any change in the spectral exponent.

In all cases the mean of the increments is zero within the error of the fit to the Gaussian probability distribution. The normal probability plots indicate that all data sets follow a Gaussian probability distribution within two or more standard deviations of the mean. There is some divergence from a Gaussian distribution for larger increment sizes. Further discussion regarding the applicability of the Gaussian increment model may be found in Section 4.2.1.

Data Set	α	c_γ	σ_i
1 (Figure 4.3)	2.64 ± 0.03	$2.9 \times 10^{-13}\,\mathrm{hPa}^2/\mathrm{hPa}$	$0.588 \pm 0.008\,\mathrm{hPa}$
2 (Figure 4.4)	2.42 ± 0.02	$4.2 \times 10^{-12}\,\mathrm{hPa}^2/\mathrm{hPa}$	$0.840 \pm 0.009\,\mathrm{hPa}$
3 (Figure 4.5)	2.67 ± 0.03	$3.2 \times 10^{-13}\,\mathrm{hPa}^2/\mathrm{hPa}$	$0.278 \pm 0.009\,\mathrm{hPa}$
4 (Figure 4.6)	2.65 ± 0.03	$3.0 \times 10^{-15}\,\mathrm{Hz}^2/\mathrm{Hz}$	$0.0034 \pm 0.0001\,\mathrm{Hz}$
5 (Figure 4.7)	2.43 ± 0.08	$7.6 \times 10^{-12}\,\mathrm{hPa}^2/\mathrm{hPa}$	$0.58 \pm 0.02\,\mathrm{hPa}$

Table 4.1: Summary of the spectral exponent α and noise strength c_γ for data modelled by a fractional Brownian motion noise process. Data Sets 1,2,3, and 5 are time-series of atmospheric pressure at Christchurch airport (sets 1 and 2) and the ring-laser cavern (sets 3 and 5). Data Set 4 is a time-series of the C-II gyroscope beat frequency taken concurrently with set 3. σ_i is the standard deviation of the distribution of increments.

Table 4.1 hints at an interesting result. The spectral exponents and noise strengths of data sets 1 and 3 are in close agreement. The origin of the data sets is very different. Data Set 1 was recorded at Christchurch airport. Data Set 3 was recorded using a pressure sensor attached to C-II using the C-II data-logging equipment and is 26 days long. There is also strong similarities between Data Sets 2 and 5. They both possess spectral exponents that are smaller than those of Data Sets 1 and 3 as well has having greater noise strengths. The interesting subtleties in the behaviour of the atmospheric pressure drift processes are beyond the scope of this investigation. The important point to note is that a spectral exponent of $\alpha \approx 2.5$ is characteristic of the drifts in atmospheric pressure. Moreover if atmospheric pressure and the gyroscope beat frequency are correlated the dominant drift process in the gyroscope beat frequency also has a spectral exponent $\alpha \approx 2.5$. This is demonstrated by Data Sets 3 and 4. The relative noise strength of Data Sets 3 and 4 indicates that an atmospheric pressure excursion through the maximum range will induce a change in the gyroscope beat frequency

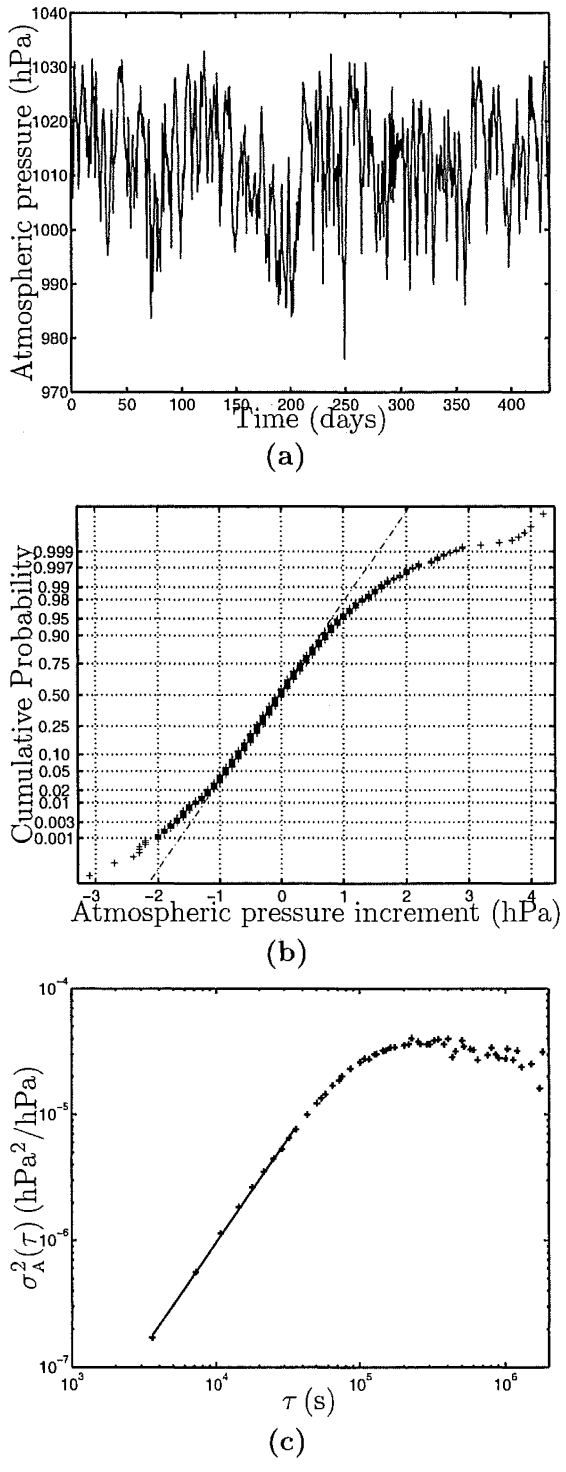

Figure 4.3: Data Set 1: (a) time-series of atmospheric pressure data recorded at Christchurch airport, (b) normal probability plot of the pressure increments between each reading, and (c) Allan variance density of atmospheric pressure.

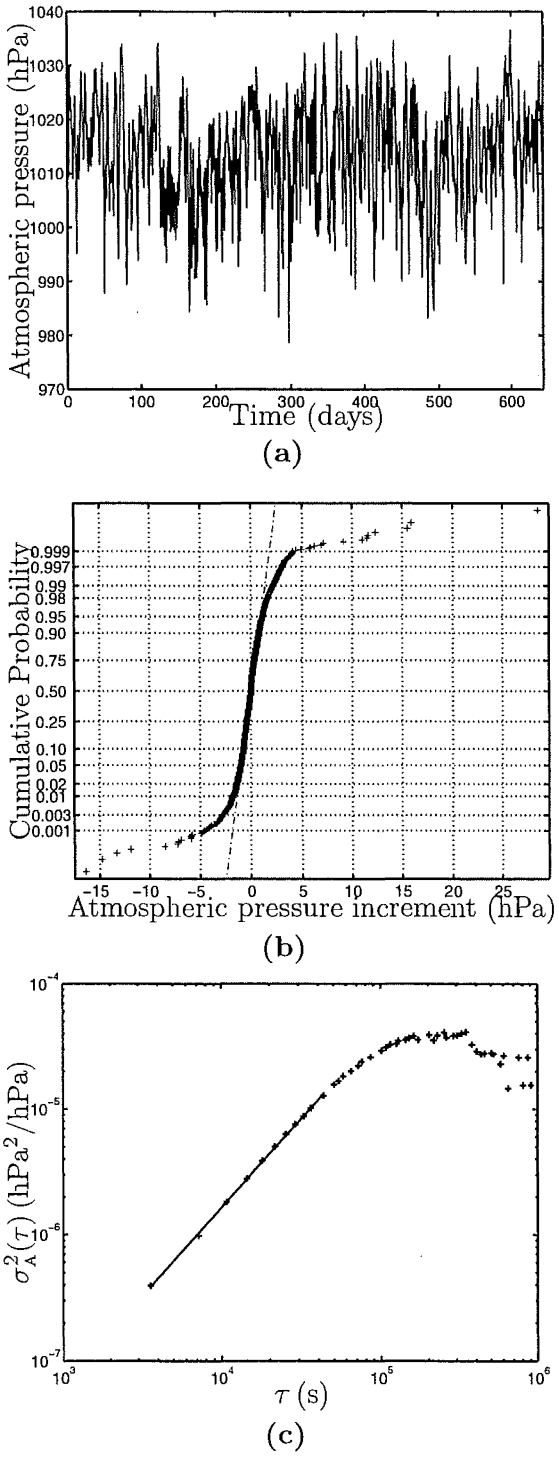

Figure 4.4: Data Set 2: (a) time-series of atmospheric pressure data recorded at Christchurch airport: (b) normal probability plot of the pressure increments between each reading, and (c) Allan variance density of atmospheric pressure.

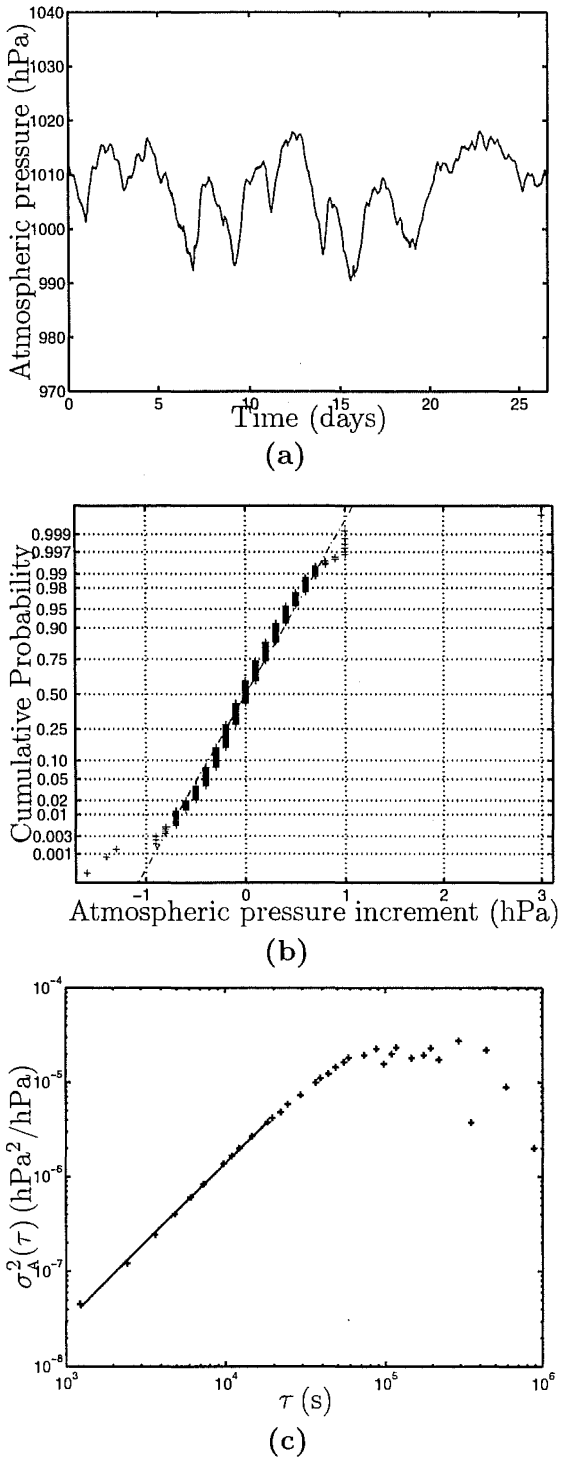

Figure 4.5: Data Set 3: (a) time-series of atmospheric pressure data recorded at the ring-laser cavern: (b) normal probability plot of the pressure increments between each reading, and (c) Allan variance density of atmospheric pressure.

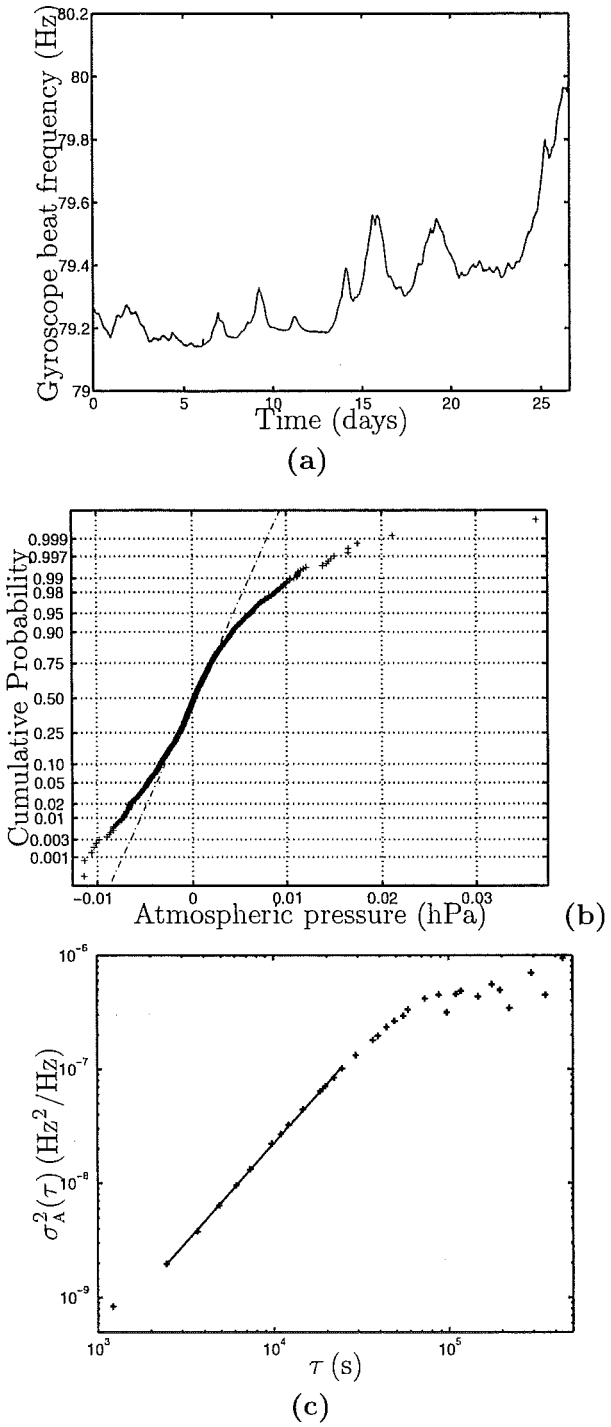

Figure 4.6: Data Set 4: (a) time-series of gyroscope beat frequency data recorded at the ring-laser cavern: (b) normal probability plot of the pressure increments between each reading, and (c) Allan variance density of the gyroscope beat frequency.

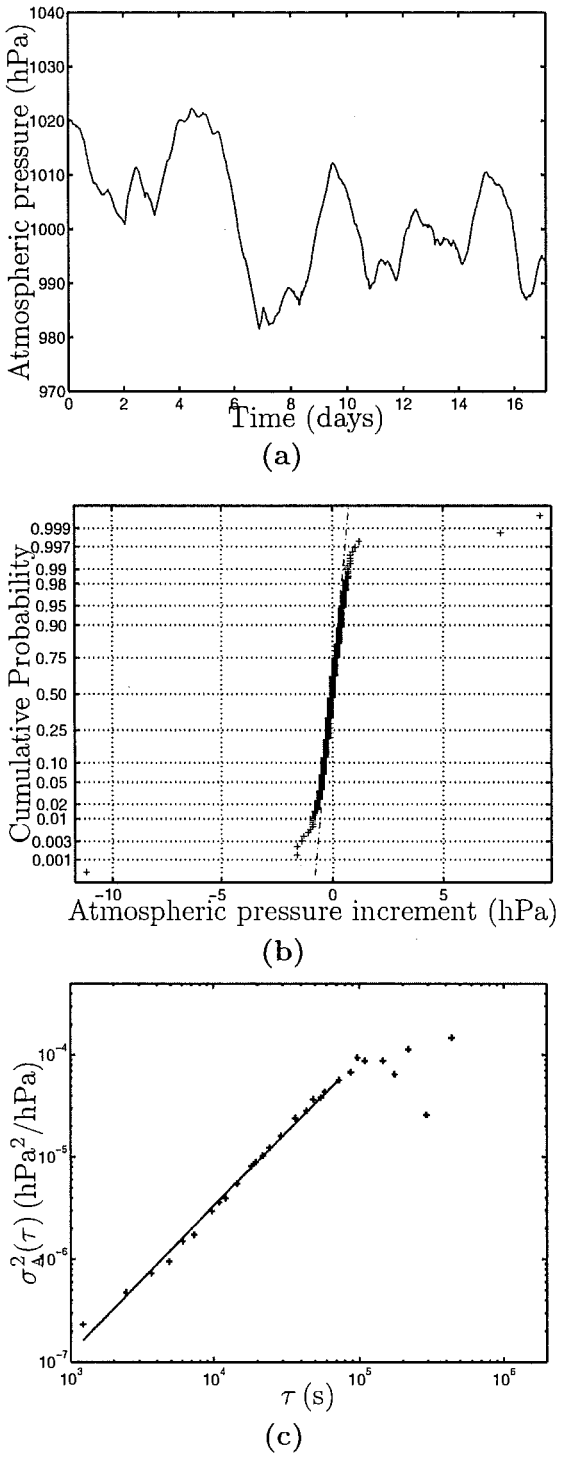

Figure 4.7: Data Set 5: (a) time-series of atmospheric pressure data recorded at the ring-laser cavern: (b) normal probability plot of the pressure increments between each reading, and (c) Allan variance density of atmospheric pressure.

of a few tenths of a Hertz. This is in qualitative agreement with observation. In addition, it should be noted that the noise process changes character on a timescale of approximately 10^5 s for all data sets. This is indeed evidence of the expected low-frequency cutoff.

It is necessary that care be taken in choosing the length of the data set in order to properly characterise the noise process. A good example seen with C-II has been reported in Ref [4]. Analysis of a particular data collection run[4] showed an Allan variance power law dependence of τ^2 for time scales longer than the white noise regime (¿1000 s). The main source of drift leading to this dependence was atmospheric pressure variation. This result is not, however, in contradiction with the material presented here since, by chance, there was a roughly monotonic increase in atmospheric pressure during the ~10 hr measurement time of the data used. As may be seen from the definition of the Allan variance (Equation (B.2)) a frequency ramp causes the difference in successive measured frequencies to increase linearly over time [10].

4.2.1 Fractional Lévy Motion

Fractional Brown motions are a subset of broader class of stochastic processes known as fractional Lévy motions. The Lévy probability distribution for the stochastic variables x is [50]

$$P(x) = \frac{1}{\pi}\int_0^{\infty} \exp\left[-(C\omega)^{\beta}\right]\cos(\omega x)\,\mathrm{d}\omega, \tag{4.14}$$

where $0 < \beta \leq 2$ and $C > 0$. Two special cases of the Lévy distribution are of interest. When $\beta = 2$ the Lévy distribution reduces to the Gaussian distribution and when $\beta = 1$ the Cauchy distribution is obtained. Since the Lévy distribution cannot be obtained in closed form, estimation of C and β is difficult and may be subject to some inaccuracies [104]. Fractional Lévy motions possess stationary increments that conform to the Lévy distribution. When $\beta = 2$, fractional Brownian motion is recovered as a special case of fractional Lévy motion. An example of fractional Lévy distribution in a physical setting may be drawn from porosity logs (with depth) taken from Middle East oil fields [50]. Most oil fields have low and relatively constant porosities. However, rare events, such as fractures or faults with a large porosity, cause the distribution of increments to have a long tail and fit well to the Lévy distribution.

In Figure 4.9 the logarithmic plot of the binned distribution for Data Set 1 shows that the deviation from the normal probability distribution previously noted is minor. If the Lévy distribution does provide a better model the parameter β is close to the Gaussian limit $\beta = 2$ and the fBm model is adequate for this investigation. It makes sense that the pressure estimates do not conform to a

[4]This is identified as TST1-30, 26 July 1997 in the local records.

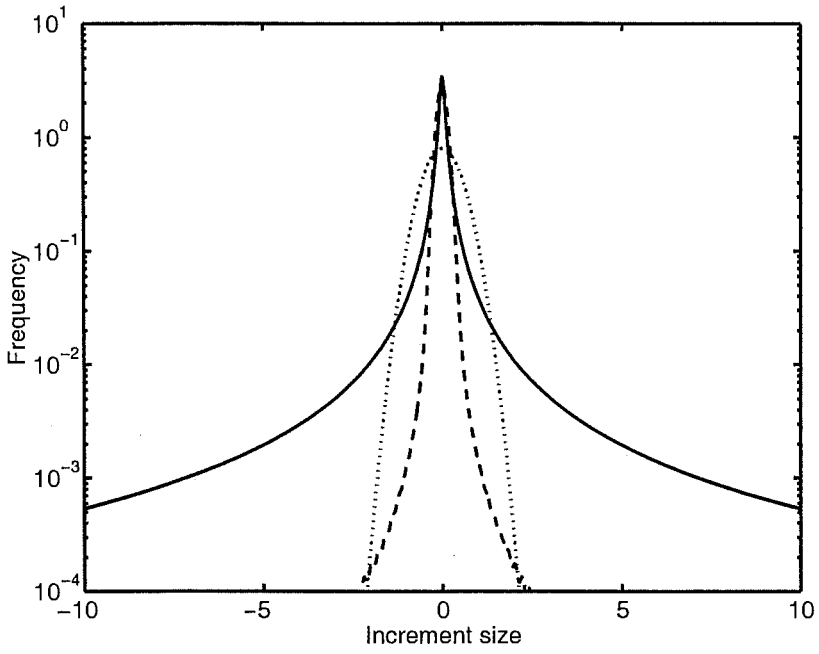

Figure 4.8: The Lévy distribution (solid and dashed lines) has much longer wings than the Gaussian distribution (dotted line). The parameters for the solid line and dashed line plots of the Lévy distribution are $\beta = 0.87, C = 0.1$ and $\beta = 0.1.9, C = 0.1$ respectively. The Gaussian has a standard deviation of 0.5.

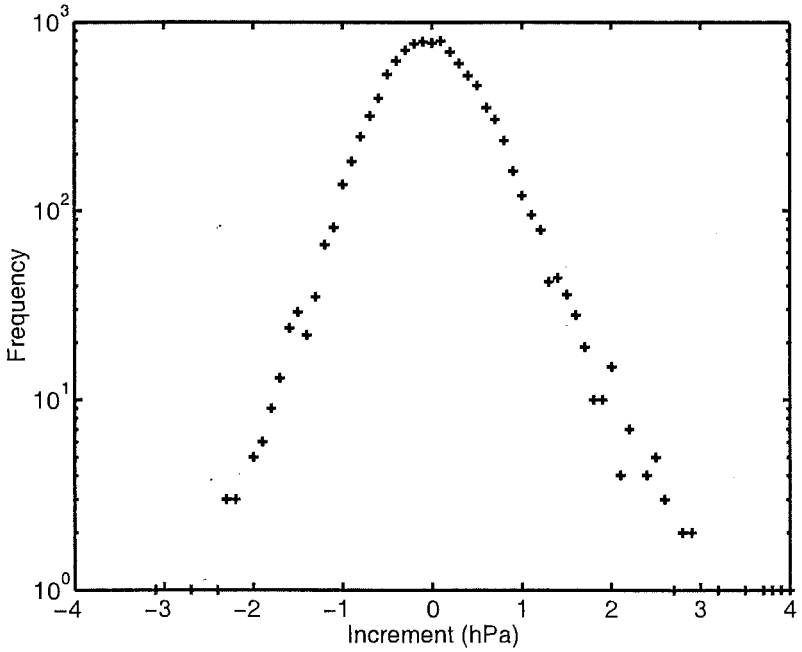

Figure 4.9: A logarithmic plot of the probability density for Data Set 1 shows that any deviation from the Gaussian increment model is minor.

Lévy distribution where β is not close to 2. This is because large increments in the change in atmospheric pressure with time are unexpected on the timescale of up to an hour or two.

4.2.2 Using the fBm Model

To the author's knowledge, the concept of tailoring the spectral characteristics of a drift process in order to optimise resolution is novel. In practice it may prove difficult to implement such tailoring. Understanding and modelling drift processes is a non-trivial exercise. The potential benefits of further work probably do not justify the effort required in terms of the goals of the Canterbury ring-laser project. However it is an interesting problem from an intellectual and experimental control theory point of view that has potential application well beyond the field of ring-laser gyroscopes.

However the noise strength of the drift processes is of critical importance to the optimisation of the ring-laser. If it is necessary that the maximum averaging time be increased then the only course of action is to reduce the noise strength of the drift processes. As long as the criterion (5.81) that states the noise introduced on a given timescale by any stabilisation process is less than the quantum-limited white noise contribution for that averaging time then the noise characteristics of the stabilisation scheme are irrelevant in terms of the performance on timescales less than the optimal averaging time τ_0. Therefore there is freedom to design the stabilisation scheme in a manner that inhibits the drift processes even if the design does not lead to the minimum possible introduced noise on timescales less than τ_0. In this the way the noise strength in the drift process may be reduced further than it would by the simple "compare and correct" stabilisation method described in Chapter 5. This will lead to commensurate increase in the optimal averaging time τ_0 as described by Equation (4.13) and the desired improvement in the resolution of Earth rotation.

The obvious question to ask is: how does one go about designing a stabilisation scheme that minimises the drift noise strength? This is not something that is well understood. However we may begin with the simple statement that $1/f^{\alpha}$ noise processes possess a "memory". In other words, $1/f^{\alpha}$ noise processes possess long range correlations in one form or another depending on the exact nature of the noise process. This suggests that a process of constraint on the long-term motion of the gyroscope beat frequency could bring about the desired reduction in the noise strength of the drift process.

It is important to realise the difference between constraint and full control. It would be a comparatively straightforward task to control the gyroscope beat as the process variable to some desired value. However this would obliterate features of interest (ie variation in Earth rotation and so on) leaving the noise of the stabilisation scheme. Constraint of the beat frequency implies that the

control is designed such that the noise strength of the drift processes is reduced while leaving sufficient freedom to, for example, observe changes in Earth rotation due to, for example, tidal effects. Constraint, when taken as describing a general approach, addresses the stochastic nature of the drift processes. Deterministic control is unable to do this.

In order to further explore the concept of constraint assume, for now, that any stabilisation does not affect the spectral characteristics of the drift processes—it simply reduces the noise strength. Equation (4.8) states the probability that the stochastic variable will have changed no more that a prescribed amount M in time T. Decreasing the noise strength will lead to an increase in the probability that the process has changed by no more than M. Conversely constraining the amount the stochastic variable changes will reduce the noise strength of the drift process.

An analogy with financial markets, which have also been modelled using this type of drift process, is illustrative. For example, consider the three year chart of the of Telecom New Zealand share price presented in Figure 4.10. Unless there is a major

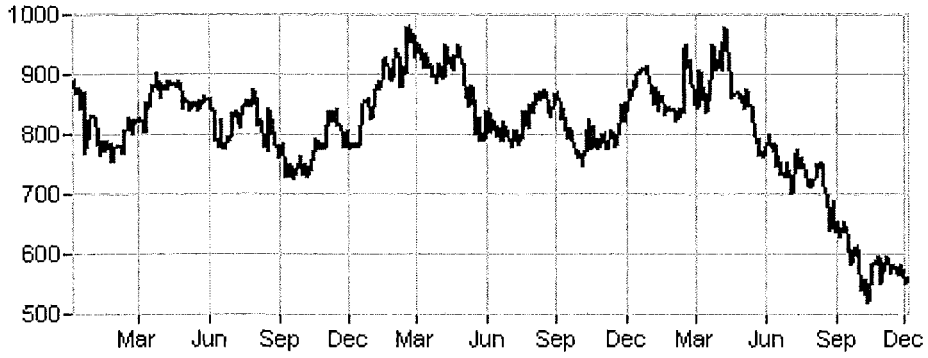

Figure 4.10: Share price of Telecom New Zealand from December 5 1997 to December 5 2000.

announcement or event that has a direct bearing on the price of a particular stock the short term fluctuations will appear somewhat random. However on the longer time-scale the stock price will drift about between highs and lows in a manner that is dependent on a highly complex set of influences relating to the company in question, events in the wider economy, and the (ir)rationality of investors. For example the upward trend in the Telecom share price between October 1999 and April 2000 was largely influenced by strong buying of telecommunications stocks worldwide. Similarly the marked decline between April and December 2000 is a result of the worldwide unpopularity telecommunications stocks and the weakness of the New Zealand dollar causing foreign investors to sell. Apart from (sometimes severe) implications relating to financial commitments these all have little impact on Telecom's ability to generate income. Therefore it would

appear reasonable that the movement of the share price due to circumstances beyond the company's control can be modelled as a stochastic drift process. This should then be added to a moving average that somehow reflects the intrinsic value of the company.

The movement of the gyroscope beat frequency due to atmospheric pressure variation is a similar sort of process. There is a major difference between a company share price and the output of a gyroscope however. In a competently managed company the basic goal of the company, and wish of the intelligent investor, is to maximise the value of the shares over the longterm, regardless of stochastic drifts in the market. On the other hand, in the case of the ring-laser gyroscope, it is required that the beat frequency be as stable as possible. In this sense stabilisation of the gyroscope is more akin to the actions of a central bank that controls the availability of money in order to meet a certain inflation target for example. When cash-flow is tightened to halt inflation the central bank is exercising a form of constraint. The goal is to smooth out the stronger variations for the longterm benefit of the economy. However if the central bank exercises too much constraint, or other influences cause the inflationary pressures to ease, there is a chance that the economy will contract which is an unhealthy outcome. Therefore the central bank must exercise a probalistic control over currency. Experience and modelling are combined to determine the action that will most likely bring the desired outcome. Transposing the jargon of the analysis presented in this Chapter, the goal is to reduce the noise density of the drift processes affecting inflation. The actions of the central bank will most likely affect the inflationary pressures. Similarly the board of directors and the behaviour of investors will have an impact on the drifts in the share price. There is a chance that this feedback will change the character of the drift process. In particular if knowledge of the noise process is used as a decision making tool the resultant decisions will tend to negate and affect the characteristics of the initial drift process. Herein lies the danger of predicting markets from stochastic analysis of historical data. Similarly any stabilisation of the gyroscope is likely to affect the spectral exponent of the fBm noise process, or may even cause the behaviour to no longer conform to the fBm model.

There are some significant and fortunate differences between drift processes that affect the gyroscope and those that affect financial markets. First of all, unlike financial markets, it is possible to obtain sufficient data for a comprehensive characterisation in a reasonable time. Furthermore the feedback mechanisms that might change the longterm drift processes that govern atmospheric pressure, for example, will change character much more slowly than the financial markets. Therefore it is possible to implement stabilisation by constraint in the knowledge that the only thing that will change the characteristics of the drift process is the stabilisation. Therefore if an unwanted change occurs in the character of the drift process it is possible to find a better set of characteristics by altering the stabilisation routine. These conclusions represent strong encouragement of

further investigations of the possibilities afforded by stabilisation by constrained feedback.

Chapter 5

Stabilisation of C-II Optical Frequency

As a prelude to the description of the method used to stabilise the optical frequency of the ring-laser gyroscope C-II, and to allow discussion of the relative advantages and disadvantages of the method employed, the first part of this chapter is used to provide an overview of the criteria that define an effective optical stabilisation scheme. This is supplemented by a description of the methods that are commonly used to achieve this with gas lasers. Sections 5.6 and 5.7 describe the method used to improve the stability of C-II and the results obtained respectively. In order to gain further understanding of the results presented in Section 5.7 a model of the stabilisation scheme and the noise introduced by the C-II pathlength corrections required to stabilise the optical frequency is developed in Section 5.8. Recommendations for the implementation of adjustments that may result in further improvements in stability are presented in Section 5.9. This includes a discussion of the problems associated with the effects of single mirror control on backscatter induced pulling and pushing of the Sagnac frequency. An important commentary on the possibilities of enhanced photo-detection methods is presented in Section 5.9.2. Any steps taken to improve this in future work will allow more flexibility and better control of the optical frequency no matter what method is employed.

5.1 What is Optical Frequency Stabilisation?

Frequency stabilised lasers are sources of coherent radiation in the optical regime, with applications in coherent communication [105, 106], gravity wave astronomy [107,108], research for new length and time standards [109], high resolution atomic and molecular spectroscopy [110] and determination of fundamental constants [111]. The frequency noise of free-running lasers is usually too high for such applications. The quantum-limited broadband white frequency noise due to the random walk in phase caused by spontaneous emission is the fundamental source of frequency noise in a laser [30]. However technical (environmental) noises reduce the frequency stability of all lasers, particularly at lower frequencies. Thus active frequency stabilisation is required in order to minimise the laser's frequency

noise that arises from technical noise sources. A general overview of stabilisation methods is given by Wallard [112].

Clearly it is important to have lasers that are as stable in optical frequency as possible for high precision applications. The ultimate goal is to achieve shot noise limited performance (due to the noise inherent in the photodetection process) over all time-scales of operation. Unfortunately this is not possible in practice so it is necessary to examine the application in order to furnish a working definition of a frequency-stable laser for the particular application.

For example, if a laser had very constant long-term average frequency then we might say it was stable. However this tells us nothing about the short-term behaviour of the laser—it may be particularly noisy. In this case it would not have a stability appropriate for, say, spectroscopic applications. Conversely a laser with very low short-term noise may have significant long-term frequency drift. This laser would be inappropriate for applications such as length standards where reproducibility is one of the key criteria for selection of a standard. One of the best ways to analyse the performance is to examine the Allan variance (see Appendix B.2) plot in order to evaluate the stability over the time-scales of interest for the application.

No matter what stabilisation method is employed a frequency reference is required. This is used to calculate an error signal based on the deviation of the laser to be stabilised from the reference. The optical frequency of the laser is then adjusted to minimise the error signal. The plot of the error signal against frequency, or some measurable directly related to frequency, is sometimes called the discriminant curve. An ideal frequency reference should be narrow and well defined to provide a sharp discriminant shape from which error signals may be derived to control the laser.

In the case of gas laser stabilisation it is the pathlength that is adjusted in order to stabilise optical frequency. Different types of lasers require different approaches. For example, the frequency of diode lasers is controlled by adjusting the injection current. There are two actuators that are commonly used to control the pathlength of gas lasers. The first is a thermo-electric heater. While this can offer large frequency corrections in the laser, the heater response bandwidth only extends to frequencies up to a few Hertz. If a larger bandwidth is required it is necessary to use a piezoelectric transducer bonded to the cavity. This provides a control bandwidth of several kiloHertz. In the case of C-II, the recently constructed pressure vessel allows control of the pathlength by means of compression/expansion of the monolith by increasing/decreasing the pressure within the vessel. Due to physical constraints, the bandwidth of the pressure vessel actuator is limited to a few mHz at best. In short, the choice of actuator is to some degree determined by the bandwidth necessary for the stabilisation scheme. This bandwidth requirement

application for which the stabilised laser is intended.

Stabilisation methods may be broadly placed into two categories: intra-cavity methods where some frequency-dependent property of the laser cavity is utilised to provide an error signal that may be used to provide a correction of the optical frequency and external reference locking methods where the error signal is derived as a function of the laser frequency in relation to the external reference. The most common implementation of this approach is the locking of the laser to an optical cavity by the various methods described in this Chapter. The passive stability of a well constructed cavity reference alone may be enough to provide an adequate frequency reference or it may be necessary to lock the cavity in turn to another reference laser.

5.2 Goals of C-II Frequency Stabilisation

The basic goal of the stabilisation of the C-II optical frequency is to place the laser in an operating regime where the Sagnac frequency of the ring-laser gyroscope is as stable as possible, maximising the resolution in the measurement of the Earth rotation rate. In order to measure the effects of Earth tides a gyroscope beat frequency stability better than parts per million is required [14,113]. Seismic events generate much larger variation in the gyroscope beat frequency. Therefore, it is important to ensure that optical frequency stabilisation does not affect any seismic signals if it is desired that they be monitored. The physical constraint is that the bandwidth of the stabilisation should be very small—the stabilisation scheme should not interact with the 22 s period P-waves arising from the seismic event [26]. In terms of the physical requirements, the goal of observing Earth tides implies optical frequency stabilisation should stabilise the perimeter to the order of a few nanometres; significantly greater perimeter changes are found to give relatively substantial Sagnac frequency drifts. In C-II this translates as the order of one part per billion of the perimeter or of the optical frequency. The level of stabilization required to reduce Sagnac drifts significantly in C-II is therefore 1 MHz or better, less than 1% of the free spectral range (FSR) of 75 MHz.

In order to determine the required characteristics of an optical frequency stabilisation scheme for C-II it is necessary to consider the stability of the free-running laser. Unfortunately there are no data available to directly assess the optical frequency stability[1]. However the close relationship between the Sagnac and

[1]To do this properly an Allan variance plot of a measurable closely related to the optical frequency is required. The obvious candidate is to use the frequency separation of C-II and the Winters iodine-stabilised laser as measured by a Fabry-Pérot cavity. Unfortunately the slow loop time of the method (as described in subsequent sections) does not produce data at closely enough placed intervals to produce an adequate characterisation of stability. However, since frequency dispersion from the gain medium is small, it is possible to obtain this information from an Allan variance plot of the FSR beat frequency.

optical frequencies means it is possible to infer the necessary information from an Allan variance plot of the free-running Sagnac frequency (Figure 4.1) with a reasonable degree of confidence. On time-scales of several hundred to a thousand seconds and less the major source of instability is the white frequency noise associated with the random walk in phase caused by spontaneous emission. The only way to change this limit is to alter laser parameters such as the cavity quality factor and the power injected per mode [3, 14]. These are independent concerns from the issues addressed by the optical stabilisation of C-II. It is on longer time-scales where the technical noise, possessing a signature $1/f^{\alpha}$ fluctuation spectrum described in Chapter 3, dominates, that optical frequency stabilisation of C-II will yield performance improvements. This is because the reduction in the effects of these noise sources allows a larger value for the optimal averaging time and hence better resolution of the Earth rotation rate. It is the intrinsic stability of the monolithic construction of C-II that gives rise to this situation. Therefore the stabilisation bandwidth need not be very large at all.

The difficulty in the stabilisation of the high-stability high-Q laser cavity arises from output power considerations rather than bandwidth considerations. Since the output power of C-II is particularly low (a few tens of pW) it was necessary to take care in order to achieve an adequate signal-to-noise ratio when generating the error signal. Some time is taken to discuss the methods used and how these may be improved in later sections.

5.3 Survey of Intra-cavity Laser Stabilisation Methods

There are a number of methods that use various internal properties of the laser to stabilise the optical frequency. In general these methods utilise a particular feature of the laser gain curve and use the change in output power corresponding to a change in frequency to calculate an error signal which is used to stabilise the pathlength. This Section is devoted to a survey of these methods to provide a point of reference against which to discuss the method employed with C-II, as well to provide the necessary background in order to suggest alternative methods that may be used to good effect.

5.3.1 Peak of Gain Profile

Locking to the peak of the laser gain curve is the simplest method of frequency stabilisation and was first employed soon after the first demonstration of the laser [114]. It has also been used in ring laser gyroscopes [73].

The operating frequency is made independent of external influences by control of the cavity pathlength using a movable mirror which tracks the position giving the maximum output power. This maximum power corresponds to the peak of

the Doppler broadened atomic response of the gain medium, which occurs at a fixed wavelength and frequency. If the laser is operated at a low input power to the discharge tube only one longitudinal mode will be above threshold. In this mode of operation the output power is strongly dependent on the operating frequency as pathlength variation causes the lasing frequency to move along the gain-frequency curve.

An oscillation is applied to the cavity pathlength to provide the control mechanism. As shown in Figure 5.1 the power displays a corresponding modulation with a modulation depth that increases as the laser is detuned from the peak of the gain curve. Demodulation of the power at the pathlength modulation frequency produces a signal that is approximately proportional to the detuning. This signal is used to drive a feedback controller that minimises the amplitude of the power modulation.

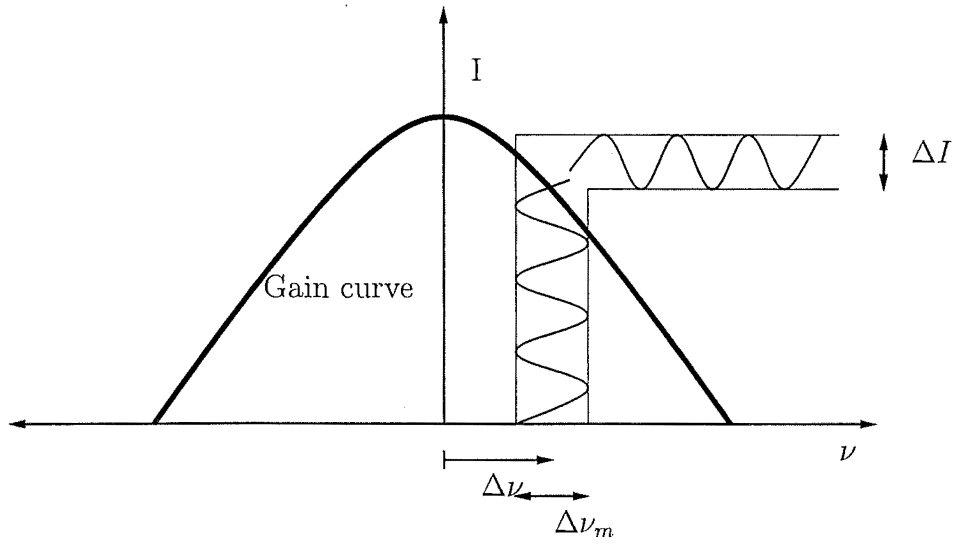

Figure 5.1: Stabilisation to the peak of the gain profile.

5.3.2 Polarisation Stabilised Lasers

A polarisation stabilised laser utilises the property that the output power of a single longitudinal mode laser will (generally) decrease as its wavelength is tuned away from the atomic line centre. If the cavity length and discharge excitation are chosen so that the laser can simultaneously support two longitudinal modes, they will have equal powers when the cavity length is adjusted such that the two modes are equidistant from the transition line centre. As long as the cavity has low anisotropy, the two modes will have orthogonal linear polarisations [115]. The two beams are separated by polarisation dependent optics and the powers compared. This information is then fed to a control loop that adjusts the pathlength to keep

the two modes at the same powers. The Newport NL-1 used by the Canterbury ring laser group employs this method to achieve a specified stability of 2 parts in 10^{10} over 5 ms, 1 part in 10^{11} over 100 s and 4 parts in 10^{11} over 1 hour [116]. This is in agreement with the measurements made within the ring laser group for the shorter timescales while the data for the longer timescales are inconclusive [117].

5.3.3 Lamb Dip

An important method of laser stabilisation is to utilise the properties of the Lamb Dip [12, p. 147-155]. The general approach is the same as that of stabilisation to the peak of the gain described in Section 5.3.1 using the pathlength oscillation to induce a power modulation however the properties of the gain-frequency curve are different due to different laser operating conditions.

The Lamb dip occurs in the centre of the power output curve as the laser is tuned over the range of frequencies available. It results from the waves running back and forth between the mirror deriving gain from the same Doppler-broadened atomic population. Consequently there is a reduction in gain when the laser is tuned to line centre compared to when there is moderate detuning and the waves interact with different parts of the Doppler shifted atomic population. Usually this dip is some $5-10\%$ of the total laser power output and may be up to 200 MHz wide [19, 112]. A limitation of this method lies in the breadth of the Lamb dip and its flatness at the centre. By comparison, the gain bandwidth for a typical 632.8 nm HeNe laser is about 1200 MHz at the half power points [73].

The laser to be stabilised is frequency modulated over an optical range $\Delta\nu_m/2$. This results in a power modulation of the laser power output. At a laser cavity detuning $\Delta\nu$ from the centre frequency of the gain curve ν_0 the amplitude modulation is in phase with the frequency modulation. As the cavity length is scanned through ν_0 the power modulation passes through zero. At a frequency $-\Delta\nu$ away from the centre frequency the power modulation is π out of phase with that at $\Delta\nu$. The magnitude of the power modulation thus gives information on how far the cavity resonance is from the atomic line centre while the phase reveals which side of the atomic line the cavity resonance lies. This makes the power modulation amenable to phase-sensitive detection (PSD) to obtain a DC voltage error signal which may be used as an input to a control loop for the cavity length.

Lamb dip lasers can achieve stabilities of the optical frequency of a few parts in 10^8 over several minutes [112]. However the long term stability is limited to 1 part in 10^7 due to diffusion of gases out of the laser tube [118]. This is because the change in gas pressure causes a slow drift in the centre frequency of the Lamb dip. A typical fill pressure of 3 torr shifts the line centre of the 633 nm transition by about 50 MHz, so a 5% change in the initial pressure would cause an error in the absolute wavelength of about 5 parts in 10^9 [5]. This property also has

the effect of meaning that two lasers with different gain tube diameters, both optimised for maximum power, will have different pressures and thus different centre frequencies of the Lamb dip. In terms of the requirements for stabilised lasers for standards this characteristic is unappealing.

5.3.4 Magnetic Field Stabilised Lasers

Further improvements in long-term stability are possible, if reference frequencies can be found which are not subject to the large helium pressure shift. Two such methods utilising the response of the gain medium to magnetic fields are described below.

A tube containing neon at a pressure of a few tenths of a torr is placed outside the cavity of a single mode laser, and a discharge is run so as to populate the lower laser level in the neon. Some of the excited neon atoms are able to absorb the laser radiation incident on the tube. If an axial magnetic field is applied to the neon tube, the absorption line is symmetrically split about its original centre by the Zeeman effect into two overlapping absorption lines. The neon absorption therefore becomes dichroic, exhibiting different absorption coefficients for oppositely-handed circularly polarised light of the same frequency. Only at the centre frequency of the unperturbed line will the absorption for both polarisations be equal. This phenomenon may be used to provide a stabilisation discriminant curve [119].

An alternative scheme involves the application of an axial magnetic field to the gain tube of an internal mirror single frequency laser. In this case the gain curve is effectively split into two oppositely-handed circularly polarised gain curves which partially overlap as before. The single laser frequency is split into two closely spaced frequencies of opposite senses of circular polarisation because of the circular birefringence of the neon [120] and only when the two frequencies are symmetrically spaced about the crossover frequency between the two gain curves will their intensities be equal. The power difference between the two polarisation modes may therefore be used to provide a frequency discriminator, referring the laser frequency to the intersection of the two gain curves.

5.3.5 Iodine-stabilised Lasers

Since an iodine-stabilised laser was used as the reference frequency for the stabilisation of the C-II optical frequency it is worth taking some time to elaborate on this method of stabilisation in order to understand the properties of these lasers that need to be taken into consideration in the discussion of the stabilisation of the C-II optical frequency. The fundamental idea behind iodine-stabilised lasers is to employ molecular absorption transitions of iodine as a set of frequency references against which the frequency of the laser is compared and controlled [121]. The

advantage of molecular absorption transitions lies in the fact that the absorption is from the ground state of the molecule so that discharge effects that may perturb the reference are entirely eliminated. The most suitable molecules are those with symmetry giving small dipole moments, thereby ensuring insensitivity to Stark shifts and also Zeeman shifts [12, 31]. Furthermore, iodine displays 21 absorption lines within the gain bandwidth of the 633 nm He-Ne laser [122] making it the obvious candidate for stabilisation of this ubiquitous type of laser. If stabilisation of an infra-red laser is required then methane provides the best selection of absorption lines [123]. The first demonstration of this stabilisation technique is found in [124] while in subsequent years the iodine-stabilised laser has become an integral tool in the maintenance of international length standards [125]. The Winters Model 100 iodine-stabilised laser used by the University of Canterbury ring laser group has an absolute frequency accuracy of 2.5 parts in 10^{11} or 12 kHz.

Component		$\nu(a_n) - \nu(i)$(kHz)	σ(kHz)
a_8	n	−162.814	0.005
a_9	m	−153.801	0.005
a_{10}	l	−137.994	0.005
a_{11}	k	−129.950	0.005
a_{12}	j	−31.565	0.005
a_{13}	i	0	
a_{14}	h	21.939	0.005
a_{15}	g	125.694	0.005
a_{16}	f	138.892	0.005
a_{17}	e	152.255	0.005
a_{18}	d	165.116	0.005
a_{19}	c	283.006	0.005
a_{20}	b	291.100	0.005
a_{21}	a	299.931	0.005

The reference component $i(a_{13})$ has a frequency
$f(i) = 473612214.705 \pm 0.0116$ MHz

Table 5.1: Iodine line frequencies ($^{127}I_2$ isotope) for Winters Model 100 [5]. σ is the estimated standard deviation for a one-second sample.

Iodine Absorption Technique

A tube containing iodine filled to a low pressure (0.1-0.2 mbar) is placed inside the laser cavity. Saturated absorption results, giving rise to a sharp Lorentzian

shaped dip at the centre of the absorption line. This dip in the absorption spectrum produces a corresponding increase in the modulated laser output as the laser is tuned through the frequency of the absorption line. As in the case of the Lamb dip the width of the dip is determined by the small natural width of the levels involved in the transition. However, the molecular lifetimes involved are much longer than those of the neon laser lifetimes, leading to a much smaller natural width of about 4 MHz [121]. Moreover the pressure broadening of the saturated absorption dip is small since the pressure of the absorbing gas is low. Temperature control of the iodine cell is often used to stabilise the cell pressure to minimise the pressure induced frequency shift of the molecular transitions which is more than an order of magnitude less than that for the Ne laser transition. Thus the problems regarding the aging of laser tubes experienced with Lamb dip, polarisation and Zeeman stabilised lasers are largely avoided with iodine-stabilised lasers. In order to observe the iodine peaks the laser must have a short term passive stability of about the same amount as the linewidth of the transitions or 1 part in 10^8 of the lasing frequency. Therefore it is necessary to construct the laser spacers from stable materials such as SUPER-INVAR^{TM}.

As in the case of Lamb dip stabilisation the cavity length is modulated with a piezoelectric transducer. The modulation is at frequency of a few kHz with a modulation depth of a few MHz. Phase sensitive detection (PSD) comparing the power modulation (due to the pathlength modulation across the gain curve) with the piezo driver frequency is performed. This signal is proportional to the first derivative of the power output. The variation of this derivative as a function of frequency may be observed by slowly scanning the length of the cavity and observing the PSD output while the modulation is still being applied. As may be seen from Figure 5.2 the first derivatives of the absorption lines appear as a fine structure of relatively small amplitude superimposed upon a curve of considerably greater variation. The latter represents a varying slope of the gain-frequency curve as it would appear without the iodine absorption.

The curve shown in Figure 5.2(a) would only be suitable for servo control to the frequency of the absorption feature where a zero PSD voltage crossing occurs. This is because, in the most simple application of PSD detection, the servo system would control the laser to zero PSD voltage. Control of the laser to any other feature would only be possible if a signal were added to the PSD output to offset the zero. The magnitude of this voltage would then depend critically on the laser power and parameters of the detection system and would therefore be particularly sensitive to drifts. If this were the case, some arbitrary criterion would be necessary for identifying the centre of a feature, to which the PSD zero is offset. Such a laser would not be reliably controlled to the true centre of the hyperfine component and the potential high reproducibility of the feature is lost. Early workers found that it was possible to place a component in the flat portion of the gain curve and so have a zero voltage crossing to which the laser could be controlled [124]. However this would not be case with a laser cavity of a

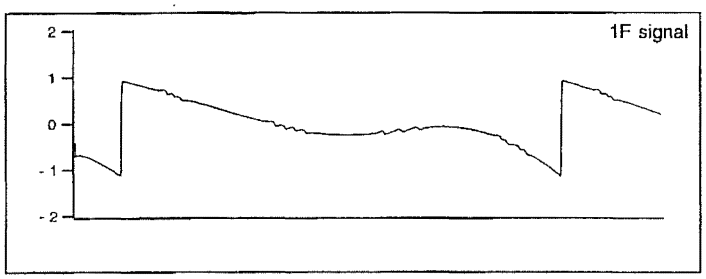

(a)

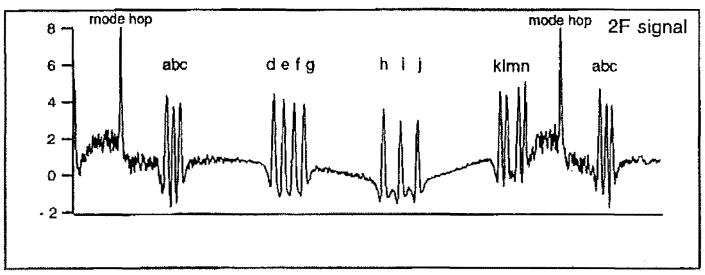

(b)

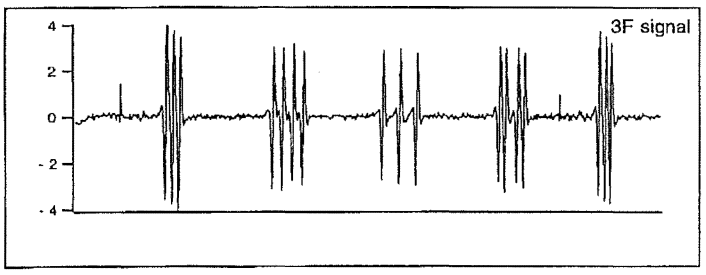

(c)

Figure 5.2: Tuning curve of Winters Model 100 iodine-stabilised laser: (a) first derivative, (b) second derivative, and (c) third derivative. Reproduced from the operating manual [5].

different length making this method inconvenient and inappropriate for use as a laser standard.

To investigate this point in depth consider a laser modulated over a bandwidth $\Delta\nu_m$ and at an angular frequency Ω. The laser power P depends on the position of the laser frequency beneath the gain curve. This may be written as a function F of ν and the applied frequency modulation.

$$P(t) = F\big[\nu + \Delta\nu_m \cos(\Omega t)\big]. \tag{5.1}$$

Assuming the modulation depth $\Delta\nu_m$ is small compared to the width of the absorption feature, this expression may be expanded as a Taylor series,

$$\begin{aligned} P(t) = {} & F(\nu) + \big[\Delta\nu_m \sin(\Omega t)\big] F^1(\nu) \\ & + \left[\frac{(\Delta\nu_m)^2 \sin^2(\Omega t)}{2!}\right] F^2(\nu) + \left[\frac{(\Delta\nu_m)^3 \sin^3(\Omega t)}{3!}\right] F^3(\nu) + \ldots, \end{aligned} \tag{5.2}$$

where $F^n(\nu)$ is the nth derivative of $F(\nu)$. After grouping the terms in $\sin(\Omega t)$ a little some manipulation gives the coefficients for each harmonic of $\sin(\Omega t)$. These coefficients correspond to the irradiance of the nth harmonic of the fundamental modulation frequency in the light of the output laser. The harmonic and coefficient pairs are

$$\sin(\Omega t): \quad \Delta\nu_m F^1(\nu) + \frac{k^3}{8} F^3(\nu) + \frac{2}{960} F^5(\nu) + \ldots \tag{5.3}$$

$$\sin(2\Omega t): \quad -\frac{(\Delta\nu_m)^2}{4} F^2(\nu) - \frac{1}{96} F^4(\nu) + \ldots \tag{5.4}$$

$$\sin(3\Omega t): \quad -\frac{(\Delta\nu_m)^3}{24} F^3(\nu) - \frac{3}{2120} F^5(\nu) + \ldots \tag{5.5}$$

If phase sensitive detection at a frequency $n\Omega$ is performed, the PSD output is predominantly the nth derivative of the gain curve $F(\nu)$ with smaller contributions from the $(n+2)$th and $(n+4)$th higher harmonics. In the region of a saturated absorption feature of FWHM γ, we may write the gain curve shape as a Lorentzian function of frequency centred at $\nu = 0$, superimposed on a sloping gain curve background. This sloping background may be represented by a quadratic function of frequency with coefficients $A, B,$ and C. Thus

$$F(\nu) = \frac{\gamma^2}{\gamma^2 + \nu^2} + A\nu^2 + B\nu + C \tag{5.6}$$

Differentiating with respect to $F(\nu)$ we find

$$\begin{aligned} F^1(\nu) &= \frac{-2\nu\gamma^2}{(\nu^2+\gamma^2)^2} + 2A\nu + B \\ F^2(\nu) &= \frac{8\nu^2\gamma^2 - 2\gamma^4}{(\nu^2+\gamma^2)^3} + 2A \\ F^3(\nu) &= \frac{24\,(\nu\gamma^4 - \nu^3\gamma^2)}{(\nu^2+\gamma^2)^4} \end{aligned} \tag{5.7}$$

The first derivative, corresponding to a phase sensitive detection at the fundamental frequency gives the well known dispersion shaped curve superimposed on a sloping background. The second derivative is a symmetric function of frequency and so cannot provide a polarity change in the PSD voltage around line centre. This makes it unsuitable as a frequency stabilisation discriminant. The third derivative, however, eliminates the background effects altogether and gives a zero voltage PSD crossing at line centre.

This indicates that the serious limitations on the use of a laser controlled to saturated absorption reference imposed by deriving the error signal from a phase sensitive detection at the modulation frequency may be overcome by using the PSD signal derived from the third harmonic of the modulation frequency. This technique, known as third derivative locking, has become the standard method to stabilise a He-Ne laser with an absorption cell filled with iodine placed inside a laser cavity. This method provides a zero voltage crossing at the centre of each of the features , allowing a far more reproducible method of control, eliminating the effect of linear and quadratic slopes in the background power output curve, and producing a scan against frequency as shown in Figure 5.2(c). Care must be taken to ensure that no third harmonic of the modulation frequency is present on the laser length modulation, otherwise a sloping background on the third derivative curves will also be seen. Similarly the phase locked generation of the third harmonic reference for the PSD must not contain any fundamental frequency component.

The Iodine-stabilised Laser Length Standard

The earliest definition of the metre ("le Métre des Archives", 1799) was based upon a measurement of a meridian between Dunkerque and Barcelona and was intended to be equal to 10^{-7} of the Earth's quadrant. The first *Conférence Général des Poids et Mesures* (CGPM) established a more precisely defined and stable international prototype metre in 1889. This prototype served to define the metre until 1960, when the eleventh CGPM redefined the metre in terms of the wavelength of the $^{86}\mathrm{Kr}2\mathrm{p}_{10} - 5\mathrm{d}_5$ transition at 606 nm.

Within a few years it became evident that the krypton standard could not be realised to better than about 4 parts in 10^9. Faced with the need for a more precise

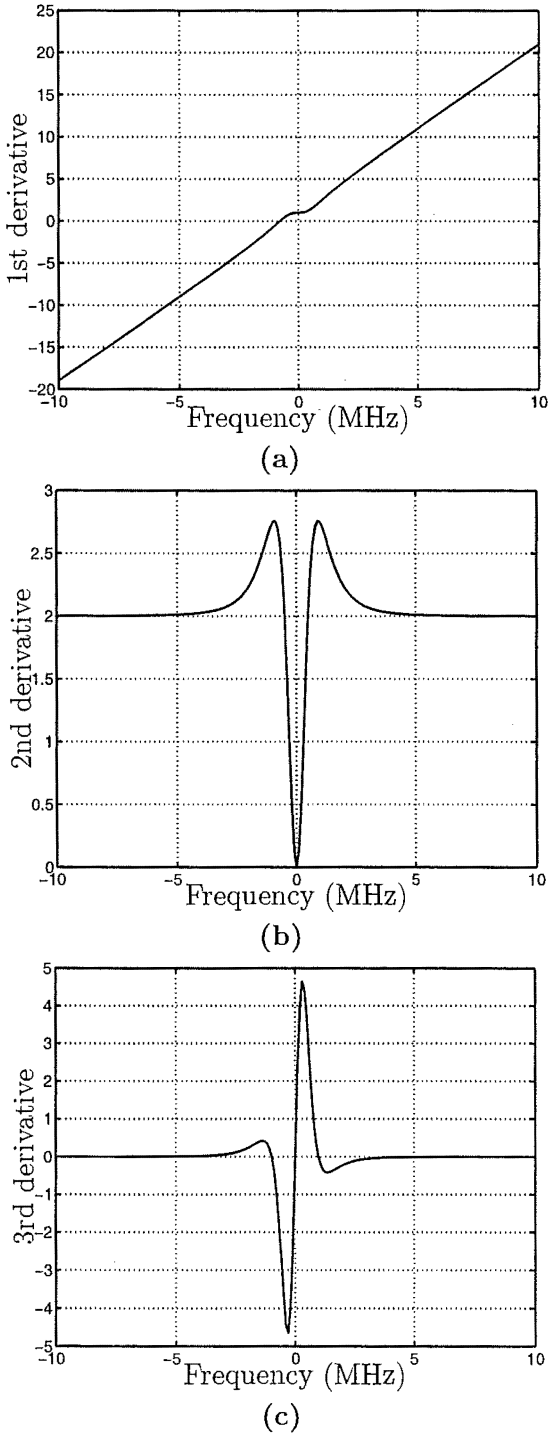

Figure 5.3: Detail of the (a) first derivative, (b) second derivative, and (c) third derivative theoretical curves of an iodine-stabilised laser power output. In this example $A = B = \gamma = 1$.

standard, the inconvenience of having a definition based on single wavelength, the availability of cesium clocks with uncertainties of less than 1 part in 10^{13}, and improvements in laser frequency stabilisation and wavelength and frequency measurement techniques, in 1983 the seventeenth CGPM adopted the current definition of the metre based upon a defined value for the speed of light 299 792 458 m/s in vacuum.

Simultaneous with the seventeenth CGPM, the Comité International des Poids and Mesures (CIPM) proposed a list of the recommended wavelengths for the practical realisation of the metre. This list includes five laser radiations stabilised to molecular transitions with saturated absorption techniques, the frequencies of which have been directly compared to the cesium time standard via frequency chains or indirectly with a combination of wavelength ratio measurements and frequency chains. Four are with iodine—the other methane.

This standard was further refined in 1992 when the CIPM decided to revise the 1983 definition of the metre [125]. This consisted of replacing the set of recommended standards wavelengths (as of 1983) with a new set that have considerably smaller uncertainties as compared with the values given in 1983. In the new definition of the metre, based on a defined value for the speed of light, one of three methods specified for the practical realisation of the metre uses molecular transitions at any of seven recommended frequencies, all corresponding to hyperfine components: one in methane and six in iodine. The most common implementation of one of these reference frequencies is the He-Ne laser operated at a wavelength of 633nm and frequency stabilised by saturated absorption in $^{127}I_2$.

Since these standards are technically complicated and their frequencies vulnerable to uncontrolled perturbations and system malfunctions a regular verification of laser performance for reliable applications is made through international comparisons [126,127]. These measurements are made by comparing the beat frequencies of the lasers over time. This provides a very sensitive means of determining the behaviour of the stabilised lasers. The relative Allan deviation (Section B.2) is a standard method of presenting the stability characteristics of the beat frequency signal of the two lasers under comparison.

Spectrum of Iodine-stabilised Lasers

The modulation necessary to lock the laser to the iodine transition is the major contributor to the lineshape of an iodine-stabilised laser. Consider the time-varying electric field,

$$\mathbf{E}(t) = E_0 \exp\left[-i(\omega_0 t - \phi(t))\right], \tag{5.8}$$

w where $\phi(t)$ is the modulated phase of the laser output and $\nu_0 = \omega_0/2\pi$ the lasing frequency. It is assumed that $\phi(t)$ is slowly varying compared to the unmodulated

phase change $2\pi\nu_0 t$ since ν_0 is at optical frequencies while the modulation is at radio frequencies. For pure sinusoidal modulation,

$$\phi(t) = \beta \sin(\Omega t), \tag{5.9}$$

where Ω is the modulation angular frequency and β, the modulation index, gives the peak phase excursion induced by the modulation. Recalling that instantaneous frequency is defined as the instantaneous rate of change of the phase it follows that

$$\nu_{inst} = \nu_0 + \Delta\nu \cos(\Omega t), \tag{5.10}$$

where $\Delta\nu = \beta\Omega/2\pi$ is the maximum frequency excursion and $\nu_0 = \omega_0/2\pi$. Note that β is the ratio of the maximum frequency excursion to the modulation frequency.

In analogy with radio terminology, the electric field described by Equation (5.8) may be decomposed into a carrier of frequency ν_0 and series of sidebands at frequencies $\pm n\Omega$ from the carrier [128, 129];

$$\begin{aligned}
\mathbf{E}(t) &= E_0 \exp\left[-i(\omega_0 t - \phi(t))\right] \\
&= E_0 \sum_{n=-\infty}^{n=\infty} J_n(\beta) \exp\left[-i(2\pi\nu_0 + n\Omega)t\right] \\
&= E_0 \Big[J_0(\beta) \exp(-i\omega_0 t) \\
&\quad + \sum_{n=1}^{n=\infty} J_n(\beta) \exp\left[-i(\omega_0 + n\Omega)t\right] + (-1)^n \exp\left[-i(\omega_0 + n\Omega)t\right] \Big],
\end{aligned} \tag{5.11}$$

where J_n is the Bessel function of order n. The sideband amplitudes are given by $J_n(\beta)$ which rapidly becomes small for $n > \beta$. Note that the total power in the beam is given by

$$\langle \mathbf{E}(t) \cdot \mathbf{E}^*(t) \rangle = E_0^2 \Big[J_0^2(\beta) + 2 \sum_{n=1}^{\infty} J_n^2(\beta) \Big] = E_0^2 \tag{5.12}$$

which is independent of β as it must be for pure frequency modulation.

In order to determine the spectrum of an iodine-stabilised laser it is necessary to convolve the modulation spectrum, simply given by delta functions at frequencies specified by each term in the series expansion (5.11), with the Lorentzian spectrum of the cavity and laser about $\omega = 0$ given by

$$\mathcal{L}(\omega) = \frac{\gamma}{\pi(\gamma^2 + \omega^2)}. \tag{5.13}$$

The resulting power spectrum is

$$P(\omega) = P_0 \left[J_0(\beta)^2 L(\omega_0) + \sum_{n=1}^{n=\infty} J_n(\beta)^2 [\mathcal{L}(\omega_0 + n\Omega) + \mathcal{L}(\omega_0 - n\Omega)] \right]. \tag{5.14}$$

For $\beta \gg 1$ the spectrum is essentially that of a laser whose frequency is slowly scanned from $\omega_0 - \Delta\omega$ to $\omega_0 + \Delta\omega$ as one would expect. This behaviour is demonstrated in Figure 5.4.

5.4 External Reference Locking: the Optical Spectrum Analyser

Instead of using the internal properties of the laser in order to stabilise its frequency it may be advantageous to use an external reference cavity. In its most basic configuration light from the laser to be stabilised is injected into the reference cavity. The pathlength of the laser is adjusted in order to ensure the light injected into the reference cavity remains at the resonance frequency of the cavity. The major advantage of this approach is that it is generally possible to construct a relatively short, and hence stable, reference cavity. However it is not possible to achieve the sort of long-term stability possible with, for example, an iodine-stabilised laser. Therefore it is common to employ the techniques of external cavity locking in combination with other methods to enhance the relative stabilities of two lasers [130, 131]. In this section a review of the properties of the Fabry-Pérot interferometer, often used as the external reference, is given. This is followed by a discussion of the various ways this device may be used to stabilise a laser.

The Fabry-Pérot Interferometer

The Fabry-Pérot interferometer is a device with a long history. Airy was the first to discuss the properties such a device would exhibit in 1831 [132]. The analysis was concerned with the fringe pattern formed by light incident on the most rudimentary form of the Fabry-Pérot interferometer consisting of two reflecting glass plates. Such a fringe pattern was first observed in 1851 [133]. However it was not until the 1890's that this type of instrument was fully investigated and its potential developed by Pérot and Fabry of the University of Marseilles [134].

Today the scanning Fabry-Pérot interferometer or optical spectrum analyser is an integral part of many optical applications including stabilisation of lasers [1, 129, 131], atomic spectroscopy [135], length standards, astronomy and astrophysics, light scattering studies of materials and metrology. The optical signal is matched into the cavity and light is transmitted if the incident wavelength is at resonance with the cavity and is reflected if the cavity and incident light are not at resonance. If the width of the cavity transmission is small compared to the width of the spectral feature then the output of the cavity as it is scanned over the spectral feature will constitute a replica of the spectral profile of the signal. A comprehensive review of applications utilising this type of device is given in

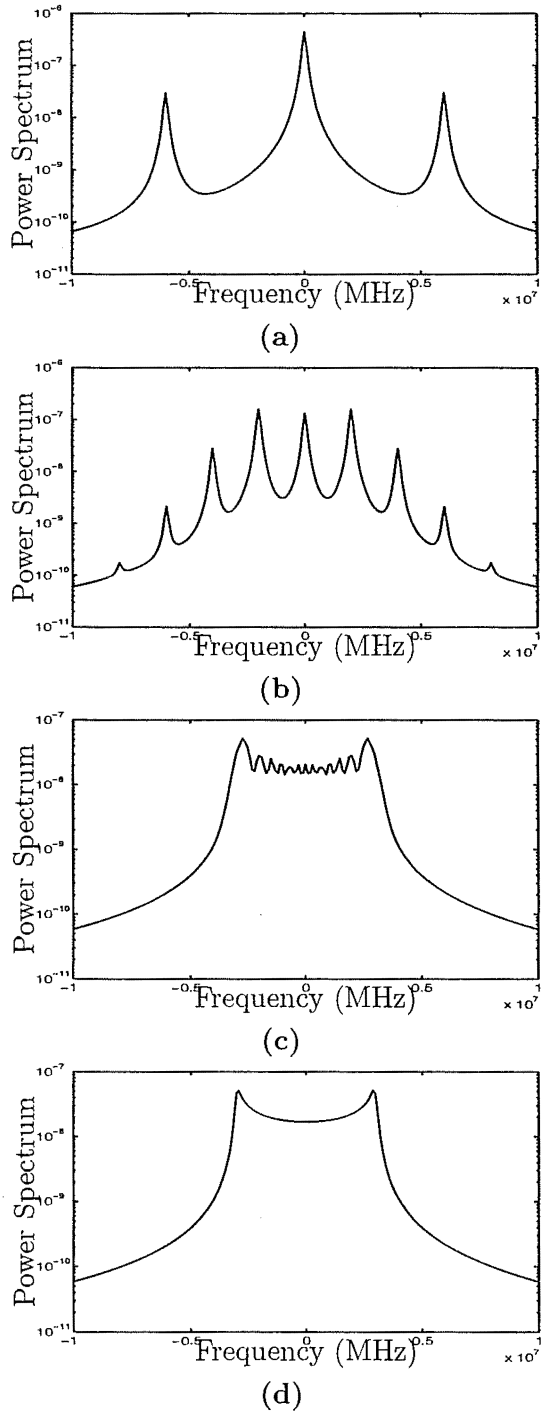

Figure 5.4: Spectra of FM modulated laser that possesses an unmodulated Lorentzian lineshape with a FWHM of 100 kHz; (a) $\beta = 0.5$ and $\Delta\nu = 6$ MHz, (b) $\beta = 1.5$ and $\Delta\nu = 2$ MHz, (c) $\beta = 20$ and $\Delta\nu = 150$ kHz, and (d) $\beta = 2560$ and $\Delta\nu = 1172$ Hz (the same as the Winters Model 100 specification). The units of the Power Spectrum are arbitrary in this example.

Vaughan [134].

5.4.1 Transmitted Power Profile

In this section the power transmission profile for the plane mirror Fabry-Pérot interferometer is derived. Quantities such as the transmission profile, finesse, resolving power and linewidth are derived using a geometric ray treatment. Later it is shown that this treatment is easily adapted to a spherical Fabry-Pérot interferometer after some simple substitutions[2]. This treatment largely follows that of Vaughan [134].

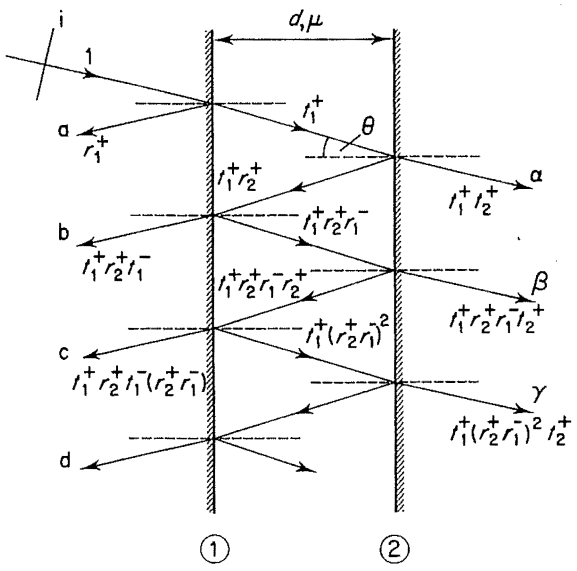

Figure 5.5: Plane mirror Fabry-Pérot interferometer.

The labelling convention for the transmission and reflection coefficients of the mirrors is shown Figure 5.5. The surface amplitude reflection and transmission coefficients (r and t respectively) for a ray traveling left to right are labelled with a '+' sign and an incident ray traveling right to left is denoted by a '−' sign. These coefficients may be complex.

Now consider the sets of successively reflected waves $a, b, c, \ldots$ and transmitted waves $\alpha, \beta, \gamma, \ldots$ shown in Figure 5.5. The relative amplitudes of each wave are displayed in the figure. The optical delay for each successive reflection gives a phase lag φ for adjacent members of each set given by

$$\varphi = \frac{4\pi n L \cos\theta}{\lambda_0}, \tag{5.15}$$

[2]This is of interest since the Newport SR-130 OSA (Optical Spectrum Analyser) used in the stabilisation of the C-II optical frequency is a spherical-mirror cavity.

where n is the refractive index of the medium inside the cavity and L is the length of the Fabry-Pérot cavity. This phase lag arises from a double passage of the cavity. Thus with the exception of the first reflection at a, both sets of beams form geometrical progressions with the same factor $r_1^- r_2^+ \exp(i\varphi)$. If the first m transmitted beams are superposed, the amplitude $E_t(m)$ of the resultant electric field vector is (assuming an incident field of unity amplitude)

$$\begin{aligned} E_t(m) &= t_1^+ t_2^+ \left[1 + r_1^- r_2^+ \exp(i\varphi) + \cdots + ((r_1^- r_2^+)^{m-1} \exp(i(m-1)\varphi)\right] \\ &= t_1^+ t_2^+ \frac{1 - (r_1^- r_2^+)^m \exp(im\varphi)}{1 - r_1^- r_2^+ \exp i\varphi}. \end{aligned} \tag{5.16}$$

For an infinite number of beams as $m \to \infty$ this becomes

$$E_t = \frac{t_1^+ t_2^+}{1 - r_1^- t_2^+ \exp i\varphi}. \tag{5.17}$$

The corresponding transmitted irradiance I_t is found from the square modulus of Equation (5.17)

$$I_t = \frac{|t_1^+ t_2^+|^2}{1 + |r_1^- r_2^+|^2 - 2|r_1^- r_2^+| \cos\psi}. \tag{5.18}$$

In this expression

$$\psi = \varphi + \epsilon, \tag{5.19}$$

where the complete phase lag ψ between adjacent members must also include the phase changes at each reflection given by

$$\epsilon = \arg r_1^- + \arg r_2^+. \tag{5.20}$$

The surface power reflection and transmission coefficients R and T are defined such that

$$t^+ t^- = T, \qquad r^+ = -r^-, \qquad r^{+^2} = r^{-^2}, \text{ and } \quad R + T = 1. \tag{5.21}$$

This leads to the following result for the transmitted irradiance profile for a beam of arbitrary incident irradiance,

$$\begin{aligned} I_t &= I_i \frac{T^2}{1 + R^2 - 2R\cos\psi} \\ &= I_i \frac{T^2}{(1-R)^2 + 4R\sin^2(\psi/2)} \\ &= I_i \frac{T^2}{(1-R)^2} \left(\frac{1}{1 + [4R/(1-R)^2]\sin^2(\psi/2)} \right) \\ &= I_i \frac{[T/(1-R)]^2}{1 + [4R/(1-R)^2]\sin^2(\psi/2)}. \end{aligned} \tag{5.22}$$

Examination of Equation (5.22) reveals that as the cavity length is scanned, the transmitted irradiance profile for a monochromatic incident beam consists of a

series of maxima, with spacing determined by the sine-squared term. Conversely if the cavity length is constant but the incident beam consists of many frequency components then there will be interference maxima for those frequencies that are at resonance with the cavity. Now we look at some quantities commonly derived from Equation (5.22). The first is the coefficient of finesse, given by

$$F = \frac{4R}{(1-R)^2}. \tag{5.23}$$

Note that coefficient of finesse is not the same as the finesse which will be defined shortly. The Airy function is defined as

$$\begin{aligned} \mathcal{A}(\psi) &= \frac{1}{1+[4R/(1-R)^2]\sin^2(\psi/2)} \\ &= \frac{1}{1+F\sin^2(\psi/2)}. \end{aligned} \tag{5.24}$$

Then Equation (5.22) may be written as

$$\frac{I_t}{I_i} = \frac{T^2}{(1-R)^2}\,\mathcal{A}(\psi). \tag{5.25}$$

The Airy function representation of the irradiance distribution is only valid for a source of constant brightness and spectral distribution and for a non-scanning interferometer. Effects, such as cavity ringing, arising from scanning the path-length of the interferometer for a cavity with $\mathcal{F} \sim 50000$, such as that used for frequency comparison in the stabilisation of C-II, have been shown to be negligible for scan rates of less than 1 GHz/s [136]. Since a Fabry-Pérot cavity of the type employed in the stabilisation of C-II typically has a FSR of a few GHz a scanning rate of 1 GHz/s corresponds to a physical motion of the mirror of the order of 100 nm/s.

The transmitted irradiance is at a maximum when $\mathcal{A}(\psi) = 1$. Therefore peak transmission is given by

$$\left(\frac{I_t}{I_i}\right)_{max} = \left[\frac{T}{1-R}\right]^2. \tag{5.26}$$

The relative irradiance $I_t/(I_t/I_i)_{max}$ is then just given by the Airy function. In this derivation it has been assumed that the transmission from outside the cavity is the same as that from the inside to the outside of the cavity. This will generally not be the case due to mirror construction. It is straightforward to deduce that the transmission from the outside is related to the transmission from the inside by $t_1^+ = kt_2^+$, where k is a constant, then Equation (5.22) need only be modified by replacing T with kT. This change does no more than affect the value of the peak transmission.

A measure of the sharpness of the fringes is given by the full-width half-maximum, γ_ψ. It is the width of the peak, in radians, when $I_t/(I_t)_{max} = 1/2$. Since the

relative irradiance of the fringes is given by the Airy function, γ_ψ satisfies the relation

$$\frac{1}{1+F\sin^2(\gamma_\psi/4)} = \frac{1}{2} \tag{5.27}$$

so that

$$\gamma_\psi = 4\sin^{-1}\left(1/\sqrt{F}\right). \tag{5.28}$$

Since $F \gg 1$ Equation (5.28) may be approximated as

$$\gamma_\psi = \frac{4}{\sqrt{F}}. \tag{5.29}$$

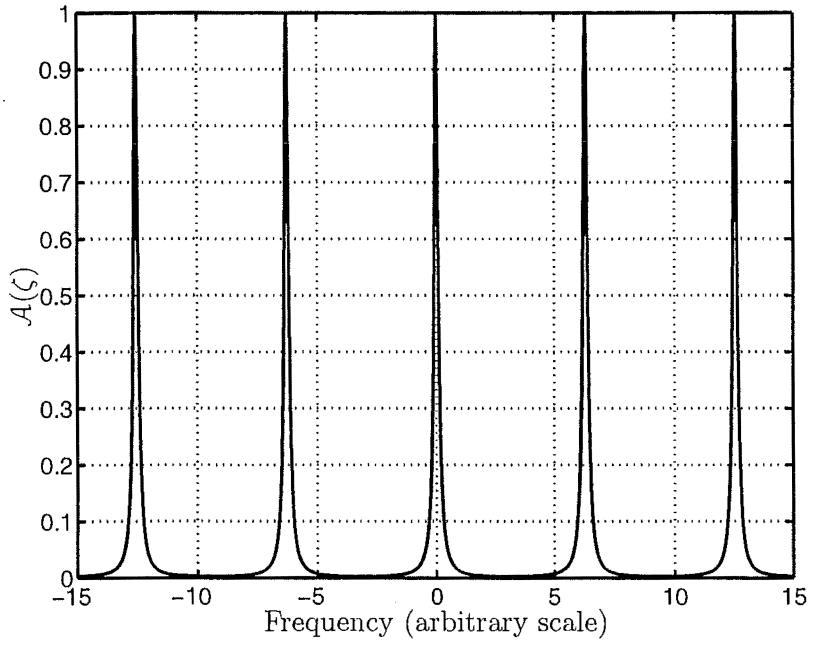

Figure 5.6: Peaks from 5 orders of a typical Fabry-Pérot interferometer. A mirror reflectivity of 0.9 is assumed.

A parameter of particular importance is the finesse $\mathcal{F}$ of the cavity. The finesse is defined as the ratio of the separation of adjacent maxima to the half-width at full maximum. It is therefore a measure of the resolving ability of the cavity. The separation is equal to 2π radians so

$$\mathcal{F} = \frac{2\pi}{\gamma_\psi} = \frac{\pi\sqrt{F}}{2} = \frac{\pi\sqrt{R}}{1-R}. \tag{5.30}$$

Over the visible spectrum, the finesse of ordinary spherical Fabry-Pérot cavities is of the order of 200. The physical limitation on the finesse is due to losses at the mirrors, including scattering from the substrate surface and coating and absorption by the coating. However when low loss mirrors are used, as is the case

with the Newport SR-130 scanning Fabry-Pérot interferometer used in the optical stabilisation of C-II, the finesse is easily increased to the order of 50000.

In order to effectively use measurements from a scanning Fabry-Pérot interferometer it is necessary to be able to calculate the frequency change of the incident beam that is at resonance with the cavity as the pathlength of the Fabry-Pérot cavity is scanned. In terms of frequency, the free spectral range of a linear cavity is given by

$$\Delta\nu_{\text{FSR}} = \frac{c}{2nL}. \tag{5.31}$$

The individual fringes of a single monochromatic component each represent different orders of the interference pattern. The transverse mode structure of the cavity is of course the standard Hermite-Gaussian formulation. It is possible to observe the excitation of these modes, generally at mirror separations that are some fraction of the free spectral range. When the phase changes by 2π next resonance is observed. Therefore the relative phase linewidth (as a fraction of an order) may be defined as $\gamma/2\pi$. Since a full order is equal to the free spectral range (FSR) of the cavity we have

$$\gamma_\nu = \frac{\gamma_\psi \Delta\nu_{\text{FSR}}}{2\pi} = \frac{\Delta\nu_{\text{FSR}}}{\mathcal{F}}. \tag{5.32}$$

In order to verify this result consider Equation (5.22). According to Equation(5.22) the transmission is at a maximum whenever

$$\psi = \frac{4\pi nL\cos\theta}{\lambda_0} = 2m\pi, \tag{5.33}$$

where m is an integer. This condition may be re-written as

$$\nu_m = m\frac{c}{2nL\cos\theta}. \tag{5.34}$$

For fixed l and θ Equation (5.34) defines the resonance frequencies of the cavity. The separation between each of the resonances for a single monochromatic component is given by

$$\Delta\nu_{\text{FSR}} = \nu_{m+1} - \nu_m = \frac{c}{2nL\cos\theta}. \tag{5.35}$$

Taking, for simplicity, the case of normal incidence ($\theta = 0$), we obtain the following expression for the change $\delta\nu$ in the resonance frequency of a given transmission peak due to a length variation δl

$$\frac{\delta\nu}{\Delta\nu_{\text{FSR}}} = \frac{\delta l}{(\lambda_0/2n)}, \tag{5.36}$$

where $\Delta\nu_{\text{FSR}}$ is the inter-mode frequency separation as given by Equation (5.35). According to Equation (5.36) the peak transmission frequency of the cavity may

be tuned by $\Delta\nu_{\text{FSR}}$ by changing its length by half a wavelength (assuming the refractive index is equal to unity). To use this result in Equation (5.33) rewrite the phase as $\psi = \psi_0 + \delta\psi$ where ψ_0 may be taken as zero without loss of generality. Differentiating Equation (5.15) with respect to l and assuming normal incidence it is straightforward to deduce that

$$\delta\nu = \frac{\Delta\nu_{\text{FSR}}\delta\psi}{2\pi}. \tag{5.37}$$

From this result it is trivial to deduce Equation (5.32).

Fourier Representation of Transmitted Irradiance Profile

It is possible to provide an alternative series formulation for the irradiance profiles of the fringes [134]. The transmitted amplitude of the transmitted beams may be written in simplified form as

$$E_t(m) = T\left[1 + R\exp(i\psi) + R^2\exp(i2\psi) + \ldots\right]. \tag{5.38}$$

Multiplying this series by the complex conjugate gives the transmitted irradiance coefficients

$$\begin{aligned} I_t &= T^2\left[1 + R^2 + R^4 + R^6 + \ldots\right] + T^2 2\cos\psi\left[R + R^3 + R^5 + \ldots\right] \\ &\quad + T^2 2\cos\psi\left[R^2 + R^4 + R^6 + \ldots\right] \\ &= \frac{T^2}{1-R^2}\left(1 + 2\sum_{m=1}^{m=\infty} R^m\cos(m\psi)\right) \\ &= \left[\frac{T}{1-R}\right]^2\left[\frac{1-R}{1+R}\right]\left(1 + 2\sum_{m=1}^{\infty} R^m\cos(m\psi)\right). \end{aligned} \tag{5.39}$$

Figure 5.7(b) shows the first four terms in this series expansion which has been found particularly useful for the detailed evaluation and computation of experimental profiles [137]. The main advantage of this approach is that it allows simple convolution with other common functions, notably Gaussian and Lorentzian functions. In the remainder of this section the irradiance profiles for Gaussian, Lorentzian and iodine-stabilised laser input spectra are derived by performing the convolution of the input spectrum with the Fourier expansion of the instrumental lineshape function.

(i) First the case of an incident beam with a Gaussian spectrum is presented [138]. This is characteristic of a laser with $1/f^2$ noise modulation [139]. Consider the normalised instrumental lineshape function that follows from Equation (5.39),

$$\mathcal{A}(\zeta) = 1 + 2\sum_{m=1}^{\infty} R^m\cos(2\pi m\zeta), \tag{5.40}$$

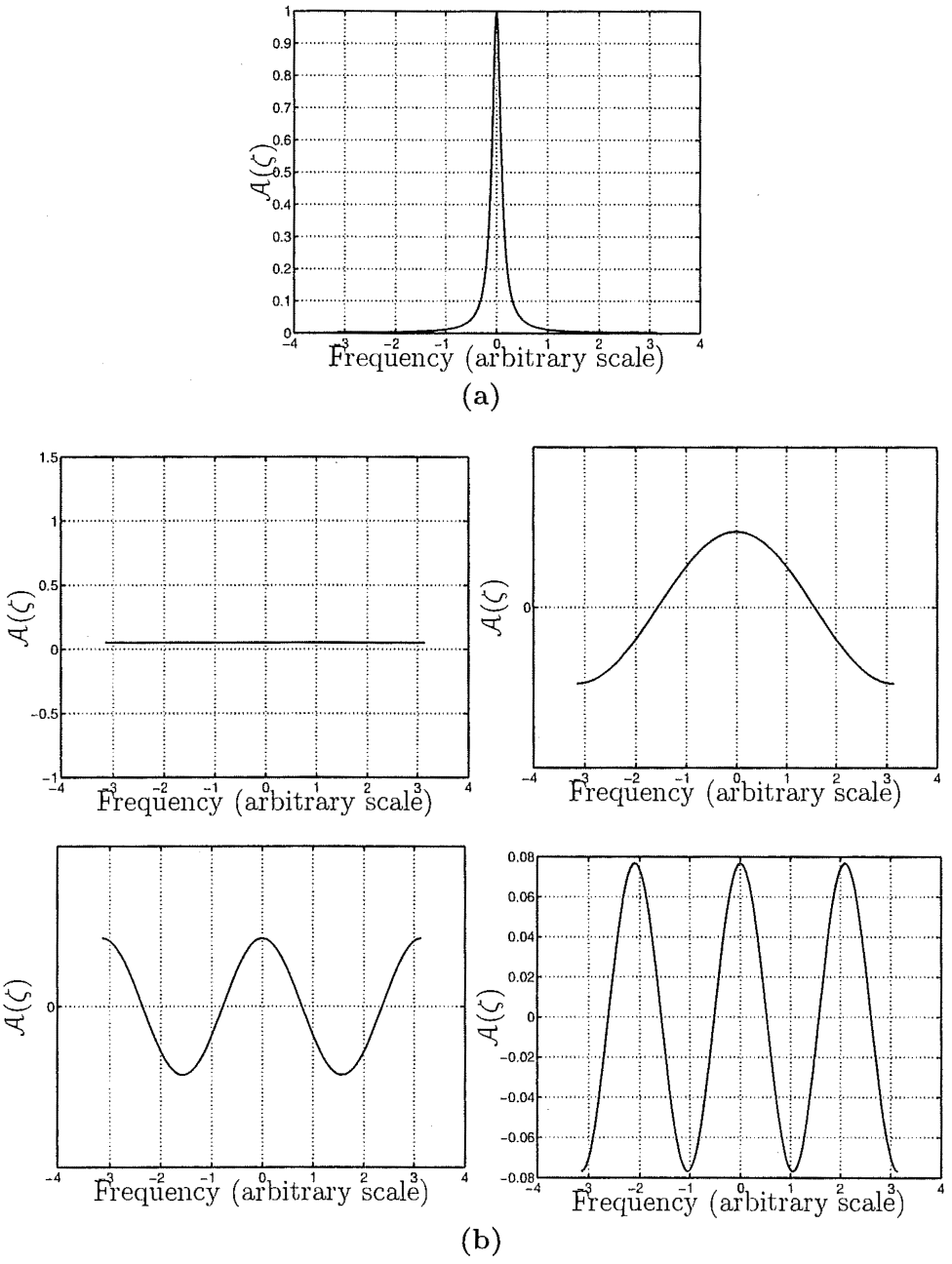

Figure 5.7: (a) The Airy distribution (Equation (5.22)) with $T = (1-R)$ and $R = 0.90$ and (b) the first four terms of the equivalent series formulation (Equation (5.39)). The scale of the x-axis is dependent on the point of reference—it might refer to optical frequency, displacement of the piezo mirror, or piezo driver voltage. The coefficients of the instrumental lineshape function (y-axis) are unitless.

where

$$\int_0^1 \mathcal{A}(\zeta)\mathrm{d}\zeta = 1. \tag{5.41}$$

The normalised Gaussian "source" function $\mathcal{G}(\zeta)$ is given by

$$\mathcal{G}(\zeta) = \frac{\exp\left(-\zeta^2/\sigma^2\right)}{\sigma\sqrt{\pi}}, \quad \text{where} \quad \int_{-\infty}^{+\infty} \mathcal{G}(\zeta)\ \mathrm{d}\zeta = 1. \tag{5.42}$$

The resulting convolution $F_{\mathcal{G}}(x)$ giving the expected lineshape is

$$\mathcal{F}_{\mathcal{G}}(x) = \int_{-\infty}^{+\infty} \mathcal{G}(\zeta)\mathcal{A}(\zeta - x)\ \mathrm{d}\zeta. \tag{5.43}$$

Substituting $\mathcal{G}(\zeta)$ and $\mathcal{A}(\zeta)$ gives

$$\begin{aligned}
\mathcal{F}_{\mathcal{G}}(x) &= \frac{1}{\sigma\sqrt{\pi}} \int_{-\infty}^{+\infty} \exp\left(-\zeta^2/\sigma^2\right) \left(2\sum_{m=1}^{\infty} R^m \cos\left(2\pi m(x-\zeta)\right)\right)\ \mathrm{d}\zeta \\
&= \frac{1}{\sigma\sqrt{\pi}} \int_{-\infty}^{+\infty} \exp\left(-\zeta^2/\sigma^2\right)\ \mathrm{d}\zeta \\
&\quad + \frac{2}{\sigma\sqrt{\pi}} \sum_{m=1}^{\infty} R^m \cos(2\pi m m) \int_{-\infty}^{+\infty} \exp\left(-\zeta^2/\sigma^2\right) \cos(2\pi m\zeta)\ \mathrm{d}\zeta \\
&\quad + \frac{2}{\sigma\sqrt{\pi}} \sum_{m=1}^{\infty} R^m \sin(2\pi m m) \int_{-\infty}^{+\infty} \exp\left(-\zeta^2/\sigma^2\right) \sin(2\pi m\zeta)\ \mathrm{d}\zeta.
\end{aligned} \tag{5.44}$$

The third integral containing the sine function is equal to zero (as may be seen from simple considerations of symmetry) and the second integral is given by

$$\int_{-\infty}^{+\infty} \exp\left(-\zeta^2/\sigma^2\right) \cos(2\pi m\zeta)\ \mathrm{d}\zeta = \sigma\sqrt{\pi}\exp\left(-(\sigma\pi m)^2\right). \tag{5.45}$$

Therefore the final result for the convolution of the Gaussian "source" profile with the Fourier expansion of the instrumental lineshape function of a Fabry-Pérot interferometer is

$$\mathcal{F}_{\mathcal{G}}(x) = 1 + 2\sum_{m=1}^{\infty} R^m \exp\left(-\sigma^2\pi^2 m^2\right) \cos(2\pi m x). \tag{5.46}$$

Comparison with Equation (5.40) shows that the convolution is derived by simple multiplication of each successive term by $\exp\left(-\sigma^2\pi^2 m^2\right)$. That is, by a sequence of Gaussian functions. The interpretation of the variable x is really dependent on whatever is the convenient representaion for the experimental data. Assuming that the Fabry-Pérot interferometer behaves in a linear fashion x may be interpreted in terms of the Fabry-Pérot piezo displacement, Fabry-Pérot piezo control voltage difference from the driver voltage or, assuming an accurate calibration is available, optical frequency.

(ii) The corresponding evaluation of the Fabry-Pérot cavity transmission function convolved with a Lorentzian function [140] is now discussed. Consider the normalised Lorentzian function,

$$\mathcal{L}(\zeta) = \frac{\gamma_\psi}{2\pi}\left[\frac{1}{(\gamma_\psi/2)^2 + (\zeta - s)^2}\right], \quad \text{where} \quad \int_{-\infty}^{+\infty} \mathcal{L}(\zeta)\mathrm{d}\zeta = 1. \tag{5.47}$$

where γ_ψ is the input beam linewidth in radians. In this instance the offset s (in radians) has been introduced to allow the output as the cavity is scanned over the laser line to be deduced whereas the result for a Gaussian input assumed that the laser line and cavity were at resonance. The convolution of the instrumental lineshape function and a a "source" possessing a Lorentzian profile $\mathcal{L}(\zeta)$ is

$$\mathcal{F}_\mathcal{L}(x) = \int_{-\infty}^{+\infty} \mathcal{L}(\zeta)\mathcal{A}(x - \zeta)\ \mathrm{d}\zeta. \tag{5.48}$$

Substituting Equation (5.47) in Equation (5.48) gives

$$\begin{aligned}
\mathcal{F}_\mathcal{L}(x) &= \frac{\gamma_\psi}{2\pi}\int_{-\infty}^{\infty} \frac{1}{(\gamma_\psi/2)^2 + (\zeta - s)^2}\Big(1 + 2\sum_{m=1}^{+\infty} R^m \cos\big(2\pi m(x - \zeta)\big)\Big)\ \mathrm{d}\zeta \\
&= \frac{\gamma_\psi}{2\pi}\int_{-\infty}^{\infty} \frac{1}{(\gamma_\psi/2)^2 + (\zeta - s)^2}\ \mathrm{d}\zeta \\
&\quad + \frac{\gamma_\psi}{\pi}\sum_{m=1}^{\infty} R^m \cos(2\pi m x)\int_{-\infty}^{\infty} \frac{1}{(\gamma_\psi/2)^2 + (\zeta - s)^2}\cos(2\pi m\zeta)\ \mathrm{d}\zeta \\
&\quad + \frac{\gamma_\psi}{\pi}\sum_{m=1}^{\infty} R^m \sin(2\pi m x)\int_{-\infty}^{\infty} \frac{1}{(\gamma_\psi/2)^2 + (\zeta - s)^2}\sin(2\pi m\zeta)\ \mathrm{d}\zeta.
\end{aligned} \tag{5.49}$$

The results for the integrals are

$$\int_{-\infty}^{\infty} \frac{\cos(2\pi m\zeta)}{(\gamma_\psi/2)^2 + (\zeta - s)^2}\ \mathrm{d}\zeta = \frac{2\pi\exp(-\pi m\gamma_\psi)}{\gamma_\psi}\cos(2\pi m s), \tag{5.50}$$

and

$$\int_{-\infty}^{\infty} \frac{\sin(2\pi m\zeta)}{(\gamma_\psi/2)^2 + (\zeta - s)^2}\ \mathrm{d}\zeta = \frac{2\pi\exp(-\pi m\gamma_\psi)}{\gamma_\psi}\sin(2\pi m s). \tag{5.51}$$

Hence the the convolution of the Lorenztian "source" profile with the Fourier expansion of the instrumental lineshape function of a Fabry-Pérot interferometer is

$$\mathcal{F}_\mathcal{L}(x) = 1 + 2\sum_{m=1}^{\infty}\big(R\exp(-\pi\gamma_\psi)\big)^m \cos\big(2\pi m(x - s)\big). \tag{5.52}$$

If the cavity and injected signal are at resonance then Equation (5.52) reduces to

$$\mathcal{F}_\mathcal{L}(x) = 1 + 2\sum_{m=1}^{\infty}\big(R\exp(-\gamma_\psi\pi)\big)^m \cos(2\pi m x). \tag{5.53}$$

The combined effect of the cavity and the non-monochromatic injected signal is to reduce the contribution of each term to the transmitted irradiance by a factor $\exp(-\gamma_\psi \pi)^m$.

(iii) Another useful result is for the iodine-stabilised laser as the provider of the input spectrum.

$$\frac{I_t}{I_i} = \sum_{n=0}^{\infty} J_n^2(\beta)\left[1 + 4\sum_{m=1}^{\infty}\left(R\exp\left(-\pi\gamma_\psi\right)\right)^m \cos(2\pi m(\omega - \omega_0 + s))\cos(2\pi mn\Omega)\right]. \tag{5.54}$$

This result is useful for the analysis of the various stabilisation methods discussed in this chapter.

5.4.2 The Spherical Fabry-Pérot Cavity

The results for a spherical mirror Fabry-Pérot interferometer are essentially the same as those for the plane mirror interferometer [134]. Although the finesse is affected by this difference a commensurate change in the effective free spectral range means that the linewidth is unaffected. This is because of the relationship between finesse and free spectral range presented in Equation (5.32).

Consider two equal mirrors (of radius of curvature e and focal length $f = e/2$) set a distance d apart. According to the standard ray treatment this is optically equivalent to a system of thin lenses of focal length f and separation d [8]. For a ray with initial co-ordinates (x_0, y_0) and slopes (x_0', y_0') at the input lens the coordinates on emerging from the nth lens are given by [141]

$$x_n = x_0\cos(n\theta) + \sqrt{\frac{d}{4f-d}}\left(x_0 + 2fx_0'\right)\sin(n\theta), \tag{5.55}$$

where

$$\cos\theta = 1 - \frac{d}{2f}. \tag{5.56}$$

A similar relation holds for y_n. It is assumed that $0 < d/f < 4$. Equation (5.55) describing the co-ordinates for the position of the circulating rays on the mirror surfaces may be re-written as

$$x_n = A\sin(n\theta + \alpha), \tag{5.57}$$

and similarly for y_n

$$y_n = B\sin(n\theta + \beta). \tag{5.58}$$

Clearly A and B represent the maximum excursions of the ray in the x and y directions on its way through the lens sequence. We now consider all the intersection points projected onto an x-y plane. The even numbered points represent

the intersections of the successively reflected ray at the input mirror and the odd numbered points are the intersections at the output mirror. In general these intersection points lie on an ellipse. For the special case $A = B$ and $\alpha = \beta \pm \pi/2$ the intersection points lie a circle.

In this case it is easy to see that the polar angle ϕ_n corresponding to the point (x_n, y_n) is given by $\phi_n = n\theta + \alpha$. The increment on each reflection is thus θ and successive points on one mirror differ in angle by 2θ. This immediately indicates the re-entrant condition. If the mirror separation is such that 2θ is an integral fraction of 2π then a ray returns to its entrance point after so many trips through the system and continues to retrace that path again and again. Thus the simplest closed path condition is

$$2m\theta = 2\pi \tag{5.59}$$

where m is an integer and $(x_0,\ y_0) = (x_m,\ y_m)$. In this case the ray is re-entrant after one circuit around the circle or, in other words, m reflections. More complex re-entrant paths are obtained for the condition $2m\theta = 2\mu\pi$ where μ is also integral, not equal to m, and gives the number of circuits before the ray becomes reentrant.

Therefore, with the aid of Equation (5.59), the various properties of the spherical cavity may be deduced by substituting R^m for R into the results for the plane-mirror Fabry-Pérot interferometer. For example the finesse becomes

$$\mathcal{F} = \frac{\pi R^{m/2}}{1 - R^m} \simeq \frac{\pi}{m(1 - R)} \tag{5.60}$$

for reflectivities close to unity. Since more circuits are required by the reentrant condition an effective free spectral range may be defined as $\frac{c}{2mL}$ for a closed path of $2m$ reflections. The reduced effective FSR, however does not affect what is observed as the cavity pathlength is scanned since, for the re-entry conditions to hold at other fringe orders, the length of the cavity can only be scanned an integral multiple of wavelengths. Thus while the effective free spectral range is reduced by a factor m the finesse experiences a commensurate reduction and the instrumental linewidth is unchanged.

5.5 Using the Fabry-Pérot Cavity to Stabilise Lasers

5.5.1 Side Locking to the Fabry Pérot Cavity Transmission Profile

Locking to the side of the transmission peak is one of the simplest locking methods. A frequency selective optical element such a Fabry-Pérot cavity that produces a voltage signal as a function of frequency is used. As long as the derivative of the voltage output with respect to frequency is nonzero an error signal ϵ may be calculated and used as an input to a feedback loop to lock the

laser to the reference frequency ν_0. Ideally one wishes to lock to the steepest part of the discriminant curve $\nabla(\nu)$ in order to provide the most sensitive control over frequency.

To prevent mixing laser amplitude noise into the frequency discriminator output, two detectors are used. One monitors the frequency-selective transmission of the resonant cavity while the other views a suitably attenuate a portion of the cavity's input beam. An appropriate choice of attenuation will cause both detectors to have the same output when the laser is tuned to the region near the high slope region of the transmission profile. The control loop monitors the difference between the two photo-currents. When the system is properly locked this difference will be equal to zero. The smallest possible linewidth is ultimately determined by the shot noise from the photon detection process as these fluctuations will be converted into frequency noise with a coefficient inversely proportional to the discriminator slope. However in practice the observed value exceeds the theoretical limit due to effects such as; (1) the limitation of the servo bandwidth and hence the useful gain due to finite rise times and delay times of the electronic setup, (2) transient problems associated with time-domain response of the electronics and/or the reference cavity, and (3) amplitude noise leaking into the servo loop. Finally, even if the performance of the electronic servo lock is adequate, the residual FM noise of the reference cavity due to technical noise sources provides a lower practical limit for the system noise performance, especially at lower frequencies [142].

To estimate the shot noise limit of the laser linewidth, we assume the laser frequency is stabilised to the half height of the transmission cavity. It is assumed that a fraction α of the total laser power P is mode matched into the cavity with a power transmission coefficient β. The powers of the broadband and transmission beam are matched. Within an integration time t, $N = P\alpha\beta\eta t/h\nu$ photons will be detected. The shot noise in the difference of the photocounts will be $\sqrt{2N}$. In an ideal control loop, this amplitude noise photocount, which is measured as a photo-current, will be converted to frequency noise by dividing this by slope of the discriminant curve. This relies on the assumption that the discriminant slope is relatively constant over the range of frequency excursions of the locked laser.

If the instrumental discriminant curve $\nabla(\nu)$ is normalised such that

$$\int_{\infty}^{\infty} \nabla(\nu)\, \mathrm{d}\nu = 1 \tag{5.61}$$

then the measured discriminant slope may be written as

$$\frac{P\alpha\beta\eta t}{h\nu}\nabla(\nu) \tag{5.62}$$

and the frequency noise injected is

$$\delta\nu = \frac{1}{\mathrm{d}2\nabla/\mathrm{d}\nu}\sqrt{\frac{h\nu}{P\alpha\beta\eta t}}. \tag{5.63}$$

5.5.2 PDH Locking

The most successful method of locking a laser and cavity is the so-called Pound-Drever-Hall (PDH) method [129]. This method has been used to stabilise the relative frequencies of two lasers to the milliHertz level [130]. A straightforward account of PDH locking is given in [143] where its implementation in a senior laboratory course at Caltech is described.

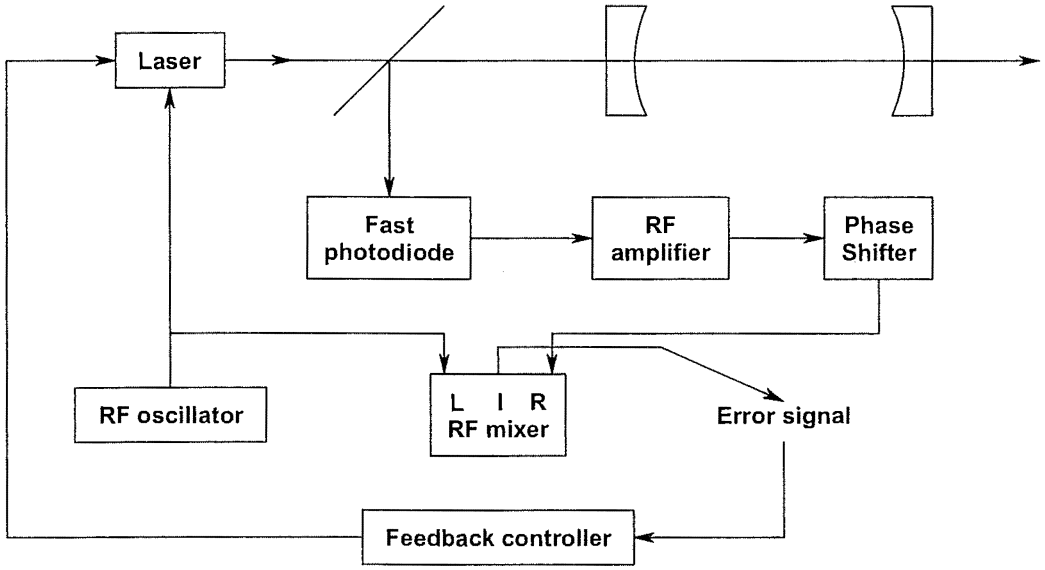

Figure 5.8: Schematic of PDH locking method. Part of the light reflecting off the Fabry-Pérot cavity falls on a fast photodiode, and the high-frequency component of the current is amplified and phase-shifted (using a length of BNC cable) before being mixed with the local oscillator to form an error signal.

The essence of the PDH locking method is encapsulated in Figure reffig:fstab:pdh. The laser light has FM sideband modulation added to the optical carrier. This may be created by either applying an RF modulation to the injection current of a diode laser or using a phase modulator crystal to produce sidebands which are located spectrally well outside the pass band of the resonator to which the laser is to be locked. These FM sidebands are basically totally reflected from the control cavity input mirror and are steered to a fast photodetector and associated preamplifier. The laser carrier frequency approximately matches the cavity resonance frequency and this leads to a buildup of intra-cavity standing wave irradiance at the laser frequency. As in the analogous microwave case [144]—the well known "Pound stabilizer"—the leakage field back toward the source is basically in anti-phase with the input field directly reflected from the coupling mirror. The approximate cancellation of these two fields (in reflection) thus leads to a small net reflection coefficient with a phase shift which is strongly frequency dependent in the vicinity of the cavity resonance. The reflected signal is heterodyned with the local os-

cillator sidebands for subsequent IF (intermediate frequency) amplification. The phase sensitive demodulation against the RF source driving the modulator crystal providing the frequency offset between the carrier and local oscillator sidebands converts the symmetric minimum in the cavity reflection coefficient into the desired antisymmetric frequency discriminator curve. A derivation of the relevant mathematical relationships is given by Bjorkland [145].

Sandford and Antill [131] demonstrated an extension of the PDH scheme which achieved a very narrow linewidth as well as excellent long term stability. Two diode lasers were PDH locked to adjacent axial modes of a high finesse optical cavity. The cavity provides the narrow linewidth while long-term stability is achieved by servoing the reference cavity length on the cavity FSR beat note to a reference quartz oscillator. It should be noted that this is a similar concept to controlling the FSR in a ring-laser. However the active nature of the Canterbury ring-lasers introduces the added complication of mode competition between the longitudinal modes. However this approach is worth further study because it can be used to provide an effective method of frequency control.

5.6 Stabilisation of C-II: Method

Before discussing the C-II stabilisation method [1] in detail in Sections 5.6.2 and 5.6.3, detailing the experiment setup and process respectively, an overview is given in Section 5.6.1 to provide a general introduction to the approach taken in the stabilisation of the C-II optical frequency. Complementary material is presented in Section 5.6.4 outlining the expected performance limitations of such a system.

5.6.1 Strategy

In the case of C-II, frequency compensation of the pressure—or temperature—induced changes of the dimensions of the ring is performed by a piezoelectric actuator pressing on the back of one of the mirrors. The construction of this is described in more detail in Section 2.4.3. In order to remove pressure-induced drift shown in Figure 2.2 it is necessary to stabilize the perimeter P against these variations, using the independent frequency reference provided by the Winters Model 100 iodine stabilised laser.

This is done by comparing the frequency separation of the C-II and Winters laser using the Newport SR-130 Fabry-Pérot cavity and correcting the C-II pathlength so this separation is held as constant as possible to minimise C-II optical frequency drift. A more detailed discussion of the degree of stabilisation required is given in Section 5.8

5.6.2 Experimental Setup

This section details the experimental setup used for the stabilisation of the C-II optical frequency. First of all an in-depth discussion of the two most important items of equipment in the stabilisation process, the Newport SR-130 OSA and the Winters model 100 iodine-stabilised laser, is included to provide the background information necessary to understand the stabilisation method.

The Newport SR-130 Optical Spectrum Analyser

The Newport SR-130 OSA is a spherical-mirror non-confocal cavity. It is non-confocal is because the distance L between the mirrors is not equal to the radius of curvature of the mirrors. The treatment of Section 5.4.2 is appropriate to give an account of the various properties of the OSA. Since the reflectivity of the mirrors varies over the passband of the SR-130 OSA the width of the fringes also varies across the passband.

Finesse	$>$ 10000 over bandpass (40000 at centre)
Free Spectral Range	6 GHz
Cavity Length	2.54 cm
Fringe Width	$<$ 300(600) kHz at centre (edge) of passband
Transmission Power Efficiency	$>$ 10%
Bandpass	580-660 nm
Ext. Scan Rate	up to 1 kHz with $\pm$15 V
Mirror radius of curvature	30 cm

Table 5.2: Specifications of the Newport SR-130 scanning Fabry-Pérot interferometer.

The Newport Model SR-D Controller was used to provide the interface between the OSA cavity and the user LABVIEW^{TM} control program. In normal use there are three major functions performed by the controller; amplification and filtering of the signal received from the photodiode attached to the OSA cavity, generation and processing of the scan signals transmitted to the piezoelectric crystal in the cavity and control of the cavity oven temperature. For the purpose of stabilisation of C-II, a photomultiplier tube was required to detect the low irradiance transmitted signals so the first function was bypassed since it was designed to work with a standard photodiode suitable for use with lasers of 1 μW or greater power. Similarly an external scan signal generated by the LABVIEW^{TM} control program was used to adjust the Fabry-Pérot cavity piezo and scan over the laser resonances. However, in order to achieve high stability, the cavity temperature control loop was left intact. It was found that adjusting the temperature control circuit as described in the user manual [146] provided a useful improvement in performance.

Careful alignment and mode matching of the input beam is required to maximise the throughput of the $\mathrm{TEM}_{0,0,q}$ Fabry-Pérot cavity mode. This step consisted of selecting and placing the appropriate lens for effective mode matching of the input beam into the cavity. The focal length of the lens required to mode match into the Fabry-Pérot cavity is about thirty times the diameter of the transverse laser mode of the incident beam. The front of the cavity is placed 3.0 cm in front of the focal length of the mode-matching lens. It is important to ensure the incident beam is centred and perpendicular to the mode matching lens for best results from the alignment of the cavity. The cavity is supplied with a custom x-y-z translation mount to allow easy adjustment of the cavity. Alignment of the cavity was achieved by making the incident beam and the retro-reflected beam from the alignment mirror near the input mirror on the front of the cavity coincident at all points in the beam path by tilting the cavity and coupling lens. If the incident beam is off-axis, wavefront aberration and loss of coupling efficiency will result. Once the cavity is translated so that the input beam is coupled into the cavity it should be possible to observe the resonance peaks as the Fabry-Pérot cavity length is scanned. This may either be done by eye for a very low powered laser (observing the standard safety rules for lasers) or by observing the photodetector output on an oscilloscope as the cavity length is scanned. Once this is done the alignment may be fine-tuned to maximise the throughput observed on the oscilloscope.

To provide a unambiguous interpretation of the spectra observed as the SR-130 was scanned over the C-II and Winters resonances it was necessary to have an independent calibration of optical frequency spanned in terms of the voltage supplied to the SR-130 piezo driver. This was performed by scanning the cavity over the full range and observing the voltages at which the $\mathrm{TEM}_{0,0}$, $\mathrm{TEM}_{0,1}/\mathrm{TEM}_{1,0}$ and $\mathrm{TEM}_{2,0}/\mathrm{TEM}_{0,2}$ modes were visible. By definition each repetition of a given transverse mode constitutes a frequency excursion of one Fabry-Pérot cavity free spectral range. Further information was obtained by comparing the resonance voltage separations of the transverse modes with the expected frequency separations. Accordingly a calibration of $200 \pm 2\,\mathrm{MHz/V}$ was obtained over the full range of operation. Nonlinearities and hysteresis in the piezo response were within the noise of the linear fit. Over the limited frequency range determined by the span of the iodine transitions the calibration was in agreement with observations made when the iodine-stabilised laser was switched between various absorption lines — a very precisely defined frequency difference.

However in other situations there may not be access to a sufficiently stable laser to allow this type of static calibration and furthermore any drifts in the resonance conditions for the Fabry-Pérot cavity will detrimentally influence the calibration. An alternative method of calibration is to utilise the sidebands created by a frequency modulated laser or the modulated output of an acousto-optic modulator. The frequency separation between the carrier and sidebands is used as a frequency reference. If the modulation is derived from a stable source an accurate

calibration may be obtained [136]. Once again it should be noted that this is a relatively small range and it is therefore dangerous to extrapolate outside of this range.

During development it was noticed that there was significant drift in the resonance frequency of the SR-130 OSA when tracking the Winters laser. It was not uncommon to observe drifts of the order of 200 MHz/hour. Upon further investigation this drift was found to strongly correlate with pressure. Hence a leak was suspected and confirmed by allowing helium to diffuse into the cavity whereby the change in the refractive index due to the presence of the helium changed the resonance conditions for the cavity. After repair, the drift of the Fabry-Pérot cavity was reduced to the order of 0.6 MHz/hour.

Winters Model 100 Iodine-stabilised Laser

The laser cavity is approximately 26 cm long with a single Brewster window laser tube. The mirror sealed to the laser tube has a radius of curvature of 30 cm and a nominal transmission of 0.7%. The modulation required to implement the stabilisation is achieved by mounting a planar mirror with a nominal transmission of 0.4% external to the cavity on a piezoelectric transducer.

The piezoelectric stack consists of two independent sections. The first is used to frequency-modulate the frequency of the laser at a frequency of 1172 Hz with a peak-to-peak frequency excursion of the laser of 6 MHz. The second section is required to sweep the laser wavelength during tuning and control of the cavity length. Sufficient short-term stability is achieved by using an invar cylinder for the main laser cavity spacer. Active temperature stabilisation, combined with the spacers' inherently low coefficient of thermal expansion, provide a high level of short-term stability. The Winters Model 100 laser uses a BIPM-manufactured iodine cell. The cell pressure is maintained at a nominal value of 17.4 Pa by controlling the temperature of the cavity with a thermo-electric heat pump and a copper coldfinger.

Typical output power	$100 - 125\ \mu$W
Minimum output power	$75\ \mu$W
Frequency stability	2.5 parts in 10^{11} (12 kHz)
Allan variance	1s 1×10^{-11}
	10s 3×10^{-12}
	100s 1×10^{-12}
	1000s 3×10^{-13}

Table 5.3: Winters Model 100 iodine-stabilised laser specification

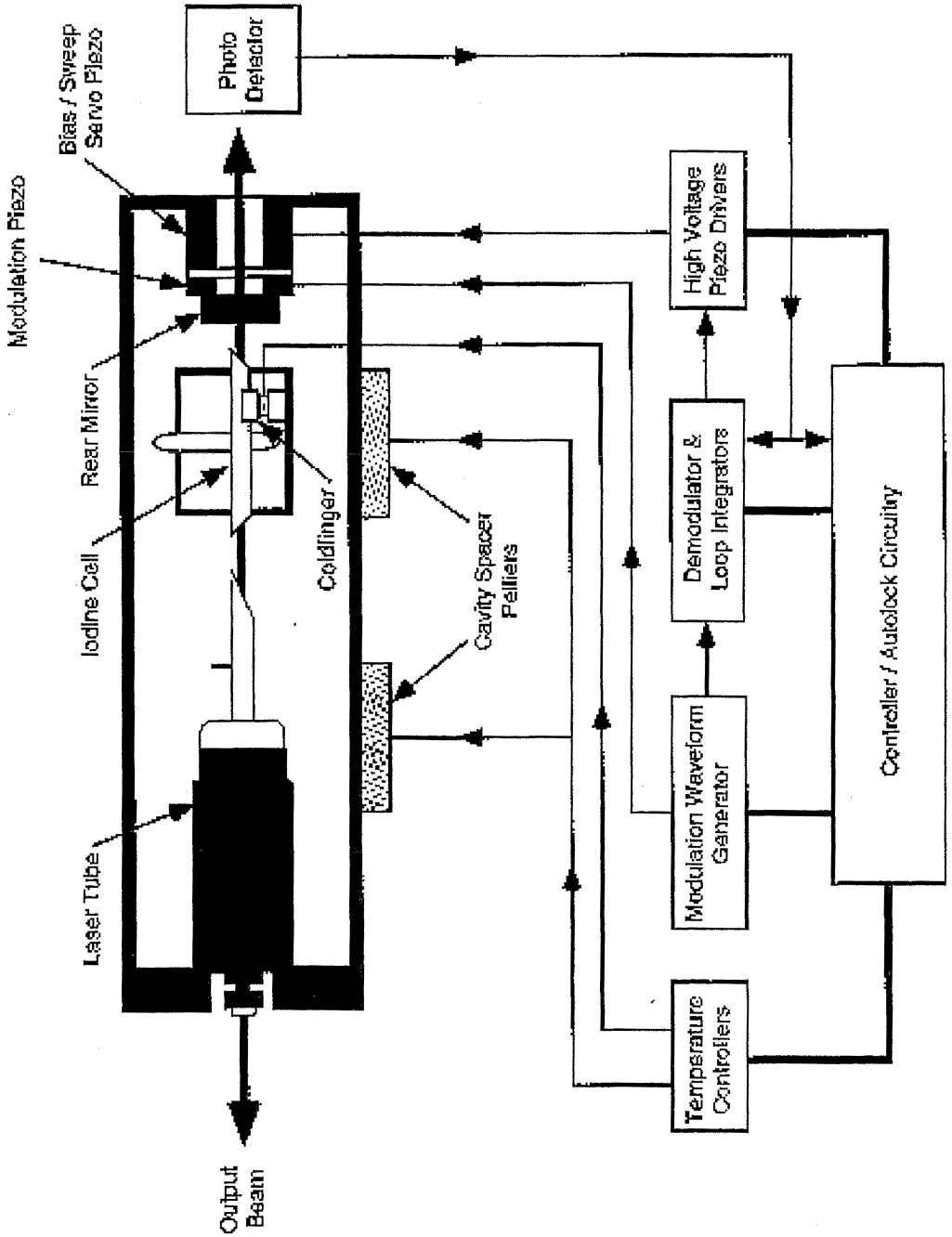

Figure 5.9: Schematic representation of the Winters Model 100 iodine-stabilised laser (reproduced from [5]).

Experimental Setup

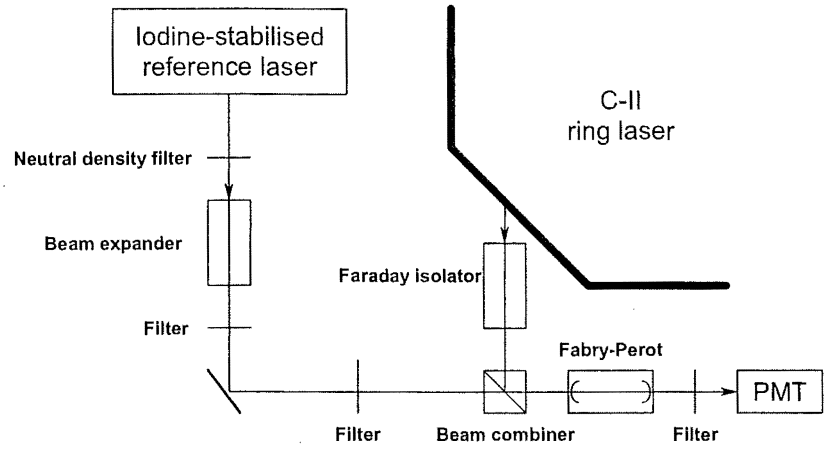

Figure 5.10: Setup for stabilisation of the C-II optical frequency.

The Winters Model 100 iodine-stabilised He:Ne laser provided the reference against which the optical frequency of C-II was compared. Either the d or f iodine laser absorption line was found to provide convenient reference frequencies and were used for this experiment. Upon extended use it was noticed that the iodine-stabilised laser occasionally jumps from one absorption line to another, and that this is sometimes not corrected by the internal circuitry of the iodine-stabilised laser. Therefore it was necessary to monitor the laser to ensure it was performing as required. This was achieved by monitoring the status of a TTL output from the laser control circuitry indicating if the laser is locked to be monitored. If this lock was lost the iodine-stabilised laser was commanded to re-acquire the correct line by applying a voltage to the external sweep to ensure that the laser unlocked from the peak it was stabilised to and re-acquired the correct peak.

It was found that optical isolation of the Winters laser was critical since light retro-reflected from various surfaces in the optical setup caused the laser frequency to jitter]. The description of this effect is similar to the simple descriptions of frequency pulling in the ring laser and may be described by the Adler equation [147]. This injection locking phenomenon may be used to couple the frequencies of two lasers if required. In the case of the Winters laser, the double transit for the retro-reflected beam through a neutral density filter (OD2) was sufficient to provide the necessary isolation. The filter was also necessary to balance the optical powers of the iodine-stabilised laser and C-II so the PMT was not saturated while the resonance of the iodine-stabilised laser transmission peak was being evaluated. The beam from the Winters Model 100 iodine-stabilized He:Ne laser also passed through a beam expander to match the beam diameters of the iodine-stabilised laser and C-II for efficient coupling of both lasers into the Fabry-Pérot cavity. Furthermore an interference spectral filter centred on the He:Ne frequency was

used to ensure that the discharge glow from the reference laser can be neglected. However, since the attenuator did not prevent light from being injected into C-II, a quarter wave plate in combination with a polarising beamsplitter (PBS) cube was initially used to provide optical isolation. This works by allowing the light to pass through the PBS cube, adjusted such that the linearly polarised light exiting the ring laser is directed into the quarter wave plate. After passing through the quarter wave plate the light becomes circularly polarised. Upon reflection from the entry port of the Fabry-Pérot cavity and a second passage through the quarter wave plate the beam is linearly polarised but orthogonal to the incident beam. Therefore the PBS cube directs the reflected beam away from the C-II mirror port. This method may be used to achieve up to 30 dB of isolation. However it was found that this did not provide sufficient isolation because the Sagnac frequency of C-II was observed to be particularly noisy. Therefore a Faraday isolator (Optics for Research IOT-3-633-LP dual Faraday rotation isolator) with isolation > 60 dB and transmission $> 86\%$ was used instead. This proved entirely satisfactory.

Initially the major limitation found in the implementation of this stabilisation method was the resolution of the digital to analogue conversion performed by the data acquisition card. This was because it was not possible to perform a coarse scan and then a fine scan in the Fabry-Pérot interferometer control PZT drive voltages required to properly image the resonance peaks with a given scaling of the DAC range. Therefore it was not possible to scan over the full range with the necessary resolution to properly resolve the transmission spectra. The method used to circumvent this problem is as follows: a multi-turn potentiometer was used to set the voltage supplied to the PZT such that the mirror was positioned at the centre of the desired range of operation. The output (-10 V to +10 V range) from the DAC card passed through a voltage divider to in order to scale the control range to a range -0.5 V–0.5 V about the desired range of operation.

5.6.3 Process

The process of stabilising the optical frequency of the ring laser was as follows. First it is necessary to ensure that the iodine-stabilised laser is operating correctly and locked to an absorption transition. To achieve this the TTL lock status output from the Winters Model 100 is polled using one of the digital inputs of the data acquisition card. If the laser is in lock the stabilisation loop continues otherwise the control program forces the laser to re-acquire the absorption line. This causes the laser to sweep through the various absorption lines and lock to the requested line. Polling of the TTL signal is continued until locking is indicated. Subsequently the piezo of the Newport SR-130 is scanned such that the resonance of the iodine-stabilised laser is detected. The scan range is a relatively small window encompassing the iodine-stabilised laser line of 6 MHz width. The centre of this window is selected at the start of a run based on the position of the iodine-stabilised laser resonance in a full scan of the SR-130 piezo. The centre of

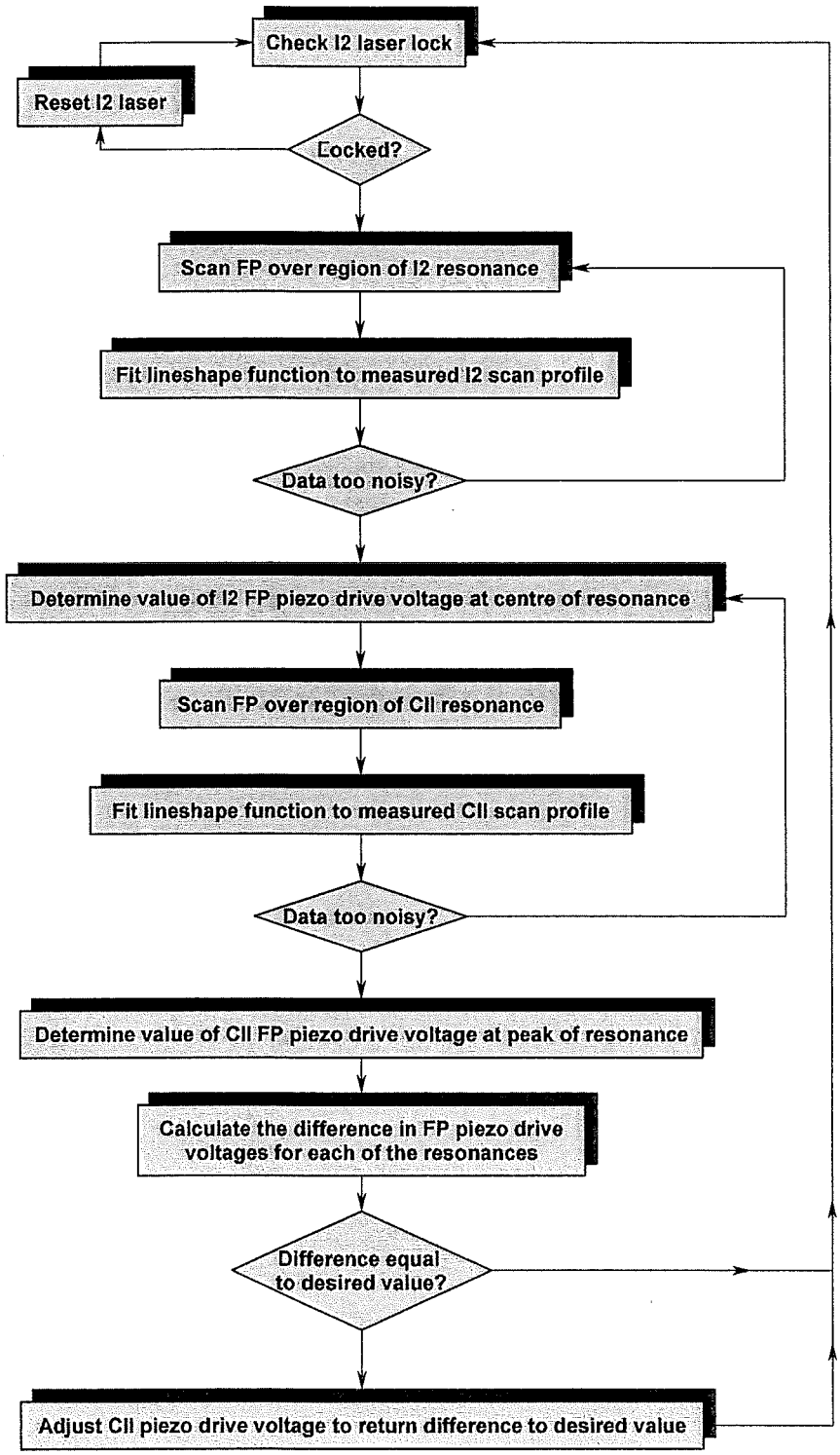

Figure 5.11: Flow diagram for stabilisation process indicating the actions performed by the control software.

the iodine-stabilised laser line in the previous scan is used to define an *a priori* estimate of the window centre for the current scan. Once the scan is complete a lineshape function is fitted to the iodine-stabilised profile to determine the centre frequency. In this application a second order polynomial was fitted and proved sufficient to demonstrate the principle.

A similar process is carried out for the C-II resonance. Once again a quadratic is fitted to the C-II line.

Since mirror transmission in the Fabry-Pérot is not greatly in excess of absorption losses, the maximum throughput is only $\sim 10\%$ [136], so that the photomultiplier (PMT) detector receives a beam power of only a few hundred femtowatt from each source. Therefore, in order to obtain an adequate signal-to-noise ratio (SNR), it was necessary to acquire some 2000 samples of the PMT output for a given Fabry-Pérot cavity pathlength setting. Hence it was necessary to take only a few data points across each transmission profile in order to estimate of the frequency separation in a suitably short time. In the case of C-II these data points were spaced 30 kHz apart.

Typically the d or f iodine laser absorption line was chosen. C-II was operated such that the separation between the resonances of the iodine-stabilised and CII is of the order of a few tens of MHz and the lines are readily identified in the presence of Fabry-Pérot cavity resonance frequency drift of approximately 0.6 MHz/hour. Since the two Fabry-Pérot cavity pathlength-control PZT drive voltages required for resonance are known the position of the C-II peak relative to the stabilised iodine-stabilised laser peak is simply found by subtracting the two values. If the difference is equal to the desired value no correction to the C-II perimeter is performed. If there is a difference the C-II perimeter is adjusted in order to bring the frequency separation back to the desired value. The software operated in a loop, repeating this process over and over. Since noisy scans of either the C-II laser line or the frequency-modulated reference line are eliminated and a majority vote is made from 5 such determinations of the line separation one acquisition cycle then takes approximately 2 minutes.

5.6.4 Performance Limitations

In this section a thorough investigation of the performance limitations of this method of stabilisation is made. There are several areas that should be investigated to ensure that it is possible to achieve a level of performance and low enough noise level from each of the components to ensure that the stabilisation process is possible.

Noise Limits from Photodetection Process

The first point to be discussed is the influence that the noise introduced by the photo-detection process has on the stabilisation process. The design and characteristics of the Hamamatsu R3896 photomultiplier tube used for optical detection in the stabilisation scheme were discussed in Section 2.4.1. Estimates of the detection limitations imposed by the anode dark current and photon shot noise based on the specifications given in Section 2.4.1 for the stabilisation scheme are presented here.

The detection limit imposed by the dark current from the photomultiplier tube may be deduced from Equation (2.6). Substitution of the relevant values gives the minimum optical power necessary to produce a required signal-to-noise ratio (SNR) as 15·SNR fW. The dark current with an anode-cathode voltage difference of 1000 V is the only value given in the specifications therefore this is an indicative value calculated using the appropriate value for the gain. However it is clear that an adequate SNR ratio will be obtained with the optical power exiting the Fabry-Pérot interferometer at the level of few hundred femtowatts.

It is also important that the shot noise from the photo-detection process is not such that an adequate estimate of the transmission profile in a suitably short time is impossible. From equation (2.7) the integration time required to produce a given SNR may be deduced. This assumes all photo-electrons emitted at the cathode are collected at the anode and counted as pulses by the electronics that follow the PMT in the detection chain. An incident power of 100 fW is assumed in order to obtain an upper bound on the required integration time. This leads to a minimum integration time of $t = 22 \cdot \text{SNR}^2\ \mu\text{s}$ or a few hundred microseconds to achieve an adequate signal-to-noise ratio. The shot noise dependence on optical power (P) goes as $1/P$ so there is a strong incentive to operate the laser at the highest possible power as well as to align and mode match the cavity as well as can be done to maximise the Fabry-Pérot interferometer transmission. Furthermore note that it will take an integration time of approximately 1 ms for the shot noise contribution to fall below that of the dark current. Therefore it is the shot noise that presents the major detection limit inherent in the photo-detection process for measurement times of the order of those used in the stabilisation of C-II[3].

Effect of Changing the Ringlaser Geometry

In the context of the discussion of Chapter 3 it was found that cross-pushing was minimised, and in fact is predicted to disappear, when the longitudinal mode of the laser is at the peak of the gain-frequency curve. If this point is chosen in order to minimise drift in the gyroscope beat frequency due to cross-pushing as the

[3]See Section 5.9.2 for more information relating to this remark.

relative intensities drift then it is expected that backscatter induced frequency drifts will become important. In this Section it is noted that the change in geometry of the cavity that results from the single-mirror correction that is used to stabilise the pathlength is detrimental to the stability of the gyroscope beat frequency. This effect reduces the benefits of stabilising the pathlength. It is also worth noting that any stabilisation will reduce the effects that occur with the changes in any aperture dimensions that have been mooted as a potential cause of changes in the relative intensities [4]. This, in turn, will reduce the beat frequency variation due to cross-pushing.

It is clear that stabilisation of the optical frequency should yield some improvement in the Sagnac frequency stability. However it is necessary to consider distortion of the ring geometry caused by the moving of a single mirror and the resultant changes in the backscatter properties of the ringlaser to gain an indication of how effective such an approach should be. In light of this complication it is shown that a given improvement in the stability of the optical frequency does not guarantee a commensurate improvement in the Sagnac stability in a large number of cases. This is because the inter-mirror separations change the frequency pulling and pushing as described in Section 2.2.1 and hence this will vary with pressure despite the perimeter being held constant. The effects of the change in geometry of the beam path is further complicated by the movement of the beam spots due to the mirror radii of curvature.

As discussed in Section 2.2.1 the separations of the scatterers (as a net effect over all scatterers) critically affects the pushing and pulling of the Sagnac frequency in ring laser gyroscopes. This dependence of pulling on mirror separation was demonstrated by earlier workers [148]. The backscattering phase term $\exp\left(\pm\frac{2i\omega z_n}{c}\right)$ [1,14,15] indicates that the minimum pulling period ΔX_n for a given scatterer separation X_n is $\Delta X_n = \lambda/2$. To demonstrate further, consider the simple case where the change in perimeter is shared equally between the four sides. The contribution of backscatter effects from adjacent mirrors (for the beam that travels the shortest path between the mirrors) gives a periodicity in the pulling due to perimeter variation of $\Delta L = 2\lambda$. Similarly, scattering from diagonally opposed mirrors will contribute a cycle of period $\Delta L = \lambda$ and scattering for beams that take the long path between adjacent mirrors will contribute a cycle with a period given by a perimeter variation of $\Delta L = 2\lambda/3$. If the changes in perimeter are not distributed equally between the mirror separations, as is the case with C-II stabilisation, a more complicated description is required. Note, however, that all of the described pulling periods are of the order of a wavelength.

In order to gain a fuller understanding it is necessary to include the variation of wavelength with perimeter in the analysis. Assuming the laser operates within a single longitudinal mode, wavelength and perimeter are proportional. This assumption is valid for the relatively small excursions in the C-II perimeter due to variation in atmospheric pressure (see Section 2.4.3). Begin by considering a small

variation in the term $\phi = 2kz$ which governs the backscatter properties of the ring laser. If z changes by a small amount δz there is a change $\delta k = k - k_0 = -k_0 \delta L / L_0$ in the wavenumber k. Here δL is the small variation in perimeter related to the nominal value L_0 by $\delta L = L - L_0$. Hence $\delta\phi = 2k\delta z + 2z\delta k$ is given by

$$\delta\phi = 2k_0 \left(\delta z - z \frac{\delta L}{L_0} \right), \tag{5.64}$$

since $\delta z \delta k \ll k_0 \delta z$. Therefore if the perimeter change δL is divided evenly between the four mirror separation increments δz_n, $\delta\phi$ vanishes and there is no change in the net backscatter phase. In other words all values of $\delta z_n / z_n$ must be the same. This is guaranteed if the shape of the ring is not altered. However this condition is not necessary for all $\delta z_n / z_n$ to be the same. For example, consider a square diagonal cavity like C-II at the time of optical frequency stabilisation in which a flat mirror M_1 is pushed diagonally by a distance d. (Note that the mirrors are labelled in an anti-clockwise fashion from M_1). The distance moved by the beam spots on the adjacent mirrors M_2 and M_4 is [149]

$$\varepsilon = \frac{d}{[2(1 - \sqrt{2}L/4e)]}, \tag{5.65}$$

where e is the radius of curvature of the adjacent mirrors. By symmetry, the spot at M_3 does not move. This gives the mirror separation changes δz_M the values

$$\delta z_{12} = \delta z_{14} = \frac{\varepsilon - d}{\sqrt{2}}, \quad \delta z_{23} = \delta z_{43} = -\frac{\varepsilon}{\sqrt{2}}. \tag{5.66}$$

Hence if $R \to \infty$, $\varepsilon \to \delta/2$ and all mirror separations change by the same amount ($\delta z_{12} = \delta z_{23}$) despite the change in shape. It should be noted that this configuration is on the edge of the stability diagram and is therefore not particularly viable. The correct conclusion to draw is that with such a mirror geometry increasing the mirror curvature will reduce the effects of variations in $\delta\phi$.

It is worth taking the time to investigate the implications of Equation (5.66) with the substitution of the relevant C-II parameters. Consider the typical perimeter change (over the observed atmospheric pressure range) $\delta L = 92$ nm as described in Section 2.4.3. If uniformly distributed, this changes each mirror separation δz_M by 23 nm. The resulting perimeter change can be cancelled by moving the PZT-driven mirror M_1 inwards by 65 nm. From Equation (5.66) such a motion on its own induces changes in the mirror laser spot separations of approximately $\delta z_{12} = -15.5$ nm and $\delta z_{32} = -30$ nm, with an average value of -23 nm. When however this is done to compensate for the pressure-induced change in perimeter, the net shifts in spot separation (averaging of course to zero) are individually ± 14 nm, and so are reduced by 40% of their initial average. Under such PZT-induced motion, the magnitudes of the various ΔX_n (Equation 5.66) differ from the value, $\delta/\sqrt{2}$, that they would have had were they to scale with the perimeter (and so give a vanishing $\delta\phi$ in Equation 5.66) by about 40% in C-II.

5.7 Stabilisation of CII: Results

Figure 5.12 shows the observed lineshapes for the Winters Model 100 laser and C-II. These are similar to the expected profiles. It was common to observe an asymmetry in the Winters profile where the measured transmission profile showed one peak of higher amplitude than the other. This was a result of the detection process where only a small number of Fabry-Pérot pathlengths were used to determine the full transmission profile. This approach was necessary because of the integration time required to achieve an adequate SNR.

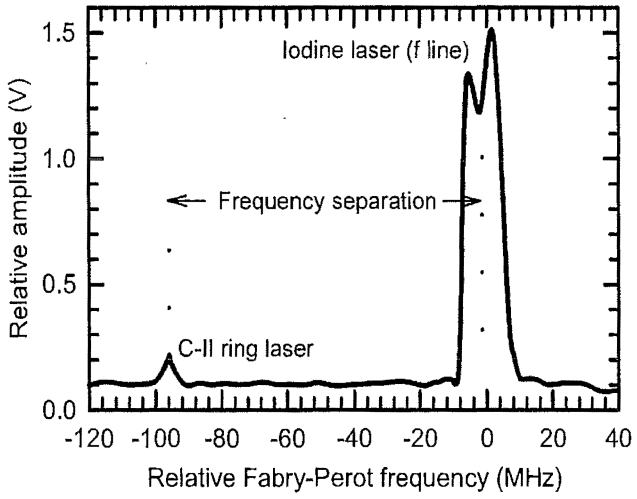

Figure 5.12: Separation of the Iodine-stabilised laser and C-II in the Fabry-Pérot interferometer transmission profile.

Note the spiky nature of the time-series of the iodine-stabilised laser-C-II separations shown in Figure 5.13(c). There are two possible explanations for this observation. The first is that the frequency difference estimation process has a noise level of the magnitude observed in Figure 5.13. The second is that the control loop over-corrects.

To gain an estimate of the noise contribution the probability distributions of the iodine-stabilised laser and C-II frequencies are required. First of all it is necessary to de-drift the time-series of each laser's set of frequency observations in order to remove the effects of the drift of the Fabry-Pérot cavity. This was achieved by making a simple second-order polynomial fit to each data set, averaging the

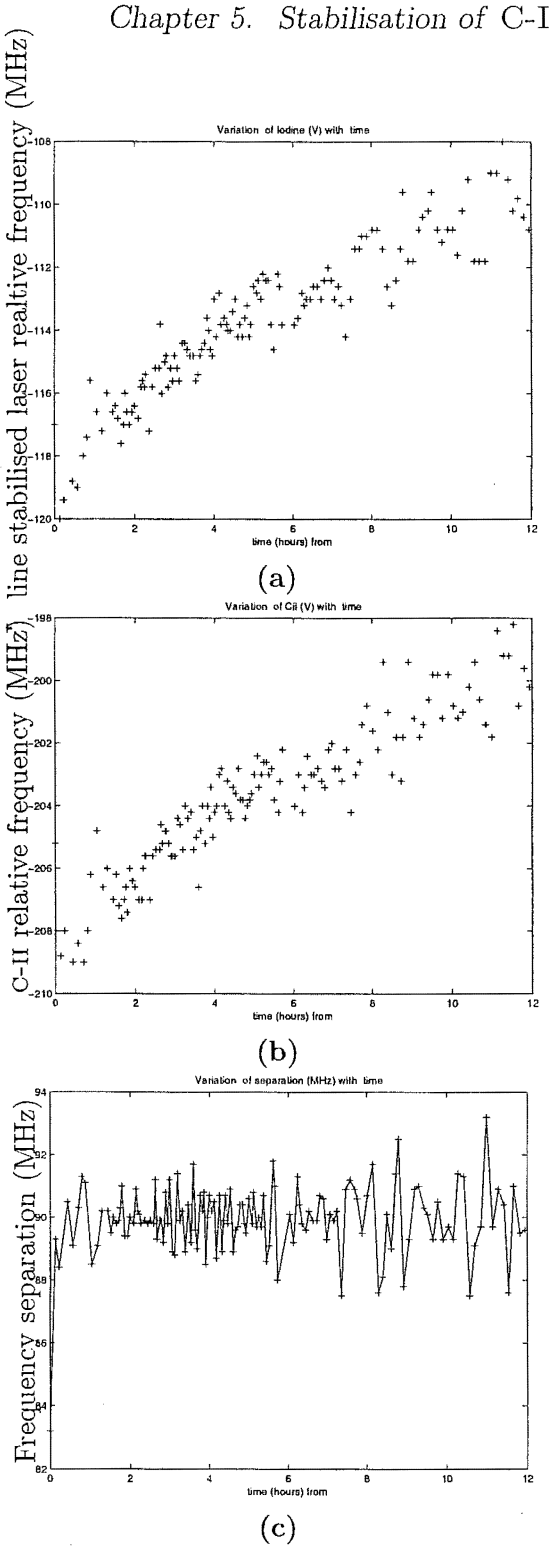

Figure 5.13: Typical time series during stabilisation of (a) Winters Model 100 optical frequency measured by the Newport SR-130 OSA (the drift is due to the OSA), (b) C-II, and (c) the iodine-stabilised laser-C-II optical frequency separation. This data set begins at 10:00:11.52 on February 1, 1998.

coefficients of t^2 and t respectively and then refitting the data with these new coefficients by adjusting the coefficient for t^0 such that the residuals were minimised. This accounts for the fact that we are correcting both time-series for the same drift.

Data	Estimate		95% confidence interval		99% confidence interval	
	μ (MHz)	σ (MHz)	μ (MHz)	σ (MHz)	μ (MHz)	σ (MHz)
C-II	0	0.873	0.148	0.106	0.198	0.140
I_2	0	0.813	0.138	0.098	0.182	0.130
SEP	89.980	0.969	0.164	0.117	0.217	0.155

Table 5.4: Mean and standard deviation with respective confidence intervals of stabilisation data for day 32, 1998. Probability distributions are shown in Figure 5.14.

If the estimates of the iodine-stabilised laser and C-II optical frequencies are independent then the covariance $\mu_{11} = \langle xy \rangle$ must vanish. Consideration of the variance of the separation leads to the result that the sum-of-squares of the standard deviations of the measurements of the iodine-stabilised laser and C-II optical frequencies should equal the variance of the separation if this is to hold[4].

From the data presented in Table 5.4 it may be deduced that (within the confidence limits of the data) the measurements are uncorrelated. There may, of course, be small correlations that may be discerned from a larger data set that yields smaller confidence intervals. However any such correlations are insignificant when compared with the noise introduced from the detection process itself.

Two interesting results may be inferred from Table 5.5. First of all, the least squares fitting shows that any residual drift in the C-II optical frequency due to variation in atmospheric pressure is below the noise level of other effects. Thus the pressure dependence (Figure 2.2) has been reduced to a level less than that of other noise sources. The most important of these residual effects is the noise introduced in the estimation of the frequency of each of the lasers. This indicates that optical frequency stabilisation has achieved its primary goal of eliminating the effects of atmospheric-pressure induced drift of the optical frequency. Furthermore note that the standard deviations of the separations analysed in Table 5.5 are about half that of the data used to calculate the results presented in Table 5.4.

[4]Consider the probability density $p(x, y)$. To simplify calculation the means of the stationary processes may all be shifted to zero without loss of generality. Then

$$\begin{aligned}\mu_2(x-y) &= \langle (x-y)^2 \rangle \\ &= \langle x^2 + y^2 - 2xy \rangle \\ &= \mu_{20} + \mu_{02} - 2\mu_{11} \\ &= \sigma_x^2 + \sigma_y^2 - 2\mu_{11}.\end{aligned}$$

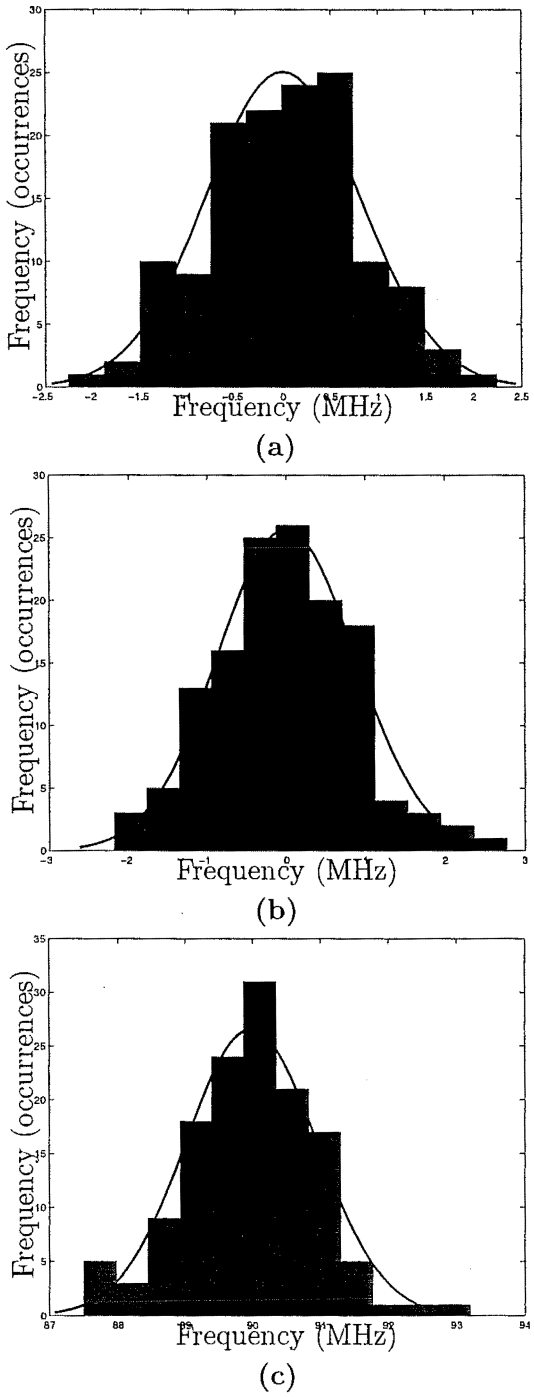

Figure 5.14: Probability distributions of dedrifted frequency estimations for (a) Winters Model 100 iodine-stabilised laser, (b) C-II, and (c) raw iodine-stabilised laser-C-II frequency separation

Time (fractional day)	$\Delta\nu_{sep}/P$ (kHz/hPa)	σ_{sep} (MHz)
7.4116	-5.8 ± 10.4	0.32
7.6906	0.6 ± 23.0	0.40
7.9609	(0.00 ± 0.02)	0.40
8.2371	-20 ± 12	0.36
8.4008	-14 ± 40	0.34
8.9051	60 ± 20	0.34

Table 5.5: Characterisation of the Winters laser-C-II separation during optical frequency stabilisation of C-II. $\Delta\nu_{sep}/P$ is the least squares fit of the optical frequency separation against pressure and σ_{sep} is the standard deviation of th frequency separations for each data set. The data sets originate from January 1998 where each data set consisted of 6 hours of data starting at the indicated time in fractional days (UT). Note that stabilisation was continuous and this division is simply a useful approach for data storage and analysis.

This value was found to vary over time as experimental conditions changed. The main contributors to this variation were drifts in the optical power of either of the lasers and mechanical drift of the Fabry-Pérot interferometer mount causing the transmission of the cavity to drift away from the optimum value. These changes lead to variations in the amount of noise in the frequency separation calculated from the fitting process.

5.8 Modelling Noise Input of Stabilisation Scheme

It is always useful to have a model of any stabilisation scheme in order to determine if the observations conform to expectations and to allow prediction of the possible effects of any alterations. For example one of the basic requirements in the stabilisation of C-II is that any noise injected by the stabilisation scheme does not degrade the stability of the laser on any timescale of interest, regardless of any improvements that may have been made on other timescales. In the case of C-II we are primarily concerned with noise injected on timescales of the order of several thousand seconds and less where the white frequency noise due to spontaneous emission dominates.

5.8.1 The Model

An appropriate model for the stabilisation scheme may be deduced by consideration of Figure 5.15. Note that on timescales less than ~ 600 s the Allan variance plot of the PZT command voltage indicates that the spectral type of the PZT command voltage time-series is predominantly white. This implies that a simple model of the stabilisation scheme consists of a series of zero mean

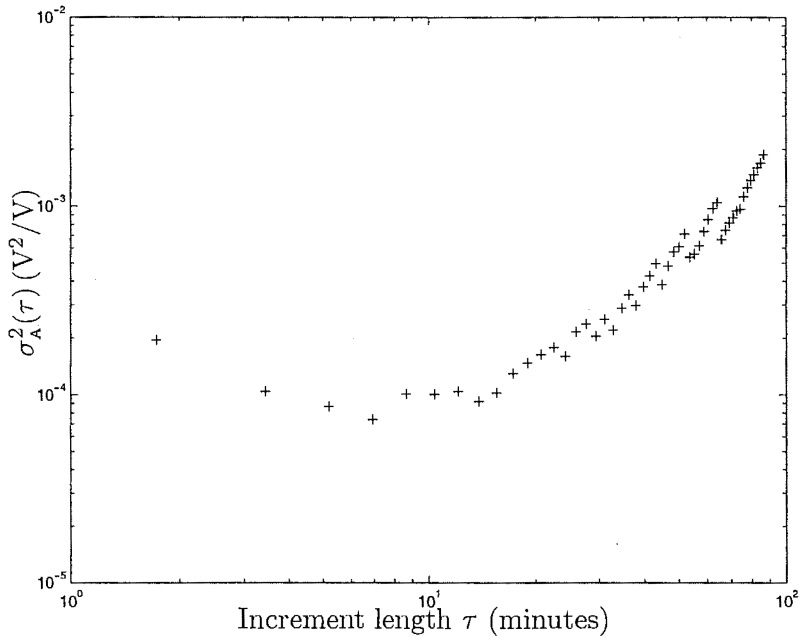

Figure 5.15: Allan variance of PZT command voltage (dedrifted).

Gaussian distributed values representing the PZT being stepped through various control voltages. In practice this means that the piezo is set to the first value in the Gaussian series and held for a time equal to the loop time T_l, before being commanded to the next value in the series for a time T_l. This model is only justified on timescales less than $\sim 600\,\mathrm{s}$. For longer times drift noise becomes significant. However it is the effect of the stabilisation on the timescales where the stepped Gaussian model is valid and C-II is at the quantum limit that we are interested in. Thus there is no need to explicitly model the drift noise.

5.8.2 Limits on Noise Due to Stabilisation Scheme Deduced from the Model

This model can be thought of as a combination of a discrete sequence of N zero-mean Gaussian distributed delta-correlated values $\bar{x}(t)$ and a sequence of steps alternating between the values $+1$ and -1,[5]

$$\bar{x}(t_i) = \left\{\bar{x}(t=0), \bar{x}(t=T_l), \bar{x}(t=2T_l), \ldots, \bar{x}(t=NT_l)\right\}, \tag{5.67}$$

$$\text{and} \quad \bar{y}(t_i) = \left\{1, -1, 1, -1, \ldots\right\}. \tag{5.68}$$

The symmetry of the Gaussian distribution ensures that the step function has no impact on the statistics of the resultant sequence representing PZT control

[5]The barred notation $\bar{x}(t)$ is used to indicate a discrete sequence while the continuous representation of the signal is denoted as $x(t)$.

voltages or mirror displacements. One quantity of interest is the autocorrelation function of the modelled PZT control voltage signal. Since the Gaussian sequence is delta-correlated no correlations between different values of PZT control voltage exist. Therefore it is only necessary to consider values of the delay τ where it is possible that $x(t)$ is still at the same value as it was at the reference time $t = t_0$ of the autocorrelation function. In other words,

$$\Gamma_y(\tau) = \begin{cases} 1 & 0 \leq \tau - t_0 < T_l, \\ 0 & \text{otherwise.} \end{cases} \tag{5.69}$$

At $\tau = 0$ the autocorrelation function is determined by the autocorrelation of the Gaussian noise given by

$$\begin{aligned} \Gamma(0) &= \langle x(t)^2 \rangle \\ &= \int x^2 \frac{1}{\sqrt{2\pi}\sigma_s} \exp\left(-\frac{x^2}{2\sigma_s^2}\right) \\ &= \sigma_s^2. \end{aligned} \tag{5.70}$$

Therefore the autocorrelation of the PZT control voltage is simply

$$\Gamma(0) = \sigma_s^2. \tag{5.71}$$

For non-zero delays τ the absolute value of the autocorrelation is always less than or equal to $\Gamma(0)$[6]. In the case of the steps the joint probability that the value will be within the same part of the duty cycle at times t_1 and t_2 is

$$p(y_2, t_2; y_1, t_1) = 1 - \frac{|t_2 - t_1|}{T_l} \tag{5.72}$$

where T is the period. Taking into account the influence of the delta-correlated Gaussian noise we have

$$p(y_2, t_2; y_1, t_1) = \begin{cases} 1 - \frac{|t_2 - t_1|}{T_l} & 0 \leq t_2 - t_1 < T_l, \\ 0 & \text{otherwise.} \end{cases} \tag{5.73}$$

thus the autocorrelation is

$$\begin{aligned} \Gamma(\tau) &= \sigma_s^2 \langle y(t) y(t+\tau) \rangle \\ &= \sigma_s^2 \int y_1 y_2 p(y_2, t_2; y_1, t_1)\, \mathrm{d}y_1\, \mathrm{d}y_2 \\ &= \sigma_s^2 \left(1 - \frac{|\tau|}{T_l}\right), \end{aligned} \tag{5.74}$$

[6]This property follows from the Schwarz inequality:

$$|\Gamma(\tau)|^2 = |\langle z*(t) z(t+\tau) \rangle|^2 \leq \langle z*(t) z(t) \rangle \langle z*(t+\tau) z(t+\tau) \rangle = \Gamma^2(0).$$

which implies that $|\Gamma(\tau)|$ can never exceed its initial value $\Gamma(0)$, although it can fall below $\Gamma(0)$ and return to $\Gamma(0)$.

where $\tau = t_2 - t_1$.

The Wiener-Khintchine theorem [31] may be used to calculate the power-spectral-density. Since autocorrelation functions are always even functions of τ, it follows that the auto-spectrum $G_{xx}(f)$ is given by the real part of the Fourier transform-autocorrelation pair

$$\begin{aligned} G_{xx}(f) &= 2\int_{-\infty}^{+\infty} \Gamma(\tau)\cos(2\pi f\tau)\ \mathrm{d}\tau \\ &= 4\int_{0}^{\infty} \Gamma(\tau)\cos(2\pi f\tau)\ \mathrm{d}\tau. \end{aligned} \tag{5.75}$$

Thus the power spectral density is, on a $\mathrm{Hz}^2/\mathrm{Hz}$ basis,

$$G_{xx}(f) = \sigma_s^2\left(\frac{1-\cos(2\pi f T_l)}{\pi^2 f^2 T_l}\right). \tag{5.76}$$

The point of main concern is whether or not the noise introduced by the stabilisation exceeds the influence of the white frequency noise from spontaneous emission. This is because once noise of spectral type $1/f^{\alpha}$ dominates, the resolution of the ringlaser gyroscope deteriorates. In terms of power spectra, we require that the power within a frequency band in the stabilisation frequency noise input be less than the variance, $\sigma_w(t)^2$, of fluctuations of the spontaneous emission component.

$$\sigma_w(t)^2 \geq \sigma_s^2\left(\frac{1-\cos(2\pi f T_l)}{\pi^2 f^2 T_l}\right), \tag{5.77}$$

where it is understood that the power is to be evaluated within a small bandwidth around the nominal frequency such that the amplitude of the stabilisation PSD does not change significantly. Consider the upper envelope of $G_{xx}(f)$,

$$\frac{2\sigma_s^2}{\pi^2 f^2 T_l},$$

that defines the maximum power in the stabilisation fluctuation spectrum over any localised frequency range. Then the requirement stated in Equation (5.77) becomes

$$\begin{aligned} \sigma_w(t)^2 &\geq \frac{2\sigma_s^2}{\pi^2 f^2 T_l} \\ \therefore \sigma_s^2 &\leq \frac{\sigma_w(t)^2\pi^2 f^2 T_l}{2} \\ \therefore \sigma_s &\leq \frac{\sigma_w(t)\pi f\sqrt{T_l}}{\sqrt{2}}. \end{aligned} \tag{5.78}$$

It is necessary that Equation (5.78) be true on all relevant timescales as determined by the stability characteristics of the laser.

A sinusoidal oscillator with white noise produces a Lorentzian spectral line. The full linewidth at half maximum is related to the variance by [3]

$$(\delta f)_{FWHM} = 4\pi[\sigma_w(t)]^2_{t=1}. \tag{5.79}$$

The linewidth is written in terms of the cavity quality factor Q and the power injected per mode P as [14]

$$\delta f_{FWHM} = \frac{2\pi h\nu^3}{Q^2 P}, \tag{5.80}$$

where h and ν are Planck's constant and the optical frequency respectively. Hence the condition on the standard deviation of the Gaussian sequence representing the stabilisation control signal to avoid degrading the ring-laser performance becomes

$$\sigma_s \leq \sqrt{\frac{h\nu^3}{Q^2 P t^3}}\frac{\pi\sqrt{T_l}}{2}, \tag{5.81}$$

where t is the integration time of the measurement. Therefore as the measurement bandwidth decreases (or integration time increases) the constraint on the fluctuations of the stabilisation signal become tighter. This is consistent with the Allan variance representation of the white noise due to frequency fluctuations from spontaneous emission. As the measurement time τ is increased the white frequency noise contribution from spontaneous emission decreases, leading to the requirement that there also be a commensurate reduction in the noise introduced by the stabilisation scheme on that timescale. Consequently for a given set of laser parameters the only way to extend the observation time that does not induce degradation of the laser output is to reduce the loop time.

The passive cavity quality factor Q is given by [72, Appendix G],

$$Q = \frac{2\pi L}{\lambda\gamma}, \tag{5.82}$$

where γ is the total loss per pass of the interferometer. The limit on the maximum introduced noise then becomes

$$\sigma_s(t) \leq \frac{\gamma\lambda}{4L}\sqrt{\frac{h\nu}{Wt^3}}\sqrt{T_l}\ \text{Hz}. \tag{5.83}$$

The result of Equation (5.83) places an upper bound on the Sagnac frequency fluctuations that the stabilisation scheme should introduce. Using the nominal Sagnac frequency-perimeter calibration for the typical operating region described in Section 3.1 of 1.8 Hz/μm we find that the fluctuations (in μm) of the perimeter must obey

$$\sigma_s(t) \leq \frac{\gamma\lambda}{7.2L}\sqrt{\frac{h\nu}{W}}\frac{\sqrt{T_l}}{t}\ \mu\text{m}. \tag{5.84}$$

Since $Q \sim 6 \times 10^{11}$ and $W \sim 5.6\,\mathrm{nW}$ [1] a linewidth of $\delta f_{\mathrm{FWHM}} = 220\,\mu\mathrm{Hz}$ is implied. This is in approximate agreement with observed values of $172\,\mu\mathrm{Hz}$ [58][7]. Substitution of these values, and using a loop delay of 120 s into Equation (5.83), gives an indicative range of maximum frequency fluctuations of $\sigma_s \leq 750/\sqrt{t^3}\,\mu\mathrm{Hz}$ for a given integration time.

Now consider the Allan variance plot of piezo command voltages shown in Figure 5.15. Although the loop time is not short enough to provide a decisive estimate of the amount of noise introduced, an approximate estimate made at an averaging time of 60 s implies an introduced fluctuation of $1.7 \times 10^{-6}\,\mu\mathrm{m}^2/\mathrm{Hz}$. This may be compared with a maximum value from the model of $5.3 \times 10^{-6}\,\mu\mathrm{m}^2/\mathrm{Hz}$. This value may be inferred from the calibration of the piezo displacement. Since they are of the same order of magnitude and the white noise level fluctuates with power it may be concluded that the noise injected by the stabilisation method is close to the maximum permissible value that will not severely degrade performance.

The above results have implications for any type of stabilisation that may be implemented. From Equation (5.83) it is clear that any increase in the stabilisation loop frequency bandwidth (decrease in T_l) leads to a tighter constraint on the noise that can be introduced without degrading the performance of the ring-laser.

It is also apparent that improving the quality factor by reducing scattering and increasing the perimeter, which both enhance sensitivity to Earth rotation makes the task of stabilisation more difficult. The PZT noise standard deviation σ_s scales as with the perimeter L as $1/L$ for a given loss while, on the other hand, the allowable noise deviation σ_s is directly proportaional to the total loss per pass γ which is heavily dependent on the mirror scattering losses.

5.9 Fine Tuning of Employed Method

5.9.1 Improved Transmission Profile Fitting

One of the most obvious areas where improvements can be made is in the fitting of the transmission profiles of the iodine-stabilised laser and C-II. This is most apparent in the case of the iodine-stabilised laser. The quadratic fit used generally provided a reasonable estimate of the centre frequency of the transmission profile however it was possible for the estimation to be inaccurate due to the influence of one of the "horns" of the transmission profile, particularly if the asymmetry described in Section 5.7 was present. Therefore a more appropriate test function such as the series expansion of Equation (5.14)) would no doubt lead to improved results. However, since fitting to this series would prove to be computationally

[7]The dependence on optical power means that in practice there is variation of this magnitude from run to run depending on the precise operating conditions.

intensive it may be more appropriate to fit the observed transmission profile to a function such as [150]

$$G_{xx}(\nu) = \begin{cases} \frac{2}{\Delta\nu_m}\sqrt{1-\frac{4(\nu-\nu_0)^2}{\Delta\nu_m^2}}, & \text{if} |f-f_0| \leq \frac{\Delta\nu_m}{2}, \\ 0 & \text{otherwise.} \end{cases} \tag{5.85}$$

Since the linewidth of C-II is much smaller than that of the SR-130 the scan of this transmission profile essentially maps out the transmission profile of the Fabry-Pérot interferometer with C-II acting as delta-function probe. Therefore it would be more appropriate to fit the Airy function (5.24). However since both functions possess mirror symmetry around the central frequency (in experimental observation as well as theoretically) this does not degrade the determination of the peak frequency badly but will reduce the accuracy. Apart from being the physically incorrect profile to fit to the transmission profile a quadratic with the same FWHM as the Airy function has a larger kurtosis (see Equation (A.7)) and thus is a less precise discriminator of the centre frequency.

5.9.2 Improved photo-current measurement

Before considering potential improvements in photo-current detection a small detour is needed to expand on the sampling methods used in data acquisition boards. There are two methods that may employed in the application of analogue-to-digital conversion. The most cost-effective is to use a multiplexer. In this configuration when acquiring data from several input channels, the analog multiplexer connects each signal to the analogue-to-digital converter (ADC) in turn. This method, known as continuous scanning, is significantly less expensive than having a separate amplifier and ADC for each input channel. Because the multiplexer switches between channels, a time skew is generated between each channel sample. The multiplexer selects and routes one channel to the ADC for digitizing, then switches to another channel and repeats. Because the same ADC is sampling many channels, the effective rate of each individual channel is reduced in proportion to the number of channels sampled. In multichannel scanning mode, the maximum sampling rate per channel is the maximum sampling rate of the board, divided by the number of channels scanned. As an example, a board sampling at 500 kS/s on 10 channels will effectively sample each individual channel at 50 kS/s per channel. This method is appropriate for applications where the time relationship between sampled points is unimportant or where the temporal offset due to multiplexing is not of concern. For those applications where the time relationship between inputs is important (such as phase analysis of AC signals), it is advantageous to sample simultaneously. Data acquisition boards capable of simultaneous sampling use sample-and-hold circuitry for each input channel.

There are two approaches to multiplexing: round-robin scanning or interval

scanning. In round-robin scanning, the board arranges the sequential sampling of channels so that the times between consecutive scans on all adjacent channels (in terms of sampling order) are the same. On the other hand, interval scanning employs the tactic of acquiring the data for all channels as quickly as the multiplexer will allow then waiting to repeat the scan at the time specified by the sampling rate. The input channels are scanned within microseconds, creating a close approximation of simultaneous sampling of the input channels. We now note that the gate time of each sample is defined by the maximum sampling rate. For example the National Instruments PCI-MIO-16XE-4 card with a maximum sampling rate of 500 kS/s has a maximum sample interval of 2 μs where the relatively small ADC/amplifier rise times have not been taken into account. This has serious implications for photo-detection of low power lasers by the methods used for the C-II optical frequency stabilisation. For example, acquiring 200 samples in 0.1 s, as was done to acquire each data point in the Fabry-Pérot transmission profile, results in a total acquisition time of 400 μs. If the output from the Fabry-Pérot is of the order 100 fW then only about 300 000 photons per second will strike the cathode. From Equation (2.7) the signal-to-noise ratio due to shot noise is thus only about 4 for a total integration time of 400 μs when using the Hamamatsu R3896 PMT. This estimate is based solely on photon counting statistics and does not take into account other factors such as background light and secondary emission which will further reduce the relevant SNR. In fact, as previously described, the use of red filters and pinholes to reduce background light was absolutely necessary in order to properly detect the Fabry-Pérot cavity resonances at standard operating powers. However if all pulses in (say) a 1 ms interval were measured using photon counting techniques a satisfactory SNR of 17 for each data point in the transmission profile scan would be achieved with a factor of 10 reduction in the total acquisition time. Any reduction in the stabilisation loop time T_l that does not affect the noise injected by the stabilisation loop will allow the loop to be useful at lower values of $\sigma_w(t)$ (see Equation (5.78)). Therefore removing the restriction imposed by round-robin sampling will improve the performance of the stabilisation loop.

5.10 Alternative Methods

This section discusses alternative methods of obtaining a discriminator curve in order to stabilise the laser. Any improvements in these methods do not avoid the problems arising from a changing ring geometry, as discussed in Section 5.6.4, when the perimeter is controlled by a piezo on a single mirror. One obvious solution to this problem is to place each mirror under piezo control and supply an equal displacement to each mirror. Alternatively, since a very low bandwidth is all that is required, the pressure stabilisation vessel briefly described in Section 2.3.2 could be used to provide the necessary control over the perimeter of the ring

without altering the geometry[8].

5.10.1 RF beat methods

One of the most simple methods of stabilising a laser by comparison with another stable laser is to control the beat frequency between the two lasers to a constant value by control of the pathlength of the laser to be stabilised. The required optical setup is shown in Figure 5.16.

There are two approaches that may be taken to derive an error signal using the laser beat frequency. The most sensitive method is to apply PSD control methods, demodulating the beat frequency against a reference oscillator and controlling the laser pathlength such that a zero PSD crossing occurs. The alternative is to use an estimate of the beat frequency itself to generate the error signal. This method has the disadvantage of significantly reducing the control bandwidth due to the time required to obtain a suitably accurate estimate of the beat frequency.

In the PSD control method the beat frequency observed at the optical detector is passed to the PSD electronics which produces an error signal that is a function of the frequency separation between the beat frequency and the reference oscillator. It is assumed that the reference oscillator is highly stable and operates at a frequency of a few kHz to MHz as appropriate. The error signal is used to control the pathlength and hence frequency of the slave laser. A zero PSD crossing will occur when the reference oscillator and the beat frequency are $\pi/2$ out of phase.

The white frequency noise that produces the characteristic Lorentzian lineshape of a quantum-limited laser is due to the random walk in phase induced by spontaneous emission [30, 51, 139]. It is an unavoidable consequence that this phase noise will be translated into frequency noise by the control loop. This presents a control bandwidth versus accuracy dilemma because averaging the PSD signal will reduce the injected noise while reducing the response time of the control loop.

There are also difficulties regarding the required mechanical stability of the system as a whole. Consider the 2×2 unitary transformation matrix for the electric field amplitudes exiting the beam-splitter used to mix the two laser beams [31],

$$\begin{pmatrix} E_{1o} \\ E_{2o} \end{pmatrix} = \begin{pmatrix} \sqrt{\eta} & \sqrt{1-\eta} \\ -\sqrt{1-\eta} & \sqrt{\eta} \end{pmatrix} \begin{pmatrix} E_{1i} \\ E_{2i} \end{pmatrix}, \tag{5.86}$$

where η is the irradiance transmission coefficient. It is easy to show that the irradiance from port 1 of the beam-splitter measured at the photo-detector is modulated such that

$$I_1 = E_1^2 + E_2^2 + 2E_1E_2\cos(\delta\omega t + \phi). \tag{5.87}$$

[8] One caveat regarding this method relates to the effects of the pressure-vessel flexure causing a slight deformation of the granite base of C-II, adversely affecting C-II in the process.

If there is a constant PSD voltage then the beat frequency is the same as that of the reference oscillator and $\delta\omega = 0$. It is the phase term, ϕ, that points to the major drawback of this method. This phase term is the phase difference between the two beams at the optical frequency. Therefore a phase difference of 2π radians is equivalent to a pathlength difference of one wavelength in the distances between the laser ports and the beam-splitter. In practice the sort of stability required to keep this value constant is not possible to achieve. For example motion of the cavity ports (even if the total length is compensated) with thermal expansion and contraction will induce changes that are a substantial fraction of a wavelength. This should be contrasted with case of the irradiance modulation schemes discussed elsewhere. In these cases it is the modulation wavelength that is important in deriving the PSD signal. Since these frequencies are much smaller than optical frequencies the problem of mechanically-induced phase shift is much less of a problem.

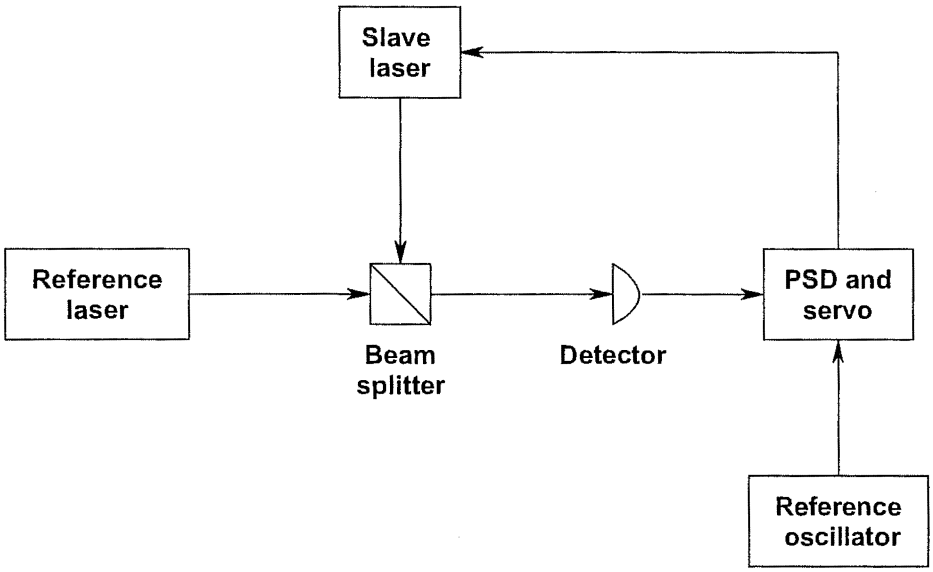

Figure 5.16: Laser stabilisation using the beat frequency with a stable reference laser.

The alternative to a PSD approach is to use estimates of the frequency separation to control the laser. In this case it is the ability to perform an accurate estimation of the frequency that limits the accuracy with which the laser may be controlled. It is undesirable that noise from the frequency estimation process be translated into laser noise. However, with the use of AR2 estimates and some averaging it would be possible to control a stable laser that operated in the white frequency noise regime for some time and reduce the long-term drift by comparison with a stable source such as an iodine-stabilised laser.

The major problem with the beat signal approach for the ring lasers at Canterbury is due to the high-Q of the cavities. This means that exit powers are small

and it is hard to obtain a beat frequency that rises above the noise floor. In order to partially circumvent this difficulty, an investigation of frequency-space compression of the Winters laser-C-II-beat frequency spectrum was made [150]. The goal of this was to reduce the width and increase the power in a small bandwidth coherently to raise the signal above the noise.

The frequency-space compression of the Winters laser-C-II beat signal is described in detail in a paper that is awaiting publication [150]. The salient features of the method are reported here. The raw optical beat signal and a frequency-modulated local oscillator signal are combined in a mixer. When the local oscillator waveform matches that of the reference laser, the output of the mixer is demodulated. Consequently the power spectral density of the signal is increased. This technique increases the signal-to-noise ratio and hence ease of detection of the signal.

It was found that most of the effect of the modulation required to lock the Winters laser to the iodine transition is removable. The residual frequency width of the demodulated beat signal was found to be due to jitter in the iodine-stabilised laser's frequency servo. The 6 MHz frequency width of the iodine-stabilised laser signal was reduced to 390 kHz, improving the visibility of the signal. The minimum detectable optical power was reduced by a factor of approximately 1.7.

5.10.2 Cavity Methods

Due to the low signal levels and the limitations discussed in Section 5.10.1 cavity methods are of the most interest. There are several possible combinations of techniques that may be employed to achieve the basic goals of (a) locking the reference cavity to the reference laser and (b) locking the ring-laser to a reference cavity. The two most distinct approaches are described in this Section.

Side Locking

Locking the lasers to the side of the Fabry-Pérot interferometer transmission profile as described in Section 5.5.1 is one of the simplest and potentially most effective methods available. The initial step is to approximately tune both lasers to the same frequency. Once this is achieved the goal is to (a) control the pathlength of the Fabry-Pérot cavity so that a steep part of the iodine-stabilised laser transmission profile is at resonance with the cavity and (b) control C-II such that its frequency derivative with respect to its scan across the cavity is large. It is necessary to monitor the radiant power of each laser to account for any drift in irradiance. In this way the C-II optical frequency may be constantly compared with, and corrected to follow, the iodine-stabilised laser. A chopper allows detection to alternate between the two lasers at a convenient rate. The major advantage of this method compared to the method described in this Chapter is

that both lasers operate at the same frequency. Therefore it is not necessary to scan the Fabry-Pérot cavity over a relatively wide frequency range between the resonances of the two lasers or perform a fine-scale scan to determine the centre of each resonance. This means that it is possible to achieve a much better signal-to-noise ratio as well as increasing the servo bandwidth. The disadvantage of this approach is that the beam intensities must be independently monitored. Therefore drift in the detector responses will lead to drift in the frequency of the controlled laser.

Derivative (peak) locking

In order to avoid the problems associated with detector drift the length of Fabry-Pérot cavity may be modulated. First of all the Fabry-Pérot cavity position offset, about which the slow modulation is performed, is adjusted to a portion of the iodine-stabilised laser spectrum which is flat. A suitable modulation will allow the Fabry-Pérot interferometer pathlength offset to be adjusted such that the output from PSD detection using the modulation signal as a reference gives zero output. With the aid of a chopper this process alternates with detection of the C-II line. In this case the spectral line Fabry-Pérot cavity is much wider than the C-II line. Therefore the modulation has the effect of monitoring the peak of the Fabry-Pérot interferometer transmission profile with C-II acting as a probe. Since the Fabry-Pérot is locked to the iodine-stabilised laser the C-II pathlength may be adjusted to maintain a zero PSD crossing. Therefore C-II is locked to the iodine laser. This has the same advantages of the peak locking method over the method described in this Chapter. However the modulation requires that some care is taken to achieve an adequate signal-to-noise ratio from the photo-detection process.

Either of the cavity-locking approaches described in this Section would offer some useful advantages over the method described in this Chapter. In particular there is no need to scan across the entire transmission profile. This may prove useful in terms of stability of the reference cavity and the accuracy with which the frequency difference between the iodine-stabilised laser and C-II may be measured. It would also be possible to increase the loop bandwidth significantly. Although the result of this is to tighten the constraint of the amount of noise that may be injected by the stabilisation scheme without degrading performance it may be found that tighter control allows the noise injected by the stabilisation scheme to be significantly reduced. Therefore the stricter criterion would be met. An effect such as this would depend on the details of a particular stabilisation scheme.

Finally, it is also worth noting that the low power output of the high-Q lasers would most probably mean that, although PDH locking has been shown to be the most effective method with higher power lasers, it is likely that detection of the modulated laser beam would be difficult when attempting to PDH lock C-II

to the reference cavity. This would rule out the PDH locking method as a viable alternative to the method described in this Chapter.

Chapter 6

The Ring-laser Gyroscope and Injected Noise

The effects of coupling between the counter-propagating waves due to backscattering from the laser mirrors for small rotation rates has already been briefly discussed in Chapters 2 3. The lock-in effect causes the gyroscope's beat frequency to vanish for small rotation rates. When the mirrors are sufficiently clean, all of the Canterbury ring-lasers unlock at the Earth rotation rate. C-I in particular operates relatively close to the lock-in band and therefore the effects of frequency pulling are observed. A significant amount of work has been carried out on methods that allow the effects of the lock-in dead band to be reduced or circumvented in some way. One of the main goals of this work was to develop gyroscopes suitable for guidance purposes. One approach to reduction of the dead-band consists of *dithering* the ring-laser [18, 151]. This is done by adding a known external rotation such that the laser operates outside of the dead-band most of the time. Another approach that can reduce the dead-band was discovered in the course of a general investigation of quantum noise [34–37]. In this series of papers it was shown that the white frequency noise due to spontaneous emission reduced the size of the dead-band. By way of introduction to the coloured noise theory this work is summarised in Section 6.2. Use of this effect to reduce pulling effects is not sensible with high-precision gyroscopes because, in order to reduce lock-in effects, it is necessary to increase the noise. This approach would therefore counteract the goal of reducing the quantum noise level by increasing the power in order to improve the gyroscope's resolution as discussed in Section 2.3.1. However introduction of external noise which necessarily possesses a nonvanishing correlation time may also be used to reduce the lock-in bandwidth [6,38–40]. The theoretical basis of this approach is described in Section 6.3. One advantage of the injected external noise is that it is possible to perform correlation analysis and subtract the effects of the injected noise from the observed gyroscope beat frequency. This, of course, is not possible in the case of white frequency due to spontaneous emission. The description and results of an experimental investigation of injected coloured noise in C-I are presented in Sections 6.4 and 6.4.4 respectively. However, before these more detailed discussions are presented, an overview of the Fokker-Planck

approach [33] to the treatment of stochastic differential equations that is the cornerstone of the approach used to characterise the stochastic behaviour of the ring-lasers is given in Section 6.1.

6.1 Stochastic Differential Equations

To demonstrate the important features consider the generalised stochastic equation for N variables ($i = 1, 2, \ldots, N$),

$$\dot{\zeta}_i = h_i(\{\zeta\}, t) + p_i(\{\zeta\}, t)\zeta_i + g_{ij}(\{\zeta\}, t)F_j(t), \tag{6.1}$$

where the coefficients $h_i(\{\zeta\}, t)$ are the deterministic, but possibly nonlinear, terms in the stochastic differential equation, commonly referred to as the *Langevin equation*. In the context of Equation (6.1), $F_j(t)$ represents *additive noise* while $p_i(\{\zeta\}, t)$ represents *multiplicative noise* due to its relationship with ζ_i. All of the work presented in this Chapter is concerned with additive noise. The connection between the general stochastic equation of motion given by Equation (6.1) and the equations of motion for the ring-laser gyroscope is discussed in Section 6.2.

The behaviour of the intensities of the counter-propagating beams in the presence of additive white noise in ring-laser gyroscopes has been investigated by Mandel and Tehrani [152, 153]. In particular, the correlation functions where mode competition due to spectral hole burning at gain-centre is important are derived. The beat-frequency characteristics are of more interest to the Canterbury ring-laser group. An extensive investigation of the spectral behaviour for operation in the locked regime, in the transition region where frequency pulling is significant, and well outside the locked regime when additive white noise is present is presented by Cresser *et al.* [34–36]. The relevant aspects of this work are reviewed in Section 6.2 to provide an introduction to the theory of additive coloured noise in ring-laser gyroscopes that was originally presented by Vogel *et al.* [6, 38–40]. The final Sections in this Chapter provide an account of an experimental investigation of the effects of coloured noise in C-I. To the author's knowledge, this is the first such investigation and test of the theory [6, 38–40].

Saturation effects on the statistical properties of the cavity irradiance when additive noise is present are discussed in Ref. [154]. Autocorrelation and cross-correlation of the steady state intensities where multiplicative and additive noise are present but without backscattering is discussed in Ref. [41]. When the laser is operated far above threshold there is almost no difference between the models with and without multiplicative noise. However in the threshold regime the pump fluctuations do have a strong effect on the irradiance correlations.

6.1.1 The Fokker-Planck Equation

The general Fokker-Planck equations for N variables has the form [33, p. 5]

$$\frac{\partial P}{\partial t} = \left[-\sum_{i=1}^{N} \frac{\partial}{\partial x_i} D_i^{(1)}(\{x\}) + \sum_{i,j=1}^{N} \frac{\partial^2}{\partial x_i \partial x_j} D_{ij}^{(2)}(\{x\}) \right] P. \tag{6.2}$$

$D_i^{(1)}$ and $D_{ij}^{(2)}$ are known as the drift vector and the diffusion tensor respectively. They generally depend on the N macroscopic variables $x_1, x_2, \ldots, x_N = \{x\}$. Equation (6.2) is an equation of motion for the probability distribution $P(\{x\}, t)$ of N variables $\{x\}$.

In a deterministic treatment the fluctuations of the macroscopic variables are neglected. In the context of the Fokker-Planck Equation (6.2) this means that the diffusion term is set to zero. In this case Equation (6.2) is equivalent to the following system of differential equations;

$$\frac{\mathrm{d}x_i}{\mathrm{d}t} = D_i^{(1)}(\{x\}), \tag{6.3}$$

where $i = 1, \ldots, N$.

If $D^{(1)} = 0$ and $D^{(2)} = b$ we obtain the Fokker-Planck equation that describes the *random walk* or *Wiener process* [83, 84]. It is a diffusion process that obeys a Gaussian probability distribution and is of zero mean and has a variance that increases with time;

$$\langle x^2 \rangle = bt.$$

This special case of the Fokker-Planck equation is more commonly encountered in the description of Brownian motion which was briefly discussed in Section 4.1.1. Ideally one would like to begin with equations describing the microscopic variables of the systems and derive the macroscopic equations from these. The deterministic treatment then follows by neglecting the fluctuations in the macroscopic variables. In practice this will often prove to be very complicated or even impossible. In this case it is necessary to resort to heuristic arguments to obtain the stochastic description. This is usually done by adding what is known as a Langevin force to the deterministic Equations(6.3). It is then possible to obtain the Fokker-Planck equation from the Langevin equation that results from the addition of the noise term by means of established methods [33, Chapter 3].

For N variables the general Langevin equations are of the form ($i = 1, 2, \ldots, N$)

$$\dot{\zeta}_i = h_i(\{\zeta\}, t) + g_{ij}(\{\zeta\}, t) F_j(t). \tag{6.4}$$

$F_j(t)$ is the Langevin force. It is zero-mean and δ-correlated. The 2nd-order correlation functions are normalised such that a factor of two appears in front of the δ-function. Hence

$$\langle F_i(t) \rangle = 0, \tag{6.5}$$

and

$$\langle F_i(t)F_j(t+\tau)\rangle = 2\delta_{ij}\delta(\tau). \tag{6.6}$$

The drift vector and diffusion tensor are found from what is known as the Kramers-Moyal expansion [155]:

$$D_i^{(1)}(\{x\}) = h_i(\{x\},t) + g_{kj}(\{x\},t)\frac{\partial}{\partial x_k}g_{ij}(\{x\},t), \tag{6.7}$$

and

$$D_{ij}^{(2)}(\{x\},t) = g_{ik}(\{x\},t)g_{jk}(\{x\},t). \tag{6.8}$$

For an explanation of how the Kramers-Moyal expansion is used to find $D^{(1)}$ and $D^{(2)}$ see Risken [33, p. 54-59]. Siegert *et al.* discuss how the drift and diffusion coefficients may be extracted from noisy data sets [156].

6.1.2 Methods of Solution of the Fokker-Planck Equation

There are a number of approaches to solving the Fokker-Planck equation. Many of these are detailed in Chapters 5 and 6 of Risken [33] for Fokker-Planck equations of one or several variables respectively. Two approaches are applied to the Fokker-Planck equations that relevant to the ring-laser gyroscope. In both cases the steady-state probability density, $P_{ss}(\{x\},t)$, is calculated where

$$\frac{\partial P(\{x\},t)}{\partial t} = 0.$$

Minimal Diffusion Approximation

The first approach employs the approximation that the stochastic variables do not diffuse very far from their steady-state values. It is also assumed that the solution of the relevant deterministic equation does not vary in time. This allows the stochastic variables to be written as

$$\zeta_i = \zeta_{i,ss} + \theta_i,$$

where $\theta_i \ll 1$. The steady-state value $\zeta_{i,ss}$ of the stochastic variable must be determined from the solutions to the determined from the solutions to the deterministic approximation of the equations of motion for ζ_i. This simplification often allows one to write down relatively simple Fokker-Planck equations for θ_i which describe the behaviour of ζ_i about its steady-state value. When this approximation is applied to real data it is necessary to ensure the assumption of minimal diffusion is appropriate.

Continued Matrix Fractions

The numerical methods of *continued scalar fractions* and *continued matrix fractions* provide a reliable means of finding solutions to the Fokker-Planck equation [33, Chapter 9]. For a full description the reader is referred to the book by Risken [33]. Section 6.3.3 describes the *scalar continued fraction* approach required to solve the equations of motion for a ring-laser gyroscope when additive white noise is present. A description of the *continued matrix fraction* approach required to solve the equations of motion of a ring-laser in the presence of coloured noise is given in Section 6.3.3.

6.2 White Noise in Ring-laser Gyroscopes: A SDE Approach

The important results found by application of the SDE approach to additive white noise in ring-laser gyroscopes [34–37] gives an introduction to the salient SDE concepts while working with a noise source that produces effects that are well known within the ring-laser gyroscope community.

6.2.1 Equations of Motion in the Presence of Noise

We begin by neglecting deterministic backscattering. This will be re-introduced at a later point without loss of generality. The Langevin equation for the phase ϕ_+ one direction of propagation is the same as that of a single mode laser as [12],

$$\frac{\mathrm{d}\phi_+}{\mathrm{d}t} = \frac{1}{2i\sqrt{\bar{n}}}\left[\exp(-i\phi_+(t))G_+^\dagger(t) - \exp(i\phi_+(t))G_+(t)\right] + \text{constant}, \tag{6.9}$$

where the quantum noise operator $G_+(t)$ has zero-mean as well as possessing the second-order correlation functions,

$$\begin{aligned} &\langle G_+^\dagger(t)G_+(t+\tau)\rangle + \langle G_+(t)G_+^\dagger(t+\tau)\rangle = 4\bar{n}D\delta(\tau) \\ &\text{and} \\ &\langle G_+(t)G_+(t+\tau)\rangle = \langle G_+^\dagger(t)G_+^\dagger + (t+\tau)\rangle = 0. \end{aligned} \tag{6.10}$$

$\bar{n}$ is the average number of photons in the field and $D = \nu/(2Q\bar{n})$ is the diffusion constant of spontaneous emission [157]. In the classical limit where the various operators commute the second order correlation functions that results from

Equation (6.9) is independent of ϕ_+:

$$\left\langle \frac{\mathrm{d}\phi_+(t)}{\mathrm{d}t}\frac{\mathrm{d}\phi_+(t+\tau)}{\mathrm{d}t} \right\rangle = \frac{1}{(2i)^2\bar{n}} \Big\langle \Big[\exp(-i\phi_+(t))G_+^\dagger(t) - \exp(i\phi_+(t))G_+(t)\Big] \times \Big[\exp(-i\phi_+(t+\tau))G_+^\dagger(t+\tau) - \exp(i\phi_+(t+\tau))G_+(t+\tau)\Big] \Big\rangle = D\delta(\tau). \tag{6.11}$$

Therefore the noise source in Equation (6.9) can be replaced by the equivalent Langevin force $F_+(t)$,[1] where

$$\langle F_+(t)\rangle = 0, \quad \text{and} \quad \Gamma(\tau) = \langle F_+(t)F_+(t+\tau)\rangle = D\delta(\tau) \tag{6.12}$$

After following the analogous argument for the equation of motion for ϕ_- we may write the equation of motion for the phase difference between the two counter-propagating modes as

$$\frac{\mathrm{d}\psi}{\mathrm{d}t} = \frac{\mathrm{d}\phi_+}{\mathrm{d}t} - \frac{\mathrm{d}\phi_-}{\mathrm{d}t} = \text{constant} + F_+(t) - F_-(t). \tag{6.13}$$

Since $F_+(t)$ and $F_-(t)$ are uncorrelated noise sources $F_+(t) - F_-(t)$ may be replaced by $F(t) \equiv F_+(t) - F_-(t)$, where

$$\langle F(t)\rangle = 0, \quad \text{and} \quad \Gamma(\tau) = \langle F(t)F(t+\tau)\rangle = 2D\delta(\tau). \tag{6.14}$$

Inserting the simplest equation (3.22) for the deterministic backscattering and Sagnac terms we arrive at the working Langevin equation,[2]

$$\frac{\mathrm{d}\psi}{\mathrm{d}t} = 2\pi f_s + 2\pi f_l \sin\psi + F(t). \tag{6.15}$$

From the Langevin Equation (6.15) the mean beat frequency is

$$\langle\dot{\psi}(t)\rangle = 2\pi f_s + 2\pi f_l \langle\sin\psi(t)\rangle \tag{6.16}$$

since the fluctuating force $F(t)$ averages to zero.

We are now in a position to find the drift and diffusion coefficients ($D^{(1)}(\psi)$ and $D^{(2)}(\psi)$ for the Langevin equation (6.15). Substitution of these coefficients in the 1-dimensional Fokker-Planck equation leads to an equation of motion for the probability distribution for the phase difference between the counter-propagating waves in a ring-laser with additive white noise. By inspection

$$h(\psi,t) = 2\pi f_s + 2\pi f_l \sin\psi, \qquad g(\psi,t) = 1.$$

[1] A more rigorous justification for eliminating the $\exp(i\phi)$ contribution from the equation of motion has been given by Haken [158].

[2] It should be kept in mind that, as discussed in Chapter 3, there are a number of assumptions required to arrive at the simple deterministic equation of motion for the phase difference between the counter-propagating waves.

Therefore the Fokker-Planck equation for the probability distribution of the phase difference between the counter-propagating waves in a ring-laser that is operating in the locked regime is

$$\frac{\partial P}{\partial t} = -\frac{\partial}{\partial \psi}\left[(2\pi f_s + 2\pi f_l \sin\psi)P\right] + D\frac{\partial^2 P}{\partial \psi^2}. \tag{6.17}$$

6.2.2 Phase Distribution in the Locked Region

Following Cresser *et al.* [35] an approximate form of the steady-state probability distribution $P_{ss}(\psi)$ may be found by using the *minimal diffusion approximation.*

The first step is to linearise the Langevin equation (6.15) by defining a new variable θ that represents the motion of ψ about its steady-state value ψ_{ss};

$$\psi = \psi_{ss} + \theta, \tag{6.18}$$

where

$$\psi_{ss} = \pi + \sin^{-1}\left[\frac{f_s}{f_l}\right]$$

in accordance with the deterministic solution discussed in Section 3.4.1. Since

$$2\pi f_s + 2\pi f_l \sin\psi \approx \xi\theta,$$

where

$$\xi = \sqrt{2\pi(f_l^2 - f_s^2)},$$

it is possible to obtain a simple equation of motion for θ;

$$\dot{\theta} = -\xi\theta + F(t). \tag{6.19}$$

It is of interest that Equation (6.19) is formally equivalent to the Langevin equation for Brownian motion [33, p. 31-34]. Evaluation of the drift and diffusion constants is trivial and the Fokker-Planck equation for $P(\theta, t)$ is

$$\frac{\partial P}{\partial t} = -\xi\frac{\partial[\theta P]}{\partial \theta} + D\frac{\partial^2 P}{\partial \theta^2}. \tag{6.20}$$

This may be solved using the boundary condition

$$P(\theta t|\theta_0, 0) \longrightarrow 0 \quad \text{as } \theta \longrightarrow \pm\infty, \tag{6.21}$$

and initial condition

$$\lim_{t=0} P(\theta, t|\theta_0, 0) = \delta(\theta - \theta_0) \tag{6.22}$$

The Fokker-Planck equation is solved to give [35]

$$P(\theta, t|\theta_0, 0) = \sqrt{\frac{\xi}{2\pi D(t)}} \exp\left(\frac{-\xi(\theta - \theta_0 \exp(-\xi t))^2}{2D(t)}\right), \tag{6.23}$$

where

$$D(t) = D(1 - \exp(-2\xi t)).$$

At steady-state $P_{ss}(\theta) = P(\theta, t \to \infty|\theta_0, 0)$, and

$$P_{ss}(\theta) = \sqrt{\frac{\xi}{2\pi D}} \exp\left(\frac{-\xi\theta^2}{2D}\right). \tag{6.24}$$

As one would expect intuitively a Gaussian probability distribution results. The variance is

$$\langle\theta^2\rangle = \frac{D}{\xi} = \frac{D}{\sqrt{2\pi f_l^2 - 2\pi f_s^2}}.$$

In summary the probability distribution for the phase difference between the counter-propagating waves in the locked region is a Gaussian distribution centred on the noise-free value of the phase difference. The width increases with increasing noise. Furthermore, close to the lock-in threshold, $\langle\theta^2\rangle$ also increases. This may be understood in a physical context by considering that close to the lock-in threshold, the coupling between the counter-propagating waves is less than when the laser is well within the locking region. Therefore the noise will cause the phase difference between the counter-propagating waves to vary a lot more when the laser is close to the lock-in threshold.

6.2.3 Mean Beat Frequency with Additive White Noise

This Section only details the relevant results for the steady-state case. For the generalisation that includes transient phenomena the reader is referred to Cresser *et al.* [34].

It is assumed that the steady-state probability distribution may be expanded as follows;

$$P_{ss}(\psi) = \frac{1}{\sqrt{2\pi}} \sum_{m=-\infty}^{+\infty} S_m \exp(im\psi). \tag{6.25}$$

Substitution of Equation (6.25) in the Fokker-Planck equation (6.17) produces a recurrence relation for the coefficients S_m,

$$0 = -\frac{b}{2}S_{m+1} + (i2\pi f_s + mD)S_m + \frac{b}{2}S_{m-1}. \tag{6.26}$$

$P_{ss}(\psi)$ must be normalised to unity over $(0, 2\pi)$. From the definition of $P_{ss}(\psi)$ (6.25) $s_0 = 1/\sqrt{2\pi}$. The probability distribution must also be real. This

leads to the requirement $S_{-m} = S_m^*$. Substitution of the iteration

$$S_m = R_m S_{m-1} \tag{6.27}$$

leads to

$$R_m = \frac{-2\pi f_l}{[2(i2\pi f_s + mD) - 2\pi f_l R_{m+1}]}. \tag{6.28}$$

Since the Langevin force $F(t)$ is zero-mean the Langevin equation (6.15) implies that, in the unlocked case, the mean beat frequency $\langle\dot{\psi}(t)\rangle$ is given by

$$\langle\dot{\psi}(t)\rangle = 2\pi f_s + 2\pi f_l \langle\sin\theta(t)\rangle. \tag{6.29}$$

$\langle\sin\theta(t)\rangle$ is found directly from the series expansion for $P_{ss}(\psi)$ as well asthe result $S_{-1} = S_1^*$. The average beat frequency is therefore

$$\langle\dot{\psi}(t)\rangle = 2\pi f_s - \sqrt{2\pi}2\pi f_l \Im(S_1). \tag{6.30}$$

Figure 6.1 shows the effects of the white noise on the gyroscope beat frequency. When the gyroscope is operating well outside of the locking region the beat frequency is the same as that predicted by the deterministic theory. However for rotation rates close to the lock-in threshold a new feature which is not predicted by the deterministic theory appears. The unlocking tends to occur at smaller rotation rates for increased noise.

6.3 Ring-laser Gyroscope with Additive Coloured Noise

In Section 6.2 it was shown that additive white noise has the effect of reducing the tendency of the ring-laser gyroscope to lock. Consequently it is of interest to investigate the effects of injection of external noise. The external noise must possess a nonzero correlation time. This section deals with Lorentzian coloured noise which has an exponentially decaying autocorrelation function. The noise is injected by control of a piezoelectric transducer bonded to one of the mirrors. This allows for a noise bandwidth up to a few kilohertz.

6.3.1 The Fokker-Planck Equation Describing a Ring-laser Gyroscope with Additive Coloured Noise

A fluctuation in the perimeter due to injected noise is equivalent to fluctuation in the rotation rate. Therefore we may write the equation of motion for the phase difference between the counter-propagating waves as

$$\frac{\mathrm{d}\psi}{\mathrm{d}t} = 2\pi f_s + 2\pi f_l \sin\psi + \varepsilon(t). \tag{6.31}$$

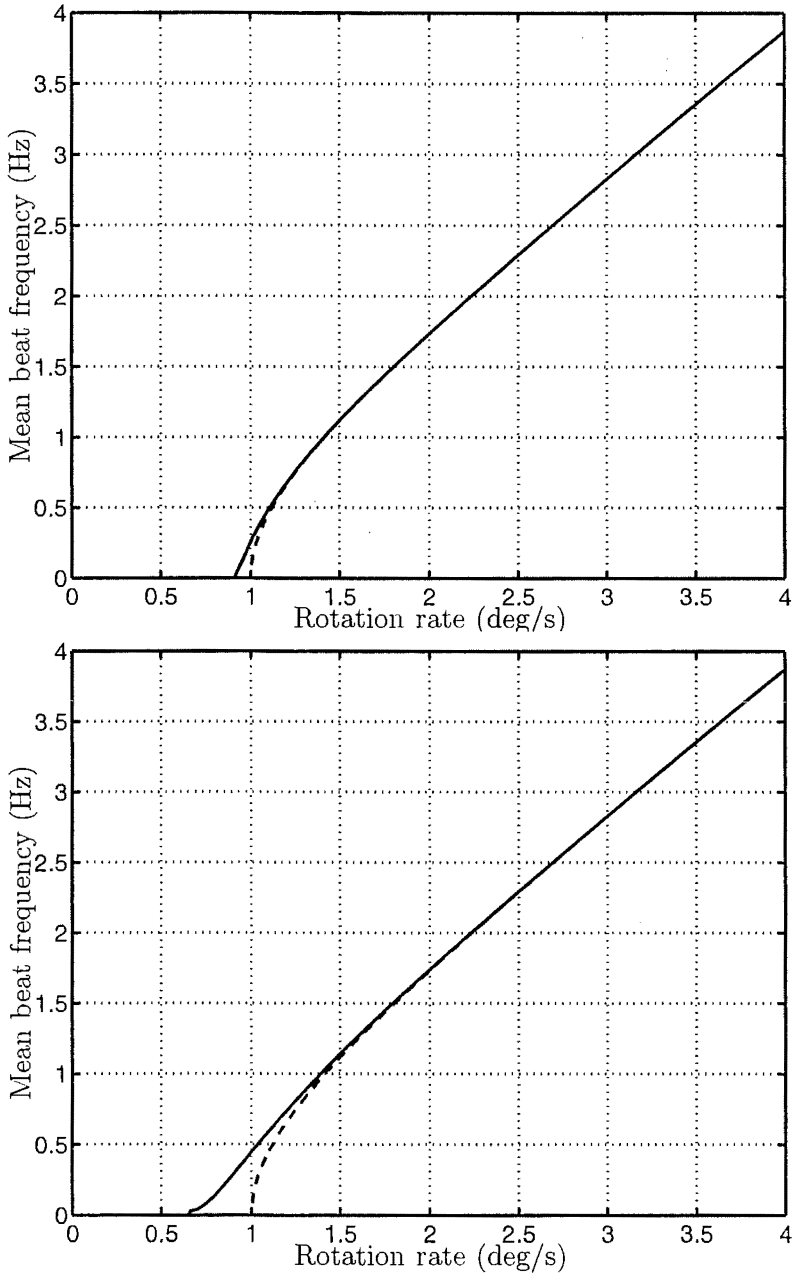

Figure 6.1: Mean gyroscope beat frequency in the presence of white noise (solid line) and noise-free response (dashed). The strength of the noise is (a) $D = 0.01$ and (b) $D = 0.05$. White noise clearly decreases the width of the dead band. The beat frequency was calculated using the continued scalar fraction method described in the text.

In this instance the "rotation" fluctuation $\varepsilon(t)$ is assumed to be Gaussian coloured noise of strength D;

$$\begin{aligned}\Gamma_\varepsilon(\tau) &= \langle \varepsilon(t)\varepsilon(t+\tau)\rangle \\ &= \left(\frac{D}{\tau_c}\right)\exp\left(\frac{-|\tau|}{\tau_c}\right),\end{aligned} \tag{6.32}$$

where τ_c is the *correlation time* of the noise process. $\varepsilon(t)$ is assumed to be a zero-mean noise process;

$$\langle \varepsilon(t)\rangle = 0. \tag{6.33}$$

The power spectral density $S(\omega)$ of $\varepsilon(t)$ may be shown to a one-sided Lorentzian using the Wiener-Khincthine theorem [31, p. 59-63];

$$S(\omega) = \frac{2D}{1+(\tau_c\omega)^2}. \tag{6.34}$$

The Allan variance of the Lorentzian coloured noise is given by

$$\sigma_A^2(\tau) = \frac{D\tau_c^2}{2\tau^2}\left[2\exp\left(-\frac{\tau}{\tau_c}\right) - \exp\left(-\frac{2\tau}{\tau_c}\right) + \frac{2\tau}{\tau_c} - 3\right]. \tag{6.35}$$

The reader is referred to Appendix B.2.1 and Ref. [99] for more details of this derivation. For large τ the Lorentzian coloured noise is indistinguishable from white noise.

The Lorentzian coloured noise process $\varepsilon(t)$ does not constitute a Langevin force term in Equation (6.31). Therefore it is not possible to find the Fokker-Planck equation for probability distribution of ψ from Equation (6.31). However if the noise process $\varepsilon(t)$ is described by the process

$$\frac{\mathrm{d}\varepsilon}{\mathrm{d}t} = \frac{-\varepsilon}{\tau_c} + F(t) \tag{6.36}$$

where

$$\begin{aligned}\Gamma_F(\tau) &= \langle F(t)F(t+\tau)\rangle \\ &= \left(\frac{2D}{\tau_c^2}\right)\delta(\tau),\end{aligned} \tag{6.37}$$

and

$$\langle F(t)\rangle = 0,$$

it is possible to find a Fokker-Planck equation for the joint probability density $P(\psi,\varepsilon)$. If a stationary random process $x(t)$ is differentiable then $\dot{x}(t)$ is a wide sense stationary random process of zero mean with an autocorrelation given by [31, p. 54-55]

$$\Gamma_{\dot{x}}(\tau) = -\ddot{\Gamma}_x(\tau). \tag{6.38}$$

The two-time cross-correlation between $x(t)$ and its derivative is [31, p. 55]

$$\langle x(t)\dot{x}(t+\tau)\rangle = \dot{\Gamma}_x(\tau). \tag{6.39}$$

From Equation (6.36) we require for all τ that

$$\langle F(t)F(t+\tau)\rangle = \frac{1}{\tau_c^2}\langle \varepsilon(t)\varepsilon(t+\tau)\rangle + \langle \dot{\varepsilon}(t)\dot{\varepsilon}(t+\tau)\rangle + \frac{2}{\tau_c}\langle \dot{\varepsilon}(t)\varepsilon(t+\tau)\rangle. \tag{6.40}$$

The second term on the right hand side of Equation (6.40) may be found using Equation (6.38). The third term is found to be zero using Equation (6.39) and the symmetry property of the autocorrelation for a real process,

$$\dot{\Gamma}(-\tau) = -\dot{\Gamma}(\tau).$$

Substitution of Equation (6.32) shows that the equality (6.40) is indeed satisfied, and the stochastic variable, $\varepsilon(t)$, defined in this way, satisfies Equations (6.32) and (6.33).

Now that we have the appropriate Langevin equations (6.31) and (6.36) for the stochastic variables $\psi(t)$ and $\varepsilon(t)$, the drift vector and diffusion tensor may be found from Equations (6.7) and (6.8). The components of these quantities are

$$D_{\psi}^{(1)} = 2\pi f_s + 2\pi f_l \sin\psi + \varepsilon, \tag{6.41}$$

$$D_{\varepsilon}^{(1)} = -\frac{1}{\tau_c}, \tag{6.42}$$

$$D_{\varepsilon\varepsilon}^{(2)} = \frac{D}{\tau_c^2}, \tag{6.43}$$

and

$$D_{\psi\varepsilon}^{(2)} = D_{\varepsilon\psi}^{(2)} = D_{\psi\psi}^{(2)} = 0. \tag{6.44}$$

Substitution of the drift vector and diffusion tensor into the general Fokker-Planck equation leads to the following equation of motion for the joint probability distribution of the stochastic variables $\psi(t)$ and $\varepsilon(t)$;

$$\frac{\partial P}{\partial t} = -\frac{\partial}{\partial \psi}\left[(2\pi f_s + 2\pi f_l \sin\psi + \varepsilon)\right] P + \frac{1}{\tau_c}\frac{\partial(\varepsilon P)}{\partial \varepsilon} + \frac{D}{\tau_c^2}\frac{\partial^2 P}{\partial \varepsilon^2}. \tag{6.45}$$

6.3.2 Steady-state Solution for the Minimal Diffusion Approximation

It is possible to gain some important insight into the effects of additive coloured noise on the ring-laser gyroscope by following the approach of the *minimal diffusion approximation* described in Section 6.1.2 for additive white noise.

When the laser is locked the phase difference between the counter-propagating waves in the absence of noise is given by Equation (3.23)[3]

$$\psi = \pi + \sin^{-1}\left(\frac{f_s}{f_l}\right).$$

If it is assumed that the noise is weak we expect the phase not to diffuse very far from its equilibrium point. Consequently ψ may be written as a small perturbation θ about its steady-state value ψ_{ss},

$$\psi = \psi_{ss} + \theta,$$

where $|\theta| \ll 1$. Once again we may write

$$2\pi f_s + 2\pi f_l \sin\psi \approx -\xi\theta,$$

where

$$\xi = \sqrt{2\pi f_l^2 - 2\pi f_s^2}.$$

The Fokker-Planck Equation (6.45) reduces to

$$\frac{\partial P}{\partial t} = \xi\frac{\partial}{\partial\theta}(\theta P) - \varepsilon\frac{\partial P}{\partial\theta} + \frac{1}{\tau_c}\frac{\partial}{\partial\varepsilon}(\varepsilon P) + \frac{D}{\tau_c^2}\frac{\partial^2 P}{\partial\varepsilon^2}. \tag{6.46}$$

The solution to this equation that gives an approximate probability distribution for the steady state value of the pulled frequency is [6],

$$P_{ss}(\psi,\varepsilon) = \frac{\sqrt{\xi\tau_c}}{2\pi D} \times \exp\left(-\frac{\tau_c\xi(\tau_c^2-1) + [\varepsilon^2 - 2\xi\varepsilon(\psi-\psi_{ss}) + \xi(\xi+1/\tau_c)(\psi-\psi_{ss})^2]}{2D\tau_c}\right) \tag{6.47}$$

This expression differs from that of Vogel *et al.* [6] due to the application of the normalisation

$$\int_{-\infty}^{\infty}\int_{-\infty}^{\infty} P_{ss}(\psi,\varepsilon)\,\mathrm{d}\psi\,\mathrm{d}\varepsilon = 1.$$

Figure 6.2 emphasises the most interesting result of the coloured noise in a locked ring laser gyroscope—the probability distribution is skewed. This results from a coupling of the two stochastic variables ψ and ε due to the nonvanishing correlation time τ_c.

[3]Note that the slightly different definition of the equation of motion for ψ requires the addition of π.

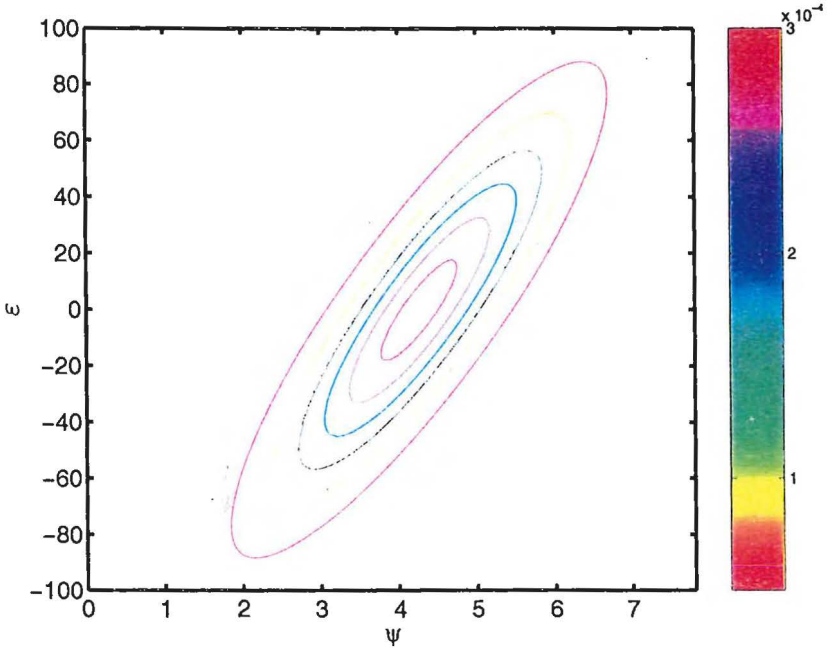

Figure 6.2: Contour map of the steady state phase distribution in the presence of coloured noise using the analytical approximation (6.47). The various noise parameters used to generate the plot are: $2\pi f_s = 68, 2\pi f_l = 75, \tau_c = 0.1$, and $D = 50$.

The second-order moments of $P_{ss}(\psi, \varepsilon)$ are of particular interest:

$$\begin{aligned}
\langle \psi^2 \rangle &= \int_{-\infty}^{\infty} \int_{-\infty}^{\infty} \psi^2 P(\psi, \varepsilon)\, \mathrm{d}\psi\, \mathrm{d}\varepsilon \\
&= \psi_{ss}^2 + \frac{D}{\xi} \\
&= \psi_{ss}^2 + \frac{D}{\sqrt{2\pi f_l^2 - 2\pi f_s^2}} \\
&= \psi_{ss}^2 + \frac{D \tan \psi_{ss}}{2\pi f_s},
\end{aligned} \tag{6.48}$$

$$\begin{aligned}
\langle \varepsilon^2 \rangle &= \int_{-\infty}^{\infty} \int_{-\infty}^{\infty} \varepsilon^2 P(\psi, \varepsilon)\, \mathrm{d}\psi\, \mathrm{d}\varepsilon \\
&= D\left(\xi + \frac{1}{\tau_c}\right) \\
&= D\left(\sqrt{2\pi f_l^2 - 2\pi f_s^2} + \frac{1}{\tau_c}\right) \\
&= D\left(a \cot \psi_{ss} + \frac{1}{\tau_c}\right),
\end{aligned} \tag{6.49}$$

and

$$\begin{aligned}\langle\psi\varepsilon\rangle &= \int_{-\infty}^{\infty}\int_{-\infty}^{\infty}\psi\varepsilon P(\psi,\varepsilon)\,\mathrm{d}\psi\,\mathrm{d}\varepsilon \\ &= D.\end{aligned} \tag{6.50}$$

In general, increasing the noise strength D has the effect of increasing all second-order moments. From Equation (6.48) we see that the more "tightly locked" the gyroscope the narrower the distribution in ψ. As the laser nears the lock-in threshold from the locked regime $\langle\psi^2\rangle$ increases. Consequently the likelihood of $\psi \longrightarrow \psi + 2\pi$ is significantly increased. This hints at the result discussed in the next section where the presence of the noise is shown to have an effect on the characteristics of the beat frequency close to the lock-in threshold. The probabilistic description also shows how the distorted waveforms observed close to the lock-in threshold arise. This comment is also valid for the ring-laser gyroscope with additive white noise.

To complete this Section two further quantities that are used in the analysis of the experimental data are calculated;

$$\begin{aligned}\tilde{P}(\psi) &= \int_{-\infty}^{\infty} P(\psi,\varepsilon)\,\mathrm{d}\varepsilon \\ &= \sqrt{\frac{\xi}{2\pi D}}\exp\left(-\frac{\xi(\psi-\psi_{ss})^2}{2D}\right),\end{aligned} \tag{6.51}$$

and

$$\begin{aligned}\tilde{P}(\varepsilon) &= \int_{-\infty}^{\infty} P(\psi,\varepsilon)\,\mathrm{d}\psi \\ &= \sqrt{\frac{\tau_c}{2\pi D(\xi\tau_c+1)}}\exp\left(-\frac{\varepsilon^2\tau_c}{2D(\xi\tau_c+1)}\right).\end{aligned} \tag{6.52}$$

At this point it is worth stating that $\tilde{P}(\varepsilon)$ is not equal to

$$P(\varepsilon) = \sqrt{\frac{\tau_c}{2\pi D}}\exp\left(-\frac{\varepsilon^2\tau_c}{2D}\right). \tag{6.53}$$

It is standard practice [33, p. 15] to denote the stochastic variable and the variable in the distribution function by the same symbol. Equation (6.53) is the ordinary probability distribution for the stochastic input noise while $\tilde{P}(\varepsilon)$ is derived from the joint probability distribution $P(\psi,\varepsilon)$ describing the system.

The Limit $\xi \ll \tau_c$

A useful simplification may be made if $\xi \gg 1$ and $\tau_c \gg 1$ (or more generally $\xi\tau_c \gg 1$) is satisfied. In this approximation the we may set the term

$$\xi(\xi + 1/\tau_c) \longrightarrow \xi^2$$

in the exponential of Equation(6.47). This allows Equation (6.47) to cast in the form a bivariate Gaussian distribution (A.18),

$$P'_{ss}(\psi,\varepsilon) = \sqrt{\xi\tau_c}\frac{\xi\tau_c+1}{2\pi D}\exp\left(-\frac{\xi}{2D/\tau_c^2}\right)\exp\left[-\frac{\tau_c}{D}\left(\frac{\varepsilon^2}{\sigma_\varepsilon^2}-\frac{2\varepsilon\varphi}{\sigma_\varepsilon\sigma_\varphi^2}+\frac{\varphi}{\sigma_{\varphi^2}^2}\right)\right] \tag{6.54}$$

where $\varphi = \psi - \psi_{ss}$, $\sigma_\varepsilon = 1$, and $\sigma_\varphi = 1/\xi$.

It has already been mentioned that the coloured noise causes a skewing of the two-dimensional probability distribution. The approximation that allows $P'_{ss}(\psi,\varepsilon)$ to be written as a bivariate Gaussian allows a transparent characterisation of the quantities of importance. Given a bivariate Gaussian distribution (6.54) the two new variables u, v defined by the transformation,

$$u = x\cos\vartheta - y\sin\vartheta, \tag{6.55}$$

$$v = x\sin\vartheta + y\cos\vartheta, \tag{6.56}$$

also define a bivariate Gaussian distribution. The angle ϑ_i for which u and v are statistically independent is given by (see Appendix A.6.1),

$$\begin{aligned}\vartheta_i &= \frac{1}{2}\tan^{-1}\left[\frac{2\xi}{\xi^2-1}\right] \\ &= \frac{1}{2}\tan^{-1}\left[\frac{4\pi f_s\cos\psi_{ss}}{2\pi f_s\cos\psi_{ss}-\sin\psi_{ss}}\right].\end{aligned} \tag{6.57}$$

An important consequence of this result is that when this approximation is valid the lock-in threshold $2\pi f_l$ (relative to the rotation rate $2\pi f_s$) determines the amount of skewing of the probability distribution that is observed. The correlation time and strength of the noise only serve to determine the scale of the distribution. Inspection of the results of Vogel *et al.* [6,38–40] shown in Figure 6.4 shows that numerical evaluation of $P_{ss}(\psi,\varepsilon)$ using continued matrix fractions indicates the same results for appropriate parameter values. The implication is that an experiment where coloured noise is applied via a piezoelectric transducer allows an estimation of the lock-in threshold. The skewing expected as a function of the ratio of the rotation rate to lock-in threshold is plotted in Figure 6.3. It is shown that this variation in the ϑ_i could only be useful as a diagnostic tool for small gyroscopes experiencing small rotation rates.

6.3.3 Exact Solution Using Continued Matrix Fractions

The approach to the numerical solution of the Fokker-Planck equation (6.45) is analogous to the method of continued scalar fractions used to solve the Fokker-Planck equation describing the ring-laser gyroscope with additive white noise. However the addition of the stochastic variable $\varepsilon(t)$ means that the scalar recurrence relation is replaced by a vector recurrence relation which is solved in terms

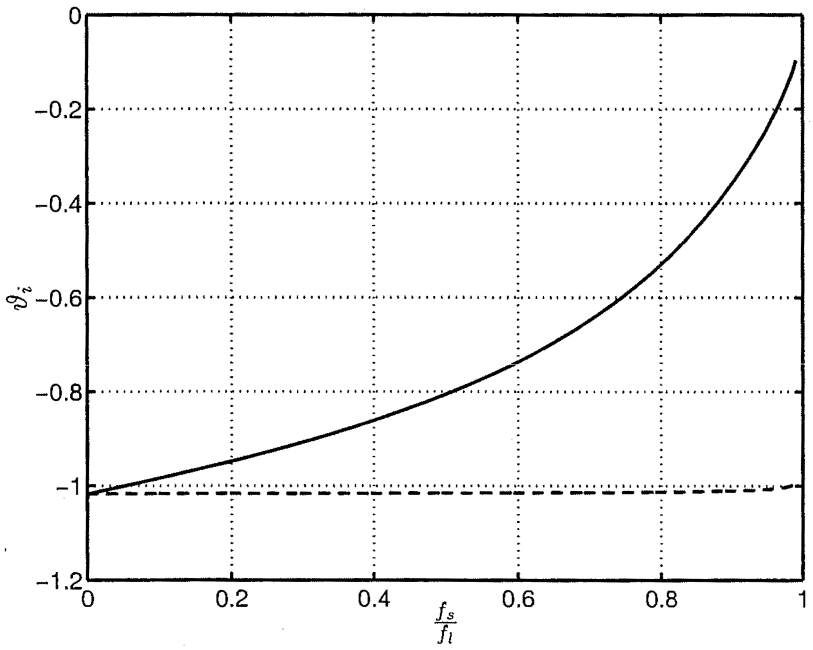

Figure 6.3: Skewing of the bivariate Gaussian approximation of the steady-state probability density as a function of the ratio of the nominal beat frequency to the lock-in threshold. Two nominal beat frequencies are assumed: 0.1 Hz (dashed line) and 10 Hz (solid line).

of matrix fractions. This Section summarises the work of Vogel *et al.* [6, 38, 39] who employed the method of continued matrix fractions to find exact numerical solutions to the Fokker-Planck equation (6.45).

Derivation of Scalar Recurrence Relation

We begin by trying a solution of the form [6, 38, 39]

$$P(t,\psi,\varepsilon) = \frac{1}{\sqrt{2\pi}}\mathcal{H}_0(\varepsilon)\sum_{m=0}^{\infty}\sum_{n=-\infty}^{+\infty} S_{m,n}(t)\mathcal{H}_m(\varepsilon)\exp(in\psi) \tag{6.58}$$

where

$$\mathcal{H}_m(\varepsilon) = N_m \exp\left(-\frac{\varepsilon^2}{4D/\tau_c}\right) H_m\left(\frac{\varepsilon}{\sqrt{2D/\tau_c}}\right). \tag{6.59}$$

The normalisation factor N_m is

$$N_m = \frac{1}{\sqrt{m!2^m}}\left(\frac{2\pi D}{\tau_c}\right)^{-1/4},$$

and H_m are the Hermite polynomials [159, p. 609-616]. Substituting Equation (6.58) into Equation (6.45) results in the differential recurrence relation for the coefficients $S_{m,n}$

$$\begin{aligned}\dot{S}_{m,n} = &-(in2\pi f_s + m/\tau_c)S_{m,n} + \frac{n2\pi f_l}{2}(S_{m,n+1} - S_{m,n-1}) \\ &- in\sqrt{\frac{D}{\tau_c}}\left(\sqrt{m+1}S_{m+1,n} + \sqrt{m}S_{m-1,n}\right).\end{aligned} \tag{6.60}$$

Since P is real

$$S_{m,-n} = S^*_{m,n} \tag{6.61}$$

it is only necessary to solve Equation (6.60) for $n \geq 0$. Defining the vector $\mathbf{S}_m$ by its components

$$(\mathbf{S}_m)_n \equiv S_{m,n}, \tag{6.62}$$

Equation (6.60)can be recast as a three term *vector recurrence relation* as

$$\dot{\mathbf{S}}_m = \mathbf{B}_m\mathbf{S}_{m+1} + \mathbf{A}_m\mathbf{S}_m + \mathbf{C}_m\mathbf{S}_{m-1}, \tag{6.63}$$

where the matrices $\mathbf{A}_m$, $\mathbf{B}_m$, and$\mathbf{C}_m$ are defined by

$$(\mathbf{A}_m)_{n,n'} = -(in2\pi f_s + m/\tau_c)\delta_{n,n'} + \frac{n2\pi f_l}{2}(\delta_{n+1,n'} - \delta_{n-1,n'}), \tag{6.64}$$

$$(\mathbf{B}_m)_{n,n'} = -in\sqrt{\frac{D(m+1)}{\tau_c}}\delta_{n,n'}, \tag{6.65}$$

and

$$(\mathbf{C}_m)_{n,n'} = -in\sqrt{\frac{Dm}{\tau_c}}\delta_{n,n'}. \tag{6.66}$$

Steady-state Probability Distribution: Solution of the Vector Recurrence Relation

In the steady-state $\dot{\mathbf{S}}_\mathbf{m} = 0$, and the vector recurrence relation becomes

$$0 = \mathbf{B}_m\mathbf{S}_{m+1} + \mathbf{A}_m\mathbf{S}_m + \mathbf{C}_m\mathbf{S}_{m-1}. \tag{6.67}$$

The recurrence relation can be solved using the iteration [33, Chapter 9]

$$\mathbf{S}_m = \mathbf{R}_m\mathbf{S}_{m-1} \quad \text{for } m \geq 1. \tag{6.68}$$

which, upon substitution in Equation (6.67), leads to

$$0 = (\mathbf{B}_m\mathbf{R}_{m+1}\mathbf{R}_m + \mathbf{A}_m\mathbf{R}_m + \mathbf{C}_m)\mathbf{S}_{m-1}. \tag{6.69}$$

This equation is satisfied by the infinite matrix continued fraction

$$\mathbf{R}_m = \frac{-\mathbf{C}_m}{\mathbf{A} + \mathbf{B}_m\mathbf{R}_{m+1}}. \tag{6.70}$$

Equations (6.67), (6.68), and (6.70) are the matrix analogues of the scalar expressions (6.26), (6.27), and (6.28). The start vector $\mathbf{S}_0$ is determined from Equation (6.67) for $m = 0$ by observing that $\mathbf{C}_0 = 0$ from (6.66) and using the iteration (6.68) whereupon

$$(\mathbf{A}_0 + \mathbf{B}_0\mathbf{R}_1)\mathbf{S}_0 = 0 \quad \text{with } S_{0,0} = \frac{1}{\sqrt{2\pi}}. \tag{6.71}$$

The recurrence relation is solved for $\mathbf{S}_m$ using downward iteration [33, Chapter 9] approach. The steady-state probability distributions that result from the solutions of the recurrence relation for particular parameter values are shown in Figure 6.4. Increasing the correlation time is seen to markedly increase the ratio of peak height to saddle-point probability densities. This tendency for the phase difference to held to constant values separated by 2π may be interpreted physically a result of the gyroscope showing a stronger tendency to lock for longer noise correlation times. This effect is clearly demonstrated by the calculation of the mean beat frequency with rotation rate given in the next section. The skewing previously described in the minimal diffusion approximation is also seen in the exact numerical solutions. For strongly coloured noise more skewing is observed[4]. At this point it should be noted that it is the statistics of the probability distribution described by Equations (6.48) and (6.49) are the quantities that are examined in more detail in the experimental investigation described in the next Section. The main intention of this Section is to provide a little more understanding of the behaviour of the probability distribution of the phase difference between the counter-propagating waves of a ring-laser gyroscope in the presence of injected coloured noise.

[4]Note that the dependence of the skewing on the noise correlation is not in disagreement with Equation (6.57) since the assumptions required to arrive at Equation (6.57) are violated by the choice of parameters in Figure 6.4.

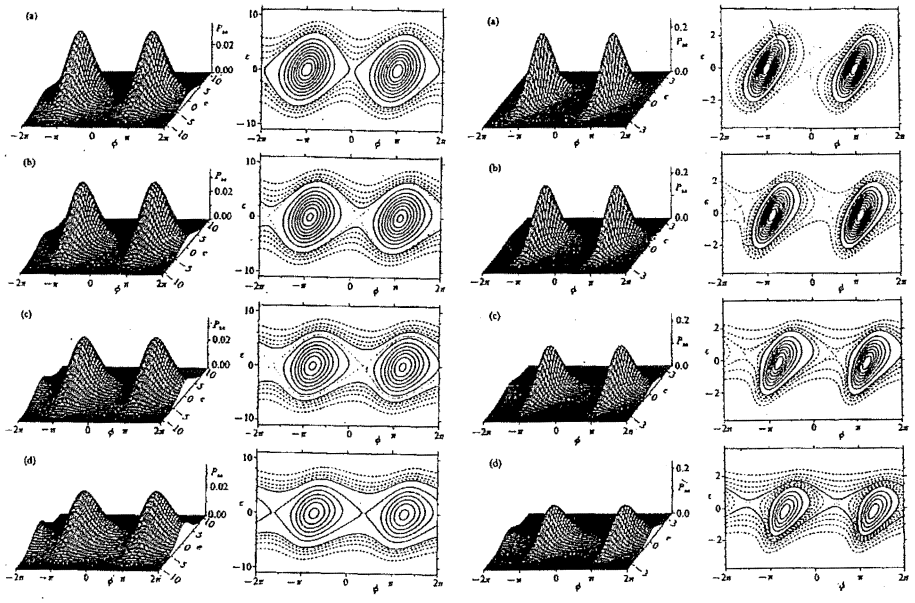

Figure 6.4: Steady probability distributions $P_{ss}(\psi, \varepsilon)$ found using matrix continued fractions. For the left surface plot and corresponding contour map $D = 2\pi f_l = 1$ and the noise correlation time is $\tau_c = 0.1$. In the case of the right surface plot and corresponding contour map $D = 2\pi f_l = 1$ and the noise correlation time is $\tau_c = 1$. In both plots the rotation rate for each of (a), (b), (c), and (d) is $2\pi f_s = 0, 2\pi f_s = 0.5, 2\pi f_s = 1$, and $2\pi f_s = 1.5$ respectively. Reproduced from Vogel *et al.* [6].

Mean Beat Frequency

The skewing of the probability distribution in the presence of additive coloured noise has a significant effect on the lock-in characteristics of the gyroscope. The method required to determine the mean beat frequency is analogous to the white noise case described previously.

Taking the expectation value over all values of $\varepsilon(t)$ and time,

$$\left\langle \left\langle \dot{\psi} \right\rangle_{\varepsilon} \right\rangle_{t} = 2\pi f_s + 2\pi f_l \left\langle \left\langle \sin\psi \right\rangle_{\varepsilon} \right\rangle_{t}. \tag{6.72}$$

If it is assumed that the gyroscope has reached steady-state before measurement is made the mean beat frequency is simply

$$\left\langle \left\langle \dot{\psi} \right\rangle_{\varepsilon} \right\rangle_{t} = \int_{-\pi}^{+\pi} \mathrm{d}\psi \int_{-\infty}^{+\infty} \mathrm{d}\varepsilon \sin\psi P_{ss}(\psi, \varepsilon). \tag{6.73}$$

Using orthogonality of $\mathcal{H}_m$ and substituting (6.58) into Equation (6.73) the mean beat frequency is found to be

$$\left\langle \left\langle \dot{\psi} \right\rangle_{\varepsilon} \right\rangle_{t} = 2\pi f_s - 2\pi f_l \sqrt{2\pi} \Im(S_{0,1}). \tag{6.74}$$

The mean beat frequency as a function of rotation rate for various noise correlation times is plotted in Figure 6.5. As the correlation time of the noise is increased the gyroscope is predicted to exhibit a stronger tendency to lock. In the limit $\tau_c \to \infty$ the deterministic result is recovered. An interesting feature is that for strongly coloured noise ($\tau_c = 10$) the lock-in curve moves below the deterministic curve for certain rotation rates. On the other hand the white noise curve ($\tau_c = 0$) always lies above the deterministic curve.

6.4 Experimental Investigation of Injected Coloured Noise in Ring-laser Gyroscopes

The basic goal of the experimental work presented in this Section is to observe the behaviour of the phase difference between the counter-propagating waves of the locked ring-laser when coloured noise is injected via a piezoelectric transducer bonded to one of the mirrors. The analysis consists of comparing the appropriate sample statistics with the predicted results discussed in the previous Sections that were concerned with the characterisation of the theory of Vogel *et al.* [6, 38–40].

The complete experimental setup is shown in Figure 6.6. Since it is a little complicated the description is divided into two Sections. Section 6.4.1 is dedicated to a description of the approach used to generate and inject the coloured noise into the ring-laser. Section 6.4.2 describes the equipment used to collect the data

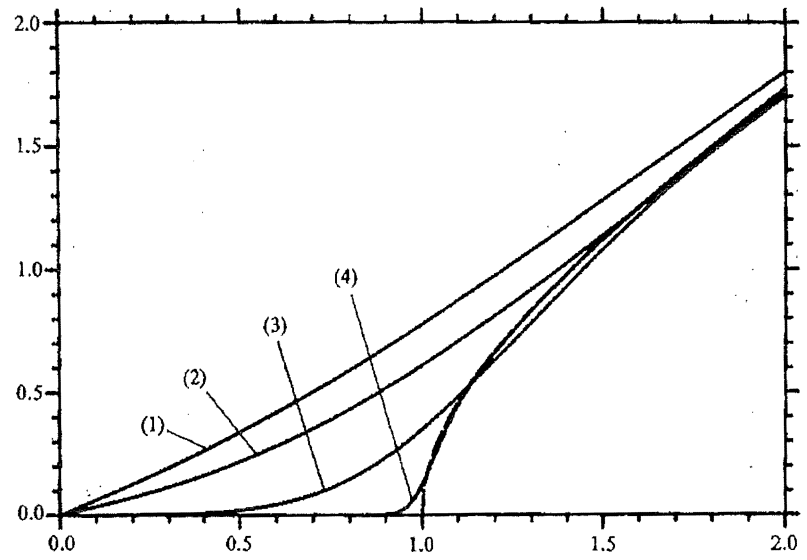

Figure 6.5: Mean beat frequency as a function of rotation rate for $D = 2\pi f_l = 1$ and noise correlation time (1) $\tau_c = 0$, (2) $\tau_c = 1$, (3) $\tau_c = 10$, and (4) $\tau_c = 500$. Reproduced from Ref. [6].

required to evaluate the effect of the coloured noise on the ring-laser gyroscope. The details of the experimental process used to collect the data are described in Section 6.4.3.

Examples of the raw CCD images are presented in Section 6.4.4. The processing that was necessary to compare the experimental results with the predictions made by the coloured noise theory of Vogel *et. al* [6,38–40] is described in Section 6.4.5. The results of this processing are presented in Section 6.4.6. Finally these results are compared with the theoretical predictions in Section 6.4.7.

In order to efficiently organise the LABVIEW^{TM} control program, a three-tier design structure was used. The upper tier consisted of a *test executive* VI. The main role of this VI is to control the various middle-tier subroutines that, in turn, control the bottom-tier which contains the VIs that perform data processing and control the interaction with the external hardware for example. Further discussion of the three-tier approach may be found in Appendix D.2. Since the process of experimental control and data acquisition lends itself to a *state-machine* description this architecture was used in the test executive. Further discussion of the principles and advantages of state-machine design may be found in Appendix D.2.

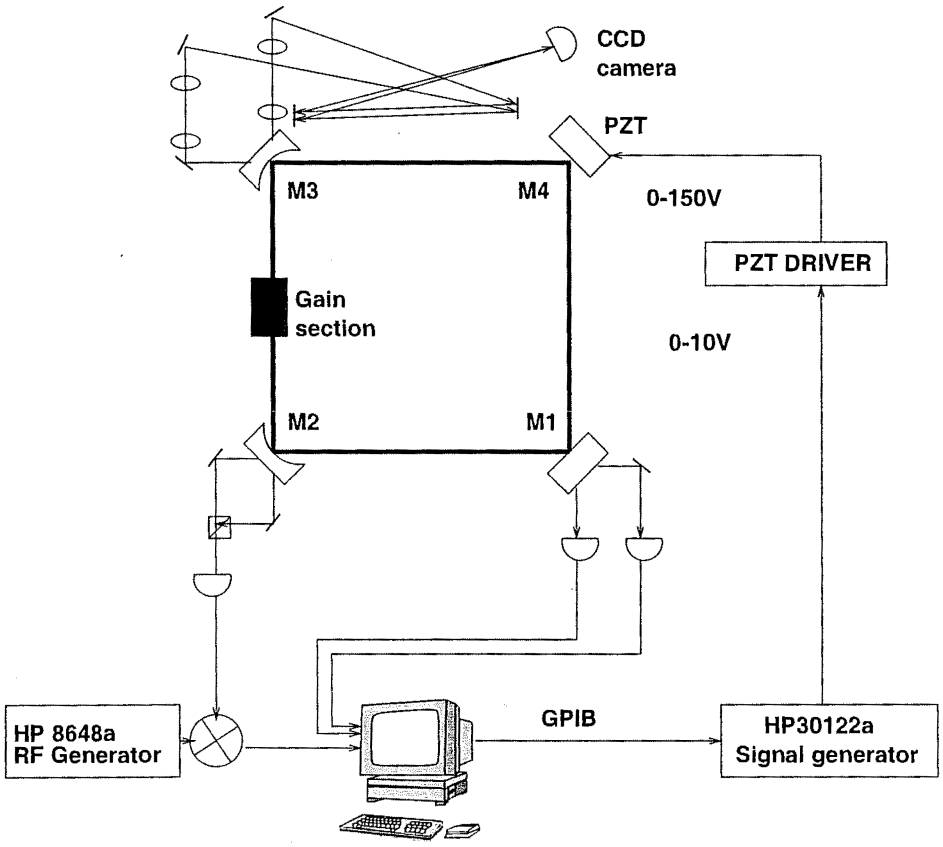

Figure 6.6: Experimental setup for observation of locked phase distribution.

6.4.1 Description of Experiment: Noise Generation

In order to obtain a valid comparison between the experimental observations described in this Chapter and the theoretical predictions of Vogel *et. al* [6,38–40] it is necessary that the injected noise possess the same characteristics as that used to develop the theoretical model. There are two conditions that must be met in order to satisfy this requirement. The first is that the noise waveform that is used to drive the piezo conforms to the requirements defined by Equations (6.32) and (6.33). The second is that the piezo is able to respond in a linear fashion to the maximum frequency component of the signal. If it cannot do this then it will have the effect of a low-pass filter on the control signal. As discussed in Sections 6.4.2 and 6.4.3 the maximum frequency component applied to the piezo in these experiments is only 80 Hz. The frequency response of the piezo is much greater than this. Furthermore testing by the manufacturer shows that the nonlinearity in the piezo displacement as a function of drive voltage is relatively small and is not a concern in comparison with, for example, the significant thermal drifts encountered in C-I.

An effective approach to generating sample sequences of coloured noise data is described in Refs. [160] and [161]. It is shown that a coloured noise sequence may be derived in a straightforward manner using the following sample-to-sample update formula,

$$y(t+\Delta t) = y(t)\exp\left(-\frac{\Delta t}{\tau_c}\right) + \sqrt{2D\tau_c\left(1-\exp\left(-\frac{\Delta t}{\tau_c}\right)\right)}g_i, \qquad (6.75)$$

where g_i is a sample from the Gaussian random distribution. Any term that follows the initial, arbitrarily chosen, term, g_i, in the coloured noise sequence has a contribution due to the initial value that decays exponentially from the initial value with a time constant that is defined by the correlation time of the coloured noise. When Equation (6.75) is used as a sample-to-sample update formula for evenly spaced samples this term acknowledges the fact that coloured noise possesses a correlation function that is not a delta-function. The second term, however, represents the purely stochastic component of coloured since it is a weighted value from the normalised Gaussian distribution. It is clear that any increase in the noise strength D will lead to the coloured noise sequence appearing to be more random in nature. The initial value, $y(t)$, of the experimental noise sequences was set to zero since a zero-mean process is assumed in the theoretical treatment. Figure 6.7 shows some sample realisations of coloured noise processes similar to those used in the experiments described in this Section.

The remaining part of the description of the injection of the coloured noise is concerned with the technique used to take the noise sequence described by Equation (6.75) and convert it into an analogue signal that could be used to drive the piezoelectric transducer. This was achieved by using a number of features of the HP33120A arbitrary waveform generator made by Hewlett Packard. In particular

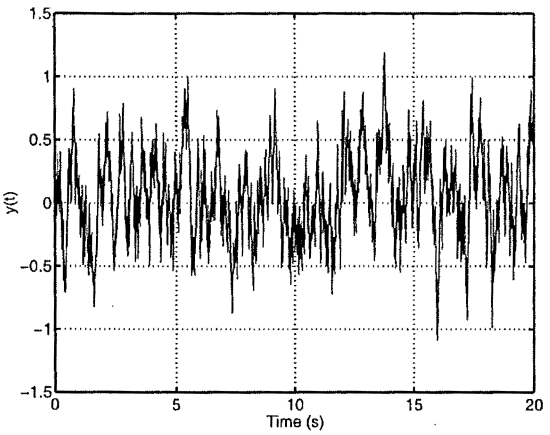

(a)

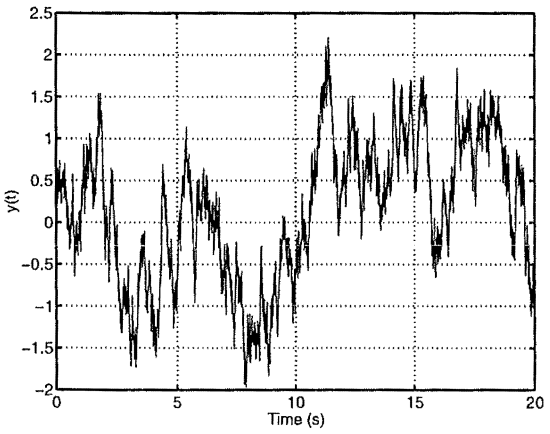

(b)

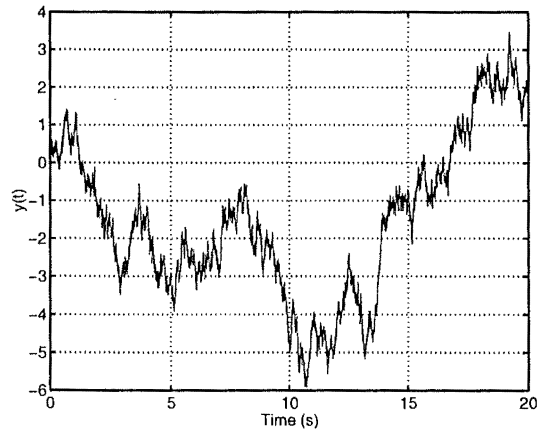

(c)

Figure 6.7: Three sample realisations of coloured noise: (a) $\tau_c = 0.1\,\mathrm{s}$, (b) $\tau_c = 1\,\mathrm{s}$, and (c) $\tau_c = 10$. In all cases the coloured noise strength (see Equation (6.32)) is $D = 10$.

it is possible to upload arbitrary waveforms, represented by a digital sequence up to 16000 thousand samples long, into the memory of the HP33120A. Up to four such waveforms may be stored in the HP33120A memory at any one time. Each of these waveforms may be selected with the same choice of amplitude and frequency parameters that are available for the standard factory-defined waveforms. Upload and control of the waveforms was performed via the HPIB/GPIB bus with LABVIEW^{TM} routines written according to the guidelines presented in Appendix D.2. Therefore the output range of -10–+10 V of the HP33120A was used to provide an analogue input voltage to the piezo controller in the required 0–10 V range. The piezo driver then stepped this voltage up to the range 0–150 V in order to control the displacement of the piezoelectric transducer. The piezo controller also has a manual control. The output voltage due to the manual control and the analogue input are additive. This property was utilised by making use of the manual control to provide an offset that corresponded to half of the output range. The noise sequence from the HP-332120A was zero-mean and the noise amplitude was limited so that the analogue input was always with the range -5–+5 V.

6.4.2 Description of Experiment: Data Acquisition

There are three parts to the data acquisition setup. The fundamental component is the CCD camera that was mounted, along with the necessary matching optics, at mirror $M3$. In addition the intensities of each of the counter-propagating beams were recorded at mirror $M1$. This made it possible to check that there was little or no correlation between the beam intensities and the observed fringe pattern in the regime that the laser operated in. If this were the case then the theoretical model based on Equation (3.22) which, as described in Section 3.4.1, depends on the assumption of constant intensities, would have to be called into question. Furthermore if there was significant drift in the power of either of the beams in a particular run that data set was discarded. At this point it is pertinent to note that in order for C-I to be operated well within the locked regime it was necessary that the mirrors were much more contaminated than is the case with normal operation. Therefore the discussion in this Chapter does not in anyway contradict the findings of Chapter 3 which is concerned with the operation of C-II far away from the locking region. Finally, since the theory depends on the assumption of a single longitudinal mode, it was necessary to monitor for the presence of more than one longitudinal mode. This was done using the RF-beat method described in Section 3.1. The frequency of the HP8648a RF signal generator was set such that the beat with any FSR signal would be in a range of a few hundred Hertz. This beat signal was monitored using the analogue input of the PC data-acquisition card to record the FSR beat signal. The PC data acquisition card was a National Instruments 16-bit card—PCI 16-XE-50.

The use of the CCD is now considered in more detail. The CCD camera (Electrim

EDC-1000) was used to record the fringe pattern created by the overlap of the counter-propagating beams. When the counter-propagating beams are completely locked together the phase difference between the beams is constant and a static fringe pattern is expected. When pathlength noise is injected the phase difference between the counter-propagating beams will change, causing the fringe pattern to move about on the CCD chip. As long as the noise power is small enough to avoid any momentary unlocking of gyroscope, leading to 2π phase jumps, all movement of the fringe pattern will be about the fringe position that defines the peak of the probability distribution of the phase differences between the counter-propagating beams. The extended beam path between the exit ports of the gyroscope and the CCD camera allowed the angle of incidence between the incoming beams to be reduced. The smaller the angle of incidence the wider the observed fringes were. The beam path and position of the two mirrors that followed the beam expander for each beam were adjusted in order to obtain ~ 12 fringes across the width of the CCD camera. The area of CCD chip is $6.97\,\mathrm{mm}^2$ with 192 pixels in the horizontal direction and 162 pixels in the vertical direction. Since the various optical components were aligned to ensure that the fringes were vertical there were $\approx \frac{192}{12} = 16$ pixels per fringe period. The spatial sampling rate is therefore 72727 pixels/mm. The Nyquist limit is therefore $\approx$ 36300 pixels/mm. The matching optics generated a spatial frequency of the fringe waveform of $\approx$ 6000 pixels/mm—well below the Nyquist limit. Therefore a good balance between spatial resolution and obtaining a sufficient number of periods in order to make a good estimate of the relative phase difference was achieved. The lens arrangement placed in the path of both beams acted as a beam expander. The aim of this was to provide reasonably uniform illumination across the entire CCD chip surface. In order to minimise the effects of stray light an adjustable aperture and 633 nm interference filter were placed immediately in front of the CCD camera.

Since the CCD chip is recessed into the camera housing it was not easy to align the beam directly onto the CCD camera. Therefore both beams were superimposed on a screen placed close to the plane of the CCD chip for alignment purposes. The CCD was mounted on a kinematic mount so the camera and screen could be interchanged with ease. The CCD camera was held by a rotating mount with the axis of rotation parallel to the beam path. Once an image was formed the camera was rotated so that the fringes were vertical.

The RF frequency (32.0000 MHz) and pumping power were kept the same throughout the experiment.

6.4.3 Description of the Experiment: Process

An overview of the experimental process is presented in Figure 6.8. The general approach was to capture as many images as possible during a period specified by the length of the data set uploaded to the HP33120A. In order to avoid any false

correlations between the observed fringe patterns and injected noise waveforms the maximum data acquisition time was determined by the number of samples (16000) that may be used to define each arbitrary waveform that may be uploaded to the HP33120A waveform generator. Two HP33120A output frequency settings used; 10 mHz and 2 mHz. If the HP33120A output frequency was 10 mHz it took 100 s to output one complete period of the coloured noise sample sequence stored in the HP33120A memory. Since the waveform pattern contained 16000 samples the analogue coloured noise signal was generated at a rate of 160 samples/s. Similarly, if the output frequency of the coloured noise sequence was 2 mHz correspond the digitised sequence of data values was converted to an analogue signal at a rate of 32 samples/s. An appropriate anti-alias filter was placed between the HP33120A output and the piezo controller at all times. It is essential that the frequency band corresponding to the noise correlation time is less than the value set by the Nyquist limit of the sampling output rate. It is preferable that the correlation bandwidth be somewhat less than this limit in order for the signal driving the piezo to give a good representation of the continuous coloured noise process. It is also required that the acquisition time includes a sufficient number of correlation times in order for the measured phase distribution to reflect the effects due to action over the full range of the noise process. This places a limit on the maximum correlation time that may be investigated with a pre-defined acquisition time. In the data reported here the maximum correlation time is 10 s with a total acquisition time of 500 s. This is sufficient in order to obtain a reasonable sample of the full effects of the coloured noise. The signal output parameters for the data sets collected at each correlation time are summarised in Table 6.1.

An exposure of approximately 20–30 ms was used to obtain each image. This was value was chosen by operating the laser at the highest power possible in order to minimise the exposure time while maintaining an adequate signal. In addition to the exposure time there was a delay of the order of 100 ms in the retrieval of each image. This limited the acquisition rate to approximately 8 frames per second. The delay was kept to a minimum by employing approaches such as streaming all the images into a single file which remained open for the entire acquisition period. Each image was extracted from the large file during post-processing. This avoided the overhead associated with opening and closing files.

During development a software timer was used to determine if the total acquisition time, at which point the program would stop acquiring images and begin processing the data, had been reached. This consisted of a simple polling of the PC clock and comparison with the start time to determine if the required elapsed time had been reached. It was observed that the actual acquisition time was significantly longer (up to 50%) than it should have been. It was determined that the heavy process load associated with constant image acquisition was interfering with the PC clock. It is well documented that a PC clock has a precision of the order of 1 ms that varies a little depending on the operating system. However it

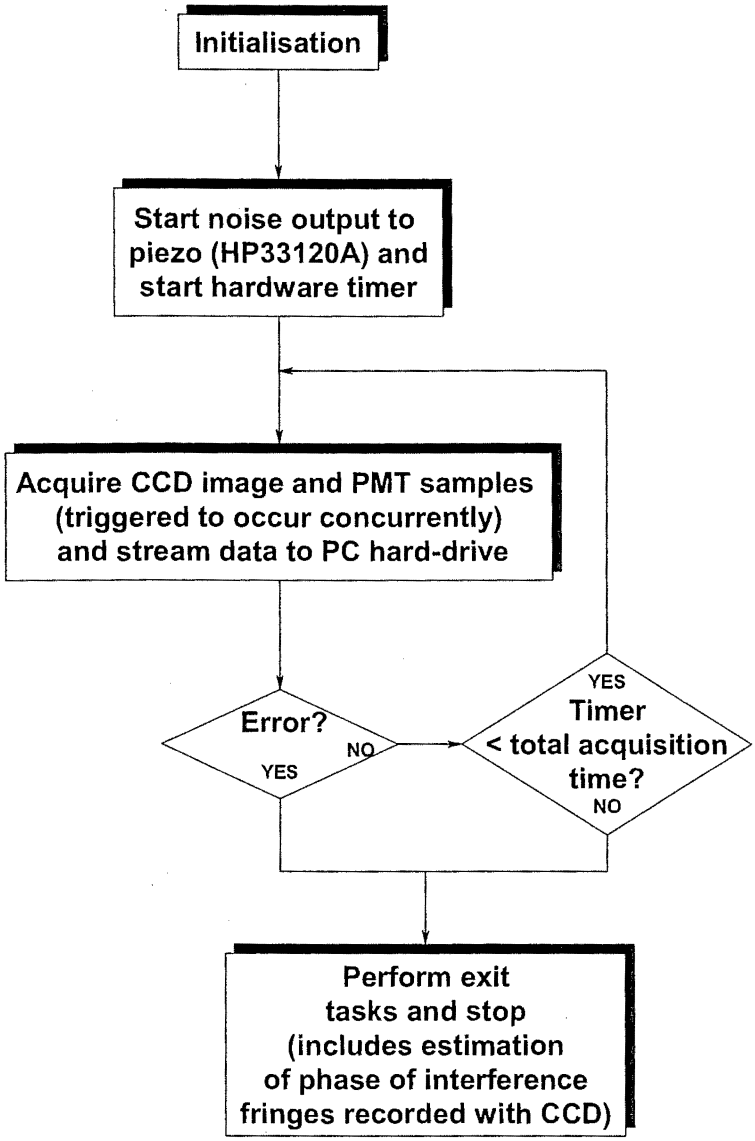

Figure 6.8: Schematic of data acquisition process for steady state phase distribution. For the sake of clarity the variety of initialisation procedures required are not described in detail. These do not have any bearing on the final results.

Correlation time τ_c (s)	Length (s)	Approx. frames	samples/sec
0.1	100	800	160
0.5	100	800	160
1	100	800	160
1	500	4000	32
2	500	4000	32
5	500	4000	32
10	500	4000	32

Table 6.1: Parameters used to sample output correlation time noise.

was unexpected that such substantial inaccuracy in timing occurred over a period of 100–500 s. The solution to this problem was found by resorting to hardware timing of the acquisition period. A 10 Hz TTL signal from a waveform generator was sent to the counter input of the data acquisition card. When the number of counts reached 10 times the desired acquisition time CCD image capture was stopped. Since the counter clock is in the PC data-acquisition card and completely independent of the PC clock the problem associated with software timing was completely eliminated.

The behaviour of the phase difference distribution with varying correlation time τ_c and the noise strength D is the quantity of interest. In the investigation of the variation of the phase distribution statistics with noise strength the values of D were chosen to be 0.1, 0.2, 0.4, 0.6, 0.8, and 1. The correlation time was 0.5 s. For the complementary investigation of change of the phase distribution statistics with correlation time, τ_c was set to the values 0.02 0.05 0.1, 05, 1, 2, 5, and 10. The noise strength was set to 0.4. It should be noted that, since the pathlength is uncalibrated, the noise strength is also uncalibrated. In order to properly calibrate the the noise strength at the moving mirror a calibration of pathlength variation for a given piezo control voltage is required. Calibrations based on the FSR method were rejected on the basis of the finding in Section 3.1 that this method could be unreliable. In the case of C-I, unlike C-II, the piezo did not move far enough to infer a calibration from the separation of longitudinal mode hops.

It was important that the environment was as "quiet as possible". When locked the ring-laser is sensitive to vibration. For example when the vacuum pumps were operating the phase distribution was almost uniform.

6.4.4 Experimental Observations: Examples of Raw CCD Images

Figure 6.9 shows an example of a raw fringe pattern. The position of the fringe pattern on the CCD chip is dependent on the pathlength difference between the

counter-propagating beams. Since there is a constant component of the phase difference that arises from the difference in paths outside the ring-laser cavity all measurements of changes in the phase difference between the counter-propagating beams only provide information on the fluctuations in the phase difference between the counter-propagating beams within the cavity. In addition to the vertical interference pattern resulting from the superposition of the counter-propagating beams there is a circular interference pattern with an origin beyond the bottom right-hand corner of the Figure. This was due to the matching optics and was not able to be removed. There are also several dead spots on the CCD chip where individual pixels have failed.

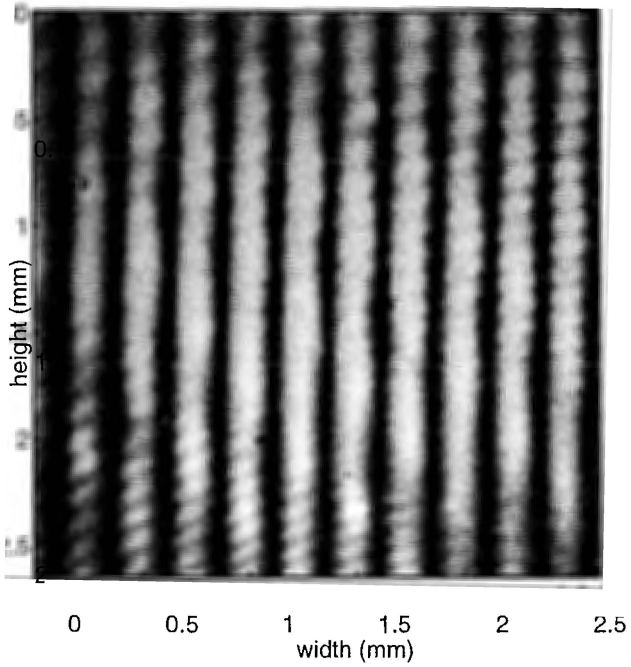

Figure 6.9: Example fringe pattern formed by the superposition of the counter-propagating waves in a locked ring-laser gyroscope. The pattern is a greyscale image of raw 8-bit image data recorded with the Electrim EDC-1000 CCD camera via the LABVIEW^{TM} control software developed for the experiment.

6.4.5 Data Processing

The various steps of the data-processing necessary to obtain a phase estimate from the interference fringes recorded with the CCD camera that mirrors the fluctuations in the phase difference between the counter-propagating beams gives some insight into the relationship between the experiment described in the previous section and the theoretical account presented earlier in the Chapter. In this Section the processing steps required to obtain data in a form that may be compared with the theoretical predictions are described.

The first phase of data processing was performed immediately after a data acquisition for a particular set of noise parameters. This was necessary because each of these data sets consisted of approximately 800 images. Since each image is 31.5 kbytes, a prohibitively large amount of data would have been collected had the raw images been archived. As previously stated, all of the images for a data acquisition run were stored in a single file in order to speed-up the image acquisition rate by reducing the time the PC was required to spend opening and closing files. Therefore the first step in the processing procedure was to recover the individual images from the large data file. This was done image by image with the processing for each image being performed before the next image was retrieved.

The first step in the processing of each image was to pass it through a median filter (See Appendix B.4). This removed salt and pepper noise due to "dead" CCD pixels while preserving the interference pattern with a "slow" spatial variation. Figure 6.10 shows the effect of applying the rank–4 median filter to the example fringe pattern shown in Figure 6.9.

The next step in the data processing was to sum over each column of pixels. This resulted in a clean sinusoidal waveform with an amplitude envelope that is related to the transverse irradiance variation of the beams across the CCD chip. An example of the column sum is shown in Figure 6.11.

In addition to the CCD images a separate file was used to store single beam PMT data, FSR beat frequency data, and the noise waveform. Since the acquisition of these data was triggered at the start of the CCD image acquisition these data were matched with their corresponding image to within 1 ms. Each set of waveform data was sampled at 5000 samples/s for a time equal to the CCD exposure time. Since no such correlations were observed these data will not be discussed any further.

The fluctuations in the phase difference between the counter-propagating waves were calculated from the column sum. In a nutshell the approach consisted of finding the phase difference between a column sum like the example shown in Figure 6.11 and a reference sine wave of the same spatial frequency as the column sum. The phase difference was calculated using the *cross-spectral density* which is described in Appendix B.1. The cross-spectral density may be used to obtain a robust estimate of the phase difference between two waveforms even in the presence of substantial noise. In particular the amplitude envelope did not impact on the cross-spectral density phase difference estimates where, on the other hand, it was found that the amplitude could introduce inaccuracy if curve fitting was used to estimate the phase difference between the column sum and the reference waveform. The cross-spectral density estimate for the example fringe pattern given in Figure 6.10 is shown in Figure 6.12.

The use of the cross-spectral density to estimate the phase difference between

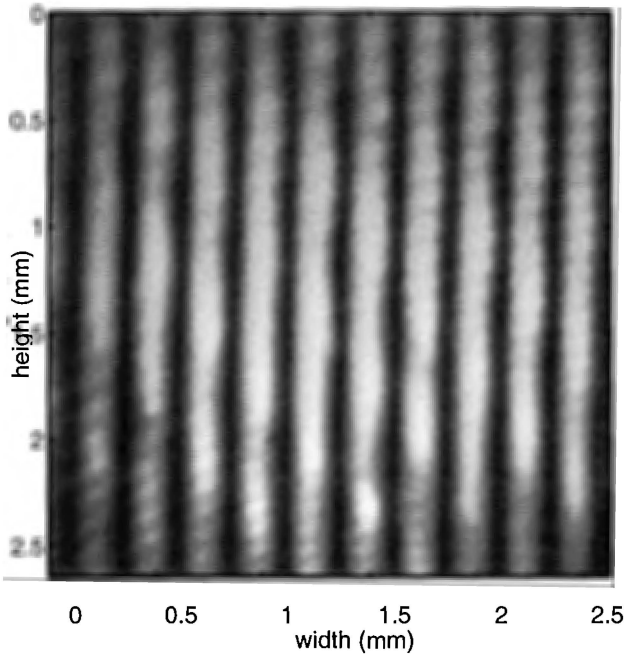

Figure 6.10: Example fringe pattern formed by counter-propagating beams in a locked ring-laser processed using a rank-4 median filter.

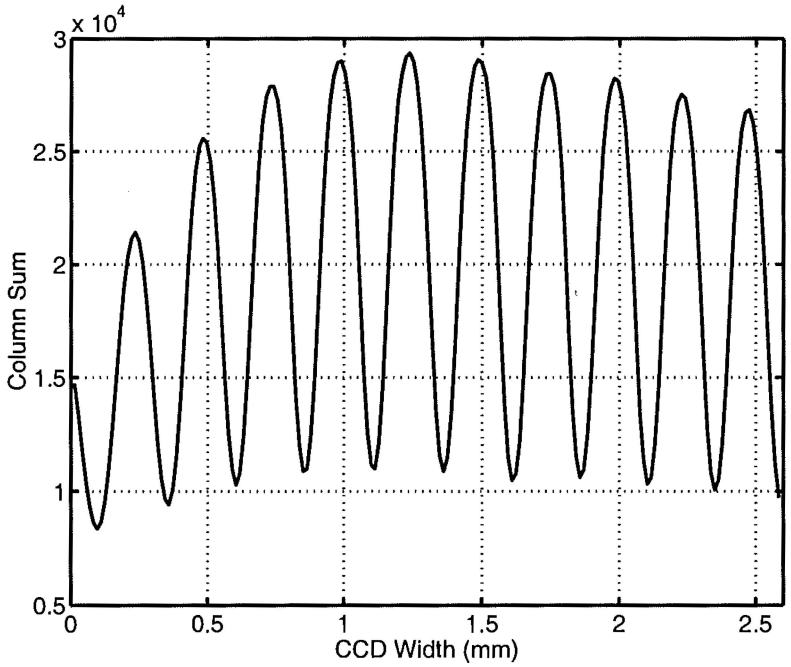

Figure 6.11: Sum of the columns of the fringe pattern 6.10.

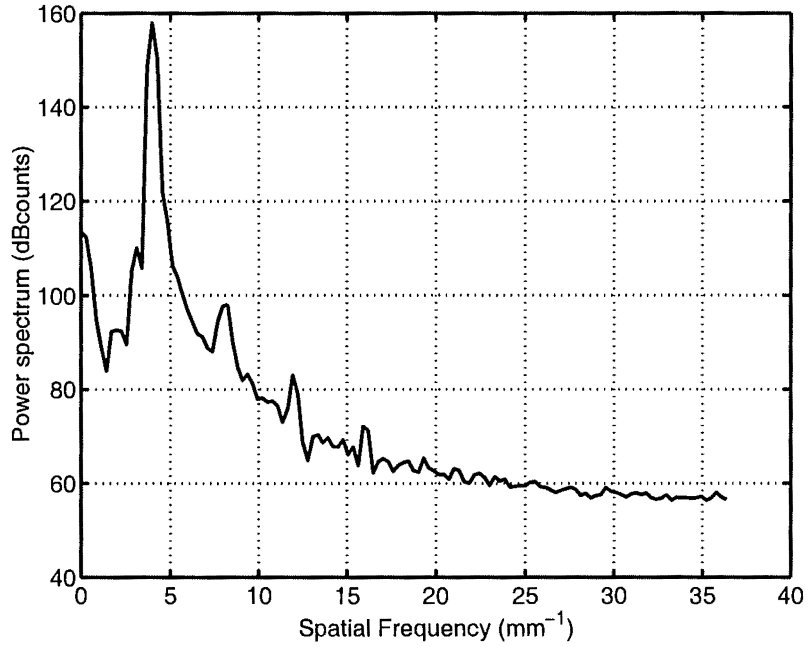

(a)

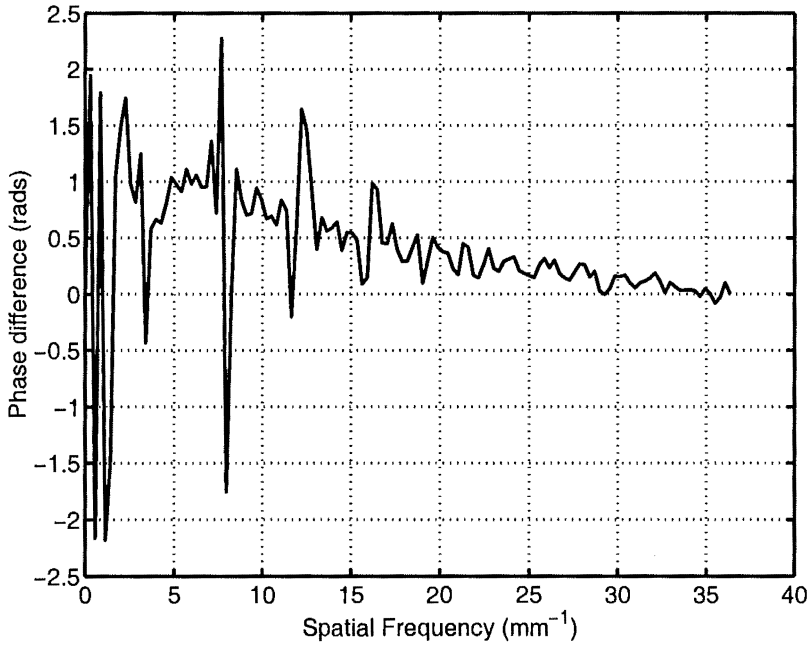

(b)

Figure 6.12: Example of the cross-spectral density estimation of phase. The real part (a) of the cross-spectral density indicates the frequency component f_0 with the most power. The argument (b) of the cross-spectral density estimate shows the phase difference between the reference waveform and the column sum of the CCD image over a range of frequency bands. Calculation of the phase difference at $f = f_0$ for this example results in a phase difference of 0.6628 rads between the reference waveform and the column sum of the fringe pattern on the CCD chip.

the counter-propagating waves is now discussed in more detail. Consider the mathematical representation of the column sum $y(x)$ and the reference waveform $w(x)$,

$$w(x) = \sqrt{2} y_{\text{RMS}}(2\pi f_0 x + \phi_0) \tag{6.76}$$

$$y_i(x) = A_i(x)(2\pi f_0 x + \phi_0 + \phi_i) \tag{6.77}$$

where $A_i(x)$ is the low frequency modulation envelope, f_0 is the spatial frequency, ϕ_0 is the phase offset of the reference waveform, and $\langle \phi_i \rangle$ is the estimate of the phase difference between the column and the reference waveform for the i-th image. The amplitude y_{RMS} was estimated from the RMS value of the column sum.

Since the cross-spectral density estimate provides a phase angle between $-\pi$ and π it was necessary to ensure that the phase of the reference waveform was closely matched to the column sum in order to avoid spurious results due to phase-jumps arising from the processing. In other words, it was required that, on the average, ϕ_i be close to zero. To this end each set of phase estimates was calculated twice. The first time the phase offset ϕ_0 of the reference waveform is initially taken to be zero. After the phase $\langle \phi_i \rangle$ for each image in the data set is calculated the reference phase offset for the next is image is taken as the mean of all images calculated at that point. Obviously the set of phases that results from this is meaningless. Hence the estimated phase differences were estimated again using the final value of the running mean of first the set of estimates ψ_i as the reference offset ϕ_0. The experimental steady state phase difference of the i-th image, $\langle \psi_{i,e} \rangle = \phi_0 + \langle \phi_i \rangle$, is related to the theoretical steady-state phase difference ψ_{ss} between the counter-propagating waves within the cavity by an unknown additive constant. The data analysis required that there be no apparent drift in the phase difference between the counter-propagating waves within a data set for a particular pair of noise parameters.

Once $\langle \psi_{i,e} \rangle$ has been calculated for all images for a given pair of noise parameters the statistics described by Equations (6.48) and (6.49) were calculated. The statistic $\langle \psi^2 \rangle - \phi_0^2$ was calculated using two equivalent methods. The mean and variance, with associated 95% confidence intervals, were calculated from a fit to the normal distribution using the MATLAB routine *normfit*. The 95% confidence intervals were also calculated in order assess the quality of the estimate. The confidence intervals are shown graphs reporting the results for this statistic in the next Section. The sample variance was compared to the estimate from the fitting procedure as a check on the results of the data processing. Both methods gave results that were in good agreement. A different approach was required in order to estimate the statistic $\langle \varepsilon^2 \rangle$. Each data set for a pair of noise parameters was binned into a two-dimensional histogram. The integral described was by Equation (6.52) was performed numerically. It was then possible to determine $\langle \varepsilon^2 \rangle$ by performing a Gaussian simplex fit to the marginal probability distribution using the MATLAB function *fminsearch*. The error bars were determined somewhat arbitrarily by

evaluating the range of $\langle \varepsilon^2 \rangle$ with a 5% error assigned to each numerical integration required to obtain the marginal probability distribution.

6.4.6 Results: Processed Data

The behaviour of the statistics $\langle \psi^2 \rangle - \phi_0^2$ and $\langle \varepsilon^2 \rangle$ as the noise strength D and correlation time τ_c is varied is described in this Section. The quantity ϕ_0 appears on the axis labels. This is experimentally determined from the phase difference between the reference waveform and the column sum of the fringe pattern. The actual steady-state phase difference between $\psi_{ss}$the beams within the cavity differs from ϕ_0 by an additive constant which depends on the path difference between counter-propagating beams that is external to the cavity. Figure 6.13 shows the

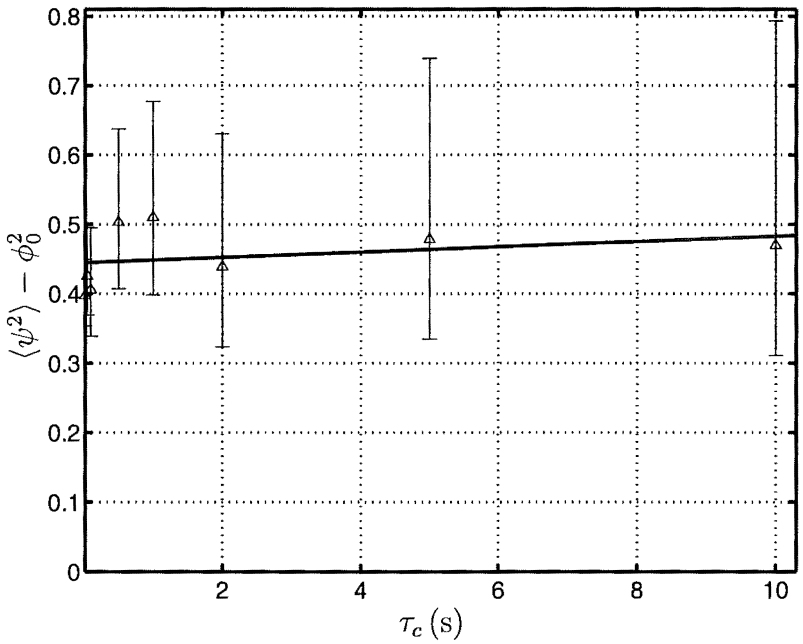

Figure 6.13: Variation of $\langle \psi^2 \rangle - \psi_e^2$ with noise colour.

variation of $\langle \psi^2 \rangle - \phi_0^2$ with the noise colour. A noise strength of 4 was used to obtain these results. The best fit line is $\langle \psi^2 \rangle - \phi_0^2 = (0.004 \pm 0.005)\tau_c + (0.438 \pm 0.021)$.

Figure 6.14 shows the variation of $\langle \varepsilon^2 \rangle$ with noise colour. Once again a noise strength of $D = 4$ was used. The best-fit relationship, $\langle \varepsilon^2 \rangle = 2.319 + 0.048/\tau_c$, was found using the MATLAB *fminsearch* simplex algorithm.

Figure 6.15 shows the behaviour of the distribution of phase differences as the noise strength is varied. The correlation time was 0.5 s. A least-squares fit yielded the result $\langle \psi^2 \rangle - \phi_0^2 = (0.539 \pm 0.049)D + (0.350 \pm 0.017)$.

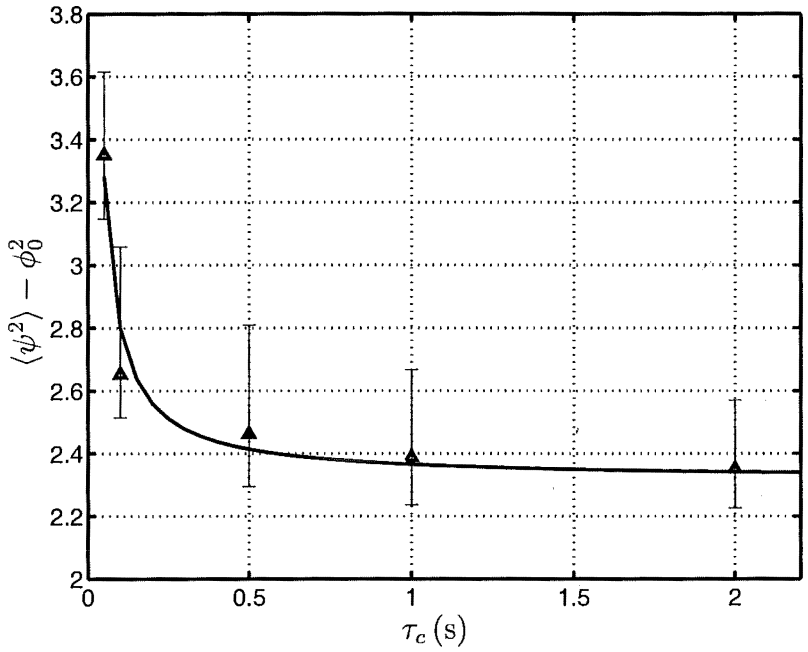

Figure 6.14: Variation of $\langle\varepsilon^2\rangle$ with noise colour.

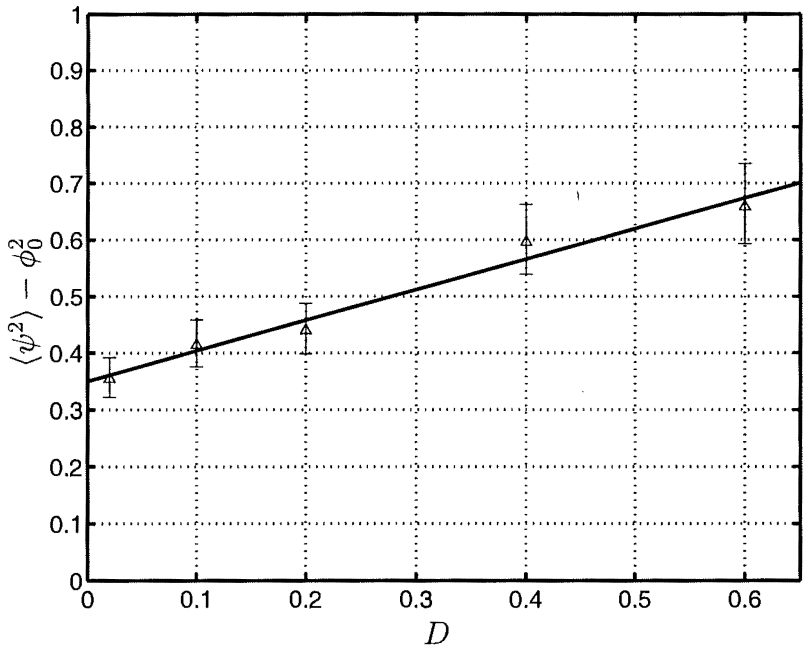

Figure 6.15: Variation of $\langle\psi^2\rangle - \phi_0^2$ with noise strength.

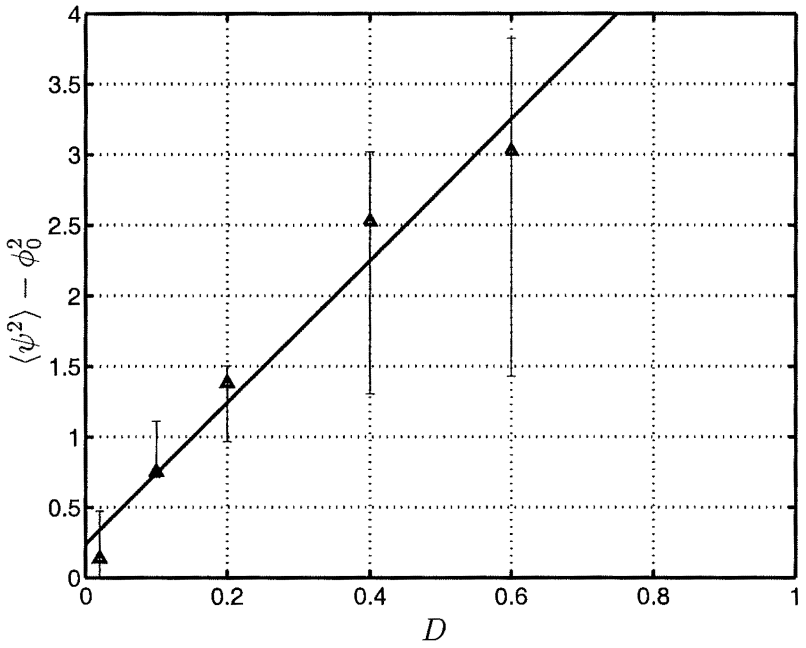

Figure 6.16: Variation of $\langle\varepsilon^2\rangle$ with noise strength.

Figure 6.16 shows the behaviour of $\langle\varepsilon^2\rangle$ as the noise strength is varied. Once again $\tau_c = 0.5$. A fit of $\langle\varepsilon^2\rangle = (5.02 \pm 0.53)D + (0.23 \pm 0.18)$ resulted from a least-squares fit.

6.4.7 Comparison of Experimental Results with Theoretical Predictions

Figure 6.13 shows no variation of $\langle\psi^2\rangle - \phi_0^2$ with correlation time τ_c. This is in agreement with the expected behaviour of this quantity predicted by Equation (6.48). Since the noise strength used to obtain the results in this Figure was chosen because it was found by trial-and-error to be a suitable value and is uncalibrated, it is not possible to draw any conclusions from the value of the intercept.

Figure 6.14 demonstrates that the variance of the stochastic variable ε is inversely proportional to the correlation τ_c. In this case the observations are in agreement with the predictions of Equation (6.49).

According to Equation (6.48) a line that passes through the origin of Figure 6.15 is expected. Although the linear behaviour is observed the data clearly do not pass through the origin. This is attributed to residual background vibrations which mean that it is impossible to obtain a distribution of arbitrarily small variance even if no noise is injected into the cavity. For the values of D and τ_c in Figure 6.15

that are equal with the values of D and τ_c in Figure 6.13 the variance is a little smaller than that of in Figure 6.13 than in Figure 6.15. This may be a result of the influence of the ambient vibrations. Since the data were recorded at different times it is expected that there should be a small variation in the magnitude of the ambient vibrations.

Figure 6.16 shows the linear relationship between $\langle \varepsilon^2 \rangle$ that is predicted by Equation (6.49). For the values of D and τ_c in Figure 6.16 that are equal with the values of D and τ_c in Figure 6.14 the variances in Figures 6.14 and 6.16 are in agreement.

Unfortunately it was not possible to compare the experimental behaviour of the phase distributions with the predictions in a fully quantitative manner. This is a result of being unable to determine a reliable calibration of the displacement of the piezoelectric transducer with drive voltage. The reasons for this problem were discussed in Sections 6.4.1 and 3.1. However, within the limitations imposed by the absence of a reliable piezo calibration, all results are in good agreement with the predictions of Equations (6.48) and (6.49). Therefore it might reasonably be inferred that in this initial experimental investigation of coloured noise in ring-lasers that the theory of Vogel *et al.* [6, 38–40] does indeed describe the behaviour of ring-lasers in the locked regime. However it is an open question as to whether or not the theory provides an accurate description of an unlocked ring-laser with injected coloured noise. This is because the assumptions required to arrive at Equation (3.22), which is a basic equation in the coloured noise theory, are unlikely to be fulfilled with a ring-laser gyroscope operating in the unlocked regime. The reasons for this were discussed in Chapter 3.

Chapter 7

Conclusion

In this thesis I have explored a number of avenues which all, in some way, may be employed to optimise the performance of a ring-laser gyroscopes. Furthermore, performance criteria, by which the optimisation process may be assessed, have been developed.

It was found that it was possible to operate C-I at a higher optical power while maintaining single mode operation by increasing the gas pressure so that homogeneous broadening became dominant. The advantage of increasing the optical power is that there is a reduction in the white frequency noise due to spontaneous emission. These results were in agreement with a previous study using GO [2]. A characteristic region that appeared to support single mode operation where it might not have been expected was characterised. Two possible explanations of such a region of apparent single mode operation were proposed. Unfortunately there were insufficient data to differentiate between each explanation. However the steps that are necessary to proceed in the investigation were outlined. In particular it was noted that the presence of longitudinal modes separated by two FSR from the dominant longitudinal mode should be monitored as well as the presence of adjacent longitudinal modes.

In Chapter 3 cross-pushing of the counter-propagating waves in the presence of unequal powers for the counter-propagating beams was found to play a significant role in determining the amount of pushing and pulling of the gyroscope beat frequency when inhomogeneous broadening is dominant. The amount of pulling predicted by the cross-pushing contribution to the third-order theory of the laser was found to be in reasonable agreement with observation. This indicates that cross-pushing must be included in any models attempting to investigate the effects of backscatter as the cavity perimeter changes. Since it was found in Chapter 2 that it is advantageous to operate the laser in the homogeneously broadened regime useful further work would include a study of cross-pushing in the homogeneously broadened regime with a view to ascertaining if it plays a similarly important role in the determination of the observed pushing and pulling. One issue that is not well understood is the mechanism that causes the relative powers of the counter-propagating modes to change in a cyclic fashion as the

cavity perimeter is scanned through several wavelengths. Further consideration of this may yield the understanding necessary to control this parameter and hence reduce the drift in the gyroscope beat frequency due to cross-pushing.

Chapter 4 classified the $1/f^{\alpha}$ noise sources observed in C-II when the gyroscope beat frequency drift was found to be strongly correlated with atmospheric pressure changes. In particular it was found that the fractional Brownian motion (fBm) model described the processes well. An initial investigation of how knowledge of the drift process may be used in any stabilisation scheme was made. To the author's knowledge the concept of tailoring the spectral characteristics of a drift process in order to optimise resolution, as discussed in Chapter 4, is novel. In practice it may prove difficult to implement such tailoring. Understanding and modelling drift processes is a non-trivial exercise. The potential benefits of further work probably do not justify the effort required in terms of the goals of the Canterbury ring-laser project since there are other, less speculative, avenues which may be explored to improve the the resolution of Earth rotation. However it is an interesting problem from an intellectual and experimental control theory point of view that has potential application well beyond the field of ring-laser gyroscopes.

However the noise strength of the drift processes is of critical importance to the optimisation of the ring-laser. If it is necessary that the maximum averaging time be increased then the only course of action is to reduce the noise power of the drift processes. As long as the criterion (5.81) that states the noise introduced on a given timescale by any stabilisation process is less than the quantum-limited white noise contribution for that averaging time then the noise characteristics of the stabilisation scheme are irrelevant in terms of the performance on timescales less than the optimal averaging time τ_0. Therefore there is freedom to design the stabilisation scheme in a manner that inhibits the drift processes even if the design does not lead to the minimum possible introduced noise on timescales less than τ_0. In this the way the noise power in the drift process may be reduced further than it would by the simple "compare and correct" stabilisation method described in Chapter 5. This will lead to commensurate increase in the optimal averaging time τ_0 as described by Equation (4.13) and the desired improvement in the resolution of Earth rotation.

The optical frequency stabilisation of C-II was described and analysed. A performance criterion that stated the maximum amount of noise a stabilisation scheme may introduce without degrading short-term performance was deduced. Alternative stabilisation methods were described.

Finally an initial investigation of the behaviour of ring-lasers when operating in the locked regime in the presence of injected coloured noise was performed. It was found that the statistics relating to the variance of the phase difference between the counter-propagating waves and the stochastic variable describing the noise

input were in agreement with the theoretical predictions. This would appear to be the first experimental support for the coloured noise theory of Vogel *et al.* [6, 38–40] in a locked ring-laser gyroscope. Further work might include the testing of the coloured noise theory when the laser is unlocked since operation in this region is of much more interest than operation in the locked region.

Appendix A

Statistics of Stochastic Processes

A.1 The Ensemble Average

Since the random process $x(t)$ does not depend on t deterministically its values must be described statistically by a probability distributed or probability density. For each time t, $x(t)$ is a random variable with probability density $p(x,t)$ where

$$\int_{-\infty}^{\infty} p(x,t) = 1, \tag{A.1}$$

as usual for a probability density. However the time dependent probability density $p(x,t)$ does differ from the time-independent probability density $p(x)$ in that it stands for an *infinite family* of probability distributions rather than a single probability distribution. The expectation of x at time t is given by

$$\langle x(t) \rangle = \int_{-\infty}^{\infty} xp(x,t)\ \mathrm{d}x. \tag{A.2}$$

Alternatively, the set of all possible realisations of the function $x(t)$ may be considered. The countable collection of all possible realisations is known as the *ensemble* of $x(t)$. If each realisation is labelled ${}^{(1)}x(t)$, ${}^{(2)}x(t), \ldots$ the average or expectation of x at time t is formed by averaging over the ensemble of all realisations,

$$\langle x(t) \rangle = \lim_{N\to\infty} \frac{1}{N} \sum_{r=1}^{N} {}^{(r)}x(t). \tag{A.3}$$

In practice the difference between the definitions (A.2) and (A.3) is insignificant. However in the case of small data sets, for example, it may be necessary to consider the difference between the definitions (A.2) and (A.3).

A.2 Moments

The *r'th moment* of x is defined in terms of the probability distribution $p(x)$ as

$$\upsilon_r \equiv \langle x^r \rangle = \int_{-\infty}^{\infty} x^r p(x)\, \mathrm{d}x. \tag{A.4}$$

The mean $\langle x \rangle$ is simply the first moment υ_1. Equation (A.4) defines the moments of x about the origin. However it is generally more useful to consider the *central moments*, μ_r, given by

$$\mu_r \equiv \langle (x - \langle x \rangle)^r \rangle = \int (x - \langle x \rangle)^r p(x)\, \mathrm{d}x. \tag{A.5}$$

The *central moment* is the moment about the mean value of x. By definition $\mu_1 = 0$. The second central moment μ_2 is known as the *variance* or the *mean-squared deviation* or the *dispersion.* It is important because it provides a measure of the width of the probability density. The square root of the variance is known as the *root-mean-squared deviation* or the *standard deviation* σ. As well as being the most commonly quoted measure of the width of a probability density function the standard deviation is used to normalise higher order moments and provide dimensionless quantities that allow probability density functions to be compared. For example the *coefficient of skewness*, defined as

$$\alpha_3 = \frac{\mu_3}{\sigma^3}, \tag{A.6}$$

provides a dimensionless measure of the asymmetry of a probability density. Similarly the *kurtosis*, defined as

$$\alpha_4 = \frac{\mu_4}{\sigma^4}, \tag{A.7}$$

is a useful way to distinguish probability distributions that are tall and thin (smaller values of α_4) from those that are short and wide (larger values of α_4). An alternative interpretation of the kurtosis is as a measure of how outlier-prone a distribution is[1]. The kurtosis of the normal or Gaussian distribution is 3. Distributions that are more outlier-prone than the normal distribution have kurtosis greater than 3; distributions that are less outlier-prone have kurtosis less than 3.

It is also common to express quantities in terms of the *deviation*

$$\Delta x \equiv x - \langle x \rangle. \tag{A.8}$$

[1]Consequently the fractional Lévy distribution discussed in Section 4.2.1 has a greater kurtosis than the Gaussian distribution.

In particular, consider the definition of moments for several random variables x, y, z,... with a joint probability density $p(x, y, z, \dots)$. The central moment of order l, m, n,... is defined as

$$\mu_{lmn\dots} \equiv \left\langle (\Delta x)^l (\Delta y)^m (\Delta z)^n \dots \right\rangle . \tag{A.9}$$

Equation (A.9) leads to the result that for two random variables there are three different variances. The first two (μ_{02} and μ_{20}) are variances for each of the random variables while $\mu_{11} = \langle \Delta x \Delta y \rangle$ is known as the *covariance*. From the Schwarz inequality it is easy to deduce that

$$|\mu_{ij}|^2 \leq \mu_{ii}\mu_{jj} = \sigma_i^2 \sigma_j^2. \tag{A.10}$$

A.3 Joint Probabilities and Correlations

The autocorrelation function is a useful way to extract the information encapsulated in the time-dependent joint probability density. This is necessary because the time-dependent probability density does not contain any information about the possible correlations between $x(t_1)$ and $x(t_2)$. Such information is provided by the joint time-dependent probability density $p_2(x_2, t_2; x_1, t_1)$. The two-time correlation is defined as

$$\Gamma(t_1, t_2) \equiv \langle x(t) \rangle = \int_{-\infty}^{\infty} \int_{-\infty}^{\infty} x_1 x_2 p_2(x_2, t_2; x_1, t_1) \, \mathrm{d}x_1 \, \mathrm{d}x_2. \tag{A.11}$$

Evidently Equation (A.11) only contains information about the correlations between $x(t_1)$ and $x(t_2)$. To gain further information we might consider the three-fold probability density $p_2(x_3, t_3; x_2, t_2, ; x_1, t_1)$ and so on. However it may be shown [31] that the second-order autocorrelation contains all the information about higher order correlations. $\Gamma(0) = \langle x(t_0)^2 \rangle$ is dependent on the value of $x(t)$ at $t = t_0$ or, in other words the variance of the distribution at $t = t_0$.

A.4 Stationary processes

A stochastic process $x(t)$ is said to be *strict-sense stationary*, if its probability density functions are independent of a shift in the time origin. That is, if the two ensemble measurements $x(t)$ and $x(t + \tau)$ have the same probability density for any time delay τ, they constitute a strict-sense stationary process. The processes $x(t)$ and $y(t)$ are said to be jointly stationary if the joint statistics of the two processes are time invariant. A process is classified as *wide-sense stationary* if its mean value is constant and its auto-correlation $\Gamma(t + \tau)$ depends only on the time difference τ;

$$\begin{aligned} \langle x(t) \rangle &= k, \\ \langle (x(t + \tau) x(t) \rangle &= f(\tau). \end{aligned} \tag{A.12}$$

Clearly a strict-sense stationary process is also wide-sense stationary. However wide sense stationarity does not require the probability density to be time-invariant.

Stationary processes for which the time average equals the or ensemble average are called *ergodic*. Not all stationary processes are ergodic.

A.5 White Noise processes

In the case of white noise probability density $p(x(t))$ is the same as the conditional probability density,

$$p\left(x, t_2 : x, t_1\right)) = p\left(x(t)\right). \tag{A.13}$$

The implication is that (a) white noise sequences do not posses any memory and (b) the present is independent of the past, and the future is independent of the past. This may be expressed in terms of the auto-correlation function as

$$\Gamma(\tau) = \delta(\tau). \tag{A.14}$$

A.6 The Gaussian Distribution

The *Gaussian* or *normal*,

$$p(x) = \frac{1}{\sqrt{2\pi}\sigma} \exp\left(-\frac{(x\langle x\rangle)^2}{2\sigma^2}\right), \tag{A.15}$$

is ubiquitous and does not require further introduction.

A.6.1 Unitary Transformation of Bivariate Gaussian Distribution

It is shown that when the *unitary* transformation,

$$u = x\cos\vartheta - y\sin\vartheta, \tag{A.16}$$
$$v = x\sin\vartheta + y\cos\vartheta, \tag{A.17}$$

is applied to the bivariate Gaussian distribution,

$$P_G(x,y) = \frac{1}{2\pi\sigma_x\sigma_y\sqrt{1-\rho^2}} \exp\left[-\frac{1}{2(1-\rho^2)}\left(\frac{x^2}{\sigma_x^2} - \frac{2xy}{\sigma_x\sigma_y} + \frac{y^2}{\sigma_y^2}\right)\right], \tag{A.18}$$

the new variables u and v also form a bivariate Gaussian distribution. Furthermore the angle ϑ_i for which u and v are statistically independent is found.

We begin by re-writing P_G in the form,

$$P_G(x,y) = \frac{1}{2\pi\sigma_x\sigma_y\sqrt{1-\rho^2}} \exp\left[-\tfrac{1}{2}\mathbf{X}^T\mathbf{A}\mathbf{X}\right], \tag{A.19}$$

where

$$\mathbf{X} = \begin{bmatrix} x \\ y \end{bmatrix}, \tag{A.20}$$

and

$$\mathbf{A} = \frac{1}{1-\rho^2}\begin{bmatrix} 1/\sigma_x^2 & -1/(\sigma_x\sigma_y) \\ -1/(\sigma_x\sigma_y) & 1/\sigma_y^2 \end{bmatrix}. \tag{A.21}$$

The unitary transformation matrix $\mathbf{U}$ is defined as

$$\mathbf{U} = \begin{bmatrix} \cos\vartheta & -\sin\vartheta \\ \sin\vartheta & \cos\vartheta \end{bmatrix}. \tag{A.22}$$

Then the transformed probability distribution $P'_G(x,y)$ may be written as,

$$P'_G(x,y) = \frac{1}{2\pi\sigma_x\sigma_y\sqrt{1-\rho^2}} \exp\left[-\tfrac{1}{2}\mathbf{X}^T\mathbf{U}^T\mathbf{A}\mathbf{U}\mathbf{X}\right]. \tag{A.23}$$

The eigenvalues of $\mathbf{A}$ are $\lambda_1 = 0, \lambda_2 = 2$. Eigenvectors of a symmetric matrix that correspond to different eigenvalues are orthogonal. This is manifest in the choice of the (x,y) co-ordinate system. Similarly $\mathbf{U}^T\mathbf{A}\mathbf{U}$ is symmetric with eigenvalues $\lambda_1 = 0, \lambda_2 = 2$, implying u and v are orthogonal as expected. It is a property of the *similarity transformation* $\mathbf{W} = \mathbf{U}^T\mathbf{A}\mathbf{U}$ that the eigenvalues are unchanged. Since the matrix representation of the linear transformation is orthogonal the linear transformation itself is orthogonal and the form of the distribution is preserved [162, p.353-357].

To find the angle ϑ_i for which u and v are statistically independent it is necessary to find the value of ϑ for which the coefficient of the cross-term in f $\mathbf{X}^T\mathbf{U}^T\mathbf{A}\mathbf{U}\mathbf{X}$ vanishes. Expansion of $\mathbf{X}^T\mathbf{U}^T\mathbf{A}\mathbf{U}\mathbf{X}$ yields the result,

$$\vartheta_i = \frac{1}{2}\tan^{-1}\left[\frac{2\sigma_x\sigma_y}{\sigma_x^2 - \sigma_y^2}\right]. \tag{A.24}$$

Appendix B

Signal Processing

B.1 Cross-spectral Density

The cross-spectral density (CSD) is defined using a *generalised Wiener-Khincthine* theorem [31, p. 62-65]. In other words, the CSD is the Fourier transform of the cross-correlation function;

$$W_{ij}(\omega) = \frac{1}{2\pi} \int_{-\infty}^{\infty} \Gamma_{ij}(\tau) \exp(i\omega\tau)\, \mathrm{d}\tau. \tag{B.1}$$

Unlike the power spectral density, the cross spectral density is not necessarily real. The imaginary part of the CSD provides a robust estimate of the phase difference between two waveforms. It is much less susceptible to poor estimation due to noise than curve fitting approaches.

B.2 Allan Variance

The Allan variance [51] was initially used to characterize the stability of atomic frequency standards [100]. It is a measure of the variability of consecutive finite length estimates of the process mean. The Allan variance is defined as the set of variances of the differences, $\bar{y}(t) - \bar{y}(t-\tau)$, between the length τ estimates, $\bar{y}(t)$, of the mean of a random variable $y(t)$, as a function of τ;

$$\sigma_{\mathrm{A}}^2(\tau) = \frac{\left\langle (\bar{y}(t) - \bar{y}(t-\tau))^2 \right\rangle}{2}. \tag{B.2}$$

The averaging time, or duration of the measurement, τ has the effect of selecting a characteristic time for which σ_{A}^2 is used to determine the dominant noise source. The square root of σ_{A}^2, referred to as the *Allan deviation*, is sometimes used an equivalent measure of oscillator stability.

In order to compare the stability of oscillators of different frequencies the Allan variance, or Allan deviation, are often scaled by the mean frequency squared

or the mean frequency of the oscillator. These quantities are referred to as the relative Allan variance and relative Allan deviation respectively. Dead-time between measurement clusters will affect the Allan variance estimate if the noise process has significant power within the frequency bandwidth defined by the dead-time [100, 163]. Care must be exercised if this is the case.

An in-depth discussion of the uncertainty of the Allan variance may be found in Ref. [164]. However the $1-\sigma$ estimate of Ng and Pines [10] is sufficient for use in the characterisation of ring-laser gyroscopes; by [10]

$$\frac{\delta\left(\sigma_{\mathrm{A}}^2\right)}{\sigma_{\mathrm{A}}^2} = \frac{1}{\sqrt{2(K-1)}}. \tag{B.3}$$

B.2.1 Allan Variance–Power Spectral Density Transform

As yet, it has not been shown how the Allan variance provides an effective method of characterisation of noise sources. In this Section the relationship between the Allan variance and the power spectrum of the fluctuations of the stochastic variable is summarised. The intimate connection between these two quantities reveals the part of the usefulness of the Allan variance in the characterisation of oscillator stability. In addition the Allan variance possesses a significant advantage over the spectrum of frequency fluctuations because it provides a much more transparent differentiation of noise types when plotted on the appropriate axes.

The spectral density $S(f)$ (on a per Hertz basis) of the instantaneous frequency fluctuations is related to the Allan variance by the integral transform [99],

$$\sigma_{\mathrm{A}^2} = 2\int_0^\infty \frac{\sin^4(\pi\tau f)}{(\pi\tau f)^2} S(f)\,\mathrm{d}f \tag{B.4}$$

The integral transform acts as a high-pass filter on the instantaneous frequency fluctuation spectrum. As τ is increased the frequency with maximum gain decreases. Therefore the Allan variance is the power within the filtered frequency band possessing a maximum frequency defined by Equation (B.4). This property may be utilised to build a device that calculates a close approximation of the Allan variance using a simple filter [165, 166].

Calculation of the Allan variance from the Fluctuation Spectrum

Since the transforms (B.4) are not always easily performed it is useful to obtain another form of the transform [99]. Let $F(s)$ be the Laplace transform of $\sigma_{A^2}(\tau)$,

$$F(s) = \mathcal{L}[\sigma_{A^2}(\tau)] = \int_0^\infty \exp(-s\tau)\sigma_{A^2}(\tau)\, d\tau \tag{B.5}$$

$$= \frac{6}{\pi\tau^2}\int_0^\infty \frac{\omega^2}{(s^2+4\omega^2)(s^2+\omega^2)s} S(\omega). \tag{B.6}$$

For spectra which are even and analytic this may be written as

$$F(s) = \frac{3}{\pi\tau^2}\oint_C \frac{\omega^2}{(s^2+4\omega^2)(s^2+\omega^2)s} S(\omega)\, d\omega, \tag{B.7}$$

where C is a contour consisting of the real axis of the semi-circle in the upper plane, at infinity. For white noise, $S(\omega) = 2A$, so Equation (B.7) has upper half plane poles at $\omega = is$ and $is/2$. Upon evaluating the integral using the residue theorem we find that

$$F(s) = \frac{A}{s^2}, \quad \text{and } \sigma_{A^2}(\tau) = \frac{A}{\tau}. \tag{B.8}$$

The result for the Allan variance of white noise is the same $1/t$ scaling law exhibited by the regular variance. Examination of the definition of the Allan variance allows the same result to be deduced.

The Allan variance of Lorentzian coloured noise, characterised by an exponentially decaying autocorrelation function and a fluctuation spectrum of the form

$$S(\omega) = \frac{2D\alpha}{\alpha^2+\omega^2} = \frac{2D\tau}{1+\omega^2\tau_c^2}, \quad \text{where } \tau_c = \frac{1}{\alpha}. \tag{B.9}$$

There is now an extra pole at $\omega = i\alpha$. From the residue theorem

$$F(s) = \frac{D}{\tau^2}\left[\frac{4\alpha}{s^2(s^2-4\alpha^2)} - \frac{2\alpha}{s^2(s^2-\alpha^2)} - \frac{6\alpha^2}{s(s^2-4\alpha^2)(s^2-\alpha^2)}\right]. \tag{B.10}$$

The inverse Laplace transform yields

$$\sigma_{A^2}(\tau) = \frac{D}{2\alpha^2\tau^2}\left[4\exp(-\alpha\tau) - \exp(-2\alpha\tau) + 2\alpha\tau - 3\right]. \tag{B.11}$$

The Allan variance for a number of noise processes is summarised in Table B.2.1. The differing power law relationships for different noise sources indicate that a log-log plot of the Allan variance against τ will usually yield straight line with

characteristic slope defined by the noise source. The Allan variance is usually presented in this manner. In a real system more than one noise source will often be present. A useful model consists of a number of independent noise sources [100] that act independently. For example, the following combination is useful in the characterisation of ring laser gyroscopes in the frequency domain,

$$S_y(f) = \sigma^2 + h_{-1}f^{-1} + h_{-\alpha}f^{-\alpha}. \tag{B.12}$$

The contributions of each noise term to the Allan variance are, with the addition of a deterministic error term resulting from a frequency ramp [10],

$$\sigma_{\mathrm{A}^2} = \sigma^2\tau^{-1} + h_{-1} + h_{-\alpha}\tau^{1-\alpha} + h_{\mathrm{ramp}}\tau^2. \tag{B.13}$$

The values on the constants h_i are easily evaluated from the log-log Allan variance plot, allowing the relative strengths of the various noise sources to be determined much more easily than if $S_y(f)$ is used.

noise type	$S_y(f)$	σ_A^2
white frequency	$\propto f^0$	$\propto \tau^{-1}$
flicker phase (gas discharge)	$\propto 1/f$	$\propto \tau^0$
frequency ramp	n/a $(\omega(t) = Rt)$	$\propto \tau^2$
frequency random walk	$\propto 1/f^2$	$\propto \tau^1$
drift noise (e.g. fBm) [86]	$\propto 1/f^\alpha,\ \alpha \in (1,3)$	$\propto \tau^{\alpha-1}$
sinusoidal noise	$\frac{1}{2}[\delta(f-f_0)+\delta(f+f_0)]$	$2\pi f_0^2\left(\frac{\sin^2(\pi f_0\tau)}{\pi f_0\tau}\right)^2$

Table B.1: The Allan variance σ_{A}^2 for various noise sources. $S_y(f)$ denotes the power spectral density of $y(t)$. For a more comprehensive summary paying particular attention to ring-laser gyroscopes see Refs. [10] and [4].

B.3 AR2 Frequency Estimation

The AR2 frequency estimation algorithm is particularly well-suited for measurement of the gyroscope beat frequency in the Canterbury gyroscopes. Dr. Tom King has made an in-depth study [4, p. 60-67] of the algorithm. Therefore only the significant features are described here.

Consider the model

$$x_t + a_1x_{t-1} + a_2x_{t-} = \epsilon_t. \tag{B.14}$$

The autocorrelation is [167]

$$\Gamma(j) = \frac{(1-\mu_2^2)\mu_1^{j+1} - (1-\mu_1^2)\mu_2^{j+1}}{(\mu_1-\mu_2)(1+\mu_1\mu_2)}, \tag{B.15}$$

where the index $j \geq 0$. If both of the roots μ_1, μ_2 are real and positive the autocorrelation function $\Gamma(j)$ has a bell shape. If the roots are real and negative then the autocorrelation function has the same shape. However the sign alternates for each successive value of j. For complex roots $\Gamma(j)$ may be rewritten as

$$\Gamma(j) = a_2^{j/2} \left(\frac{\sin(j\theta + \psi)}{\sin \psi} \right), \tag{B.16}$$

where

$$\tan \psi = \left(\frac{1 + a_2}{1 - a_2} \right), \quad \text{and} \quad \cos \psi = \frac{-a_1}{2\sqrt{a_2}}.$$

Equation (B.16) gives rise to oscillations in the autocorrelation function which die away after a time determined a_1 and a_2. The power spectrum of this process is

$$S(f) = \frac{1}{2\pi} \frac{2\sigma_\epsilon^2}{1 + a_1^2 + a_2^2 + 2(a_2 + 1)\cos(2\pi f) + 2a_2 \cos(2\pi f)} \tag{B.17}$$

For narrow spectral lines the AR2 model tends toward a Lorentzian spectrum. Therefore it is an ideal model for frequency estimation with gyroscopes that operate at the quantum limit. The linewidth of the AR2 spectrum may be used to deduce the signal linewidth with appropriate scaling. This technique is discussed in Ref. [4].

B.4 The Median Filter

The median filter [168] is particularly useful for removing salt and pepper noise from digital images. This is the type of noise that might occur when a CCD camera has "dead" pixels for example. As the name implies, the median filter operates by selecting the median of a portion of the data set of specified length. The median is a more robust average than the mean and so a single very unrepresentative value in a neighbourhood will not affect the median value significantly. For an odd *rank* n the filter output $y(k)$ is

$$y(k) = median[x(k - (n-1)/2 : k + (n-1)/2)]. \tag{B.18}$$

For n even,

$$y(k) = median[x(k - n/2), x(k - (n/2) + 1), \ldots, x(k + (n/2) - 1)]. \tag{B.19}$$

For image processing the 2D median filter is the obvious and useful generalisation of the 1D definition. The 3×3 2D median filter is commonly used in image processing. Larger rank 2D filters are too computationally intensive for widespread use. In general, the median filter allows a great deal of high spatial frequency detail to pass while remaining very effective at removing noise on images where less than half of the pixels in a smoothing neighborhood have been effected.

Since the median value must actually be the value of one of the pixels in the neighborhood, the median filter does not create new unrealistic pixel values when the filter straddles an edge. For this reason the median filter is much better at preserving sharp edges than the mean filter.

The median filter is nonlinear;

$$median[A(x) + B(x)] \neq median[A(x)] + median[B(x)].$$

Consequently the filter output $y(k)$ cannot be found by a weighted sum of the neighbourhood pixels.

Appendix C

Papers

C.1 Precision Stabilisation of a Large Ring-laser Gyroscope [1]

C.1.1 Erratum

In the paper entitled *Precision Stabilisation of a Large Ring-laser Gyroscope* [1] there is discussion of an interesting and hitherto unreported phenomenon. There appeared to be a dependence in the cyclic behaviour of the CII gyroscope beat frequency that had a period of approximately three wavelengths. In light of the report of the subsequent calibration data presented in Section 3.1 and alternative data presented in Figure C.1 it is apparent that this phenomenom was an artifact due to a faulty calibration. Consider Figure C.1 where a scanning Fabry-Pérot interferometer was used to measure the optical frequency excursion of 20.6 MHz/V induced using by scanning the CII piezo control voltage through part of piezo scan range. This corresponds to a pathlength excursion of 174 nm/V. This is in good agreement with the calibration given in Section 3.1 of 160 nm/V, especially considering the small number of data points. The calibration of the pathlength change induced by a change in the CII piezo control voltage used to arrive at the published conclusions was 1.03 μm/V. This calibration was made by observation of the variation in the FSR beat frequency with the piezo excursion. The estimate based on the Fabry-Pérot measurements was made at the time the data presented in *Precision stabilisation of a large ring laser gyroscope* was collected. The data used in Section 3.1 was recorded after the data pertinent to the stabilisation paper was recorded when no apparent change in the operation of the piezo had been noticed. However the calibration of 1.03 nm/V was made soon after CII was installed in the Cashmere cavern. No FSR beat frequency data was recorded during the calibration therefore it was not possible to perform the deductive steps carried out in Section 3.1. During initial testing it was found that the glue bonding the piezo mount to the CII monolith did not hold the piezo solidly in place. This was replaced with a clamp arrangement before the stabilisation was performed. Hence the calibration of the piezo would be expected to be somewhat different due to the increased rigidity of the clamp arrangement.

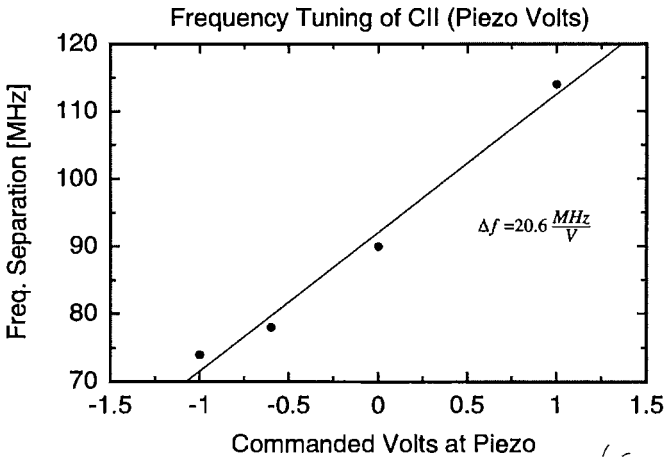

Figure C.1: Optical frequency excursion of CII due to piezo motion measured by Newport SR-130 scanning Fabry-Pérot interferometer. Data courtesy of Professor U. Schreiber.

C.2 Collision Broadening and Quantum Noise in a Very Large Laser Gyroscope [2]

Precision stabilization of the optical frequency in a large ring laser gyroscope / Ulrich K Schreiber, Clive H. Rowe, Douglas N. Wright, Steven J. Cooper, and Geoffrey E. Stedman.
Applied Optics, Vol. 37, Issue 36, pp. 8371-8381 (1998)
https://doi.org/10.1364/AO.37.008371

Abstract:
Pressure-induced fractional changes of 10^{-7} in the geometry of a large He–Ne ring laser gyroscope induce backscatter phase changes and thus a fractional pulling of the Sagnac frequency of $\sim 5 \times 10^{-3}$. To counter this, the optical frequency was stabilized against an iodine-stabilized laser with a high-finesse Fabry–Perot interferometer and piezoelectric control of the ring perimeter. This scheme, although limited in principle by residual geometric asymmetry and in practice by low beam powers (10 pW), stabilized the perimeter to 2.4 nm (6×10^{-10} or 300 kHz for the optical frequency) and the Sagnac frequency to 100 parts per million over several days.

Collision broadening and quantum noise in a very large laser gyroscope / C.P.Wyss, D.N.Wright, B.T.King, D.P.McLeod, S.J.Cooper, G.E.Stedman
Optics Communications, Volume 174, Issues 1–4, 15 January 2000, Pages 181-189
https://doi.org/10.1016/S0030-4018(99)00655-0

Abstract:
The single mode and the multimode output power are studied as a function of the input powe and the partial pressure in a very large (perimeter=14 m) He:Ne ring laser gyroscope and in a linear He:Ne laser (length=1.6 m). The effects of collision broadening on the single mode output power are discussed. For a sufficiently high He:Ne pressure, the gain of adjacent longitudinal modes is depleted and multimode emission is suppressed and hence the single mode output power of the ring laser is increased. The quantum noise and the long term drifts in the Earth rotation induced Sagnac frequency (ν_S=288.5 Hz) are investigated. The demonstrated advantages of operating a laser gyroscope at a large He:Ne pressure are: reduction in quantum noise and the freedom to choose the input power within a large range.

Appendix D

LabVIEW™

The aim of this Appendix is to provide a very brief overview of the programming environment LABVIEW™ that was used to develop all of the data acquisition and control routines used in the experiments described in this thesis. LABVIEW™ is the most well-known product made by National Instruments that uses the graphical programming language known as G. Since the distinction does not have much bearing on practicalities only LABVIEW™ is referred to in this Appendix.

D.1 The Elements of LabVIEW™

The file suffix for LABVIEW™ programs is "*.vi" where "vi" is an acronym for *virtual instrument.* In keeping with the metaphor of translating the idiom of hardware instrumentation into the software domain implied by the term virtual instrument there are two basic components contained in a LABVIEW™ program. The first is known as the *front panel* which pays the role of the control panel in a traditional hardware-based instrument. The other component is called the *wiring diagram* or simply the *diagram.* This consists of a diagrammatic representation of the various tasks that the code, once compiled into machine code, will instruct the computer to perform. The diagrammatic idiom means LABVIEW™ may be considered a true *visual* programming language unlike packages produced by other vendors which, despite having names implying there is a visual nature to the programming, are in fact based on traditional text-based languages. The term *graphical programming language* is sometimes used with respect to the LABVIEW™ approach in order to avoid confusion[1].

In terms of the hardware metaphor the LABVIEW™ diagram plays the role of the internal circuitry of a piece of hardware. In terms of the software engi-

[1]There are a number of other visual or graphical programming languages although none have achieved the level of popularity attained by LABVIEW™ . Commercially available implementations include HP VEE™ from Hewlett Packard and SOFTWIRE™ which is built upon Visual Basic.

neering paradigm the *front panel* is the *user interface* while the *diagram* replaces traditional text-based code. The LABVIEW™ compiler creates machine code from the diagrammatic representation in a manner analogous to the way a C/++ compiler, for example, would creates machine code from the text-based code. The compiled LABVIEW™ code requires the presence of various LABVIEW™ libraries, as is the case with all but the most trivial C/++ programs. The more comprehensive LABVIEW™ distributions include the *application builder* which is analogous to the *C/++ linker*—both are used to create stand-alone executables.

The Elements of the Front Panel

The LABVIEW™ front panel is composed of two basic types of element; *controls* and *indicators*[2]. Controls consist of simple numeric and string entry boxes, on/off (Boolean) switches, sliders and dials, numeric and string arrays, and menu selectors among other control types. A control is a point of input that allows the user to enter data into the LABVIEW™ program. The front panel is also used to define the programmatic interface for a VI that is called as a subroutine. A VI used in this manner is referred to as a *subVI*. A common design mistake is the placement of controls in the user interface without a clear indication of when any adjustments to the control values will be actioned. For example, if the control is "read" by the program only at start-up then confusion may arise if attempts are made to alter this control at any later stage. Therefore it is necessary to clearly indicate when any such adjustments will be acted upon. This may be done by intelligent grouping of controls with appropriate labels or preferably by placing configuration controls, for example, in a separate user interface that may only be accessed at appropriate times.

Many of the indicators are similar to controls—the only difference is that, as the name suggests, they simply serve as a reporting mechanism for results produced by the code. In addition to indicator versions of the types of control already mentioned there are gauges instead of sliders and dials, and graph indicators. As is the case with controls it is possible to cause confusion if an indicator is not regularly updated and there is not indication of this behaviour.

The Elements of the Diagram

In LABVIEW™ the human-readable representation of the machine code is graphical. Objects that perform certain tasks are connected or *wired* together.

[2]It is, in fact, possible to blur this distinction using the *VI server* functions [169]. However whether or not this technique should be advocated is a moot point since it can cause unnecessary confusion in the user if used inappropriately.

This form leads naturally to what is called the *dataflow* programming paradigm. Execution order is controlled by the flow of data that is defined by the connections made by the wires. Therefore an input to an object that is connected to an output of another object cannot execute until the first task has completed. A very simple example of a LABVIEW^{TM} *diagram*, which does not even begin to describe the power of LABVIEW^{TM}, is shown in Figure D.1. The simple example program

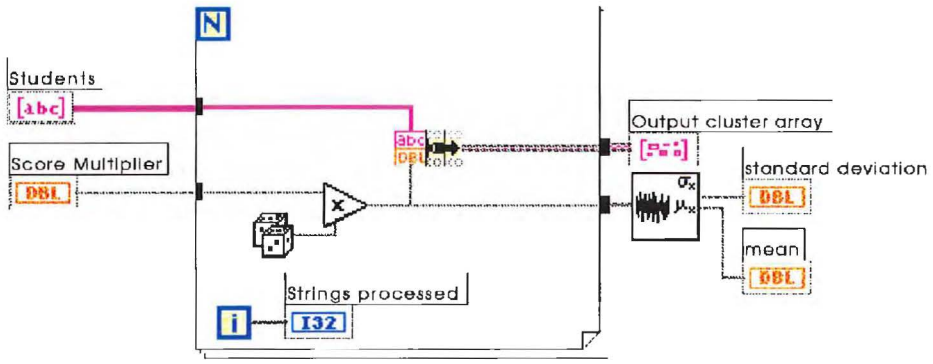

Figure D.1: Example LABVIEW^{TM} diagram.

takes a list of student names, then creates and manipulates some fictitious test scores. Two controls and four indicators appear on the front panel. One control, labelled *score multiplier*, is a simple 64-bit integer or double (DBL). The other control is an array of strings where each entry in the array is a string with the student's name entered. The *strings processed* indicator is a 32-bit integer (I32) showing how many students scores have been processed. The *standard deviation* and *mean* indicators are 64-bit integers returning these statistics for the students scores. Apart from the controls and the indicators all of the code is contained within a *for* loop. Note that the for loop contains a counter i which the *students processed* indicator is wired to and a connection labelled n which defines the maximum number of iterations the loop may perform. In this example a feature known as *array auto-indexing* is used. The number of iterations that the *for loop* will perform is equal to the size of the smallest array that enters the *for loop*[3]. In this case, there is only one input array—*students*. The code to generate the scores for the fictitious students is very simple. The score is a random number, generated by the standard LABVIEW^{TM} code represented by the dice, multiplied by the number entered in the control *multiplier*. The other object in the *for loop bundles* the disparate data types of *student* (string) and *score* (int-64) into

[3]This feature may be used to good effect with two-dimensional arrays as well as with one-dimensional arrays as is the case with this example.

a LABVIEW™ cluster which performs a function similar to *struct* found in C programming. The final object on the diagram is an example of a subVI. It is the LABVIEW™ statistics function that returns the mean and standard deviation of the input array. The array of scores that is passed to the analysis subVI is generated by *auto-indexing* of the individual scores at the exit of the *for loop*. It is straightforward to disable this feature if necessary.

D.1.1 Why Use Visual Programming?

When programmers familiar with text-based languages first encounter visual or graphical programming languages there is often some resistance with arguments along the lines of "This is much slower," or even, "How can this be a real programming language?" Once any such initial bias is overcome it becomes clear that visual programming languages have certain advantages and disadvantages when compared to text-based languages. It is the task of the programmer to select the most appropriate tool. For example LABVIEW™ was designed with data acquisition and process control in mind. Consequently it is structured in a way that readily lends itself to this role. LABVIEW™ also has excellent instrument driver support to simplify data acquisition programming. On the other hand, LABVIEW™ is much less useful for tasks that require a lot of string manipulation where PERL or PYTHON would be much more effective. Similarly MATLAB™ or the GNU scientific libraries for C would be used in preference to LABVIEW™ where substantial mathematical calculation is required.

Whitley and Blackwell [170] found that the role that visual representations can play as a documentation and communication medium is important. In fact this is a major motivation for the extended discussion of LABVIEW™ presented here. Properly designed and carefully documented LABVIEW™ code can allow much easier code modification by programmers who are subsequently required to update the code, particularly if they are not very experienced with text-based languages.

One of the key features of visually programming languages is that they tend to conform to the *dataflow* idiom. This was discussed in the description of the LABVIEW™ diagram. Some of the advantages and disadvantages of the dataflow approach are described below. In general it is a useful tool where the code is required to consist mainly of sequential tasks. However if there is a need for several parallel tasks then the dataflow approach can become cumbersome.

Dataflow model advantages:

- Good for specialised application domains (e.g. data collection and analysis, LABVIEW™).

- Good for novices and non-programmers.
- Good for data manipulation (image processing, graphics, scientific visualisation).
- Good for data transformation (filtering, CANTATA)
- Powerful if it provides extra constructs and predefined functions.

Dataflow model problems:

- Uses too much space on the screen[4].
- Not clear what high level constructs or functions should be provided.
- Not good for professional programmers. In particular the difficulty involved with implementing parallel tasks can be frustrating. In LABVIEW™ this issue has been addressed by supplying the VI server functions and synchronization functions which allow parallel tasks to be programmed with relative ease.

D.2 Virtual instrument design principles

This Section contains a summary of some useful LABVIEW™ design guidelines. The guidelines are a sysnthesis of personal experience and information available from the LABVIEW™ resorces listed in Appendix D.3.

D.2.1 The One Screen Rule

In some peoples minds there is nothing worse than a huge diagram that is much larger than the monitor size. The initial developer will know what is off-screen but it is annoying for anyone upgrading to try to interpret this code. Complex case structures such as *state machines* (see below) should definitely be contained within one screen. It is not necessary to be pedantic about the one-screen rule though. A simple linear execution sequence is not obscured by having to scroll along to see all the code. An example of this would be the creation of an html formatted file where the tags and content are built up step by step with subVIs.

[4]In some respects this criticism is invalid when one considers that in a text-based language one may be able to display 40 lines of code with an average of (say) two primitives per line. It is not unreasonable for a LABVIEW™ diagram to contain this in one screen. However the two-dimensional nature of graphical programming makes it much easier to produce code that is hard to read than with a text-based language where one is generally limited to scrolling up and down.

D.2.2 Three-tier Application Structure

A three-tier application structure is a useful method for organising large projects.

The first tier is referred to as the *executive* level. The main control VI is resident in this level. The user interface may be the front panel for the executive or it may be an independent VI placed on the second tier. The second level is responsible for performing the logic needed to execute given control and data acquisition tasks. The lowest level is referred to as the *driver* level. The driver level is responsible for performing communications with the device under test, instruments, and the like. One major advantage of a documented three-tier application structure is that it will simplify code maintenance—the strict partitioning of levels and functions maximizes code reuse and minimizes maintenance time [171]. It is preferable that the directory structure of the application reflects the three-tier structure in an appropriate manner[5].

The control and data acquisition for the investigation of coloured noise in the ring-laser gyroscope was designed using the three-tier application structure. The use of the HP33120A arbitrary waveform generator, which provided the noise patterns used to drive the C-I piezo, provides an example where a device is manipulated by code from all three levels of the application structure.

LABVIEW^{TM} drivers communicate with the waveform generator giving access to the various functions that may be used to control the HP33120A via the HPIB interface. Direct manipulation of this driver from the executive VI would have led to an overly complicated diagram or *sphagetti-code* as well as violating the principles of the three-tier application structure. Therefore a second tier VI was created. It was designed with a case structure such that the single VI performed a number of functions. The function that was called was determined by the value of an input wired to the VI *connector pane*. The various cases included code that performed initialisation of the waveform generator at start-up, selected the frequency and amplitude of the waveform, selected a new waveform that was stored in memory, and uploaded a new waveform into the HP33120A memory as well as code that started the waveform at the desired time. This subVI could then be used in the executive VI and set to perform the required task without having to re-code any detailed aspects of the communication with the waveform generator. Although it required some extra initial work this approach allowed the code contained within the subVI to be reused a number of times without modification and, perhaps more importantly, it allowed the communication with the waveform generator to be tested independently of the executive.

[5]I do not recommend the use of LABVIEW^{TM} library files (*.llb). This is an old-fashioned method of saving a number of files. In the past it had the advantage of allowing long file names and therefore was not constrained by the Windows *8+3* naming restriction. Library files do not, however, preserve directory structure. Therefore the clarity of a three-tier design will be lost. Third-party compression software such as WINZIP^{TM} should be used instead.

D.2.3 Error Checking

One of the best techniques for preserving dataflow (and ensuring reliable code) is to ensure the error cluster is used to define dataflow. Since execution of a subVI does not begin until all nodes have the data required to execute the error chain creates a dependency that ensures tasks execute in the correct order even if there is no other data dependence.

When parallel execution occurs it is important that errors that may arise from all of the parallel tasks are considered. This may be done by combining error clusters on a single diagram at a convenient point or by returning errors to a construct that has some sort of "global" property. There are a number of ways to create such a construct—they are discussed in the LABVIEW™ reference manual [169].

D.2.4 State machine

The *state machine* is one of the most powerful design constructs within the LABVIEW™ idiom. The basic building block of a state machine is a while loop containing a case structure. Each case or state contains code for a set of actions that are naturally grouped together and occur at the same time. As long as there are tasks that the VI is required to perform the while loop will move onto the next iteration executing the requested state. This is a useful way to partition a long series of tasks where a more linear design approach (ie coding vertically as one would with a textual language) quickly leads to diagrams much larger than one screen size and hard-to-read *spaghetti code.* This is difficult to debug and interpret for anybody other than the author, as well as being frustrating due to the need to scroll about when programming. On the other hand, a state machine allows a large number of distinct operations to be contained within one screen. A short description of each state and a consistent layout within each state allows easy interpretation of the diagram. Furthermore the state queue or list may be utilised to provide a powerful tool for debugging and error tracking. However the major advantage of the state machine is the flexibility it allows in choosing the execution order. It is straightforward to determine what code to execute next based on results obtained at run-time. In more complicated instances the state machine is far more transparent and easier to debug than complicated sequences of nested case structures.

An example of the LABVIEW™ state machine is shown in Figure D.2. In this example the case is set to *state 1.* At the far left of the diagram a *string array* is used to set the first two elements of the *state queue* to *state 1* and *state 4.* The

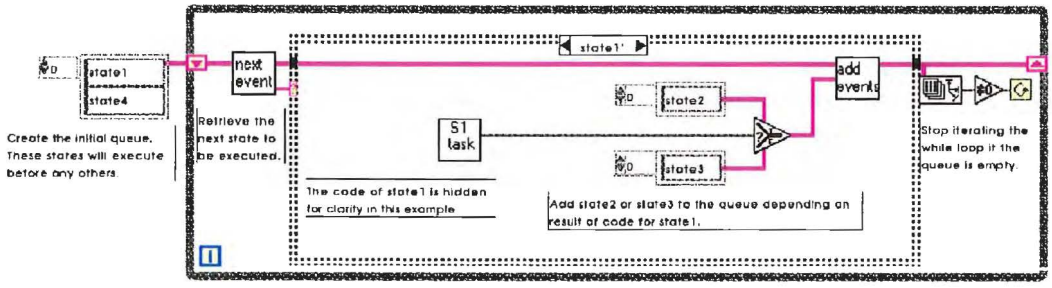

Figure D.2: The LABVIEW^{TM} state machine.

state queue is then passed to the *while loop*. The subVI labelled *next event* then retrieves the next state to be executed from the *state queue*. This string is then wired to the case selector which is denoted by a question mark in the frame of the case structure. The tasks performed by *state 1* are superfluous to this description and are therefore concealed within a subVI. The important point to note is that this subVI returns a Boolean value. One of states 2 or 3 is added to the *state queue* by the subVI labelled *add events* depending on the value of the Boolean returned by the tasks. If necessary it is not difficult to include more complicated conditions. However if it is found that the conditions become very complicated it may be an indication that more states are required. Once *state 1* has executed a check is made on the length of the *state queue*. If this array is found to be empty the while loop stops. Otherwise the next iteration of the while loop will be executed where the next state in the *state queue* is selected by the *next event* subVI.

In short, the *state queue* holds the execution order while the states perform actions and evaluate conditions. This independence of content and execution order in the state machine implementation can reap significant benefits during testing and revision.

In order to maximise the potential benefits of state machine principles careful design before beginning coding is necessary. The first step is to clearly identify the various states that will be required and specify the inputs and outputs that are required for each state. These will be passed between iterations of the while loop using a *shift register*. Initially all that is required is a simple list of tasks to be performed. Once this is available and a clear picture of the necessary states has formed the relationships between the various states may be mapped out using a flow diagram. A simple example is shown in Figure D.3.

Two types of state machine may be defined: the *static state machine* and the *dynamic state machine*. The *static state machine* is defined as a set of states that are independent within the state queue. This means that the order of execution is set when the state machine is first called and cannot be modified by any of the individual states. The static state machine lends itself to subVI's that control

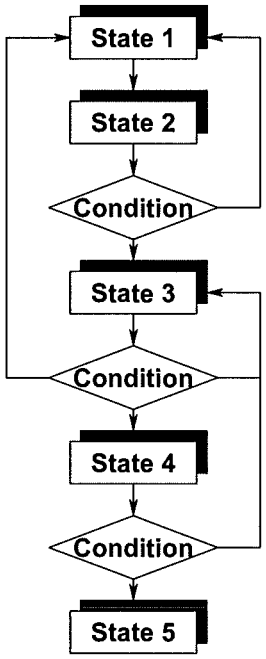

Figure D.3: Linear State Machine example.

the execution of a particular device or communication protocol implementation where discrete initialise/operate/close tasks are the norm. The flow diagram in Figure D.3 describes a *static state machine*. Note that there is no need to use the *add events* subVI in a *static state machine*. The *dynamic state machine* contains states that add events to the state queue to directly manipulate program flow. The events may be added due the results of execution within the state or because of input from the user interface or a parallel execution loop. This type of state machine will generally be found in the executive tier while static state machines lend themselves to use within the lower-tier of the application structure. Figure D.4 shows a simple example of a *dynamic state machine*.

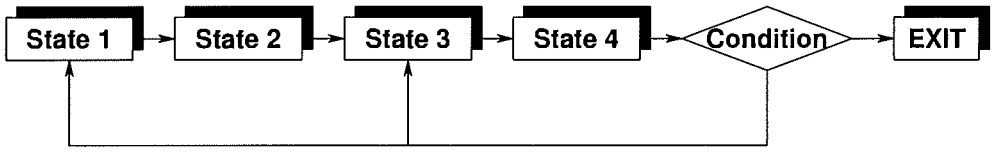

Figure D.4: Dynamic state machine where the condition cannot be evaluated to a Boolean. One of states 1, 3, or "exit" are executed depending on the value the condition returns.

Figure D.5 shows a more complicated example of a *dynamic state machine*. This example would be horrible to code in a linear style with multiple nested cases causing the logical flow of the execution flow to be obscured. Furthermore if it

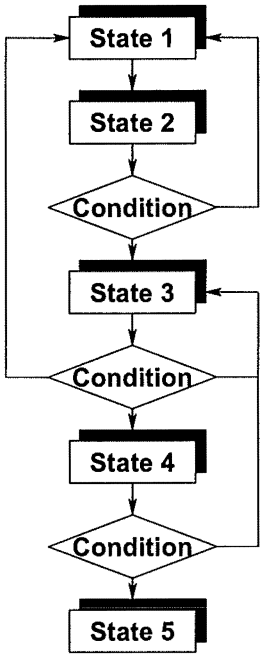

Figure D.5: A more complicated example of a dynamic state machine.

becomes necessary to modify the execution order it is likely that considerable revision of the nested cases will be necessary. However if the state machine approach is used only minor revisions of the behaviour of the conditions will be required. Furthermore individual states may be tested independently without requiring the code for all cases to be present. This is simply done by making the appropriate adjustments to the *state queue*.

The steps required to implement a state machines within the framework of the three-tier application structure may be summarised as follows.

1. Begin with a top-down design approach—make a diagram of the tasks you want the executive VI to perform with a box around each. These are your states in the executive VI. Clearly the contents of these states will include a number of subVIs.

2. Think about what is required within each state. What states have similar actions or communication with the same device? This helps define the state machines required as middle-tier subVIs.

3. Create a list of the static state machines required. Dedicate one state machine to each device to be communicated with and logical combination of events such any TCP/IP communication to be performed.

4. Draw a state diagram/flowchart for each of the static state machines. Lower-tier VIs will be used to implement these states.

5. Draw a state diagram for each of the state machines that will be used in the middle-tier.

6. Go back to the executive VI state diagram. Are any revisions needed in light of the previous step? Try to reduce the number of states where logically possible. However avoid this if it is at the expense of some flexibility that may be required in the future.

7. Decide on whether the coding (we haven't touched the keyboard yet!) will be top-down or bottom-up. Top-down coding may be appropriate for a complex application where it is necessary to evaluate and perhaps change the execution order during development. Simple dummy VIs which are replaced with fully functional VIs can be used to provide simulated data. This can avoid unnecessary coding of low-level VIs. If the application is well-defined at the outset there is little advantage to creating the dummy VIs so bottom-up coding is probably the best option. In reality the best approach will probably fall somewhere in the middle.

8. Once coding has begun, utilise selective queuing of the state machine to test portions of the execution even if other states are not yet fully functional. A good way to provide the interface to a static state machine is to use a *ring* or *enum* control of the states placed in an array that defines the state queue. *Type definitions* allow all of the interfaces across a project to updated automatically if the interface is changed at the *type definition.*

D.3 LABVIEW™ Resources

This Section contains a list of sources that provide useful information about LabVIEW™.

Internet Resources

- National Instruments (manufacturer): `http://www.ni.com`.

- Info-LabVIEW mailing list: `http://k-whiner.pica.army.mil/index.html`. This is the most popular LabVIEW™ mailing list and has a number of very knowledgeable contributors. The site also includes some useful links and it is possible to search the archives.

- LabVIEW™ FAQ: `http://www.icon-tech.com.au/`.

- Brian Renken's website contains some useful data including a summary of INI settings which may be used to customise various parts of LabVIEW™.

This is not completely documented in the user manuals. `http://Brian.Renken.com/LabVIEW/`.

- The LABVIEW™ Webring—a list of over 100 sites containing information about LABVIEW™: `http://nav.webring.yahoo.com/hub?ring=labview&list`.

Books

- Professional G Developers Toolkit Reference Manual. This is a useful book outlining strategies for developing large projects in an organised manner. Paper copies are only distributed with the LABVIEW™ professional edition. However it may be downloaded for free from `http://www.ni.com/pdf/manuals/321393a.pdf`.
- The other LABVIEW™ user manuals are also available online at `http://www.ni.com/pdf/manuals/`.
- There are a number of other books devoted to LABVIEW™ programming. A search at Amazon.com will return summaries of these books.

Bibliography

[1] U Schreiber, C H Rowe, D N Wright, S Cooper, and G E Stedman. Precision stabilisation of a large ring laser gyroscope. *Appl. Opt.*, 37:8371–8381, 1998.

[2] C P Wyss, D N Wright, B T King, D P McLeod, S J Cooper, and G E Stedman. Collision broadening and quantum noise in a very large laser gyroscope. *Optics Communications*, 174:181–189, 2000.

[3] H Statz, T A Dorschner, M Holtz, and I W Smith. In M L Stitch and M Bass, editors, *Laser Handbook*, volume 4, pages 229–332. Amsterdam-North Holland, 1985.

[4] B T King. *Ring laser dynamics.* PhD thesis, Dept of Physics and Astronomy, University of Canterbury, 1999.

[5] M Winters. *Operators Manual: Model 100 Iodine stabilized HeNe laser.* Winters Electro-Optics, Inc., 1st edition, 1994.

[6] K Vogel, H Risken, and W Schleich. Noise in a ring laser gyroscope. In F Moss and P V E McClintock, editors, *Noise in nonlinear dynamical systems*, volume 2, pages 271–292. Cambridge University Press, 1991.

[7] Hamamatsu Corporation. Hamamatsu R3986 photomultiplier tube data sheet. `http://usa.hamamatsu.com/hcpdf/et/r3896.pdf`.

[8] J T Verdeyen. *Laser Electronics.* Prentice Hall, Englewood Cliffs, New Jersey, 1995.

[9] N Harris. *Modern Vacuum Practice.* McGraw-Hill, London, 1989.

[10] L C Ng and D J Pines. Characterization of ring laser gyroscope performance using the Allan variance method. *J. Guidance*, 20:211–214, 1997.

[11] W M Macek and D T M Davis. *Appl .Phys. Lett.*, 2:67, 1963.

[12] M Sargent III, M O Scully, and W E Lamb Jr. *Laser Physics.* Addison-Wesley, Reading, Mass., 1974.

[13] R Anderson, H R Bilger, and G E Stedman. "Sagnac" effect: a century of earth-rotated interferometers. *Am. J. Phys.*, 62:975–985, 1994.

[14] G E Stedman. Ring laser tests of fundamental physics and geophysics. *Reports Progr. Phys.*, 60:1–73, 1997.

[15] G E Stedman, Z Li, C H Rowe, A D McGregor, and H R Bilger. Harmonic analysis in a large ring with backscatter-induced pulling. *Phys. Rev. A*, 51:4944–4958, 1995.

[16] C Etrich, P Mandel, R Centeno Neelen, R J C Spreeuw, and J P Woerdman. Dynamics of ring-laser gyroscope with backscattering. *Phys. Rev. A*, 46:525–536, 1992.

[17] F Aronowitz. Theory of a travelling-wave optical maser. *Phys. Rev.*, 139:A635–A646, 1965a.

[18] F Aronowitz. The laser gyro. In *Laser Applications*, volume 1, pages 133–200. Academic Press, New York, 1971.

[19] W E Lamb. Theory of an optical maser. *Phys. Rev*, 134A:A1429–A1450, 1964.

[20] T L Gustavson, P Bouyer, and M Kasevich. Precision rotation measurements with an atom interferometer gyroscope. *Phys. Rev. Lett.*, 78:2046–2049, 1997.

[21] S A Werner, J-L Staudenmann, and R Colella. Effect of Earth's rotation on the quantum mechanical phase of the neutron. *Phys. Rev. Lett.*, 42:1103–1106, 1979.

[22] G Sagnac. *Comptes Rendus*, 157:708–710, 1913.

[23] A A Michelson, H G Gale, and F Pearson. The effect of the Earth's rotation on the velocity of light. *Astrophys. J.*, 61:137–145, 1925.

[24] F Hasselbach and M Nicklaus. Sagnac experiment with electrons: Observation of the rotational phase shift of electron waves in vacuum. *Phys. Rev. A*, 48:143–151, 1993.

[25] F Riehle, Th Kisters, A Witte, J Helmcke, and Ch J Borde. Optical Ramsey spectroscopy in a rotating frame: Sagnac effect in a matter-wave interferometer. *Phys. Rev. Lett.*, 67:177–180, 1991.

[26] D P McLeod, G E Stedman, T H Webb, and U Schreiber. Comparison of standard and ring laser rotational seismograms. *Bull. Seis. Soc. Am.*, 88:1495–1503, 1998.

[27] R W Dunn. Design of a triangular active ring laser 13 m on a side. *Appl. Opt.*, 37:6405–6409, 1998.

[28] F Aronowitz and R J Collins. Mode coupling due to back-scattering in a Helium-Neon travelling-wave ring laser. *Appl. Phys. Lett*, 9:55–58, 1966a.

[29] Ziyuan Li. *Optical supercavity and precision ring laser measurements.* PhD thesis, University of Canterbury, New Zealand, 1993.

[30] A Schawlow and C Townes. Infrared and optical masers. *Phys. Rev.*, 112:1940–1949, 1958.

[31] L Mandel and E Wolf. *Optical Coherence and Quantum Optics.* Cambridge University Press, New York, 1995.

[32] T A Dorschner, H A Haus, I M Holz, I W Smith, and H Statz. Laser gyro at the quantum limit. *IEEE J. Quantum Electron.*, QE-16:1376–1379, 1980.

[33] H Risken. *The Fokker-Planck equation*, volume 18 of *Springer series in synergetics.* Springer-Verlag, Berlin, 2nd edition, 1989.

[34] J D Cresser, D Hammonds, W H Louisell, P Meystre, and H Risken. Quantum noise in ring laser gyros, II: Numerical results. *Phys. Rev. A*, 25:2226–2234, 1982.

[35] J D Cresser, W H Louisell, P Meystre, W Schleich, and M O Scully. Quantum noise in ring laser gyros, I: Theoretical foundation of the problem. *Phys. Rev. A*, 25:2214–2225, 1982.

[36] J D Cresser. Quantum noise in ring laser gyros: III: Approximate analytic results in unlocked region. *Phys. Rev. A*, 26:398–409, 1982.

[37] J D Cresser. Theory of the spectrum of the quantised light field. *Phys. Rep.*, 94:47–110, 1983.

[38] K Vogel, Th Leiber, H Risken, P Hänggi, and W Schleich. Locking equatio with coloured noise: Continued fraction solution versus decoupling theory. *Phys. Rev. A.*, 35:4882–4885, 1987.

[39] K Vogel, H Risken, W Schleich, M James, F Moss, and P V E McClintock. Skewed probability densities in the ring-laser gyroscope: A coloured noise effect. *Phys. Rev. A.*, 35:463, 1987.

[40] K Vogel, H Risken, W Schleich, M James, F Moss, R Mannella, and P V E McClintock. Coloured noise in the ring-laser gyroscope. *J. Appl. Phys.*, 62:721–723, 1987.

[41] S Zhu. Steady-state analysis of a two-mode laser with multiplicative noise. *Phys. Rev. A*, 45:8148–8153, 1992.

[42] X Zho, W Gao, and S Zhu. Satuation effcts in a two-mode ring laser with both additive and multiplicative noise. *Phys. Lett. A*, 213:43–48, 1996.

[43] H A Haus. From classical to quantum noise. *J. Opt. Soc. Am. B*, 12:2019–2036, 1991.

[44] E S Polzik, J Carri, and H J Kimble. Spectroscopy with squeezed light. *Phys. Rev. Lett.*, 68:3020–3023, 1991.

[45] L Boivin. Sagnac-loop squeezer at zero dispersion with a response time for the Kerr nonlinearity. *Phys. Rev. A*, 52:754–766, 1995.

[46] M O Scully. Correlated spontaneous-emission lasers: Quenching of quantum fluctuations in the relative phase angle. *Phys. Rev. Lett.*, 55:2802–2805, 1985.

[47] M O Scully and M S Zubiary. Theory of quantum-beat laser. *Phys. Rev. A*, 35:752–758, 1987.

[48] M O Scully. A correlated emission gyroscope. *Phys. Rev. A*, 35:452–455, 1987.

[49] J-S Leu and A Papamarcou. On estimating the spectral exponent of fractional Brownian motion. *IEEE Tran. Inf. Theory*, 41:233–244, 1995.

[50] A R Mehrabi, H Rassamdana, and M Sahimi. Characterization of long-range correlations in complex distributions and profiles. *Phys. Rev. E*, 56:712–722, 1997.

[51] D W Allan. Statistics of atomic frequency standards. *Proc IEEE*, 54:221–230, 1966.

[52] V Solo. Intrinsic random functions and the paradox of 1/f noise. *SIAM J. Appl. Math.*, 52:270–291, 1992.

[53] Paul Horowitz. *The Art of Electronics.* Cambridge University Press, Cambridge, 1980.

[54] American Radio Relay League, Newington, Conn. *The Radio Amateur's Handbook*, 54 edition, 1977.

[55] A Gersho. Principles of quantisation. *IEEE Transactions on circuits and Systems*, 25:427–436, 1978.

[56] F R Connor. *Noise.* Edward Arnold, London, 2 edition, 1982.

[57] H R Bilger, U Schreiber, and G E Stedman. Design and application of a large perimeter ring lasers. In H Sorg, editor, *Proceedings of the Symposium Gyro Technology*, pages pp 8.0 – 8.8., 1996.

[58] U Schreiber, M Schneider, G E Stedman, C H Rowe, B T King, S J Cooper, D N Wright, and H Seeger. Preliminary results from a large ring laser gyroscope for fundamental physics and geophysics. In H Sorg, editor, *Proceedings of the Symposium Gyro Technology*, pages 16.0–16.5., 1997.

[59] C H Rowe, U Schreiber, S J Cooper, B T King, M Poulton, and G E Stedman. Design and operation of a very large ring laser gyroscope. *Appl. Opt.*, 38:2516–2523, 1999.

[60] A Yariv. *Optical Electronics.* CBS College Publishing, New York, 1985.

[61] K D Mielenz and K F Nefflen. Gas mixtures and pressures for optimum output power of RF-excited Helium:Neon gas lasers. *Appl. Opt.*, 4:565–567, 1965.

[62] E I Gordon and A D White. Similarity laws for the effects of pressure and discharge diameter on gain of He:Ne lasers. *Appl. Phys. Lett.*, 3:199, 1963.

[63] W R Bennett Jr. Hole burning effect in a He:Ne optical maser. *Phys. Rev.*, 126:580–593, 1962.

[64] P W Smith. The effects of cross relaxtion on the behavior of gas oscillators. *IEEE J. Quantum Electron.*, QE-8:704–709, 1972.

[65] F A Korolev, A I Odintsov, and V M Mitsai. A study of certain characteristics of a Helium:Neon laser. *Opt. Spectrosc.*, 19:36–39, 1965.

[66] P W Smith and T Haensch. Cross relaxation effects in the saturation in the 6328å neon-laser line. *Phys. Rev. Lett.*, 26:740–743, 1971.

[67] A E Siegman. *Lasers.* University Science Books, Mill Valley, California, 1986.

[68] W W Chow, J Yea-Bancloche, L M Pedrotti, V E Sanders, W Schleich, and M O Scully. The ring laser gyro. *Rev. Mod. Phys.*, 57:61–104, 1985.

[69] H A Haus, H Statz, and I W Smith. Frequency locking of modes in a ring laser. *IEEE J. Quantum Electron.*, QE-21:78–85, 1985.

[70] L Pesquera, R Blanco, and M A Rodriguez. Statistical properties of gas ring lasers with backscattering. *Phys. Rev. A*, 39:5777–84, 1989.

[71] R J C Spreeuw, R Centeno Neelen, J van Druten, E R Eliel, and J P Woerdman. Mode coupling in a C-II ring laser with backscattering. *Phys. Rev. A*, 42:4315–4324, 1990.

[72] F Aronowitz. Theory and operation of a travelling-wave laser. Technical Report R-RD 6413-1, Honeywell Systems and Research division, 1969.

[73] J R Wilkinson. Ring lasers. *Prog. Quant. Electr.*, 11:1–103, 1987.

[74] B D Fried and S D Conte. *The Plasma Dispersion Function.* Academic Press, New York, 1961.

[75] R L Fork and M A Pollack. Mode competition and collision effects in gaseous optical masers. *Phys. Rev.*, 139(5A):A1408–A1414, 1965.

[76] F Aronowitz and R J Collins. Lock-in and intensity-phase interaction in the ring laser. *J. Appl. Phys*, 41:130–141, 1970.

[77] R Adler. A study of locking phenomena in oscillators. *Proc. IRE*, 34:351–357, 1946. Reprinted in Proc. IEEE, **61**, 1380-1385, (1973).

[78] B Vander Pol. The nonlinear theory of electric oscillations. *Proc. IRE*, 22:1051, 1934.

[79] T J Hutchings, J Wincour, R H Durrett, E D Jacobs, and W L Zingery. Amplitude and frequency characteristics of a ring laser. *Phys. Rev.*, 152:467–473, 1966.

[80] F Aronowitz, J E Killpatrick, and S P Callaghan. Power-dependent corection to the scale factor in the laser gyro. *IEEE Quant. Electron.*, QE-10:201–208, 1974.

[81] B B Mandelbrot and J W Van Ness. Fractional Brownian motion, fractional noises and applications. *SIAM Rev.*, 10:422, 1968.

[82] M S Keshner. $1/f$ noise. *Proc. IEEE*, 70:212–218, 1982.

[83] N Wiener. *J. Math. and Phys. (Massachusetts Instsitute of Technology*, 2:131, 1923.

[84] N Weiner. *Acta. Math.*, 55:117, 1930.

[85] B B Mandelbrot. *Fractals: Form chance and dimension.* W H Freeman, San Francisco, 1977.

[86] G Hazel, F Bucholtz, and D Aggarwal. Characterisation and modelling of drift noise in Fourier transform spectroscopy: Implications for signal processing and detection limits. *Appl. Opt.*, 36:6751–6759, 1997.

[87] H Guillemet, H Benali, F Preteux, and R DiPaola. Noisy fractional brownian motion for detection of perturbations in regular textures. In E R Dougherty F Preteux and J L Davidson, editors, *SPIE*, volume 2823, pages 40–51. 1996.

[88] H Potlapalli and R C Luo. Fractal-based classification of natural textures. *IEEE Transactions on Industrial Electronics*, 45:142–150, 1998.

[89] N Chakravarti and K L Sebastian. Fractional Brownian motion models for polymers. *Chemical Physics Letters.*, 267:9–13, 1997.

[90] S H Supangkat, S Kawasaki, and H Morita. On analysis of acceptable region of a statistical multiplexer based on fractional Brownian traffic models. *IEICE Transactions on Fundamentals of Electronics Communications and Computer Sciences*, E81A:295–303, 1998.

[91] G W Baxter, R Leone, and R P Behringer. Experimental test of timescales in flowing sand. *Europhys. Lett.*, 21:569–574, 1993.

[92] J Stutzki, F Bensch, A V Heithausen, and M Zielinsky. On the fractal structure of molecular clouds. *Astronomy and Astrophysics*, 336:697–720, 1998.

[93] P Rougier. Influence of visual feedback on successive control mechanisms in upright quiet stance in humans assessed by fractional Brownian motion modelling source. *Neuroscience Letters*, 266:157–160, 1999.

[94] S Mukhopadhyay and J H Cushman. Monte Carlo simulation of contaminant transport i: Long-range correlations in fracture conductivity. *Transport in Porous Media*, 31:145–181, 1998.

[95] F J Molz, H H Liu, and J Szulga. Fractional Brownian motion and fractional gaussian noise in subsurface hydrology— A review, presentation of fundamental properties, and extensions. *Water Resources Research*, 33:2273–2286, 1997.

[96] M S Taqqu. Random processes with long range dependence and high variability. *J. Geophys. Res.*, 92(D8):9683–9686, 1987.

[97] C C P Tsai. Slip, stress drop and ground motion of earthquakes—A view from the perspective of fractional Brownian motion. *Pure and Applied Geophysics*, 149:689–706, 1997.

[98] K He, W Ye, and Z He. Signal model of noise in open-loop fiber-optic gyros. *Opt. Lett.*, 22:1742–1744, 1997.

[99] C M Van Vliet and P H Handel. A new transform theorem for stochastic processes with special application to counting ststistics. *Physica A*, 113:261–276, 1982.

[100] J A Barnes, A R Chi, L S Cutler, D J Healey, D B Leeson, T E McGunigal, J A Mullen, W L Smith, R L Sydnor, R F C Vessot, and G M R Winkler. Characterisation of frequency stability. *IEEE Trans. Instrum. Meas.*, IM-20:105–120, 1971.

[101] J Theiler. Some comments on the correlation dimension of $1/f^{\alpha}$ noise. *Phys. Lett. A*, 155:480, 1991.

[102] S Grivet Talocia. On the scale dependence of fractal dimension for band-limited $1/f^{\alpha}$ noise. *Phys. Lett. A*, 200:264–276, 1995.

[103] B Ninness. Estimation of $1/f$ noise. *IEEE Transactions on Inf. Theory*, 44:32–45, 1998.

[104] S Painter. Evidence for non-Gaussian scaling behavior in heterogeneous sedimentary formations. *Water Resour. Res.*, 32:1183–1195, 1996.

[105] T Day, E K Gustafson, and R L Byer. Sub-hertz relative frequency stabilisation of two-diode laser pumped Nd:YAG lasers locked to a Fabry-Pérot interferometer. *IEEE J. Quant. Electron.*, 28:1106–1117, 1992.

[106] L G Kazovsky. Balanced phase-locked loops for optical homodyne receivers: Performance analysis, design considerations and laser linewidth requirements. *J. Lightwave Technol.*, LT-4:182–195, 1986.

[107] A Abramovici, W E Althouse, R W P Drever, Y Gursel, S Kawamura, F J Raab, D Shoemaker, L Sievers, R E Spero, K S Thorne, R E Vogt, R Weiss, S E Whitcombe, and M E Zucker. LIGO: The laser interferrometer gravitational-wave observatory. *Science*, 256:325–333, 1964.

[108] D I Robertson, E Morrison, J Hough, S Killbourn, B J Meers, G P Newton, N A Robertson, K A Strain, and H Ward. The Glasgow 10 m prototype laser interferrometric gravitational wave detector. *Rev. Sci. Instrum.*, 66:4447–4452, 1995.

[109] H Schnatz, B Lipphardt, J Helmcke, F Riehle, and G Zinner. First phase-coherent frequency measurement of visible radiation. *Phys. Rev. Lett.*, 76:18–21, 1996.

[110] K Wallmeroth and R Letterer. Cesium frequency standard for lasers at $\lambda = 1.06\,\mu$m. *Opt. Lett*, 15:812–814, 1990.

[111] T Andreae, W Konig, R Wynands, D Leibfried, F Schmidt-Kaler, C Zimmerman, D Meschede, and T W Hansch. Absolute frequency measurement of the Hydrogen $1s \rightarrow 2s$ transition and a new value of the Rydberg constant. *Phys. Rev. Lett.*, 69:1923–1926, 1992.

[112] A J Wallard. The frequency stabilization of gas lasers. *J. Phys. E., Sci. Instr.*, 6:793–807, 1973.

[113] V Rautenberg, H-P Plag, M Burns, G E Stedman, and H-U Juttner. Tidally induced sagnac signal in a ring laser. *Geophys. Res. Lett.*, 24:893–896, 1997.

[114] W R C Rowley and D C Wilson. Wavelength stabilization of an optical maser. *Nature*, 200:745–749, 1963.

[115] D Lenstra and G C Herman. Saturation-induced polarisation preferences in two-mode oscillating gas lasers. *Physica C*, 95:405–411, 1978.

[116] Newport Corporation, `http://www.newport.com`. *User's Manual: Model NL-1 frequecncy-stabilised He-Ne laser.*

[117] E F Howick. Marsden Fund University of Canterbury 513 (Ring Laser) subcontract: Year 1 progress. Technical report, Industrial Research Limited, Wellington, 1997. Industrial Research Limited Report No. 705.

[118] K D Mielenz, K F Nefflen, W R C Rowley, D C Wilson, and E Engelhard. Reproducibility of Helium:Neon wavelengths at 633 nm. *Appl. Opt.*, 7:289–293, 1968.

[119] A D White. *Appl. Phy. Lett.*, 12:222–224, 1964.

[120] M L Skolnick, T G Polanyi, and I Tobias. The measurement of magnetically induced mode splitting in lasers. *Phys. Lett.*, 19:386–3877, 1965.

[121] A J Wallard. Frequency stabilization of the helium neon laser by saturated absorption in iodine vapour. *J. Phys. E., Sci. Instr.*, 5:926–930, 1972.

[122] M Kroll. Hyperfine structure of the visible molecular iodine spectrum. *Phys. Rev. Lett.*, 23:631–633, 1969.

[123] R L Barger and J L Hall. Pressure shift and broadening of methane line at 3.39 μ studied by laser-saturated absorption. *Phys.Rev. Lett.*, 22:4–8, 1969.

[124] G R Hanes and C E Dahlstrom. *Metrologia*, 5:32–33, 1969.

[125] G Popescu, J Chartier, and A Chartier. Iodine-stabilized Helium-Neon laser at $\lambda = 633$ nm: Design and international comparison. *Opt. Eng.*, 35:1348–1352, 1996.

[126] R B Hurst, N Brown, V D Dandawate, G R Hanes, J Helmcke, H P Layer, L Zhongyou, W R C Rowley, T Sakurai, and M S Chung. International intercomparison of Iodine-stabilized Helium-Neon lasers at 633 nm involving ten laboratories. *Metrologia*, 24:39–44, 1987.

[127] J-M Chartier, H Darmedde, M Frennberg, J Henningsen, U Karn, L Pendrill, J Hu, J C Petersen, O Poulsen andP S Ramanujam, F Riehle, L Robertson, B Stahlberg, and H Wahlgren. Intercomparison of Northern European $^{127}I_2$-stabilized lasers at $\lambda = 633$ nm. *Metrologia*, 29:331–339, 1992.

[128] S Goldman. *Frequency Analysis, Modulation, and Noise.* McGraw-Hill, New York, 1948.

[129] R W P Drever, J L Hall, F V Kowalski, J Hough, G M Ford, A J Munley, and H Ward. Laser phase and frequency stabilisation using an optical resonator. *Appl. Phys. B*, 31:97–105, 1983.

[130] Ch Salomon, D Hils, and J L Hall. Laser stabilisation at the millihertz level. *J. Opt. Soc. Am. B*, 5:1576–1587, 1988.

[131] S P Sandford and C W Antill Jr. Laser frequency control using an optical resonator locked to an electronic oscillator. *IEEE J. Quant. Electron.*, 33:1991–1996, 1997.

[132] G B Airy. *Mathematical Tracts of the lunar and planetary theories, the figure of the Earth, precession and nutation, the calculus of variation and the undulatory theory of optics.* J Smith, Printer to the University, for J and JJ Deighton, 1831.

[133] W Haidinger. Die interferenzlinien am glimmer, ber uhrungsringe und plattenringe. *Poggendorff's Annal. (LPZ)*, XCVI:453–468, 1851.

[134] J M Vaughan. *The Fabry-Pérot interferometer.* Hilger, Bristol, 1989.

[135] S George, J H Munsee, and J Verges. Hyperfine measurements of the line 613.4 nm in Bismuth using a Fourier transform spectrometer. *J. Opt. Soc. Am. B*, 2:568–569, 1985.

[136] Li Ziyuan, G E Stedman, and H R Bilger. Asymmetric response profile of a scanning Fabry-Pérot interferometer. *Opt. Commun.*, 100:240–247, 1993.

[137] G Hernandez. Analytical description of the Fabry-Pérot photoelectric spectrometer. *Appl. Opt.*, 5:1745–1748, 1966.

[138] K Krebs and A Sauer. Über die intensitätsverteilung von spektrallinien im Perot-Fabry-interferometer. *Ann. Physics. Lpz*, 13:359–368, 1953.

[139] A E Siegman, B Daino, and K R Manes. Preliminary measurements of laser short-term frequency fluctuations. *IEEE J. Quant. Electron.*, QE-3:180–189, 1967.

[140] E A Ballik. The response of scanning Fabry-Pérot interferometers to atomic transition profiles. *Appl. Opt.*, 5:170–172, 1966.

[141] J R Pierce. *Theory and design of electron beams.* Van Nostrand, New York, 1954.

[142] J Helmcke, S A Lee, and J L Hall. Dye laser spectrometer for ultrahigh spectral resolution: design and performance. *Appl. Opt.*, 21:1686–1694, 1982.

[143] R A Boyd, J L Bliss, and K G Libbrecht. Teaching physics with 670-nm diode lasers-experiments with Fabry-Pérot cavities. *Am. J. Phys.*, 64:1109–1116, 1996.

[144] R V Pound. *Rev. Sci. Instrum.*, 17:490–505, 1946.

[145] C J Bjorkland et al. Frequency-modulation (FM) spectroscopy-theory of line shapes and signal-to-noise analysis. *Appl. Phys. B*, 31:145–152, 1983.

[146] Newport Corporation, `http://www.newport.com`. *Supercavity optical spectrum analyser instruction manual.*

[147] K R Manes and A E Siegman. Observation of quantum phase fluctuations in infrared gas lasers. *Phys. Rev. A*, 4:373–386, 1971.

[148] R Rodloff. A laser gyro with optimized resonator geometry. *IEEE J. Quant. Electron.*, QE-23:438–445, 1987.

[149] H R Bilger and G E Stedman. Stability of ring lasers with mirror misalignment. *Appl. Optics.*, 26:3710–3716, 1987.

[150] S J Cooper, E Howick, D Mcleod, D Wright, B T King, and G E Stedman. A method to lower the detection limit for optical beat signals from a frequency-dithered stabilised laser. *Measurement Science and Technology*, 12:1726–1733, 2001.

[151] J Killpatrick. The laser gyro. *IEEE Spectrum*, 4:44, October 1967.

[152] M M Tehrani and L Mandel. Coherence theory of the ring laser. *Phys. Rev. A*, 17, 1978.

[153] M M Tehrani and L Mandel. Intensity fluctuations in a two-mode ring laser. *Phys. Rev. A*, 17:694–700, 1978.

[154] S Zhu. Saturation effects in a two-mode ring laser. *Phys. Rev. A*, 50:1710–1715, 1994.

[155] J E Moyal. *J. Roy. Stat. Soc. B*, 11:150, 1949.

[156] S Siegert, R Friedrich, and J Peinke. Analysis of data sets of stochastic systems. *Phys. Lett. A*, 243:275–280, 1998.

[157] M O Scully and W E Lamb Jr. Quantum theory of an optical maser. *Phys. Rev*, 159:208–226, 1967.

[158] H Haken, H Sauermann, Ch Schmid, and H D Vollmer. Theory of laser noise in the phase locking region. *Z. Phys.*, 206:369–393, 1967.

[159] G Arfken. *Mathematical methods for physicists.* Academic Press, New York, 2nd edition edition, 1970.

[160] D T Gillespie. The mathematics of Brownian motion and Johnson noise. *Am. J. Phys.*, 64:225–240, 1996.

[161] R F Fox, I R Gatland, R Roy, and G Vemuri. Fast, accurate algorithm for numerical simulation of exponentially correlated colored noise. *Phys. Rev. A*, 38:5938–5940, 1988.

[162] J B Fraleigh and R A Beauregard. *Linear Algebra.* Addison-Wesley, Reading, Massachusetts, 1987.

[163] P Lesage. Characterization of frequency stability: Bias due to the juxtaposition of time-interval measurements. *IEEE Instr and Measurement.*, 32:204–207, 1983.

[164] W V Prestwich, T J Kennett, and F W Kus. The statistical properties of the Allan variance. *Can. J. Phys.*, 69:1405–1415, 1991.

[165] R G Wiley. A direct time-domain measure of frequency stability: the modified Allan variance. *IEEE Instr and Measurement.*, 26:38–41, 1977.

[166] J Rutman. Chracterization of frequency stability: a transfer function approach and its application to measurements via filtering of phase noise. *IEEE Instr and Measurement.*, 23:40–48, 1974.

[167] T J Ulrych and T N Bishop. Maximum entropy spectral analysis and autoregressive decomposition. *Rev. Geophysics and Space Phys.*, 13:183–200, 1975.

[168] W K Pratt. *Digital Image Processing.* Wiley, 2nd edition, 1991.

[169] National Instruments. *G Programming Reference Manual*, 1998.

[170] K N Whitley and A F Blackwell. Visual programming: the outlook from academia and industry. In S Wiedenbeck and J Scholtz, editors, *Proceedings of the 7th Workshop on Empirical Studies of Programmers*, pages 180–208, 1998.

[171] R Bitter, T Mohiuddin, and M Nawrocki. Process improvement through rapid application development. Technical report, Motorola.